OUKA
Osaka University Knowledge Archive

Title	Solid-state bonding using Ag nanoporous sheet for high temperature die attach
Author(s)	Kim, Minsu
Citation	大阪大学, 2016, 博士論文
Version Type	VoR
URL	https://doi.org/10.18910/59583
rights	
Note	

Osaka University Knowledge Archive : OUKA

https://ir.library.osaka-u.ac.jp/

Osaka University

Doctoral Dissertation

Solid-state bonding using Ag nanoporous sheet for high temperature die attach

Min-Su Kim

April 2016

Graduate School of Engineering
Osaka University

Supervisor

Assoc. Prof. Hiroshi Nishikawa, Ph. D.

Department of Smart Green Processing, Joining and Welding Research Institute
Osaka University

Doctoral Committee

Assoc. Prof. Hiroshi Nishikawa, Ph. D.

Department of Smart Green Processing, Joining and Welding Research Institute
Osaka University

Prof. Shinsuke Yamanaka, Ph. D.

Division of Sustainable Energy and Environmental Engineering, Graduate School of Engineering
Osaka University

Prof. Michihiko Ike, Ph. D.

Division of Sustainable Energy and Environmental Engineering, Graduate School of Engineering
Osaka University

Prof. Akio Hirose, Ph. D.

Division of Materials and Manufacturing Science, Graduate School of Engineering
Osaka University

Contents

List of figures

List of tables

Abbreviations and symbols

Abbreviations

AMB	active metal brazing
BE	binding energy
BF	bright field
CP	cross-section polisher
CTE	coefficient of thermal expansion
DBC	direct bond copper
DF	dark field
EDS	energy dispersive X-ray spectroscopy
EELS	electron energy loss spectroscopy
ENEPIG	electroless Ni/electroless Pd/ immersion Au
ENIG	electroless Ni/immersion Au
EPMA	electron probe micro-analyzer
EV	electric vehicle
FEG	field emission gun
FFT	fast Fourier transform
FIB	focused ion beam
HEV	hybrid electric vehicle
HRTRM	high resolution transmission electron microscopy
ICDD	International Centre for Diffraction Data
IFFT	inverse fast Fourier transform
LN	less noble
MIL-STD	United States Military Standards
MN	more noble
MOSFET	metal oxide semiconductor field effect transistor
NPB	nanoporous bonding
OFC	oxygen-free copper
PCU	power control unit
PDF	powder diffraction file
RIR	reference intensity ratio
RoHS	restriction of hazardous substances
SAED	selected area electron diffraction
SAT	scanning acoustic tomography
SCR	silicon controlled rectifier

SEM	scanning electron microscopy	**WBG**	wide-bandgap
STEM	scanning transmission electron microscopy	**WDS**	wavelength dispersive X-ray spectroscopy
TEM	transmission electron microscopy	**XPS**	X-ray photoelectron spectroscopy
TLP	transient liquid phase	**XRD**	X-ray diffractometer
TRIAC	triode for alternating current		

Symbols

a	lattice parameter	t	time
C_v	equilibrium concentration of vacancies	T	absolute temperature
		T_{max}	maximum soaking temperature
D	diffusivity	T_{min}	minimum soaking temperature
D_s	surface diffusivity	V_c	unit cell volume
d_{hkl}	interplanar spacing of *hkl* plane	V_m	molar volume
d_m	spacing of moiré fringe	x	diffusion length
E_b	elastic modulus of bulk material	Z	number of formula units per unit cell
E_f	formation energy of vacancy		
E_p	elastic modulus of porous material	γ	surface energy
k_B	Boltzmann constant	ΔT	temperature variation
N	number of atom	θ	diffraction angle, interplanar angle
N_a	Avogadro constant	λ	wavelength
N_v	number of vacancy	ρ_b	relative density of bulk material
r	radius	ρ_p	relative density of porous material
r_{met}	atomic radius (metallic)		

Chapter 1
Research background

1.1 Recent trends in power electronics

1.1.1 Applications of power electronics

Power electronics is a key component for the conversion, control and distribution of electrical energy. [1–4] In particular, electric powered transportations, such as electric/hybrid electric vehicles (EV/HEV) [5] and railway [6]; and renewable energy technologies, such as photovoltaic power generation [7] and wind turbine systems [8], have been received attention in order to overcome energy problem and to reduce carbon emission and air pollution. This effort to utilization of clean and renewable energy augments the demand and the importance of power electronics gradually.

Fig 1.1 shows various applications of power semiconductors with different operation frequencies and capacities. The range of applications of power semiconductors cover from home appliances to industrial applications which are powered by electricity [1]. The operating ranges of voltage, current and frequency are varied with the type of power semiconductors. The operating regions of thyristors cover low frequency (up to 100 Hz/1 kHz) and high voltage and current (over 5 kV and 2 kA). Silicon controlled rectifier (SCR), triode for alternating current (TRIAC) and gate turn-off thyristor (GTO) are a type of thyristors. Insulated gate bipolar transistor (IGBT) covers middle frequency (up to 50 kHz) and medium voltage and current (up to 3 kV and 1 kA). The operating range

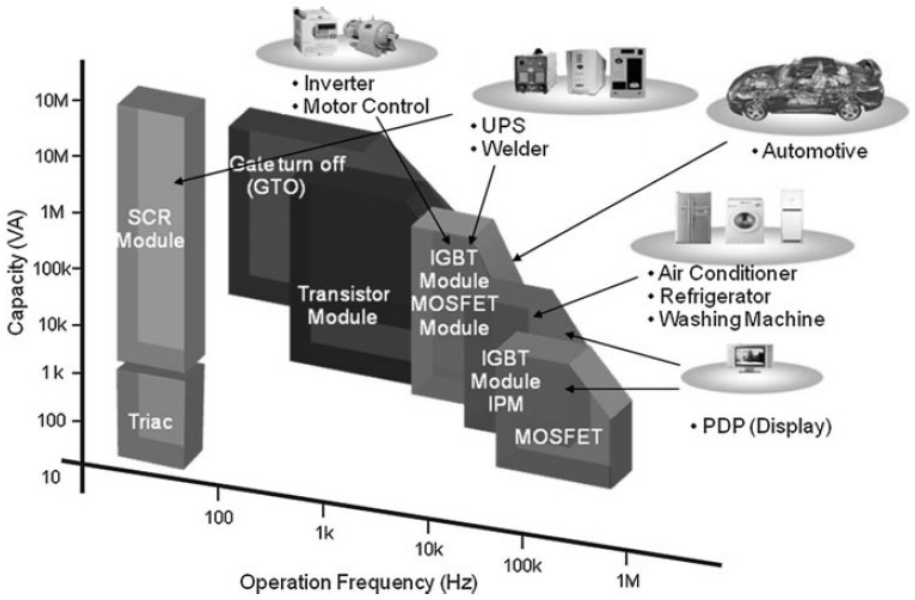

Figure 1.1 Various applications of power electronics. Reprinted with permission from [1]. Copyright 2012, Springer.

of metal oxide semiconductor field effect transistor (MOSFET) covers high frequency (up to 1 MHz) and low voltage and current (up to 1 kV and 100 A) [1,4].

1.1.2 Wide-bandgap semiconductor for next generation power electronics

A growth of power density in power electronics and a limitation of conventional silicon (Si) power semiconductor lead to develop the next generation power semiconductor [9]. Wide-bandgap (WBG) semiconductors, such as silicon carbide (SiC) and gallium nitride (GaN) could operate at higher temperature compared with conventional Si devices. The limit operating junction temperature of Si devices is 150-200 °C, which is lower than requirement of junction temperature (approximately 220 °C) for automotive applications [1,10,11]. As shown in Fig. 1.2, the performance of current Si semiconductors cannot meet the requirements for DC-DC converter in automotive application, especially thermal conductivity and limit of junction temperature [11]. Fig. 1.3 shows operation limits of conventional Si and WBG semiconductors, including SiC, GaN and diamond, where the allowing junction temperature of high-voltage (> 10kV) SiC power semiconductor is over 500 °C. The WBG semiconductors therefore have been regarded as promising materials for next generation power electronics. Physical properties of Si and typical WBG semiconductors are shown in Table 1.1 [10].

The high frequency operation of power electronics increase heat generation by switching

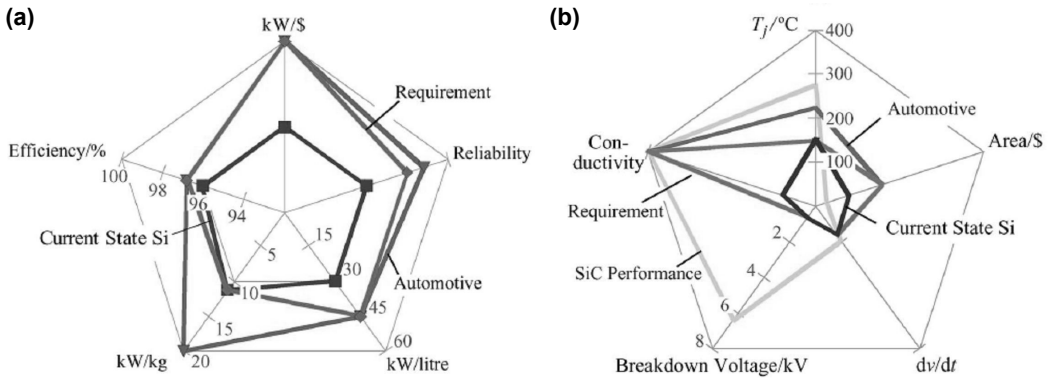

Figure 1.2 Radar charts of **(a)** system level requirements and **(b)** component level requirements for low voltage DC-DC converter in the telecommunication and the automotive applications. Reprinted with permission from [11]. Copyright 2011, IEEE.

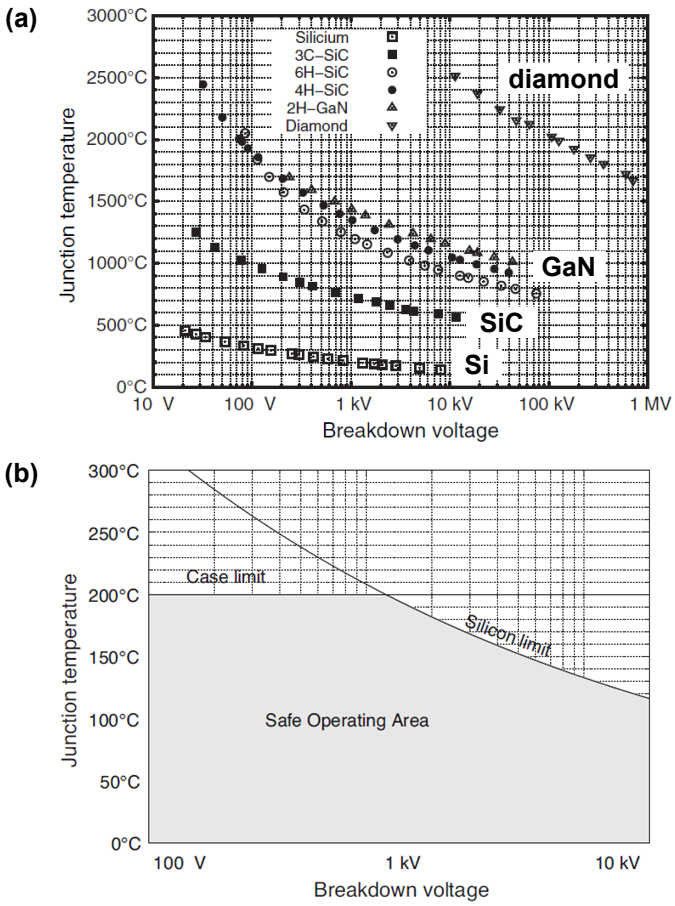

Figure 1.3 **(a)** Theoretical operation limits of Si, SiC, GaN and diamond semiconductor at the optimal structure and **(b)** the safe operating temperature of Si semiconductor, where the *case limit* corresponds to maximum operating temperature regulated by the packaging materials (such as solder, molding compound and silicon gel) and the *silicon limit* corresponds to breakdown voltage of Si as a function of junction temperature. Reprinted with permission from [10]. Copyright 2011, Elsevier.

Table 1.1 Physical properties of Si and wide-bandgap semiconductors [10].

	Si	3H-SiC	6H-SiC	4H-SiC	GaN	Diamond
Bandgap energy, E_g (eV)	1.12	2.3	2.9	3.2	3.39	5.6
Electron mobility, μ_n ($cm^2\ V^{-1}\ S^{-1}$)	1450	1000	415	950	2000	4000
Hole mobility, μ_p ($cm^2\ V^{-1}\ S^{-1}$)	450	45	90	115	350	3800
Critical electric field, E_c ($V\ cm^{-1}$)	3×10^5	2×10^6	2.5×10^6	3×10^6	5×10^6	10^7
Saturation velocity, v_{sat} ($cm\ s^{-1}$)	10^7	2.5×10^7	2×10^7	2×10^7	2×10^7	3×10^7
Thermal conductivity, λ ($W\ cm^{-1}\ K^{-1}$)	1.3	5	5	5	1.3	20
Dielectric constant, ε_r	11.7	9.6	9.7	10	8.9	5.7

loss. There are two solutions for reduction switching loss, including soft-switching converters and WBG semiconductor [2]. The WBG semiconductor devices are able to reduce switching loss approximately 70% compared with conventional Si semiconductor devices [12], which enable to reduce heat generation and to operate at high frequency.

1.1.3 Power electronics in electric powered vehicles

Power control unit (PCU) is the most important components of electric powered vehicle (Fig. 1.4), where multiple power modules are integrated in PCU to control electrical power (Fig. 1.5). An insulated gate bipolar transistor (IGBT) power module (Fig.1.6) has been used in EV/HEV for power switching in the last years. The IGBT module combines the advantages of high switching speed of MOSFET and low saturation voltage of bipolar transistor, and it make possible to use in EV/HEV [13]. The performance, reliability and efficiency of IGBT module are required for the efficiency of driving and control of electric EV/HEV [13,14].

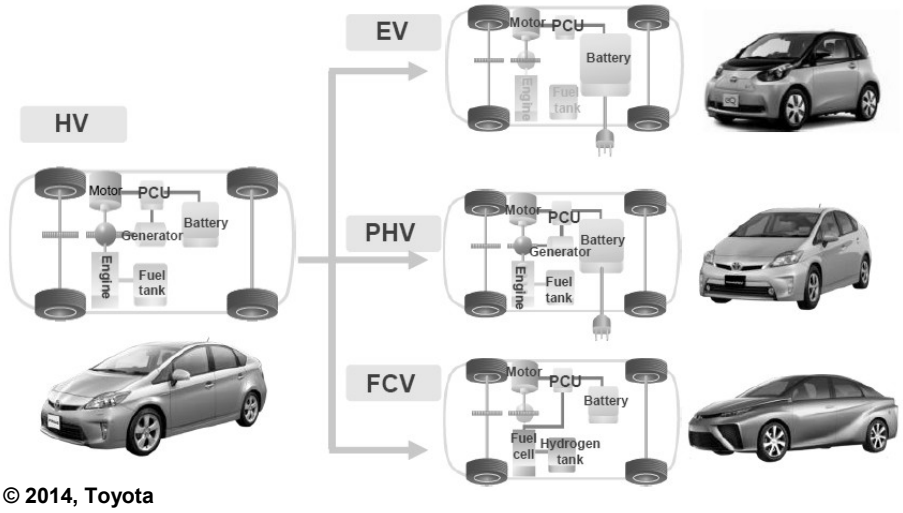

Figure 1.4 Developments and power flow in electric vehicle (EV), plug-in hybrid vehicle (PHV) and fuel cell vehicle (FCV) from hybrid vehicle (HV) technology (courtesy of Toyota Motor Corporation).

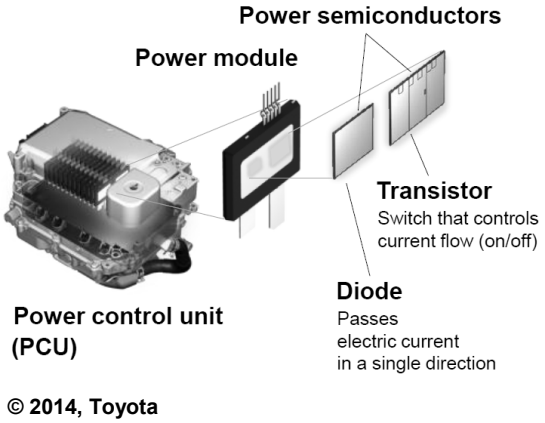

Figure 1.5 A role of power semiconductor in the power control unit (courtesy of Toyota Motor Corporation).

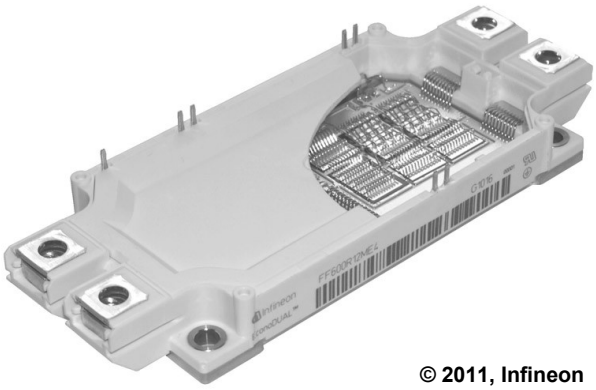

Figure 1.6 IGBT power module, EconoDUAL™ 3 of Infineon (courtesy of Infineon Technologies AG).

1.2 Immerging technology for power electronics packaging materials

Fig. 1.7 shows a typical structure of IGBT power module, employed various components from ceramics to metals. The high current density capability, high temperature durability and good thermal dissipation ability are desirable properties of packaging materials for power electronics. A considerable amount of heat is generated from the IGBT device during operation. Moreover, the power electronics for automotive application is exposed to severe service environmental, such as wide temperature variation, humid and salty environments and vibration. It is necessary to consider the failure occurrence of power electronics packaging under various service environments.

Fig. 1.8 shows typical failure locations during operating of power devices. The fatigue crack propagation and fracture of die attach joint layer (Fig. 1.8(a)), lift-off or heel crack of wire bonding (Fig. 1.8(b)) and delamination of substrate metallization (Fig. 1.8(c)) are common failures of IGBT module [15]. A cycling thermo-mechanical loading induced by mismatch of coefficient of thermal

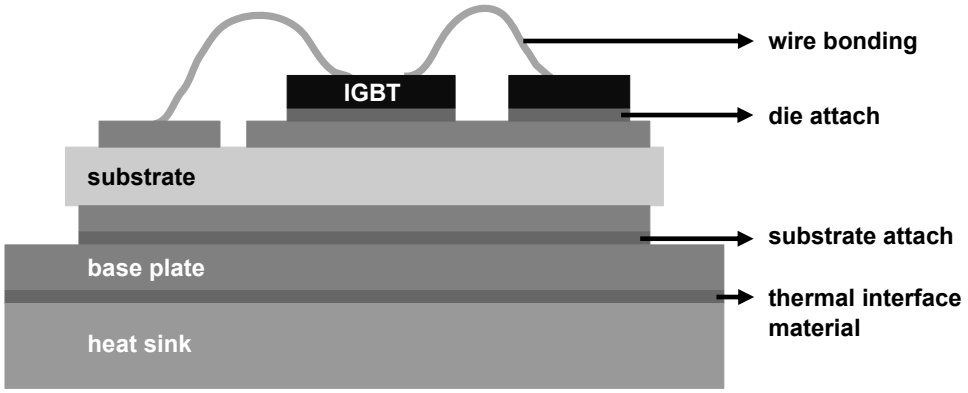

Figure 1.7 Schematic diagram of typical structure of IGBT power module (not to scale).

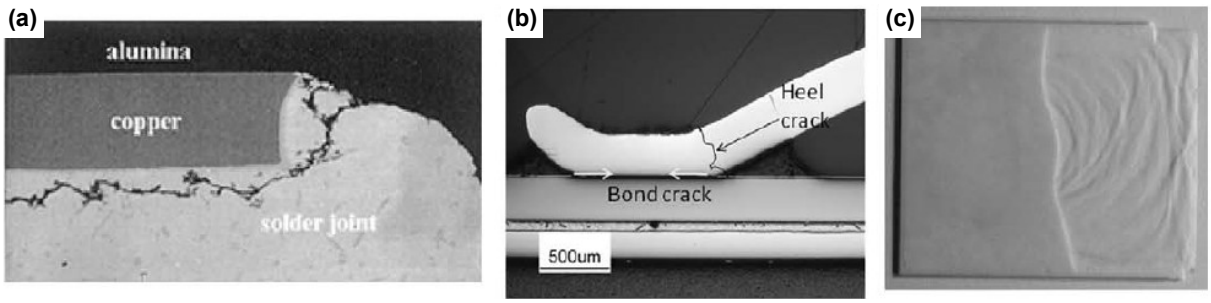

Figure 1.8 Typical failure locations under cyclic thermo-mechanical loading in IGBT module packaging: **(a)** solder joint for the die/substrate attach, **(b)** wire bonding and **(c)** substrate. Reprinted with permission from [15]. Copyright 2009, Elsevier.

Table 1.2 Thermal properties of common packaging materials [3,17].

Component	Material	Thermal conductivity, λ (W cm^{-1} K^{-1})	Coefficient of thermal expansion, α (ppm/K)
Semiconductor	Si	1.3	2.6
	SiC	5.0	3.8
	GaN	1.3	6.2
Wire bonding	Au	3.17	14.2
	Al	2.05	17
	Cu	4.0	16.5
Die attach	Pb-5Sn	0.35	29
	Au-20Sn	0.57	16
	Ag	4.06	19
Substrate	Al_2O_3	0.30	6.5
	AlN	2.0	4.5
	Si_3N_4	0.9	2.6

expansion (CTE) between dissimilar materials at the interface is main cause of these failures [15,16]. Thermal properties of typical materials for power electronics are given in Table 1.2 [3,17]. More detailed information on the failure mechanism of the wire bonding, die attach and ceramic substrate and related research trends will be mentioned in following sections.

1.2.1 Wire bonding interconnection

Wire bonding plays a role of electrical interconnection between power semiconductor and lead frame. Al wire is a conventional interconnection material generally employed in the electronics; however it is not suitable for high current power electronics due to limited current carrying capability and long-term reliability issues at elevated temperature. To address these issues, heavy Al wire or Al ribbon bonding (Fig. 1.9) [18] and Cu wire bonding (Fig. 1.10) [19] have been suggested. Cu wire bonding is more promising material due to its reasonable cost and high electrical conductivity, however there remains some challenges, such as complicated bonding process and Cu oxidation. Al/ Cu clad ribbon for the reduction of heel crack [20], Pd coated Cu for the prevention of Cu oxidation [21] have been reported in order to improve current problems of Al ribbon or Cu wire bonding.

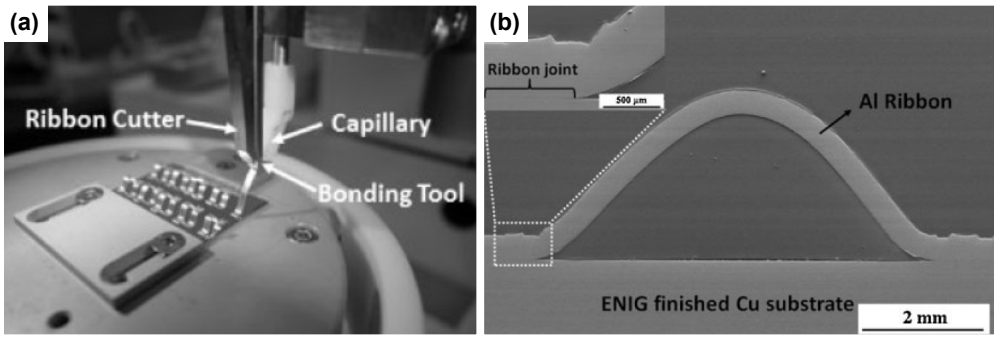

Figure 1.9 Al ribbon bonding: **(a)** bonding tool and **(b)** cross-sectional SEM image of Al ribbon bonding with ENIG substrate. Reprinted with permission from [18]. Copyright 2014, The Japan Society of Applied Physics .

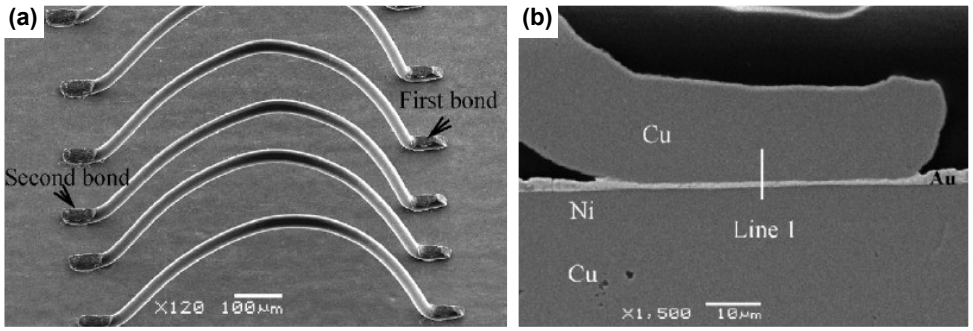

Figure 1.10 **(a)** Appearance of Cu wire bonding and (b) cross-sectional SEM image of Cu wire bonding. Reprinted with permission from [19]. Copyright 2008, Elsevier.

1.2.2 Die/substrate attach

As shown in Fig. 1.9, there are two bonding layers, including die attach (chip to substrate) and substrate attach (substrate to base plate), for mechanical bonding between the dissimilar materials. High Pb containing solders, Pb-5Sn and Pb-10Sn, have been generally employed for high temperature electronics. Alternative die attach materials is necessary to address the immersing two issues on the long-term reliability and environmental regulation on the use of Pb in electronics. Alternative bonding techniques, including high temperature solder alloys, transient liquid phase bonding and Ag nanoparticle sintering have been suggested. Fig. 1.11 shows joints of representative alternative bonding methods for power electronics die attach. Detailed information about the high temperature die attach materials will be mentioned in *Section 1.3*.

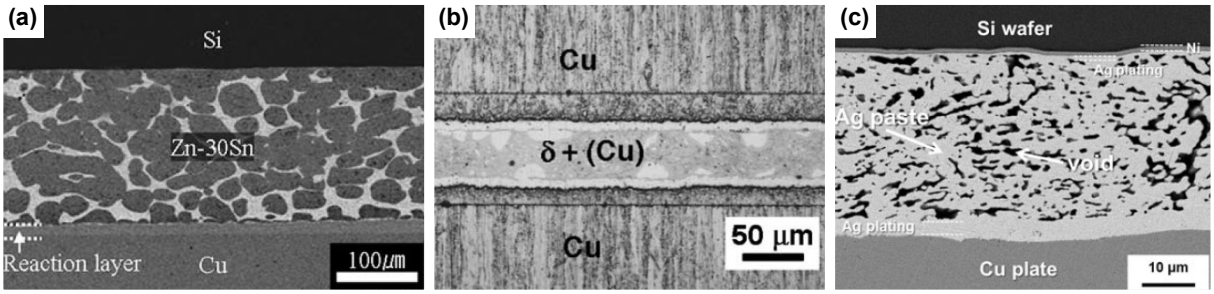

Figure 1.11 Cross-sectional SEM images of **(a)** Zn-Sn high temperature solder (reprinted with permission from [26]. Copyright 2009, Springer), **(b)** transient liquid phase bonding of Cu/Sn/Cu system (reprinted with permission from [27]. Copyright 2004, Elsevier) and **(c)** Ag flake-shape particle sintering (reprinted with permission from [28]. Copyright 2013, Springer).

1.2.3 Ceramic substrate with Cu metallization

In high power electronics, the heat generation during operation of IGBT module is abundant, and this causes temperature rise in the module. The ceramic substrate has the roles of relaxation of stress generation induced by CTE mismatch of chip and substrate and heat dissipation from the semiconductor device. Thermal management in power electronics is very important that is directly connected to the performance and the long-term reliability of device. Aluminum oxide (Al_2O_3), having the similar CTE with semiconductor materials (Table 1.2), with Cu metallization has been widely employed for ceramic substrate, usually called direct bond copper (DBC) substrate. Cu metallization

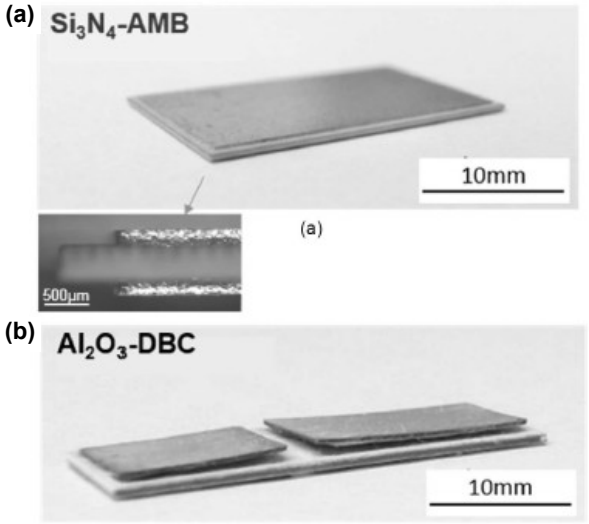

Figure 1.12 Appearances of **(a)** Si_3N_4 active metal brazed substrate after 600 cycles and **(b)** Al_2O_3 direct bond copper substrate after 100 cycles exposed to temperature cycle from –55 °C to 250 °C. Reprinted with permission from [21]. Copyright 2014, IEEE.

exhibits high peel strength (over 65 N/cm) with Al_2O_3 or aluminum nitride (AlN) through DBC process [22].

However, Al_2O_3 cannot meet the requirements for IGBT module with the growth of power density and increase of junction temperature, due to low thermal conductivity and poor thermal cycle durability at wide temperature swing [22,23]. Two promising substrate materials, AlN DBC and silicon nitride (Si_3N_4) active metal brazed (AMB) substrates have been received attention due to their superior thermal conductivity and temperature cycle durability. Fukimoto et al. [23] reported comparable research on the delamination behavior of Si_3N_4 AMB and Al_2O_3 DBC substrates during extreme temperature cycle from -55 °C to 250 °C. As shows in Fig. 1.12, the Si_3N_4 AMB exhibits excellent stability without any delamination of Cu metallization up to 600 cycles, however, the Al_2O_3 exhibits small number of cycle to failure (under 100 cycles). Typical characteristics of Al_2O_3, AlN, Si3N4 for DBC or AMB substrates can be summarized as follows.

- Al_2O_3 DBC : cheap price, low thermal conductivity poor temperature cycle durability
- AlN DBC : high thermal conductivity, moderate temperature cycle durability
- Si_3N_4 AMB: medium thermal conductivity, excellent high temperature durability

1.3 High temperature die attach

1.3.1 Current situation of environmental regulation in high temperature electronics

An eutectic Pb-Sn solder for general electronic devices has been replaced with Sn-based solders, especially eutectic Sn-Ag-Cu [24], to respond environmental regulation, “Directive 2002/95/ EC of the European Parliament and of the Council of 27 January 2003 on the restriction of the use of certain hazardous substances in electrical and electronic equipment”, referred to as RoHS [25]. However, the substitution solder alloys for high Pb containing solders, such as Pb-5Sn and Pb-10Sn, are not established yet.

At present, the high Pb containing solders have been designated as the exemption application from the environmental regulation, “Directive 2011/65/EU on the restriction of the use of certain hazardous substances in electrical and electronic equipment (recast)”, referred to as RoHS2. A list of applications exempted of use of Pb in solders from the RoHS2 is summarized in Table 1.3. The validity period for *category 7(a)*, high Pb containing solders (Pb content > 85 wt.%), is 5 years from

21 July 2011. Namely, the exemption of high Pd containing solder will be expired or renewed in 2016 [26].

As an effort to eliminate the high Pb containing solders in the high temperature electronics, a numerous alternative Pb-free bonding techniques that could be used as high temperature die attach

Table 1.3 Applications exempted from the restriction of the use of lead in solders in Directive 2011/65/EU (RoHS2) [24].

	Exemption category	Scope and dates of applicability
7(a)	Lead in high melting temperature type solders (i.e. lead-based alloys containing 85 % by weight or more lead)	
7(b)	Lead in solders for servers, storage and storage array systems, network infrastructure equipment for switching, signalling, transmission, and network management for telecommunications	
14	Lead in solders consisting of more than two elements for the connection between the pins and the package of microprocessors with a lead content of more than 80 % and less than 85 % by weight	Expired on 1 January 2011 and after that date may be used in spare parts for EEE placed on the market before 1 January 2011
15	Lead in solders to complete a viable electrical connection between semiconductor die and carrier within integrated circuit flip chip package	
24	Lead in solders for the soldering to machined through hole discoidal and planar array ceramic multilayer capacitors	
27	Lead alloys as solder for transducers used in high-powered (designated to operate for several hours at acoustic power levels of 125 dB SPL and above) loudspeakers	Expired on 24 September 2010
31	Lead in soldering materials in mercury free flat fluorescent lamps (which, e.g. are used for liquid crystal displays, design or industrial lighting)	
33	Lead in solders for the soldering of thin copper wires of 100 μm diameter and less in power transformers	

have been reported. The alternative solders that exhibit high melting temperature over 260 °C will be mentioned in *Section 1.3.2*. Other new bonding processes which can be classified as low temperature bonding techniques, including transient liquid phase (TLP) bonding and metallic nanoparticle sintering, will be mentioned in *Section 1.3.3* and *Section 1.3.4*. These bonding processes can be conducted under the temperature of 300 °C, which is similar with the melting temperature of conventional Pb-5Sn. Fig. 1.11 shows microstructural features of typical alternatives of high Pb containing solders for high temperature die attach, including Zn-Sn high temperature solder [27], transient liquid phase bonding of Cu/Sn/Cu system [28] and Ag flake sintering [29].

1.3.2 High temperature solders

Suganuma et al. [30] mentioned that high temperature solders exhibit the range of melting temperature of 260 °C to 400 °C, and summarized the requirements and applications of these high-

Table 1.4 Solidus and liquidus temperatures of typical Pb-free high temperature solders system [30].

Alloy system	Composition (wt%)	Solidus temperature(°C)	Liquidus temperature (°C)
Pb-Sn	Pb-10Sn	268	301
	Pb-5Sn	300	314
	Pb-2Sn	316	322
Au-Sn	Au-20Sn	280 (eutectic)	-
Au-Ge	Au-12Ge	356 (eutectic)	-
Bi-Ag	Bi-2.5Ag	263 (eutectic)	-
	Bi-11Ag	263	360
Zn-Al	Zn-6Al	381 (eutectic)	-
	Zn-4Al-3Mg-3.2Ga	309	347
Zn-Sn	Zn-20Sn	198	383
	Zn-30Sn	198	374
	Zn-40Sn	198	365
Sn-Sb	Sn-5Sb	245 (eutectic)	-

temperature solders, including their melting temperature, mechanical/thermal/electrical properties, and current applications. High-temperature solders should exhibit relaxation ability of thermal stress of joint, good electrical, thermal and mechanical properties and so on. Especially fatigue resistance to withstand at the high junction temperature above 200 °C is important factor for long-term reliability. Many researchers have suggested on the potential candidates for Pb-free high temperature solders in the past decade. Au- [31], Bi- [32] and Zn-based solders [27] are typical alloys of high temperature solders. The solidus and liquidus temperatures of candidates of high temperature solder alloys and their characteristics can be found in Table 1.4 and Table. 1.5 [30,33]. Further information can be found in some review articles [30,33–36].

The suggested candidates of high temperature Pb-free solder alloy remains some challenges of solving cost or reliability problems (Table 1.5). The extremely high cost of Au-based alloys discourages mass production. Bi-based alloys are brittle and exhibit poor thermal conductivity. Zn-

Table 1.5 Typical Pb-free high temperature solders system and their advantages and disadvantages [33].

Alloy system	Advantages	Disadvantages
Au-Sn	• fluxless • good creep resistance	• expensive • Brittle Au-Sn IMCs
Au-Ge	• low elastic modulus • stable microstructure • relative high strength	• expensive • difficult to manufacture
Bi-Ag	• acceptable melting point • affordable cost	• poor workability • low conductivity
Zn-Al	• low cost • no IMC formed under equilibrium	• highly corrosive • poor wetting
Zn-Sn	• low cost • no IMC formed under equilibrium • ductility improved compared to Zn-Al	• highly corrosive • formation of liquid phase at 199 °C
Sn-Sb	• stable microstructure • good creep properties	• toxic

based alloys exhibit poor corrosion resistance [33]. These drawbacks inhibit the successful adoption of these solder materials in power electronic applications that require operation in severe environments and at high-temperatures, and so it is necessary to develop these materials and processes further.

1.3.3 Transient liquid phase bonding

TLP bonding is a partial melting of interlayer with the low melting temperature and simultaneous diffusion and reaction with parent material, and has been utilized in the various applications [28,37–40]. The schematic diagram of TLP bonding process is shown in Fig. 1.13. The TPL bonding is conducted above the melting temperature of interlayer. In microelectronics packaging industry, the low melting temperature elements, such as Sn and In, have been utilized as an interlayer for TLP bonding. A numerous TLP systems including Cu/Sn, Ag/Sn, Ni/Sn and Cu/In, have been reported [37–39].

The difference between reflow solder joint and TLP bonding joint are shown in Fig. 1.14. The reflow solder joint foamed solidified solder layer and intermetallic compounds with the thickness of a few μm at the interface (Fig. 1.14(a)). In case of TLP bonding, the interlayer (low melting temperature layer) is completely consumed through the reaction with high melting temperature layer. Consequently the final joint consists of Cu and intermetallic compound (IMC) which exhibit high

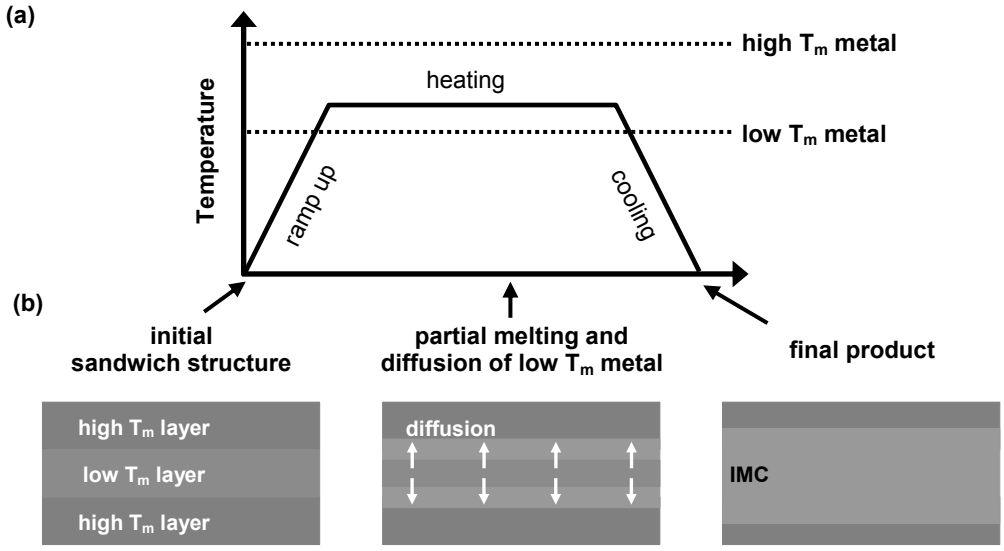

Figure 1.13 Schematic diagram of **(a)** bonding temperature profile of transient liquid phase bonding and **(b)** joint formation by partial melting and diffusion of interlayer element and subsequent formation of intermetallic compound.

melting temperatures (Fig. 1.14(b)). For example, there are two stable IMCs, including η-Cu_6Sn_5 and ε -Cu_3Sn, less than 300 °C (approximate TLP bonding temperature) in binary Cu-Sn system. Maximum stable temperatures of η-Cu_6Sn_5 and ε-Cu_3Sn are 415 °C and 676 °C, respectively, where these are higher than melting point of Sn-based solder [41]. As a result, a permissible temperature of TLP joint of Cu/Sn/Cu system exhibit over 415 °C. Chu et al. reported on the consumption of interlayer (Sn) and growth behavior of IMCs of Cu/Sn/Cu and Ni/Sn/Ni system with the various metallization (Cu and Ni) thicknesses, as shown in Fig. 1.15. According to this report, the shear strength of TLP bonding joint is affected on the interfacial reaction between Cu and Sn (or Ni and Sn), and the fracture surface exhibits intergranular fracture (at the grain boundary of IMCs) [39].

The TLP bonding technique has several advantages, such as high temperature sustainability, repeatability, reasonable cost and moderate bonding pressure/temperature, for alternative of Pb-5Sn

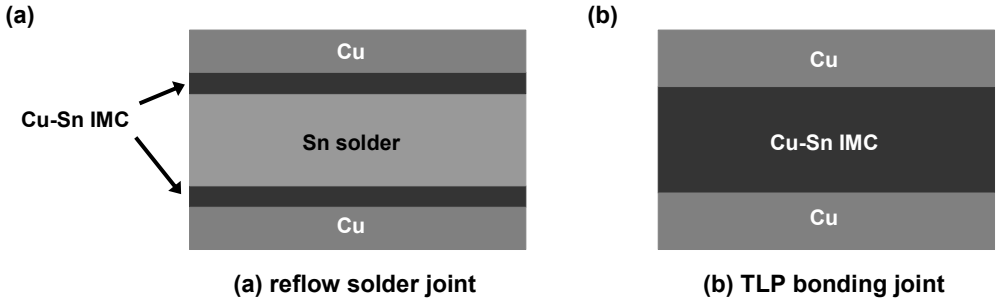

Figure 1.14 Schematic diagrams of **(a)** reflow solder joint Sn solder with Cu metallization and **(b)** Cu/Sn/Cu transient liquid phase bonding joint (not to scale).

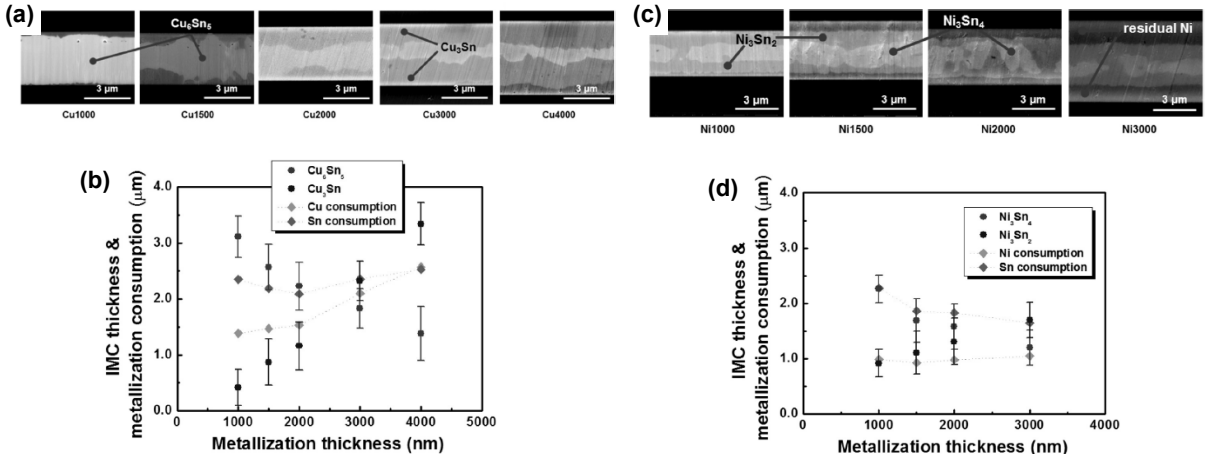

Figure 1.15 SEM images of TLP bonding joint, and growth of intermetallic compound and metallization consumption during bonding process: **(a, b)** Cu/Sn/Cu and **(c, d)** Ni/Sn/Ni systems. Reprinted with permission from [39]. Copyright 2015, Elsevier.

solder [38,42]. Moreover, two stable IMCs in Cu/Sn/Cu system, η-Cu_6Sn_5 (0.341 W cm^{-1} K^{-1}) and ε-Cu_3Sn (0.704 W cm^{-1} K^{-1}), exhibit relative higher thermal conductivities than it of Pb-5Sn solder (0.23 W cm^{-1} K^{-1}) [43]. The limitations of TLP bonding are the formation of brittle IMC or Kirkendall void at the bonding interface, which are generally detrimental effect on the cyclic loading capability of joint [34].

1.3.4 Metallic nanoparticle sintering

A die attach technique using metallic nanoparticles is a promising joining technology for use in high-temperature electronics and could potentially be substituted for conventional Pb-based die attach. Furthermore, nanoparticle sintered joint can be achieved at low temperature around 250 °C. Typical benefits of nanoparticle sintering process are superior electrical/thermal conductivities, high melting temperature and low homologous temperature compared with solder alloy [44].

Metallic fillers, such as Ag and Cu, and various organic substances employed for the formulation of Ag nanoparticle paste [29,45–48]. Siow [44] summarized typical additives for the formulation of Ag nanoparticle paste, including dispersant, binder and solvent. A typical feature of Ag nanoparticle with a passivation layer to prevent agglomeration is shown in Fig. 1.16 [45]. Sintering process is conducted with multi step temperature profile, including volatilization of organic substances and densification of metallic nanoparticle [49]. Optimum bonding process parameters, such as temperature, pressure, atmosphere, are varied with the mixture of Ag nanoparticle paste [44]. The densification sequence of Ag nanoparticle is shown in Fig. 1.17.

1.3.5 Requirement of die shear strength

A requirement of shear strength of die attach for high temperature electronics has not been established clearly. Instead of that, the requirement of joint strength of die attach is defined in “United States Military Standards (MIL-STD) 883G (test method standard for microcircuits)”, as shown in Fig. 1.18 [50], may be one of the criterion of minimum requirement of shear strength for high temperature electronics. This value is a minimum requirement of fracture load during shear test of die attachment. The minimum fracture load (in kN) linearly increases with increasing of die bonding area up to 4 mm^2, and then it certain value with the bonding area above 4 mm^2. The calculated value of die shear strength (in MPa) versus die bonding area is shown in Fig 1.18(b). The following cases are considered as that the device is failed in case of eutectic, solder, and other attachment.

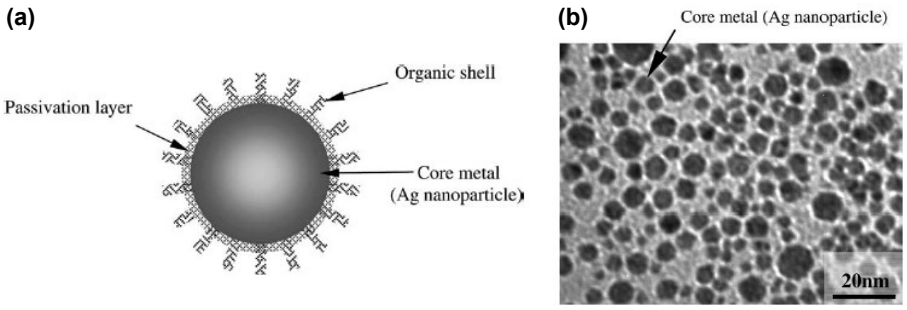

Figure 1.16 Ag metallo-organic nanoparticle: **(a)** schematic view of core-shell structure and **(b)** TEM BF image of Ag nanoparticle. Reprinted with permission from [44]. Copyright 2005, Elsevier.

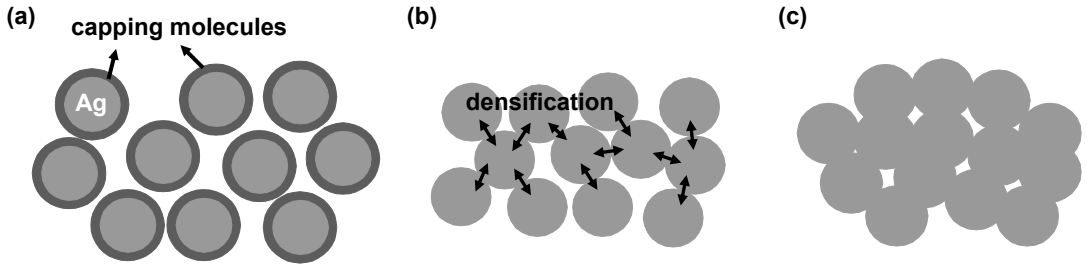

Figure 1.17 Schematic diagram of Ag nanoparticle sintering process: **(a)** initial structure of Ag nanoparticles covered with capping molecules, **(b)** removal of capping molecules and densification of Ag nanoparticles, **(c)** densified Ag structure.

(a) Fails die strength requirements (1.0x)

(b) Separation with less than 1.5 times the minimum strength (1.25x) and less than 50 percent adhesion of die attach medium.

(c) Separation with less than 2.0 times the minimum strength (2.0x) and less than 10 percent adhesion of die attach medium.

This standard should be helpful for the evaluations of quality of die attach and failure criterion after reliability test, such as thermal storage, temperature cycling and thermal shock tests. However, the value of shear strength requirement defined in MIL-STD-883G standard seems too low to evaluate the quality of joint strictly. The shear strength of Pb-5Sn die attach can be one of the criterion of shear strength requirement. Ide et al. [51] and Shi et al. [52] have been estimated the shear strength of Pb-5Sn die attach according to Japanese Industrial Standards (JIS Z 3198-5) for the comparison of Pb-free die attach, where the value of Pb-5Sn were 18 MPa and 23 MPa, respectively.

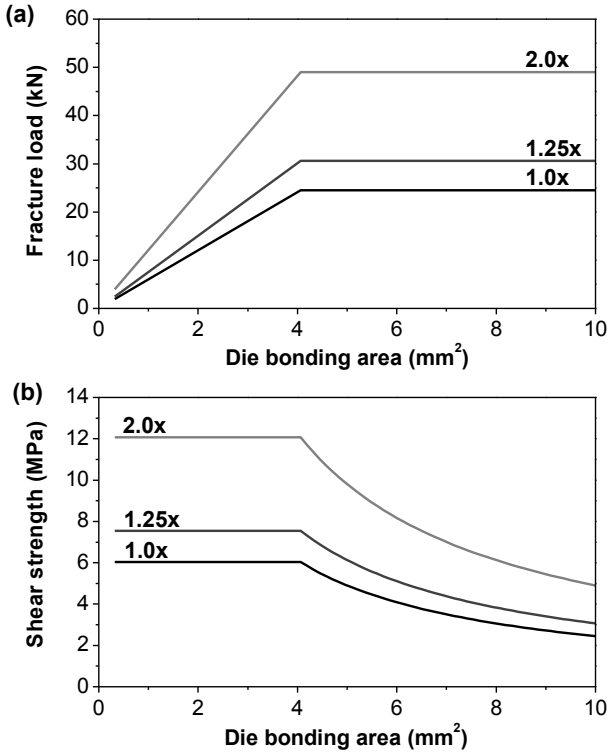

Figure 1.18 Minimum die strength criteria defined in MIL-STD-883G (method 2019.7: Die shear strength). **(a)** rescaled minimum required fracture load versus die bonding area, **(b)** calculated minimum required shear strength from *(a)* [49].

1.4 Research motivation

1.4.1 Possible problems of Ag nanoparticle sintering

As mentioned in *Section 1.3.4*, various organic substances including solvents, capping molecules, and binder have been adopted to adjust the final properties of the paste in the fabrication of the requisite nanoparticle paste [44]. For example, polyvinylpyrrolidone has been used as capping molecule to provide control over the size of the nanoparticles and to protect them against oxidation [53 –55]. These organic substances can cause some defects in the Ag nanoparticle sintered joint. Fig. 1.19 and Fig. 1.20 indicate typical defects of Ag nanoparticle sintered joint. The possible defects in Ag nanoparticle sintered joint are a formation of unfilled joint layer or an insufficient densification of Ag nanoparticle. These defects are generally detrimental to shear strength (Fig. 1.19) and thermal conductivity (Fig. 1.20) of the Ag sintered joint [56,57].

The coffee ring effect can cause of unfilled joint layer, as shown in Fig. 1.19. The sintered

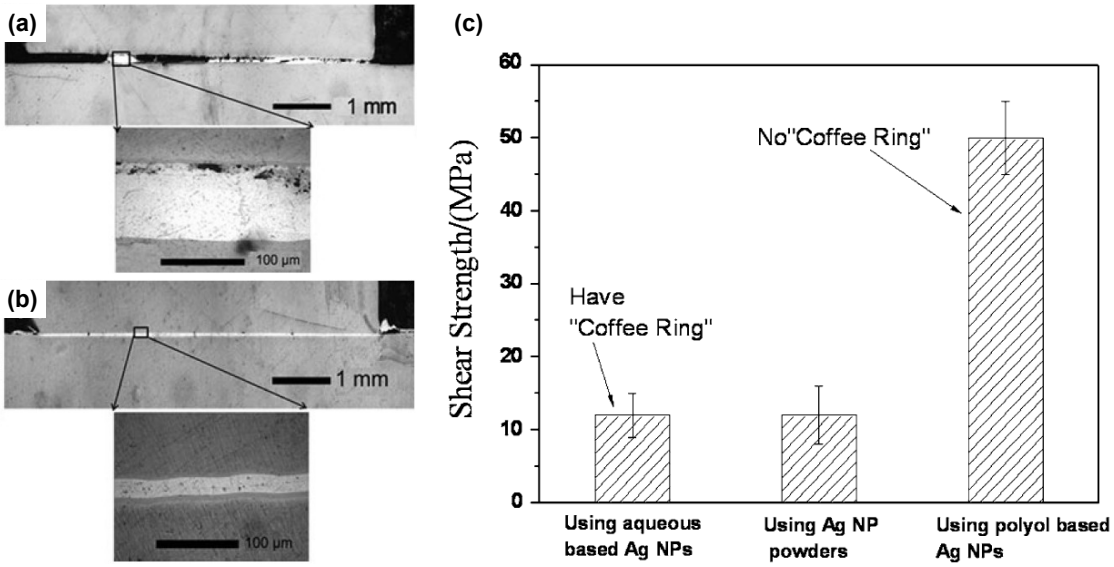

Figure 1.19 Optical microscopy images of Ag nanoparticle sintered joint using **(a)** aqueous base Ag nanoparticle and **(b)** polyol based Ag nanoparticle. **(c)** Shear strength results of sintered joint with various Ag nanoparticle. Reprinted with permission from [56]. Copyright 2012, Springer.

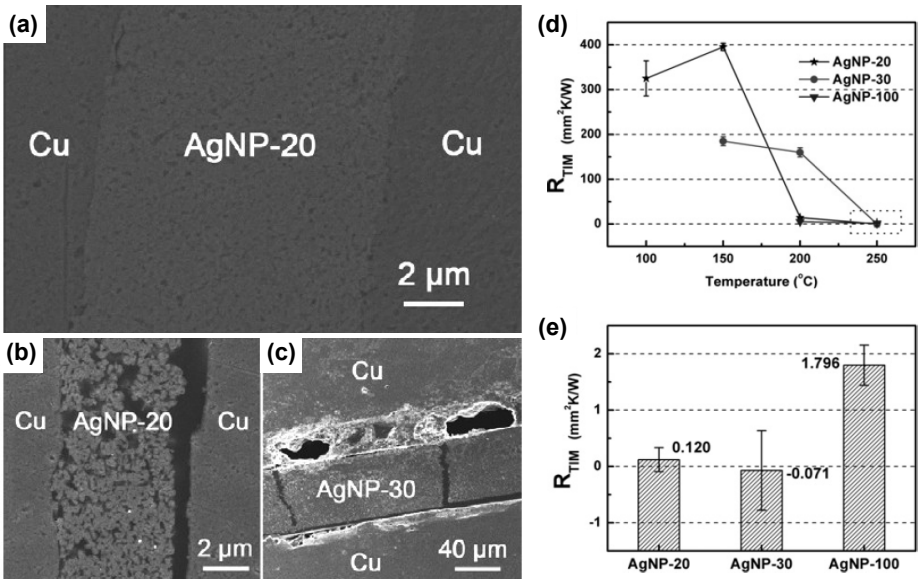

Figure 1.20 SEM images of Ag nanoparticle sintered joint of **(a)** AgNP-20 sintered at 250 °C, **(b)** AgNP-20 sintered at 200 °C and **(c)** AgNP-30 sintered at 150 °C. **(d,e)** Thermal resistance of AgNP-20, AgNP-30 and AgNP-100 joint sintered at various temperatures. Reprinted with permission from [57]. Copyright 2012, Elsevier.

Ag joint with coffee ring (Fig. 1.19(a)) exhibits lower shear strength than the case of no coffee ring (Fig. 1.19(b)). The coffee ring effect refers to ring-like deposit caused by outward flow during evaporation of liquid media containing solid substances [58]. The capillary force can cause the agglomeration of Ag nanoparticle at the edge of joint and the gaps at the center of joint. The residual organic substances by the trapping in the densified Ag or incomplete decomposition also can cause unfilled joint layer or insufficient densification of Ag nanoparticle. A dense Ag sintered layer, AgNP-20 sintered at 250 °C (Fig. 1.20(a)), exhibits low thermal resistance of 0.120 mm^2K/W, whereas the void formed Ag sintered layer, AgNO-30 sintered at 150 °C (Fig. 1.20(c)), exhibits high thermal resistance of approximately 400 mm^2K/W [57].

1.4.2 Nanoporous structure with high specific surface area

Nanoporous metals have received attentions due to its unique properties as functional applications of catalyst [59], sensor and actuator [60], hydrogen storage [61] and surface-enhanced Raman scattering substrate [62]. The unique properties of nanoporous metals are attributed to their high specific surface area to volume ratio [61–63]. The nanoporous metals can be fabricated in the shape of sheet [62], thin film [63], wire [59] and particles [64]. Dealloying is widely used to fabricate the nanoporous metal which is selective dissolution of electrochemically active element into the electrolyte solution from the precursor alloy. As the precursor alloy contacts with the electrolyte, the dissolution of less noble (LN) atoms and the agglomeration of more noble (MN) atoms are simultaneously occurred at the metal/electrolyte interface. The remained MN atoms agglomerate and form island or cluster structures owing to minimize the surface area and the curvature which act as a driving force for the surface diffusion of MN atoms [65]. A schematic diagram selective dissolution of LN atoms and formation of nanoporous structure of MN atoms is shown in Fig. 1.21.

1.4.3 Ag nanoporous structure and applying as a bonding material

The nanoporous Ag (Fig. 1.22) has received attention due to its higher electrical and thermal conductivity and relatively higher strength than Au [66]. Some dealloying methods for the fabrication of nanoporous Ag from Ag-Al [66–69] and Ag-Zn [70,71] have been reported. There are many phases of Ag-Al [72] and Ag-Zn [73] binary alloy systems, which make the metallurgical phenomena and the microstructural change occurred during the dealloying complicated in comparison with the dealloying of Au-Ag which is a single phase solid solution over the whole composition range [74]. But it is still

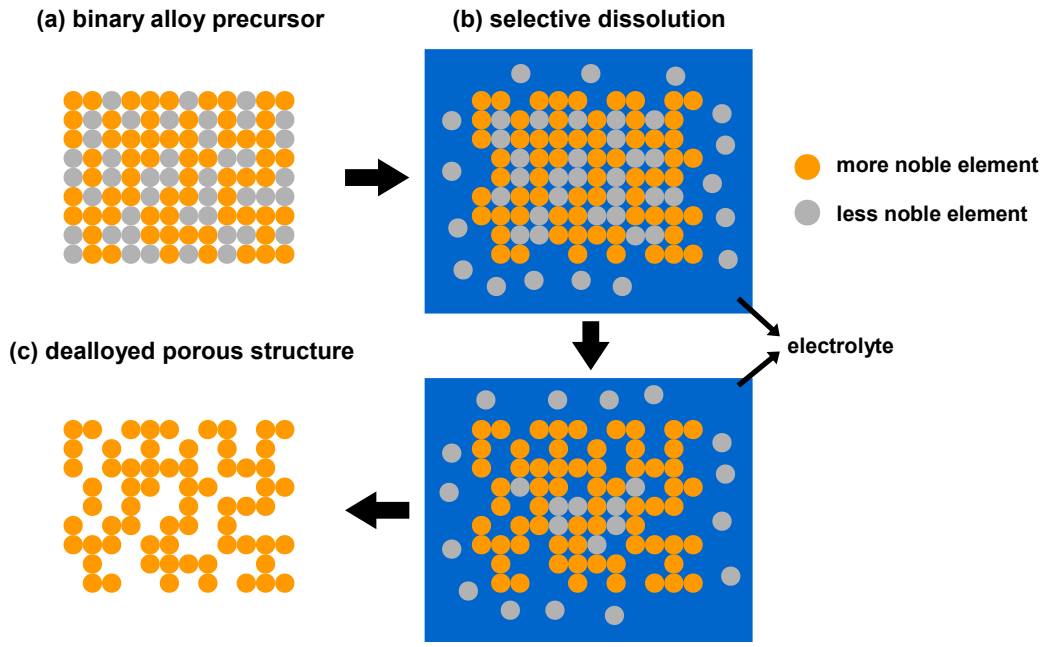

Figure 1.21 Schematic diagram of dealloying process sequence: **(a)** binary alloys precursor, **(b)** selective dissolution of less noble element into electrolyte and **(c)** dealloyed porous structure of more noble element.

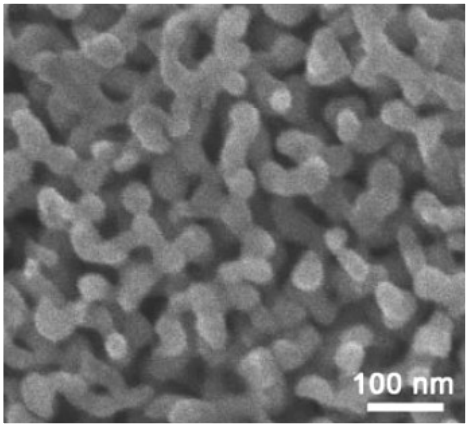

Figure 1.22 Ag nanoporous structure through dealloying method from Ag-Al precursor. Reprinted with permission from [58]. Copyright 2010, John Wiley & Sons.

not sufficient to explain the dealloying behavior of Ag-contained precursor and the evolution of Ag nanoporous structure. There is a need for further research on the dealloying behavior of Ag contained precursor alloys for the fabrication of Ag nanoporous structure.

The Ag nanoporous structure exhibits high specific surface area. Also it can maintain solid-state itself due to continuous ligament and pore structure. So, it is expected that solid-state bonding at low temperature can be possible without any organic substances through the Ag nanoporous sheet as a

bonding material. The possible concerns of Ag sintered joint, as mentioned in *Section 1.4.1*, can be solved, thereby eliminating of organic substances in bonding process. The schematic diagram of die attach process using Ag nanoporous sheet are shown in Fig. 1.23.

1.4.4 Au nanoporous bump for low temperature interconnection

Oppermann and Dietrich [75] suggested Au nanoporous bump for the low temperature interconnection, as shown in Fig. 1.24. They fabricated Au-70%Ag bump on the Si wafer by electroplating with the cyanide-based electrolyte, $KAg(CN)_2$ and $KAu(CN)_2$, and subsequent etching process in nitric acid solution in order to remove Ag from the Au-Ag alloy bump (Fig. 1.24(a)). The Au nanoporous bump exhibits low stiffness compared with bulk Au that can allow to easily deform

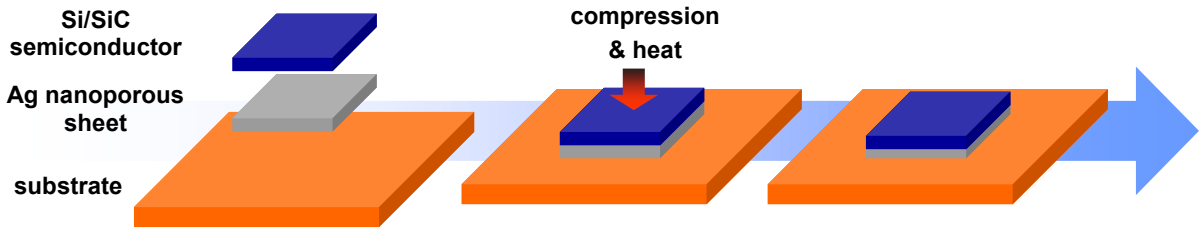

Figure 1.23 Schematic diagram of thermo-compression bonding method using Ag nanoporous sheet.

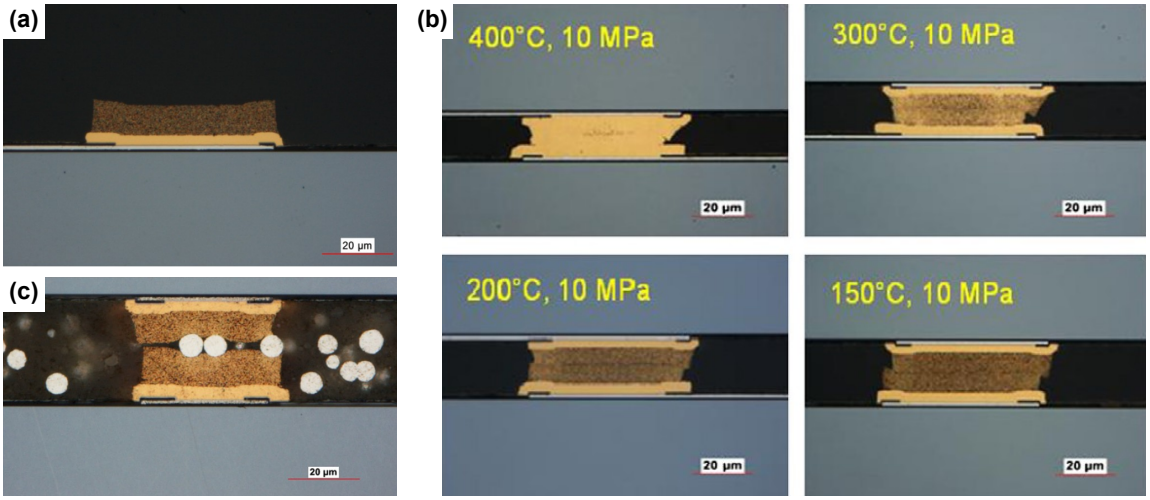

Figure 1.24 **(a)** Au nanoporous bump, **(b)** flip chip bonding using Au nanoporous bump with various bonding temperature and **(c)** possible application of Au nanoporous bump with anisotropic conductive adhesive. Reprinted with permission from [56]. Copyright 2012, Elsevier.

and densify at low temperature and pressure. It can be applied for feasible applications using Au nanoporous bump for wafer level thermocompression flip-chip bonding (Fig. 1.24(b)) and anisotropic conductive adhesive bonding (Fig. 1.24(c)). However, it is only rational to apply Au to fine-pitch interconnection [76], not a large area die attach, due to its extremely high cost.

1.5 Outline of dissertation

This dissertation covers the fabrication of Ag nanoporous sheet, establishment of Ag nanoporous bonding technique, and verification of reliability of Ag nanoporous bonding joint under the thermal storage and temperature cycling test.

In this chapter (*Chapter 1*), the brief descriptions on the background of power electronics, immersing issues of power electronics packaging and high temperature die attach are given. And a feasibility of Ag nanoporous bonding for high temperature die attach is also suggested.

In *Chapter 2*, the fabrication of Ag nanoporous sheet from Al-Ag precursor alloy using dealloying method is presented. The microstructure of Al-Ag precursor and related dealloying characteristics as a function of dealloying time were also clarified.

In *Chapter 3*, Ag nanoporous bonding (NPB) technique with electroless nickel/immersion gold (ENIG) finished Cu substrate using Ag nanoporous sheet is suggested. Mainly, the effects of bonding temperature and atmosphere on the shear strength of Ag NPB, microstructure of joint layer and fracture behavior of joint are discussed.

In *Chapter 4*, the thermal degradation behavior of Ag NPB joint with bare Cu and ENIG finished Cu during thermal storage test at 250 °C in air atmosphere is presented. The interdiffusion, oxidation and microstructure evolution at the bonding interface of Ag/ENIG and Ag/Cu during thermal storage test are demonstrated.

In *Chapter 5*, the reliability of Ag nanoporous bonding joint with Si chip and Cu metalized Si_3N_4 substrate under the temperature cycling from -55 °C to 150 °C is assessed. The long-term reliability of Ag NPB joint is estimated in terms of shear strength change after temperature cycling.

References

[1] Y. Liu, *Power electronic packaging: Design, assembly process, reliability and modeling*, Springer, New York, 2012.

[2] J. Lutz, H. Schlangenotto, U. Scheuermann, R. De Doncker, *Semiconductor power device: Physics, characteristics, reliability*, Springer, Heidelberg, 2011.

[3] T. McNutt, B. Passmore, J. Fraley, B. McPherson, R. Shaw, K. Olejniczak, A. Lostetter, "High-performance, wide-bandgap power electronics", *J. Electron. Mater.*, **43** (2014) 4552–4559.

[4] M.H. Rashid, *Power electronics handbook*, Academic Press, San Diego, 2001.

[5] P. Dietrich, "Trends in automotive power semiconductor packaging", *Microelectron. Reliab.*, **53** (2013) 1681–1686.

[6] Y. Xiong, Y. Duan, Y. Zhou, B. Zhang, J. Sun, "The electric power saving schemes of high speed electrified railway", *Energy Procedia*, **16** (2012) 1940–1947.

[7] W. Shireen, A. Nagarajan, S. Patel, R. Kotti, P. Goli, "A reliable low cost power electronics interface for photovoltaic energy systems using a single DSP controller", *Sol. Energy*, **108** (2014) 370–376.

[8] F. Blaabjerg, M. Liserre, K. Ma, "Power electronics converters for wind turbine systems", *IEEE Trans. Ind. Appl.*, **48** (2012) 708–719.

[9] K. Shenai, M. Dudley, R.F. Davis, "Current status and emerging trends in wide bandgap (WBG) semiconductor power switching devices", *ECS J. Solid State Sci. Technol.*, **2** (2013) N3055–N3063.

[10] C. Buttay, D. Planson, B. Allard, D. Bergogne, P. Bevilacqua, C. Joubert, M. Lazar, C. Martin, H. Morel, D. Tournier, C. Raynaud, "State of the art of high temperature power electronics", *Mater. Sci. Eng. B*, **176** (2011) 283–288.

[11] J. Biela, M. Schweizer, S. Waffler, J.W. Kolar, "SiC versus Si - evaluation of potentials for performance improvement of inverter and DC-DC converter systems by SiC power semiconductors", *IEEE Trans. Ind. Electron.*, **58** (2011) 2872–2882.

[12] N. Oswald, P. Anthony, N. McNeill, B.H. Stark, "An experimental investigation of the tradeoff between switching losses and EMI generation with hard-switched all-Si, Si-SiC, and all-SiC device combinations", *IEEE Trans. Power Electron.*, **29** (2014) 2393–2407.

[13] R. John, O. Vermesan, R. Bayerer, "High temperature power electronics IGBT modules for electrical and hybrid vehicles", *Proceeding of International Conference and Exhibition on High Temperature Electronics Network (HiTEN 2009)*, pp. 199–204, 2009.

[14] Y. Wang, S. Jones, A. Dai, G. Liu, "Reliability enhancement by integrated liquid cooling in power IGBT modules for hybrid and electric vehicles", *Microelectron. Reliab.*, **54** (2014) 1911–1915.

[15] H. Lu, C. Bailey, C. Yin, "Design for reliability of power electronics modules", *Microelectron. Reliab.*, **49** (2009) 1250–1255.

[16] M. Ciappa, "Selected failure mechanisms of modern power modules", *Microelectron. Reliab.*, **42** (2002) 653–667.

[17] J.F. Shackelfor, W. Alexander, *CRC materials science and engineering handbook*, 3rd edition, CRC Press, Boca Raton, 2011.

[18] S. Park, S. Nagao, T. Sugahara, K. Suganuma, "Mechanical stabilities of ultrasonic Al ribbon bonding on electroless nickel immersion gold finished Cu substrates", *Jpn. J. Appl. Phys.*, **53** (2014) 04EP06.

[19] Y. Tian, C. Wang, I. Lum, M. Mayer, J.P. Jung, Y. Zhou, "Investigation of ultrasonic copper wire wedge bonding on Au/Ni plated Cu substrates at ambient temperature", *J. Mater. Process. Technol.*, **208** (2008) 179–186.

[20] S. Park, S. Nagao, T. Sugahara, K. Suganuma, "Heel crack propagation mechanism of cold-rolled Cu/Al clad ribbon bonding in harsh environment", *J. Mater. Sci. Mater. Electron.*, **26** (2015) 7277–7289.

[21] A.B.Y. Lim, A.C.K. Chang, O. Yauw, B. Chylak, C.L. Gan, Z. Chen, "Ultra-fine pitch palladium-coated copper wire bonding: Effect of bonding parameters", *Microelectron. Reliab.*, **54** (2014) 2555–2563.

[22] J. Schulz-Harder, "Advantages and new development of direct bonded copper substrates", *Microelectron. Reliab.*, **43** (2003) 359–365.

[23] A. Fukumoto, D. Berry, K.D.T. Ngo, G.-Q. Lu, "Effects of extreme temperature swings (-55 °C to 250 °C) on silicon nitride active metal brazing substrates", *IEEE Trans. Device Mater. Reliab.*, **14** (2014) 751–756.

[24] K. Zeng, K.N. Tu, "Six cases of reliability study of Pb-free solder joints in electronic packaging technology", *Mater. Sci. Eng. R*, **38** (2002) 55–105.

[25] The European Parliament and of the Council of the European Union, "Directive 2002/95/EC of the European Parliament and of the Council of 27 January 2003 on the restriction of the use of certain hazardous substances in electrical and electronic equipment", *Off. J. Eur. Union*, **46** (2003) L 37/19.

[26] The European Parliament and of the Council of the European Union, "Directive 2011/65/EU of the European Parliament and of the Council of 8 June 2011 on the restriction of the use of certain hazardous substances in electrical and electronic equipment (recast)", *Off. J. Eur. Union*, **54** (2011) L 174/88.

[27] S. Kim, K.-S. Kim, S.-S. Kim, K. Suganuma, G. Izuta, "Improving the reliability of Si die attachment with Zn-Sn-based high-temperature Pb-free solder using a TiN diffusion barrier", *J. Electron. Mater.*, 38 (2009) 2668–2675.

[28] N.S. Bosco, F.W. Zok, "Strength of joints produced by transient liquid phase bonding in the Cu –Sn system", *Acta Mater.*, **53** (2005) 2019–2027.

[29] S. Sakamoto, S. Nagao, K. Suganuma, "Thermal fatigue of Ag flake sintering die-attachment for Si/SiC power devices", *J. Mater. Sci. Mater. Electron.*, **24** (2013) 2593–2601.

[30] K. Suganuma, S.-J. Kim, K.-S. Kim, "High-temperature lead-free solders: Properties and possibilities", *JOM*, **61** (2009) 64–71.

[31] V. Chidambaram, H.B. Yeung, G. Shan, "Reliability of Au-Ge and Au-Si eutectic solder alloys for high-temperature electronics", *J. Electron. Mater.*, **41** (2012) 2107–2117.

[32] Y. Takaku, I. Ohnuma, R. Kainuma, Y. Yamada, Y. Yagi, Y. Nishibe, K. Ishida, "Development of Bi-base high-temperature Pb-free solders with second-phase dispersion: Thermodynamic calculation, microstructure, and interfacial reaction", *J. Electron. Mater.*, **35** (2006) 1926–1932.

[33] G. Zeng, S. McDonald, K. Nogita, "Development of high-temperature solders: Review", *Microelectron. Reliab.*, **52** (2012) 1306–1322.

[34] V. Chidambaram, J. Hattel, J. Hald, "High-temperature lead-free solder alternatives", *Microelectron. Eng.*, **88** (2011) 981–989.

[35] A. Kroupa, D. Andersson, N. Hoo, J. Pearce, A. Watson, A. Dinsdale, S. Mucklejohn, "Current problems and possible solutions in high-temperature lead-free soldering", *J. Mater. Eng. Perform.*, **21** (2012) 629–637.

[36] S. Menon, E. George, M. Osterman, M. Pecht, "High lead solder (over 85 %) solder in the electronics industry: RoHS exemptions and alternatives", *J. Mater. Sci. Mater. Electron.*, **26** (2015) 4021–4030.

[37] J.F. Li, P.A. Agyakwa, C.M. Johnson, "Kinetics of Ag_3Sn growth in Ag-Sn-Ag system during transient liquid phase soldering process", *Acta Mater.*, **58** (2010) 3429–3443.

[38] J.-B. Lee, H.-Y. Hwang, M.-W. Rhee, "Reliability Investigation of Cu/In TLP Bonding", *J. Electron. Mater.*, **44** (2014) 435–441.

[39] K. Chu, Y. Sohn, C. Moon, "A comparative study of Cu/Sn/Cu and Ni/Sn/Ni solder joints for low temperature stable transient liquid phase bonding", *Scr. Mater.*, **109** (2015) 113–117.

[40] G.O. Cook, C.D. Sorensen, "Overview of transient liquid phase and partial transient liquid phase bonding", *J. Mater. Sci.*, **46** (2011) 5305–5323.

[41] N. Saunders, A.P. Miodownik, "The Cu-Sn (copper-tin) system", *Bull. Alloy Phase Diagr.*, **11** (1990) 278–287.

[42] S.W. Yoon, M.D. Glover, H.A. Mantooth, K. Shiozaki, "Reliable and repeatable bonding technology for high temperature automotive power modules for electrified vehicles", *J. Micromechanics Microengineering*, **23** (2013) 015017.

[43] H.P.R. Frederikse, R.J. Fields, A. Feldman, "Thermal and electrical properties of copper-tin and nickel-tin intermetallics", *J. Appl. Phys.*, **72** (1992) 2879–2882.

[44] K.S. Siow, "Mechanical properties of nano-silver joints as die attach materials", *J. Alloy. Compd.*, **514** (2012) 6–19.

[45] E. Ide, S. Angata, A. Hirose, K.F. Kobayashi, "Metal-metal bonding process using Ag metallo-organic nanoparticles", *Acta Mater.*, **53** (2005) 2385–2393.

[46] J.G. Bai, J.N. Calata, G.-Q. Lu, "Processing and characterization of nanosilver pastes for die-attaching SiC devices", *IEEE Trans. Electron. Packag. Manuf.*, **30** (2007) 241–245.

[47] T. Ishizaki, R. Watanabe, "A new one-pot method for the synthesis of Cu nanoparticles for low temperature bonding", *J. Mater. Chem.*, **22** (2012) 25198–25206.

[48] J. Yan, G. Zou, A. Wu, J. Ren, A. Hu, Y.N. Zhou, "Polymer-protected Cu-Ag mixed NPs for low-temperature bonding application", *J. Electron. Mater.*, **41** (2012) 1886–1892.

[49] X. Li, G. Chen, X. Chen, G.-Q. Lu, L. Wang, Y.-H. Mei, "High temperature ratcheting behavior of nano-silver paste sintered lap shear joint under cyclic shear force", *Microelectron. Reliab.*, **53** (2013) 174–181.

[50] US Military Standard, *MIL-STD-883G, Method 2019.7: Die shear strength*, 2003.

[51] E. Ide, A. Hirose, K.F. Kobayashi, "Influence of bonding condition on bonding process using Ag metallo-organic nanoparticles for high temperature lead-free packaging", *Mater. Trans.*, **47** (2006) 211–217.

[52] Y. Shi, W. Fang, Z. Xia, Y. Lei, F. Guo, X. Li, "Investigation of rare earth-doped BiAg high-temperature solders", *J. Mater. Sci. Mater. Electron.*, **21** (2010) 875–881.

[53] D. Kim, S. Jeong, J. Moon, "Synthesis of silver nanoparticles using the polyol process and the influence of precursor injection", *Nanotechnology*, **17** (2006) 4019–4024.

[54] Y. Jianfeng, Z. Guisheng, H. Anming, Y.N. Zhou, "Preparation of PVP coated Cu NPs and the application for low-temperature bonding", *J. Mater. Chem.*, **21** (2011) 15981–15986.

[55] L. Chen, Z. Li, C. Xiao, Z. Wang, W. Han, "Size-controlled synthesis of highly dispersed silver particles", *J. Mater. Sci. Mater. Electron.*, **24** (2013) 1469–1474.

[56] J. Yan, G. Zou, A. Wu, J. Ren, A. Hu, Y.N. Zhou, "Improvement of bondability by depressing the inhomogeneous distribution of nanoparticles in a sintering bonding process with silver nanoparticles", *J. Electron. Mater.*, **41** (2012) 1924–1930.

[57] H. Yu, L. Li, Y. Zhang, "Silver nanoparticle-based thermal interface materials with ultra-low thermal resistance for power electronics applications", *Scr. Mater.*, **66** (2012) 931–934.

[58] R.D. Deegan, O. Bakajin, T.F. Dupont, G. Huber, S.R. Nagel, T.A. Witten, "Capillary flow as the cause of ring stains from dried liquid drops", *Nature*, **389** (1997) 827–829.

[59] J.L. Shui, C. Chen, J.C.M. Li, "Evolution of nanoporous Pt-Fe alloy nanowires by dealloying and their catalytic property for oxygen reduction reaction", *Adv. Funct. Mater.*, **21** (2011) 3357–3362.

[60] J. Biener, A. Wittstock, L.A. Zepeda-Ruiz, M.M. Biener, V. Zielasek, D. Kramer, R.N. Viswanath, J. Weissmüller, M. Bäumer, A.V. Hamza, "Surface-chemistry-driven actuation in nanoporous gold", *Nat. Mater.*, **8** (2009) 47–51.

[61] P.J. Cappillino, J.D. Sugar, M.A. Hekmaty, B.W. Jacobs, V. Stavila, P.G. Kotula, J.M. Chames, N.Y. Yang, D.B. Robinson, "Nanoporous Pd alloys with compositionally tunable hydrogen storage properties prepared by nanoparticle consolidation", *J. Mater. Chem.*, **22** (2012) 14013–14022.

[62] L.Y. Chen, J.S. Yu, T. Fujita, M.W. Chen, "Nanoporous copper with tunable nanoporosity for SERS applications", *Adv. Funct. Mater.*, **19** (2009) 1221–1226.

[63] J. Erlebacher, M.J. Aziz, A. Karma, N. Dimitrov, K. Sieradzki, "Evolution of nanoporosity in dealloying", *Nature*, **410** (2001) 450–453.

[64] D. Wang, P. Schaaf, "Nanoporous gold nanoparticles", *J. Mater. Chem.*, **22** (2012) 5344–5348.

[65] J. Erlebacher, "An atomistic description of dealloying: Porosity evolution, their critical potential, and rate-limiting behavior", *J. Electrochem. Soc.*, **151** (2004) C614–C626.

[66] H. Qiu, Z. Zhang, X. Huang, Y. Qu, "Dealloying Ag-Al alloy to prepare nanoporous silver as a substrate for surface-enhanced Raman scattering: Effects of structural evolution and surface modification", *ChemPhysChem*, **12** (2011) 2118–2123.

[67] T. Song, Y. Gao, Z. Zhang, Q. Zhai, "Dealloying behavior of rapidly solidified Al–Ag alloys to prepare nanoporous Ag in inorganic and organic acidic media", *CrystEngComm*, **13** (2011) 7058–7067.

[68] E. Detsi, Z. Vuković, S. Punzhin, P.M. Bronsveld, P.R. Onck, J.T.M. De Hosson, "Fine-tuning the feature size of nanoporous silver", *CrystEngComm*, **14** (2012) 5402–5406.

[69] T. Song, Y. Gao, Z. Zhang, Q. Zhai, "Influence of magnetic field on dealloying of Al-25Ag alloy and formation of nanoporous Ag", *CrystEngComm*, **14** (2012) 3694–3701.

[70] Z.Q. Li, B.Q. Li, Z.X. Qin, X. Lu, "Fabrication of porous Ag by dealloying of Ag-Zn alloys in H_2SO_4 solution", *J. Mater. Sci.*, **45** (2010) 6494–6497.

[71] C. Zhang, J. Sun, J. Xu, X. Wang, H. Ji, C. Zhao, Z. Zhang, "Formation and microstructure of nanoporous silver by dealloying rapidly solidified Zn-Ag alloys", *Electrochim. Acta*, **63** (2012) 302–311.

[72] A.J. McAlister, "The Ag-Al (silver-aluminum) system", *Bull. Alloy Phase Diagr.*, **8** (1987) 526 –533.

[73] H. Okamoto, "Ag-Zn (silver-zinc)", *J. Phase Equilibria*, **23** (2002) 454.

[74] R.P. Elliott, F.A. Shunk, "The Ag-Au (silver-gold) system", *Bull. Alloy Phase Diagr.*, **1** (1980) 45–47.

[75] H. Oppermann, L. Dietrich, "Nanoporous gold bumps for low temperature bonding", *Microelectron. Reliab.*, **52** (2012) 356–360.

[76] Y.-K. Lee, Y.-H. Ko, J.-K. Kim, C.-W. Lee, S. Yoo, "The effect of intermetallic compound evolution on the fracture behavior of Au stud bumps joined with Sn-3.5Ag solder", *Electron. Mater. Lett.*, **9** (2013) 31–39.

Chapter 2

Fabrication of Ag nanoporous sheet by dealloying method

2.1 Introduction

There are two phases of α-Al solid solution and γ-Ag_2Al intermetallic, with composition range of 40-100 at% Al in the Ag-Al phase diagram, as shown in Fig. 2.1 [1]. This make the metallurgical phenomena and the microstructural change occurred during the dealloying complicated in comparison with the dealloying of Au-Ag which is a single phase solid solution over the whole composition range [2]. The researchers have been reported about the fabrication of Ag nanoporous structure from Al-Ag precursor [3–6]. It is still not sufficient, however, to explain the dealloying behavior of Ag-contained precursor and the evolution of Ag nanoporous structure.

In the eutectic point (567 °C), over 35 at% of Ag can be soluble in the α-Al matrix. But the solubility of Ag in the Al matrix is sharply decreased with the decrease of temperature and it is negligible at the room temperature. Namely, α-Al phase is consisted mostly of Al atoms in this composition range. This eutectic reaction of Al-Ag alloy can lead to non-uniform distribution of alloying elements. Consequently, the Al dissolution from α-Al will cause formation of unexpected large pore during the dealloying. So, the supersaturation of Ag in the α-Al matrix is necessary to fabricate uniform nanoporous structure by the dealloying. Rapid solidification techniques, such as the atomization [7] and the melt-spinning [8], are helpful to the supersaturation of Ag in Al matrix, due to

their fast cooling rates.

In this chapter, a fabrication of Ag nanoporous sheet by dealloying in hydrochloric acid (HCl) solution from the Al-Ag precursor was conducted. The melt-spinning technique was adopted for the preparation of precursor for the supersaturation of Ag in Al. The melt-spun ribbon dealloyed in HCl at room temperature for 10-720 min was investigated to confirm and describe the occurring phenomena during the dealloying process. Especially, the channel formation occurred at the grain boundary and the formation of Ag cluster from α-Al and γ-Ag_2Al were observed. Then the coarsening

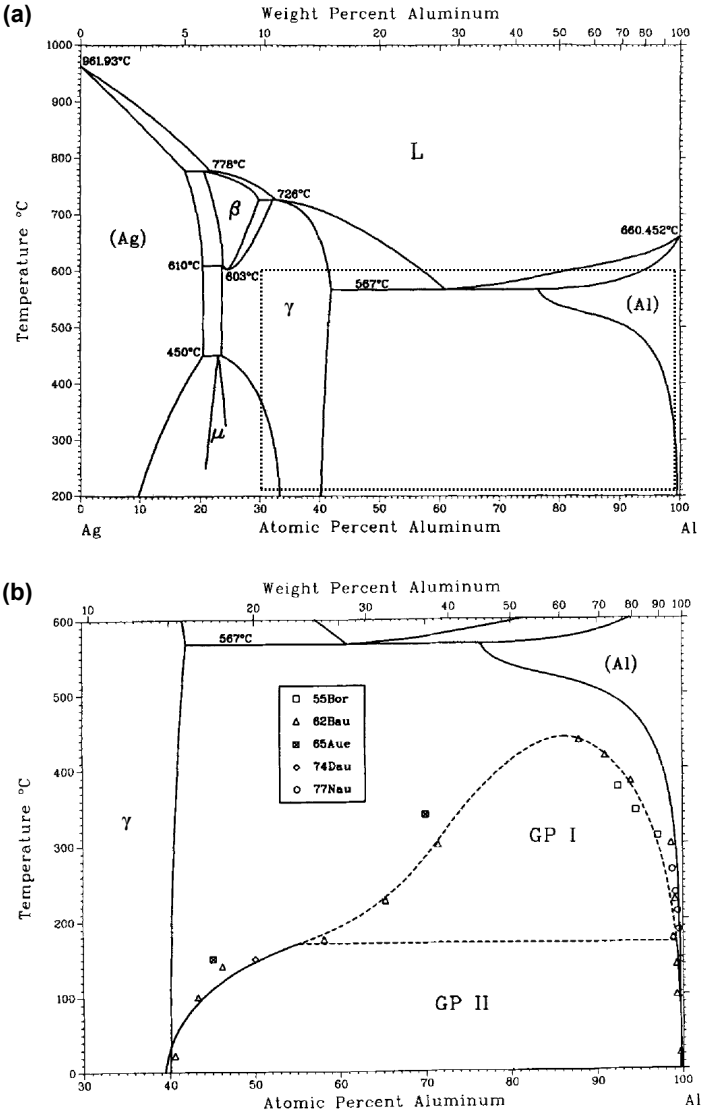

Figure 2.1 **(a)** Equilibrium phase diagram of binary Ag-Al system, **(b)** miscibility gap in the eutectic α-Al + γ-Ag_2Al field. Reprinted with permission from [8]. Copyright 1987, Springer.

behavior of Ag nanoporous structure was analyzed by coarsening mechanism which was controlled by surface diffusion of Ag in HCl solution.

2.2 Experimental

2.2.1 Fabrication of Al-Ag precursor

High purity aluminum (99.999%) and silver (99.98%) purchased from Nilaco Co. (Tokyo, Japan) were used for the preparation of precursor alloy. The precursor alloy was fabricated using single roller melt-spinning technique (Fig. 2.2). Al-20at% Ag ingot was prepared using high frequency induction melting furnace under argon atmosphere. Pre-alloyed Al-Ag ingot was remelted in the graphite crucible under argon atmosphere and then ejected through the rectangular shaped slit with the area of 0.3 mm x 20 mm on the oxygen-free copper (OFC) roller with the diameter of 305 mm. The temperature of molten metal was 750 °C at the ejection time, the ejection pressure was 55 kPa, the distance from the tip of slit to the surface of OFC roller was 0.7 mm and the linear velocity of roll was approximately 10 m/s. The melt-spun ribbon with the width of 18-20 mm and thickness of 90-100 μm can be obtained.

2.2.2 Fabrication of Ag nanoporous structure using dealloying method

The melt-spun Al-Ag was immersed into the dilute HCl solution with the concentration of 2 M at the room temperature (25 °C). For the description of dealloying behavior of Al-Ag alloy during

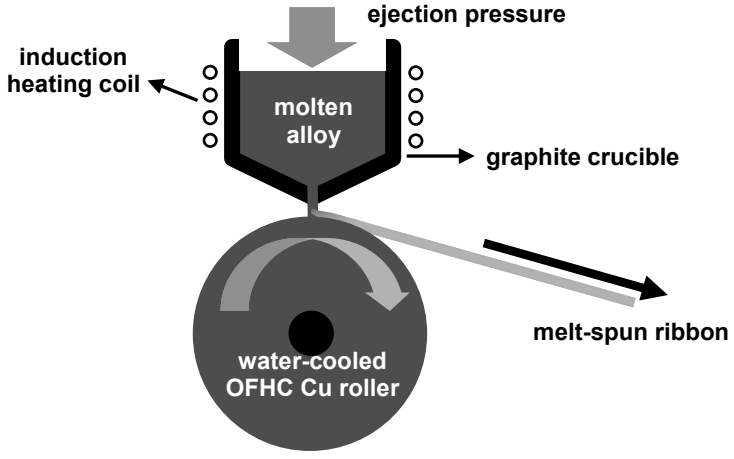

Figure 2.2 Schematic diagram of melt-spinning process.

the process, Al-Ag ribbons were treated for the various dealloying times from 3 min to 720 min. The dealloyed specimen was sequentially rinsed with distilled water and ethyl alcohol.

2.2.3 Characterization methods

The observation of microstructures and chemical analysis of melt-spun Al-Ag precursor and dealloyed nanoporous Ag and chemical analysis were conducted using scanning electron microscope (SEM, SU-70, Hitachi) equipped with energy dispersive X-ray spectrometer (EDS, Oxford Instruments), electron probe micro-analyzer (EPMA, JXA-8530F, JEOL) and transmission electron microscope (TEM, JEM-2100F, JEOL) equipped with EDS detector (JED-2200, JEOL) on scanning (S)TEM mode. *In-situ* TEM sample preparation and cross-sectioning of dealloyed sample were conducted using focused ion beam (FIB, JIB-4500, JEOL). Detailed information about the *in-situ* TEM sample preparation method can be found in *Appendix 1*. TEM image acquisition and analysis were conducted using DigitalMicrograph (Gatan). The size scale related with the dealloyed microstructure was measured using commercial image analysis program, ImagePro Plus (Media Cybernetics).

The phase constitution of each sample was measured by X-ray diffractometer (XRD, Ultima IV, Rigaku) with Cu Kα (λ = 0.154056 nm) radiation. The 2θ scan range was 30° to 90°, scan step of 2θ was 0.02° and scan rate was 2°/min. The International Centre for Diffraction Data (ICDD) powder diffraction file (PDF) cards, including #01-071-3760 for the Al, #01-071-4613 for the Ag and #01-074 -5113 for the aluminum silver (Ag0.667 Al0.333), were used as references for the identification of diffraction pattern. The quantitative phase analysis was conducted by means of the reference intensity ratio (RIR) method [9] using PDXL software (Rigaku).

2.3 Microstructural characteristics of Al-Ag precursor alloy

2.3.1 Bi-phase Al-Ag precursor

The Al-Ag precursor exhibited bi-phase structure, face centered cubic (FCC) α-Al and hexagonal γ-Ag_2Al, as shown in Fig. 2.3(a). The volume fraction of α-Al and γ-Ag_2Al were 94.4% and 5.6%, respectively. It can be confirmed that 78.59 at% and 1.85 at% of Al exists in α-Al and γ-Ag_2Al, respectively, with the combination of XRD quantitative analysis and EDS result (an initial Ag composition of Al-Ag precursor = 19.44 at%). Due to the fast cooling rate of melt-spinning process

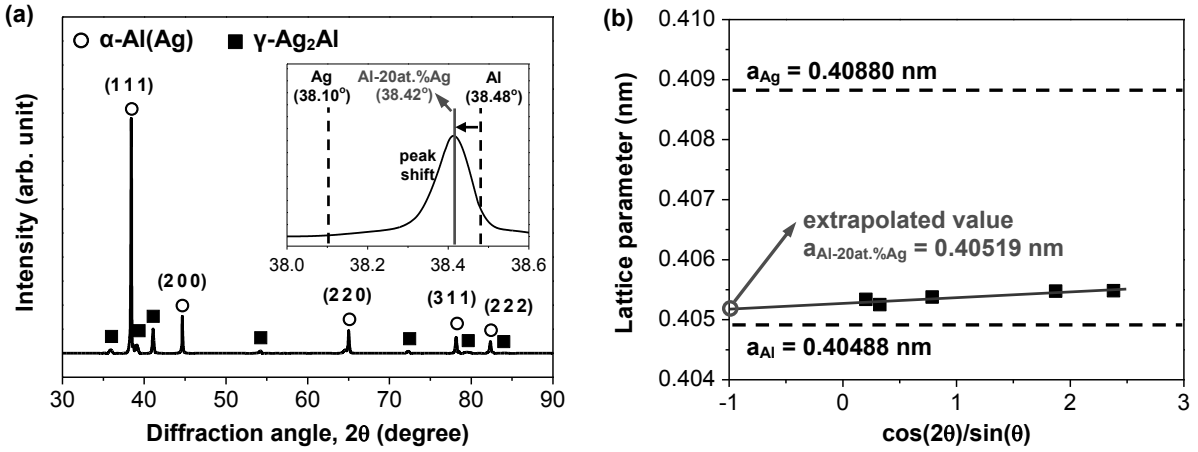

Figure 2.3 **(a)** X-ray diffraction (XRD) result of Al-Ag precursor alloy. The plane indexing indicates FCC plane and inset graph shows local XRD result of FCC (111) region. **(b)** The determination of lattice parameter of α-Al solid solution of Al-Ag precursor alloy to extrapolate to θ = 2π to reduce the systematic error.

[10,11], the supersaturation of Ag element in the Al matrix and the suppression of considerable amount of γ-Ag_2Al became possible. This supersaturation of Ag leads to expansion of lattice structure of α-Al solid solution. The lattice parameters of α-Al(Ag) from the individual reflections can be calculated using the combination of the formula for the interplanar spacing of cubic cell (equation 2.1),

$$\frac{1}{d_{hkl}} = \frac{\sqrt{h^2 + k^2 + l^2}}{a} \quad \cdots\cdots (2.1)$$

where d_{hkl} is an interplanar spacing of (hkl) plane and a is a lattice parameter of cubic cell, and the Bragg's law (equation 2.2),

$$n\lambda = 2d\sin\theta \quad \cdots\cdots (2.2)$$

where λ is the wavelength of X-ray (Cu K_α, 0.154056 nm) and θ is a diffraction angle [12]. The calculated results of lattice parameters of α-Al(Ag) phase are shown in Fig. 2.3(b). In order to reduce systematic error of sine curve, an extrapolation method to $\theta = 2\pi$ was adopted [13]. The extrapolated value of apparent lattice parameter of α-Al(Ag) phase was 0.40519 nm. According to the Vegard's law which is based on the simple linear relationship between the concentration of solute element and the lattice parameter of matrix, solute (Ag) concentration in Al matrix was approximately

13.5 at%. But it will not be an accurate result due to the quite similar values between lattice parameters of Al and Ag [14].

The microstructure of melt-spun Al-Ag precursor can be confirmed in Fig. 2.4 and Fig. 2.5. Fig.2.4 shows microstructure of Al-Ag precursor alloy and elemental distribution of Ag and Al. The plate-shaped γ-Ag_2Al precipitates were mainly observed at the grain boundary of α-Al(Ag) phase, and small amount of γ-Ag_2Al was observed as a Widmanstätten structure at the grain of α-Al(Ag). The Widmanstätten structure is generally occurred in Al-Ag alloy due to crystallographic orientation relationship, $\{1\,1\,1\}_\alpha//(0\,0\,0\,1)_\gamma$, between FCC matrix and hexagonal close packed (HCP) precipitate [15,16].

Fig. 2.5 shows of bright field (BF) and dark field (DF) TEM images of Al-Ag precursor alloy. The dark area is γ-Ag_2Al precipitate, and the bright area vicinity the γ-Ag_2Al phase is Ag depleted zone in Fig. 2.4(a). Ag depleted zone in α-Al(Ag) phase around γ-Ag_2Al precipitates will be mentioned in *Section 2.4.3*. A selected area electron diffraction (SAED) pattern (Fig. 2.5(b)), obtained using a selected area aperture with the diameter of 150 nm, exhibits bi-phase of α-Al(Ag) and γ-Ag_2Al. The γ-Ag_2Al precipitates inside the grain were oriented in the certain direction, which is known as Widmanstätten structure. The precipitation caused by the diffusion of alloying element into the grain boundary involves concentration gradient near the boundary and consequently the solute depletion zone is formed [17]. The individual DF TEM images of α-Al(Ag) using $(3\,1\,1)_\alpha$ diffraction pattern (Fig. 2.5(d)) and γ-Ag_2Al precipitates and $(1\,0\text{-}1)_\gamma$ diffraction pattern (Fig. 2.5(e)) clearly show the distributions of α-Al(Ag) and γ-Ag_2Al phases. Meanwhile, DF image of Fig. 2.5(f) exhibited both of α-Al(Ag) and γ-Ag_2Al, because of the superposition of α-Al(Ag) and γ-Ag_2Al diffraction patterns.

2.3.2 Phase separation of Ag and Al in α-Al(Ag) phase

Fig. 2.6(a) show the phase separation of Al (bright area) and Ag (dark area) in α-Al(Ag) phase, which comes from the spinodal decomposition. The spinodal decomposition and growth of γ-Ag_2Al plate can be occurred through the supersaturation of Ag and subsequent quenching of Al-Ag alloy. The α-Al(Ag) phase decomposed into Ag-rich and Ag-poor in order to lower the free energy of system [18]. The decomposed α-Al(Ag) phase shows continuous Ag-rich phase due to the high content of solute (Ag) compared with dilute Al-Ag alloy [19]. A high resolution lattice image of α-Al(Ag), as shows in Fig. 2.6(b), indicates that the separated Al and Ag show same crystallographic orientation and coherent interface. This result shows good agreement with the single FCC peak in XRD result of

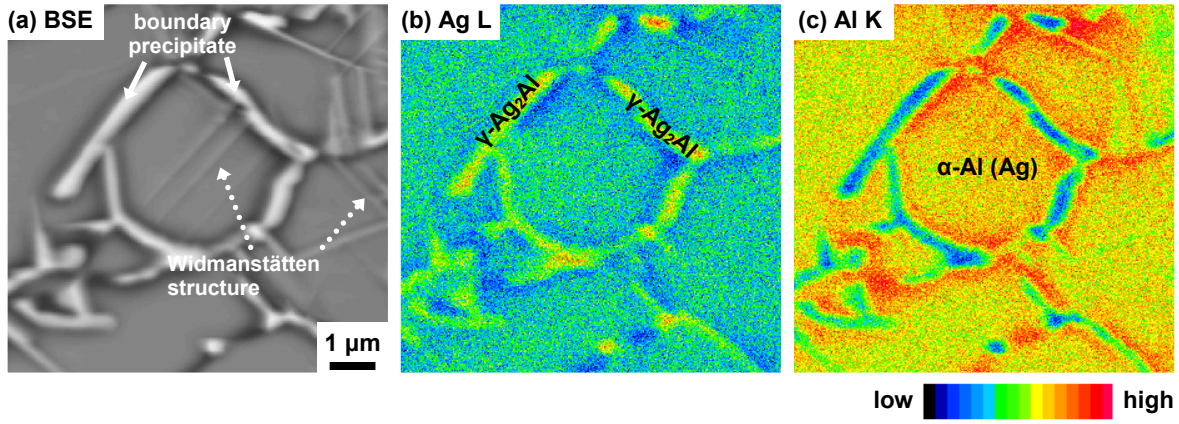

Figure 2.4 Electron probe micro-analyzer (EPMA) mapping result of Al-Ag precursor: **(a)** back-scattered electron (BSE) image, **(b)** Ag L line mapping and **(c)** Al K line mapping. *Lined arrows* and *dotted arrows* indicate boundary precipitate and Widmanstätten structure of γ-Ag_2Al, respectively.

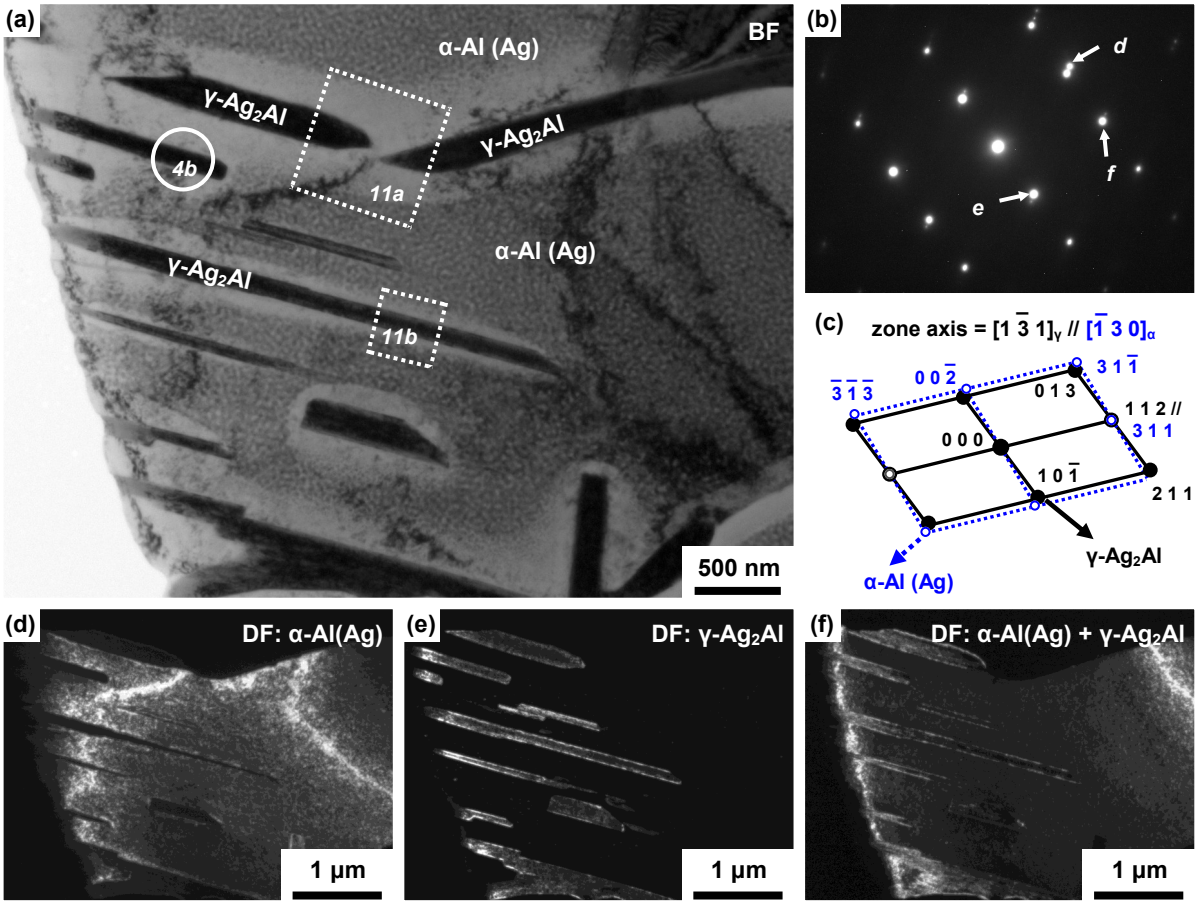

Figure 2.5 **(a)** Transmission electron microscopy (TEM) bright field (BF) image of melt-spun Al-Ag precursor, **(b)** selected area electron diffraction (SAED) pattern of vicinity of interface between α-Al(Ag) and γ-Ag_2Al denoted with *white circle* in *a*, **(c)** indexed SAED pattern, and TEM dark field (DF) images of **(d)** α-Al(Ag) using $(311)_\alpha$ spot, **(e)** γ-Ag_2Al using $(10\text{-}1)_\gamma$ spot and **(f)** α-Al(Ag) + γ-Ag_2Al using $(311)_\alpha$// $(122)_\gamma$ spot, where the diffraction spots used for DF images are denoted in *(b)*.

Al-Ag precursor (Fig. 2.3(a)). There are small lattice strain at the Ag/Al interface due to the slight difference in atomic radius between Al and Ag [20]. The measured interplanar distance of (220) plane of α-Al(Ag) phase was 0.143 nm (Fig. 2.6(b)). The interplanar distances of (220) plane of pure Al and pure Ag are 0.1431 nm and 0.1445 nm, respectively. Therefore, Ag rich region is subjected to compressive strain and Al rich region is subjected to tensile strain.

A SAED pattern of α-Al(Ag) phase (Fig. 2.6(a)) shows 6-fold {222} patterns and 1/3{422} forbidden reflections. This forbidden reflections have been reported in SAED patterns along the [1 1 1] direction in FCC metal [21–23]. Germain et al. [22] suggested some models for formation of 1/3{422} forbidden reflections in FCC structure. They argued that the presence of parallel (111) stacking fault or twin to the upper and lower surface of specimen can make 1/3{4 2 2} forbidden reflections appear in the SAED pattern with zone axis of [1 1 1].

The stacking fault is a planar defect can be easily observed FCC metal by removing (intrinsic staking fault) or inserting (extrinsic) of close-packed plane. Fig. 2.7 shows the schematic diagrams of stacking sequences of FCC structure, HCP structure and FCC with stacking fault and corresponding electron diffraction patterns when the electron beam an incident electron beam is perpendicular to the close-packed plane. The diffraction patterns of $(\text{-}12\text{-}10)_{HCP}$ and $(01\text{-}10)_{HCP}$ coincide with the diffraction patterns of $(220)_{FCC}$ and $1/3(422)_{FCC}$ patterns, respectively. The superposition of SAED patterns of FCC and HCP is seemed to be a cause of formation of forbidden reflection.

2.3.3 Growth of plate-shape γ-Ag_2Al precipitate

As shown in Fig. 2.8(a), γ-Ag_2Al precipitate was formed as a plate shape. The HRTEM images of Fig. 2.8(b) and Fig. 2.8(c) show the coherent interface and incoherent interface of α-Al(Ag) and γ-Ag_2Al. The cause of γ-Ag_2Al precipitate growth as a plate-shaped is different growing velocity in directions. Generally, the coherent and semicoherent interfaces exhibit low mobility, and the incoherent interface exhibits fast mobility. The mobility difference between coherent interface and incoherent interface leads that the precipitate grows in shape of the plate type. The morphology of interface between matrix and precipitate is closely related with the type of interface. The coherent or semicoherent interfaces exhibits planar shape and an incoherent interface exhibits round/step shape, respectively [15].

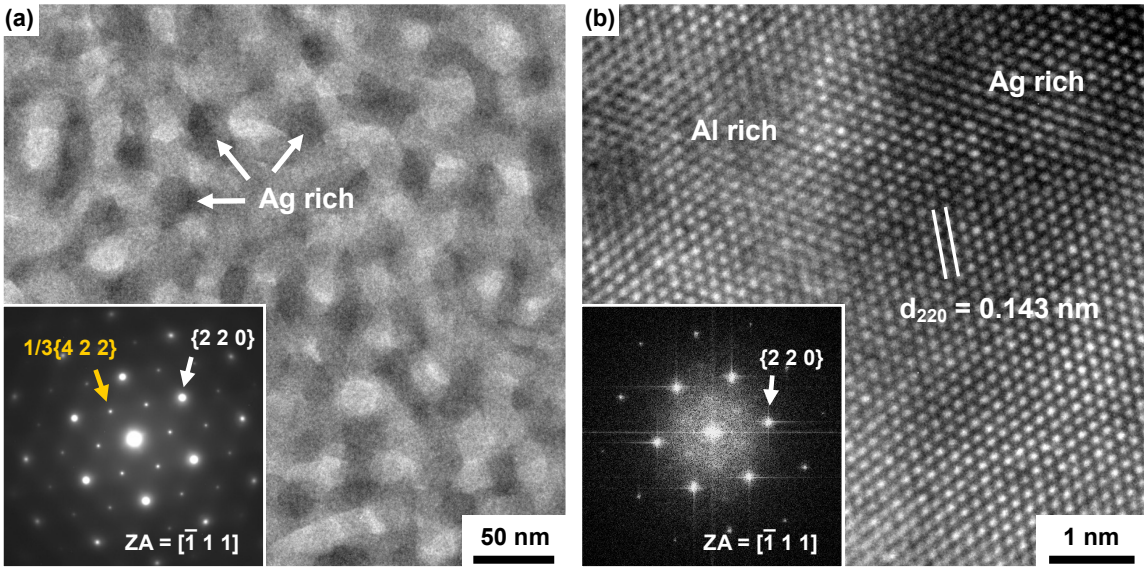

Figure 2.6 **(a)** TEM BF image and corresponding SAD pattern of α-Al(Ag) region and **(b)** high resolution TEM (HRTEM) image and corresponding fast Fourier transform (FFT) spectrum of Al and Ag phase separated region. The separated Al and Ag show same crystallographic orientation and coherent interface.

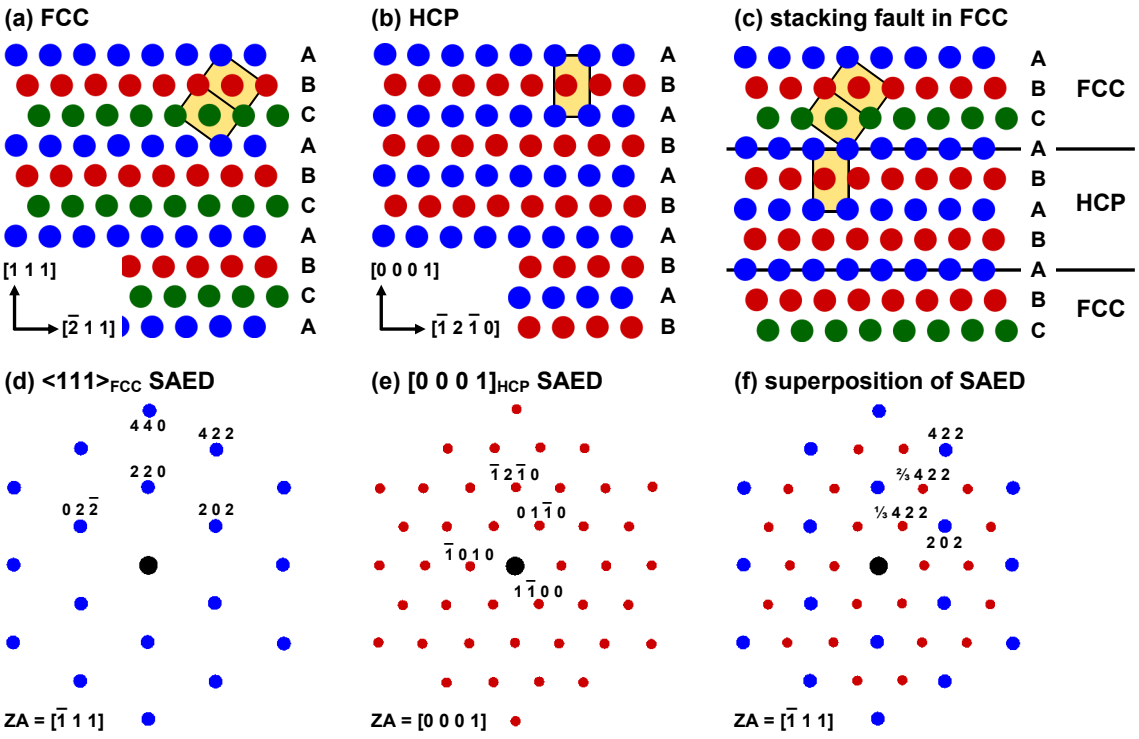

Figure 2.7 Stacking sequences of **(a)** {111} layers of FCC, **(b)** (0001) layers of HCP and **(c)** stacking fault in FCC, and corresponding SAED patterns of **(d)** <111> direction of FCC and **(e)** [0001] direction of HCP and **(f)** formation of 1/3{422} forbidden reflection by superposition of diffraction patterns of FCC and HCP.

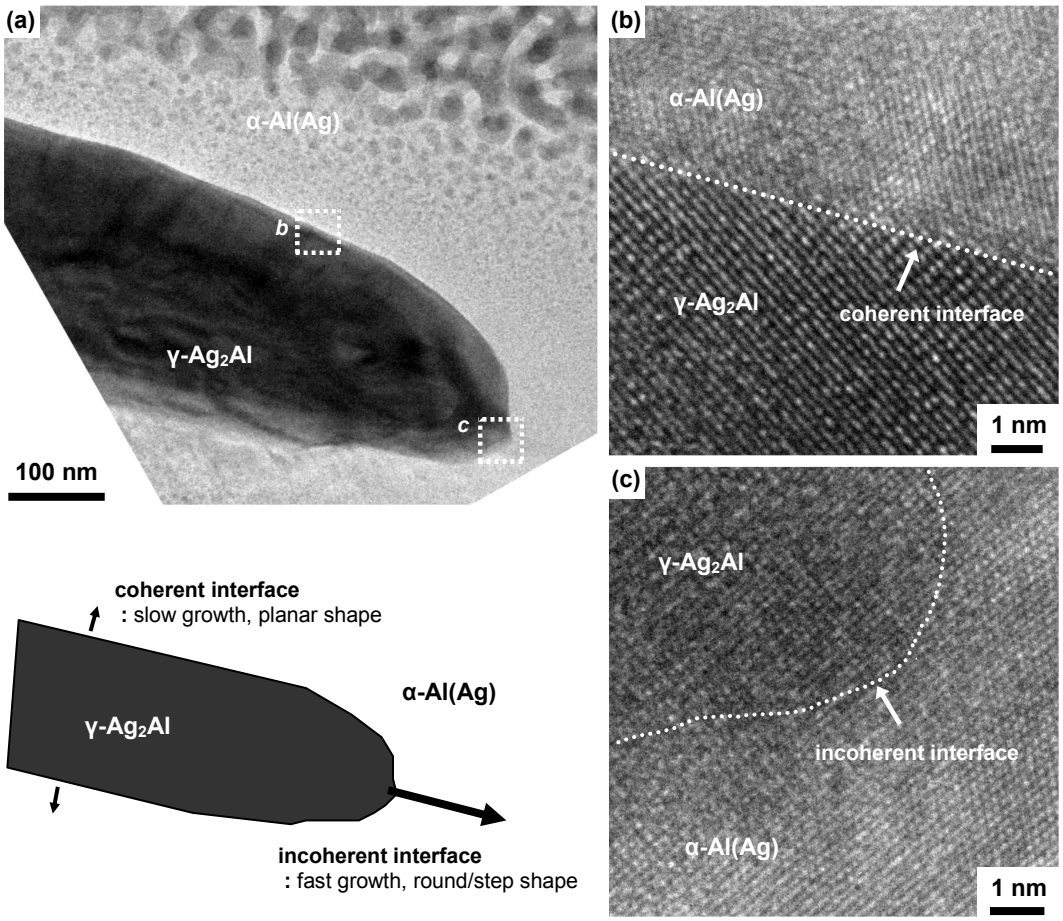

Figure 2.8 **(a)** TEM BF image of vicinity plate-shaped γ-Ag_2Al precipitate, and HRTEM images of **(b)** coherent interface and **(c)** incoherent interface between α-Al(Ag) and γ-Ag_2Al.

2.4 Dealloying behavior of Al-Ag precursor in the HCl solution

2.4.1 Change of phase constitution during the dealloying

Fig. 2.9(a) and 2.9(b) indicate XRD pattern and calculated lattice parameters of the melt-spun Al-Ag ribbon and the dealloyed samples as a function of dealloying time. The peak data of (311) and (222) plane diffraction for the FCC structure was used for the calculation to reduce systematic error. Fig. 2.9(c) shows EDS results about residual Al as a function of dealloying time. After 20 min, the 2θ position shifted into near the Ag position and widening of Al peaks were observed, which are the signs of the formation of porous Ag as a result of Al dissolution. Also the relative intensity of γ-Ag_2Al peak was increased up to 40 min. It is caused by relative increase of the volume fraction of γ-Ag_2Al due to the dissipation of α-Al. These results indicate that the dissolution rate of Al from α-Al solid solution is very fast compared with the γ-Ag_2Al. This difference of dissolution rate between two

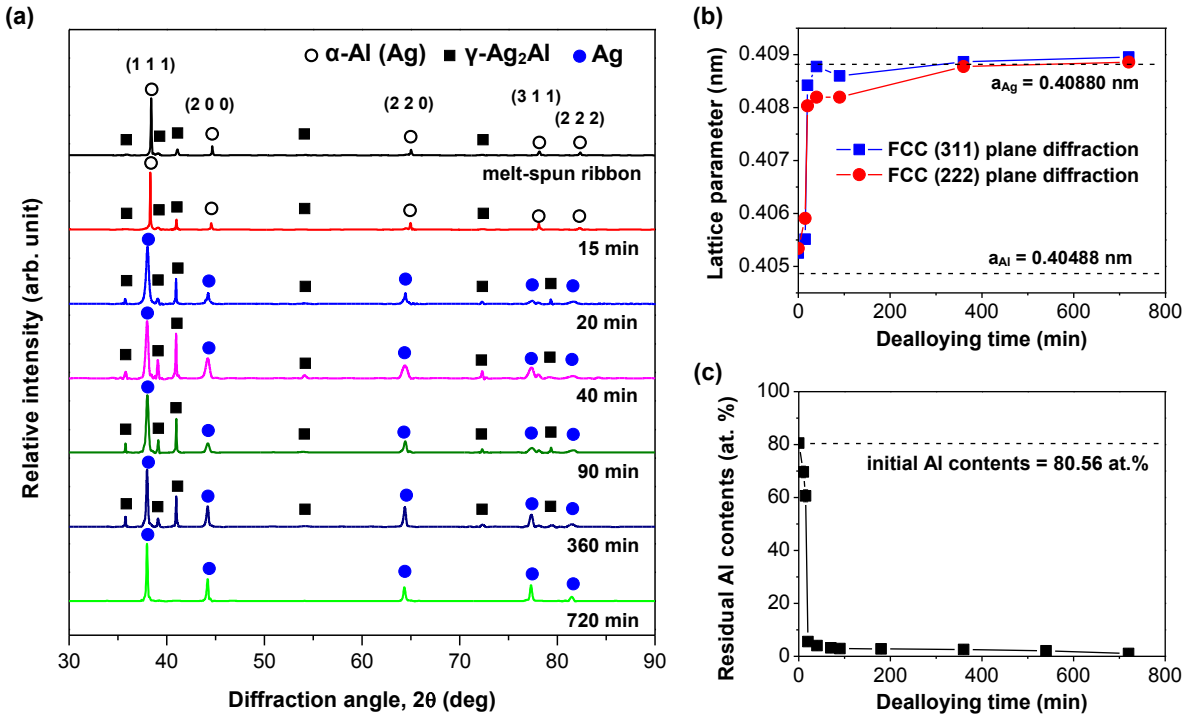

Figure 2.9 **(a)** The change of phase constitution, **(b)** the calculated lattice parameters of FCC crystal using diffraction data of $(311)_\alpha$ and $(222)_\alpha$ planes and **(c)** the residual Al measured by energy dispersive X-ray spectroscopy (EDS) during the dealloying reaction.

phases caused by the difference of electrochemical potential also can be found in the dealloying from Al-Cu alloy [24]. Also, it can be confirmed from EDS result (Fig. 2.9(c)). The contents of Al was significantly decreased and reached to about 5.6 at% for 20 min. With combination of XRD results which were mentioned above, it was confirmed that Al existed in α-Al was almost dissolved into the acid. After 360 min, the lattice parameter of FCC was nearly the same with the pure Ag. It indicates that α-Al phase was fully dealloyed and became pure Ag. And then, only FCC Ag peak was observed at 720 min.

2.4.2 Morphology change during the dealloying

The representative SEM images on the morphological change of Al-Ag precursor during the dealloying reaction with dealloying time of 10, 20, 70 and 720 min are shown in Fig. 2.10. At the early stage of dealloying process, intergranular corrosion (IGC) was occurred which is shown in Fig. 2.10 (a). After the 70 min (Fig. 2.10(c)), the plate-type precipitates of γ-Ag_2Al at the grain boundary (mean thickness of 227 ± 55 nm) and inside the grain (mean thickness of 72 ± 9 nm) were revealed. There

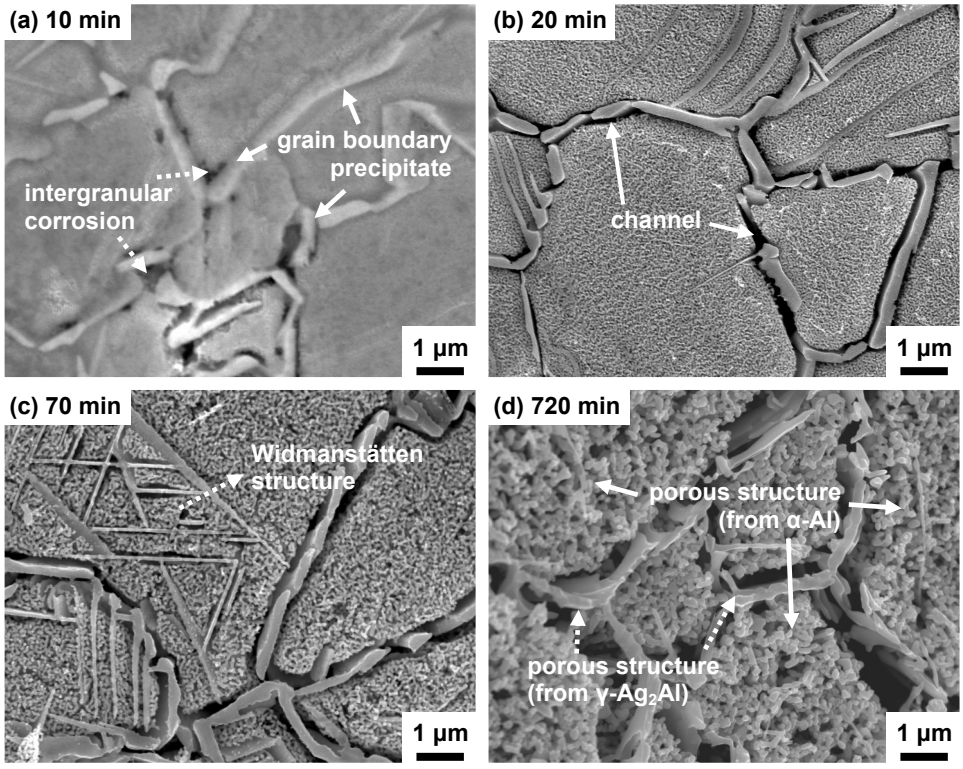

Figure 2.10 SEM secondary electron (SE) images about the change of morphology during the dealloying reaction for the dealloying time of **(a)** 10 min, **(b)** 20 min, **(c)** 70 min and **(d)** 720 min.

were deep channels (width of 50-300 nm) at the grain boundary. As shown in Fig. 2.9(d), α-Al and γ-Ag_2Al became porous structure and initial grain/intermetallic wall structure was kept in shape at 720 min. The dealloyed structure from α-Al was shown 3-dimensional bi-continuous ligament/pore structure. But the one from γ-Ag_2Al was shown pored wall structure due to the similarity between pore size and thickness of plate-type precipitates.

2.4.3 Intergranular corrosion induced by Ag depletion at the grain boundary

As shown in Fig. 2.4, the concentration of Ag shows lower value in the vicinity of interface of α-Al(Ag) and γ-Ag_2Al, compared with precipitate (γ-Ag_2Al) and inside the grain. From the EPMA mapping, the depletion of solute (Ag) in the vicinity of grain boundary γ-Ag_2Al precipitates can confirm clearly, besides, the depletion of Ag in the vicinity of Widmanstätten structure is indistinctive. The spatial resolution of X-ray spectroscopy is governed by penetration and electron trajectory in the specimen, that is approximately 1 μm^2 due to wide electron trajectory in bulk sample for SEM observation [25]. The X-ray mapping analysis with high spatial resolution can be achieved through the

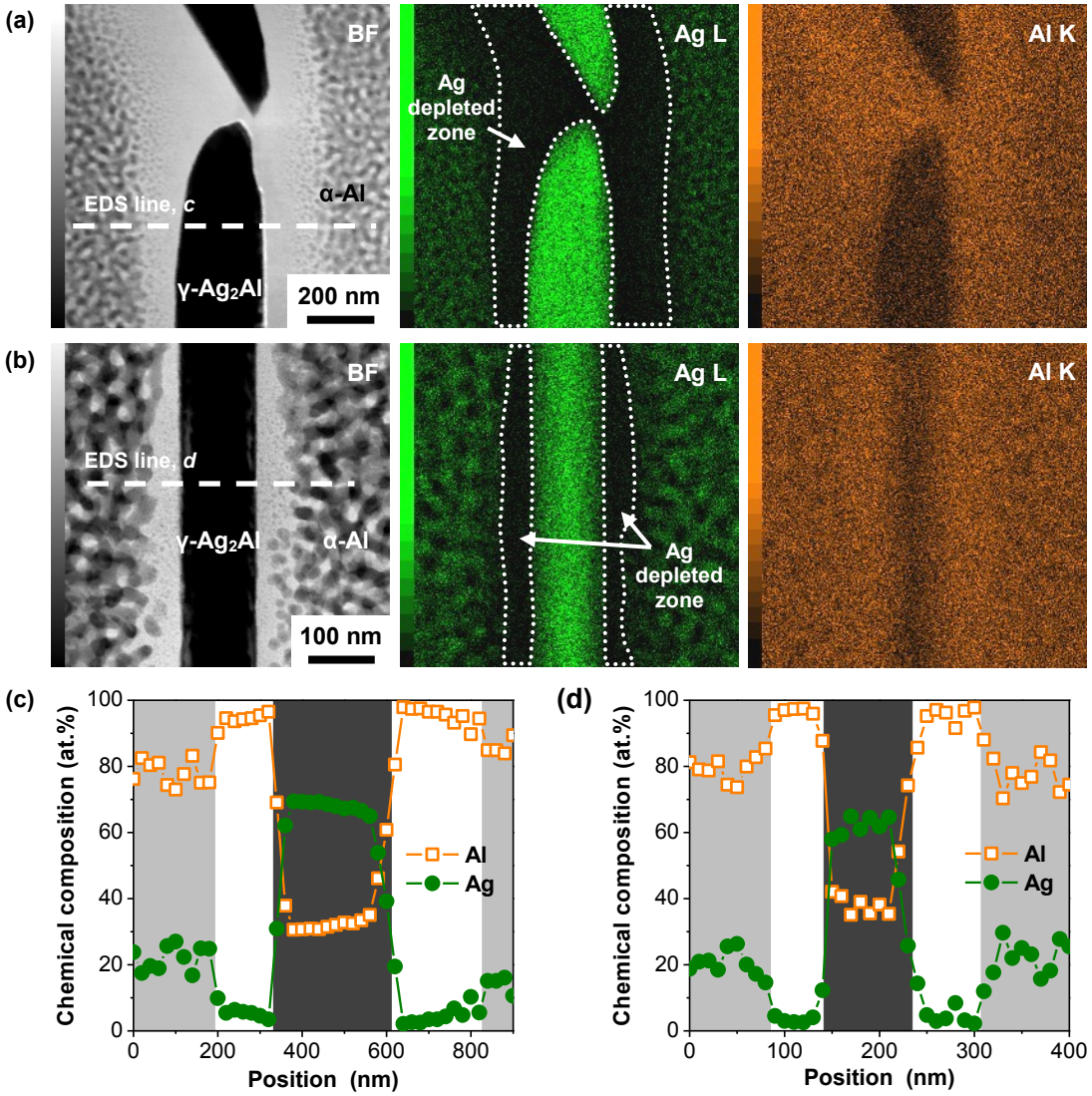

Figure 2.11 Scanning TEM (STEM) BF images, EDS mapping results of Ag and Al of **(a)** γ-Ag_2Al precipitate at the grain boundary and **(b)** γ-Ag_2Al precipitate inside the grain which are indicated white dotted area as *11a and 11b* in *Fig. 2.5*, respectively. **(c, d)** Chemical compositions of Al and Ag the dotted lines in *(a)* and *(b)*, where α-Al(Ag) and γ-Ag_2Al regions are indicated with *bright grey* and *dark grey*.

STEM based EDS analysis, as shown in Fig. 2.11. The Ag depleted zones near the γ-Ag_2Al boundary precipitates (Fig. 2.11(a)) and Widmanstätten structure of γ-Ag_2Al precipitates (Fig. 2.11(b)) were more distinct than the EPMA mapping analysis (Fig. 2.4). The concentrations of Ag (solute) in the adjacent to the γ-Ag_2Al show lower than 3 at%, due to the migration of Ag into γ-Ag_2Al for the growth of precipitates. The phase separation of Ag and Al in the in the α-Al(Ag) phase, as explained in Section *2.3.2*, led to the fluctuation of Ag concentration. The γ-Ag_2Al precipitate area exhibits a good agreement with the stoichiometric composition of γ-Ag_2Al (Fig. 2.11(c,d)).

The IGC can clearly observe in cross-section image after 3 and 5 min, as shown in Fig. 2.12. After dealloying for 3 min, there is empty space in the vicinity of γ-Ag_2Al (Ag-depleted zone) near the surface. The evolution of porosity in the α-Al(Ag) phase is insignificant. After dealloying for 5 min, the penetration depth of electrolyte increased and the α-Al(Ag) phase near the IGC is slightly dealloyed.

Fig. 2.13 shows the mechanism of channel formation during the dealloying of Al-Ag alloy at

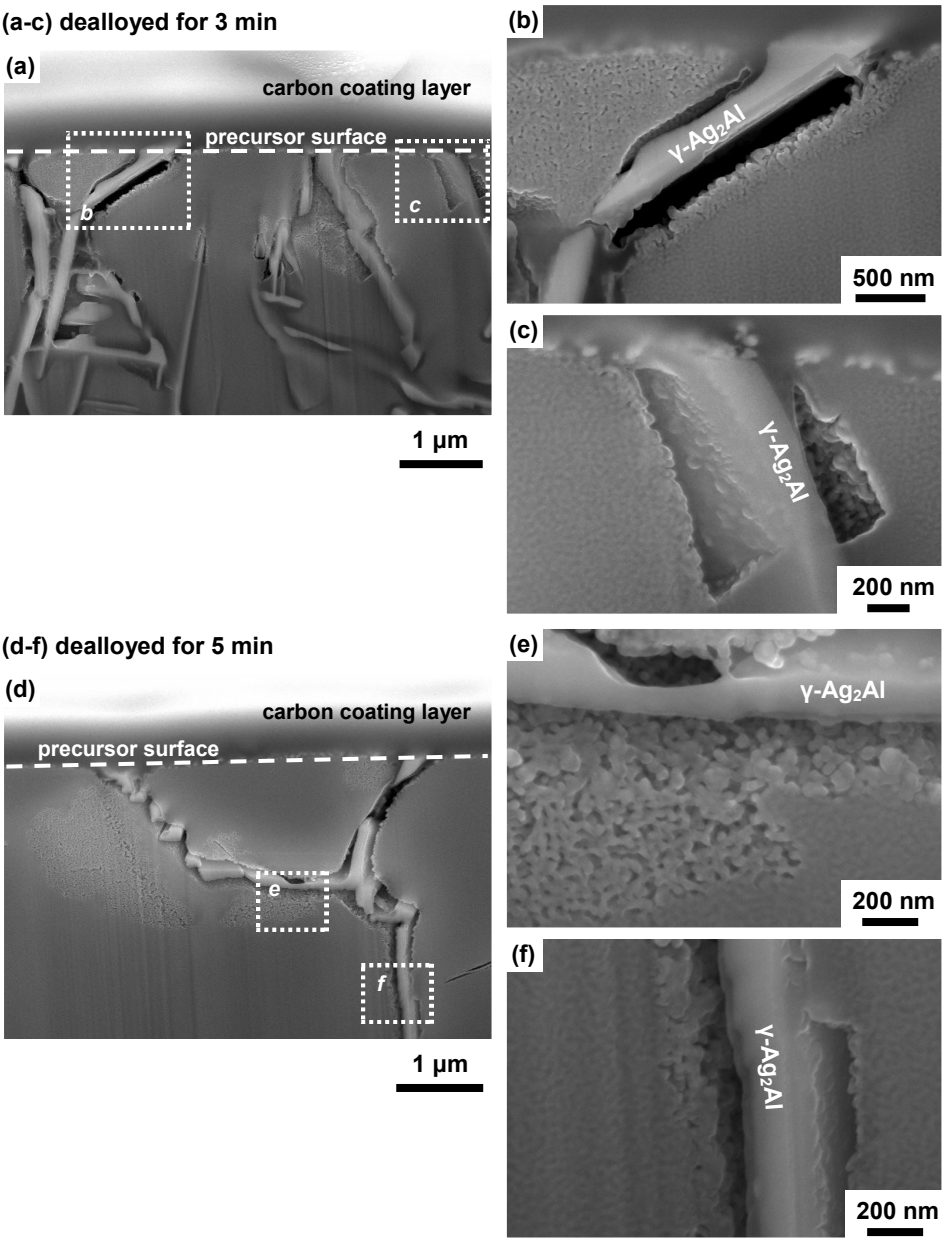

Figure 2.12 Focused ion beam (FIB) milled SEM SE images of dealloyed sample for **(a-c)** 3 min and **(d-f)** 5 min. The magnified images of **(b,c)** denoted area in *(a)* and **(e,f)** denoted area in *(d)*.

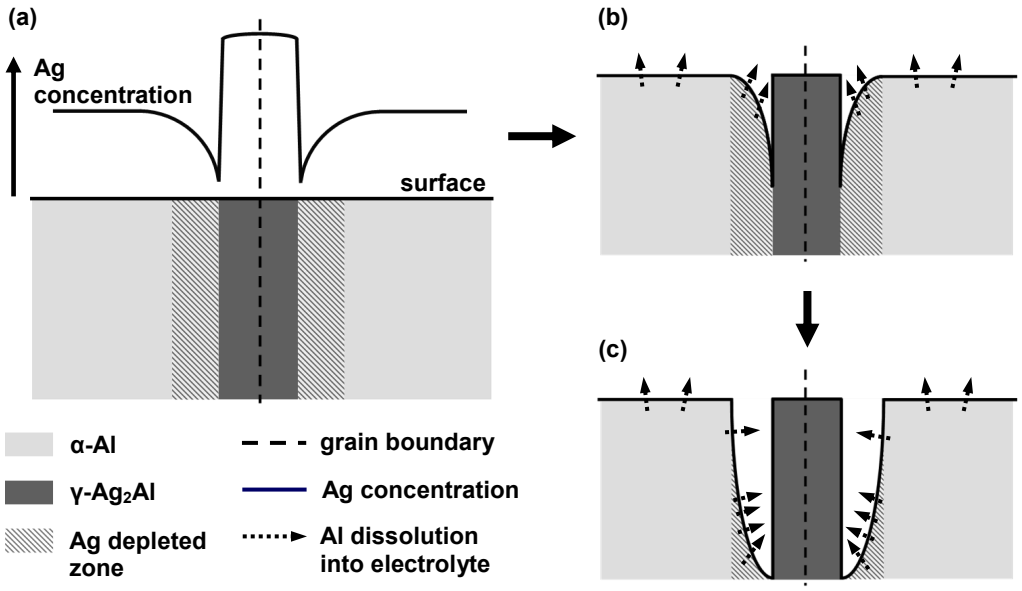

Figure 2.13 The schematic diagram of intergranular corrosion caused by formation of Ag-rich intermetallic phase and Ag depletion zone at the grain boundary: **(a)** Ag concentration around γ-Ag_2Al, **(b)** intergranular corrosion and **(c)** channel formation near the grain boundary.

the grain boundary which can be understood from Fig. 2.11 and Fig. 2.12. As shown in Fig. 2.8, γ-Ag_2Al was mainly nucleated at the boundary and grew as plate-type due to the difference of the growth rate between semi-coherent and incoherent interface [15]. The Ag depleted zone is more sensitive to the acid than α-Al and γ-Ag_2Al due to the low concentration of Ag. So, it was preferentially dissolved into the acid, as shown in Fig. 2.13(b) and 2.13(c). Consequently, the depleted zone completely disappeared and the channel was formed at α-Al/γ-Ag_2Al interface.

2.4.4 Development of porosity from α-Al and γ-Ag_2Al phases

In Fig. 2.14 and 2.15, the development of Ag cluster and the evolution to pore structure from α-Al and γ-Ag_2Al are shown. There are some evidences of Ag cluster at the surface of α-Al for 10 min (dotted arrow in Fig. 2.14(a)) and γ-Ag_2Al for 540 min (lined arrow in Fig. 2.15(c)). At these times, the scales of Ag cluster from α-Al and γ-Ag_2Al were about 10-20 nm and 80-150 nm, respectively. The Ag cluster formation from α-Al at the surface (Fig. 2.14(a)) and in the internal area (Fig. 2.14(b)) accompanied by IGC and subsequent electrolyte penetration were explained above. The α-Al at the surface became nanoporous structure for 20 min (Fig. 2.14(c)). At this time, there is no any evidence of dealloying in γ-Ag_2Al region.

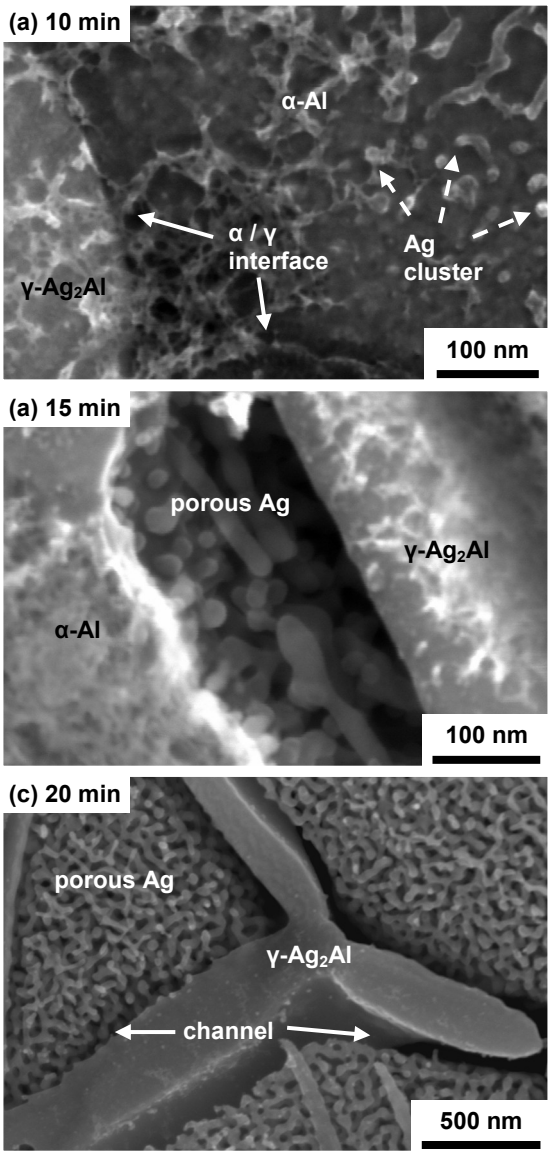

Figure 2.14 **(a)** Formation of Ag cluster from α-Al for 10 min, **(b)** development of nanoporous structure inside the sample by penetration of electrolyte along intergranular corrosion region for 15 min, and **(c)** channel formation along the grain boundary and Ag nanoporous structure of α-Al region for 20 min.

In the case of γ-Ag_2Al, as dealloying time passed by, the cluster size was increased and the step-like shape of Ag cluster was distinctly revealed (Fig. 2.15). Erlebacher [26] suggested the atomistic description that the cluster of MN elements formed and the island structure grew by gradual stripping of LN elements layer and surface diffusion of MN elements. The dissolution rate of Al from γ-Ag_2Al was considerably slow in comparison with in case of α-Al.

Volume changes during the evolution of nanoporosity from α-Al (15at%Ag supersaturated) and γ-Ag_2Al. Molar volume of crystalline material can be calculated using equation 2.3,

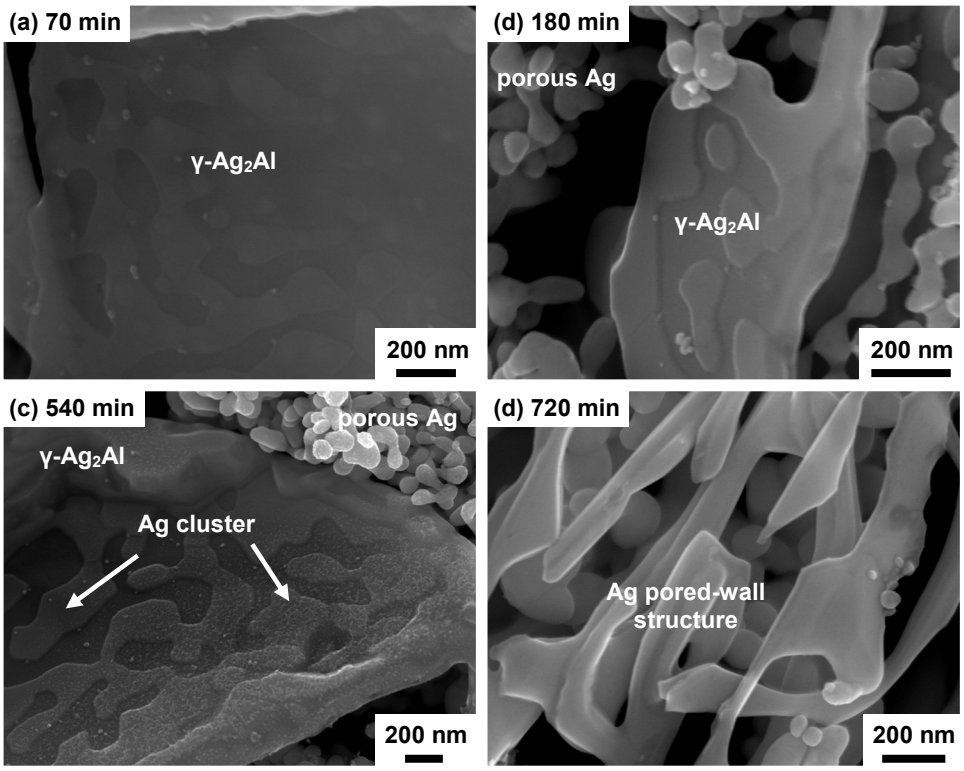

Figure 2.15 SEM SE images on the formation of Ag cluster from γ-Ag_2Al for **(a)** 10 min, **(b)** 180 min, **(c)** 540 min, and **(d)** formation of pored-wall structure for 720 min.

$$V_m = \frac{V_c N_A}{Z} \quad \cdots\cdots (2.3)$$

where V_m is a molar volume, V_c is a unit cell volume, N_a is the Avogadro constant (6.022×10^{23} mol^{-1}), and Z is a number of formula units per unit cell. Crystallographic parameters for pure Al, α-Al(Ag), pure Ag and γ-Ag_2Al are represented in Table 2.1. With an assumption that Al is completely dissolved into electrolyte, the porosity of Ag porous structure from α-Al(Ag) and γ-Ag_2Al can be calculated using equation 2.4,

$$porosity = \frac{V_{m,i} - (1 - C_{Ag})V_{m,Ag}}{V_{m,i}} \times 100\% \quad \cdots\cdots (2.4)$$

where, $V_{m,i}$ and $V_{m,Ag}$ are molar volumes of initial compound and Ag porous structure (equal to pure Ag), respectively, and C_{Ag} is an atomic concentration of Ag in initial compound (C_{Ag} of α-Al(Ag) = 15%, C_{Ag} of γ-Ag_2Al = 66.67%). The calculated volume changes as a result of dealloying from α-Al and γ-Ag_2Al were approximately 84.6% and 31.4%, respectively. According to the computational

Table 2.1 Crystallographic parameters for Al, α-Al(Ag), Ag and γ-Ag_2Al.

Phase	JSPDS no	Symmetry	Space group	a (Å)	b (Å)	c (Å)	Z	V_c (Å^3)**	V_m (Å^3/mol)
Al	71-3760	cubic	Fm-3m	4.0488	-	-	4	66.371	9.992
α-Al(Ag)*	-	cubic	Fm-3m	4.0519	-	-	4	66.652	10.015
Ag	71-4613	cubic	Fm-3m	4.0880	-	-	4	68.318	10.285
γ-Ag_2Al	74-5113	hexagonal	$P6_3/mmc$	2.8779	-	4.6255	2	33.177	9.989

* A lattice parameter of α-Al(Ag) is derived data from XRD analysis (Fig. 2.3).

** cubic: $V_c = a^3$; hexagonal: $V_c = a^2c \sin(60°)$

analysis about relationship between geometry of nanostructure and density [27], porous structure from α-Al and γ-Ag_2Al can be classified as disordered nanoporous structure and cylindrical pore structure, respectively. The high concentration of Ag in γ-Ag_2Al leads to this close-pore structure. This result has also been proved in another research about dealloyed structure from the Al-60Ag precursor [28].

2.4.5 Ligament coarsening and assessment of surface diffusivity of Ag

Fig. 2.16 exhibits the example of measurement method for ligament (fibrous connecting parts of Ag junctions in the nanoporous structure) size. The ligament size was taken as a average value on over 20 parts in each dealloying time. The growth of ligament as a function of time can be clearly identified in Fig. 2.17. The size scale of ligament is increased in accordance with the coarsening mechanism which is controlled by the surface diffusion of MN elements [29]. The ligament size of

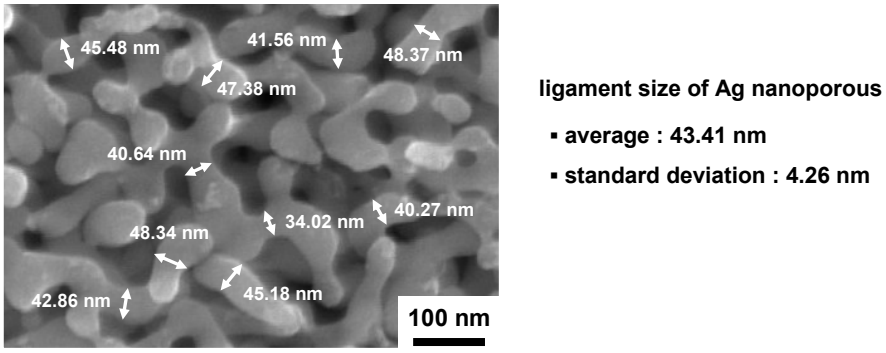

Figure 2.16 The example of ligament size measurement for Ag nanoporous structure which is dealloyed for 70 min.

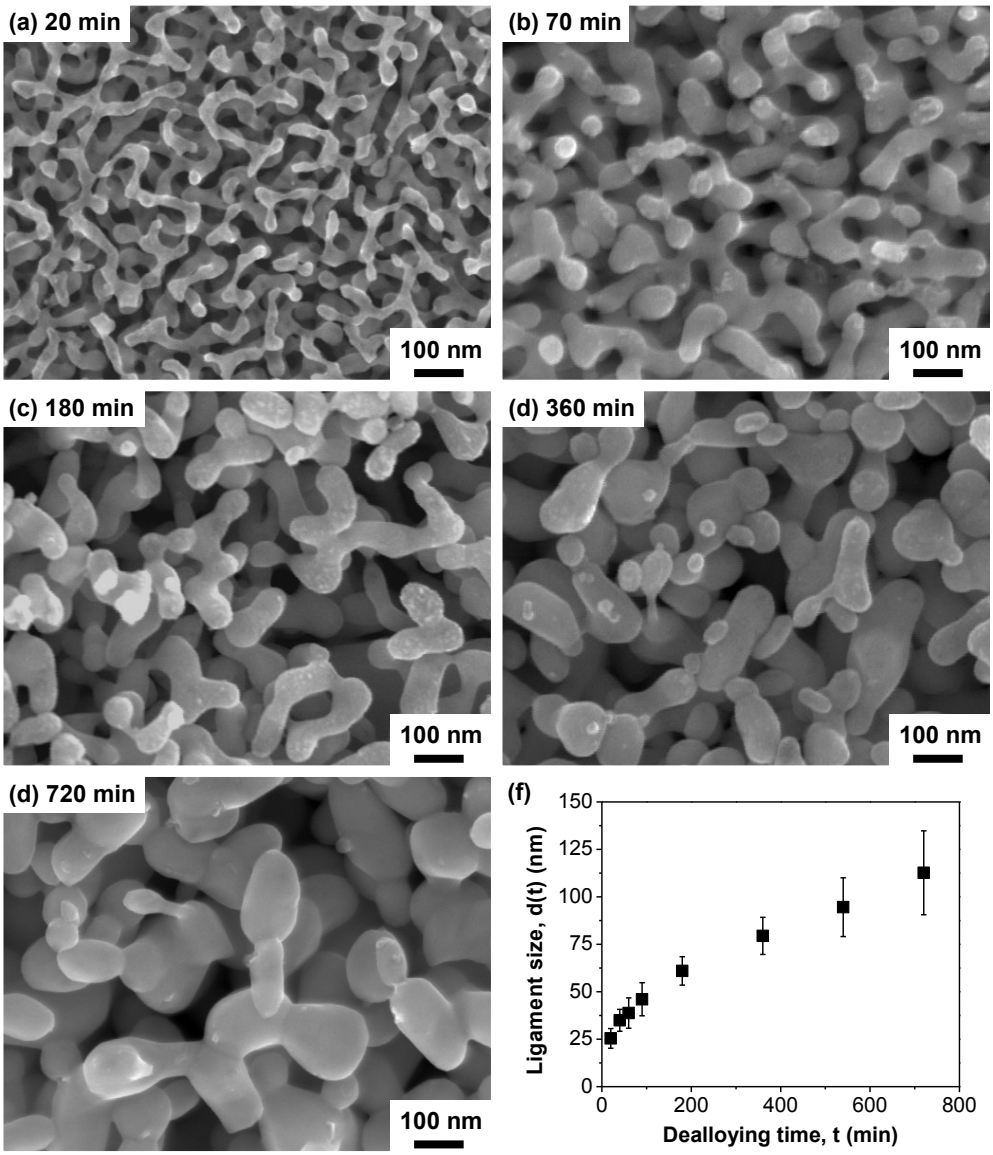

Figure 2.17 SEM SE images of nanoporous structure with different dealloying time: **(a)** 20 min, **(b)** 70 min, **(c)** 180 min, **(d)** 360 min, **(e)** 720 min and **(f)** change of ligament size as a function of time.

nanoporous Ag was gradually increased from 25 ± 5 nm to 113 ± 22 nm with the increase of dealloying time (Fig. 2.17(f)). The size scale and growth rate of nanoporous structure seems to be proportional to the surface diffusivity of MN element [4,30].

Many researchers have shown the linear relationship between columnar radius and fourth root of time, $t^{1/4}$, at the Au columnar structure and electrolyte interface [31–33]. They have expressed the time dependence of the radius of columnar structure using equation 2.5:

$$r(t)^4 = \frac{2\gamma a^4 D_s}{k_B T} \times t \quad \cdots\cdots (2.5)$$

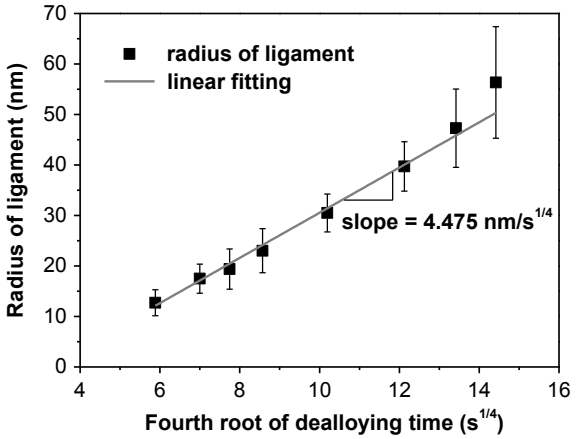

Figure 2.18 Linear plotting of the radius of ligament, *r(t),* versus the fourth root of dealloying time, $t^{1/4}$, for the calculation of surface diffusivity of Ag in HCl solution at room temperature.

where *r(t)* is the radius of columnar structure at time *t*, γ is the surface energy, *a* is the lattice parameter, D_s is the coefficient of surface diffusion at temperature *T* and k_B is the Boltzmann constant (1.380648×10^{-23} J/K). Qian and Chen [34] attempt to explain the coarsening behavior of Au nanoporous structure and calculate the surface diffusivity of Au in electrolyte during the dealloying using this relationship. And it also has been used for the expression of coarsening behavior of Ag [3] and Cu [24] nanoporous structure. For the calculation of surface diffusivity of Ag in HCl during dealloying process, the given parameters in Equation 2.5 were replaced by dealloying parameters, where *r(t)* is the radius of ligament at dealloying time of *t*, γ is the surface energy of Ag (1.24 J/m^2) [35], *a* is the lattice parameter of Ag (0.4088 nm), D_s is the coefficient of surface diffusion of Ag and *T* is the dealloying temperature.

Fig. 2.18 is shown the mean radius of ligament as a function of fourth root of time, $t^{1/4}$. The given values show relatively good linear relationship. The linear fitting was conducted using the least square regression method. The slope of the fitting line is correspond to $(2\gamma a^4 D_s/kT)^{0.25}$, so the D_s of Ag can be calculated. The calculated value of D_s of Ag in 2 M HCl at room temperature was 2.34×10^{-17} m^2/s. This value shows two orders of magnitude higher than Au ($D_s = 2.0 \times 10^{-19}$ m^2/s) at the similar dealloying temperature (298 K) [35]. It shows good agreement with the general difference of the D_s between Ag and Au [36]. In the same precursor system, our result shows quite low value in comparison with the calculation value of the D_s of Ag (4.85×10^{-16} m^2/s) in the dealloying of Al-15Ag in 5% HCl at 363 K [3]. It seems that the D_s is influenced by dealloying temperature. The temperature

dependence of D_s can be seen in the fabrication of nanoporous Au from Au-Ag precursor. The nanoporous structure is more and more coarsened and D_s is also increased with the increasing of dealloying temperature [35].

2.5 Overall description on the dealloying behavior of bi-phase Al-Ag precursor

Fig. 2.19 shows the schematic diagram about the sequential dealloying reaction of bi-phase Al-Ag precursor in the HCl. The dissolution of Al from the surface and IGC were occurred in the early stage of reaction. The electrolyte penetrated into the alloy through the channel, as shown in Fig. 2.19 (b), and open-pore, as shown in Fig. 2.19(c), and the dissolution of Al was accelerated due to the increase of contact area between the alloy and the electrolyte. The EDS result, as shown in Fig. 2.8(c) confirms this, which is shown a significant decrease of Al concentration for 10-20 min.

It is not sure whether α-Al is preferentially dealloyed than γ-Ag_2Al due to the galvanic effect or α-Al and γ-Ag_2Al is simultaneously dealloyed from the observation of microstructure. But the dealloying rate of α-Al was about 20 times faster than γ-Ag_2Al in HCl. So, α-Al was transformed into

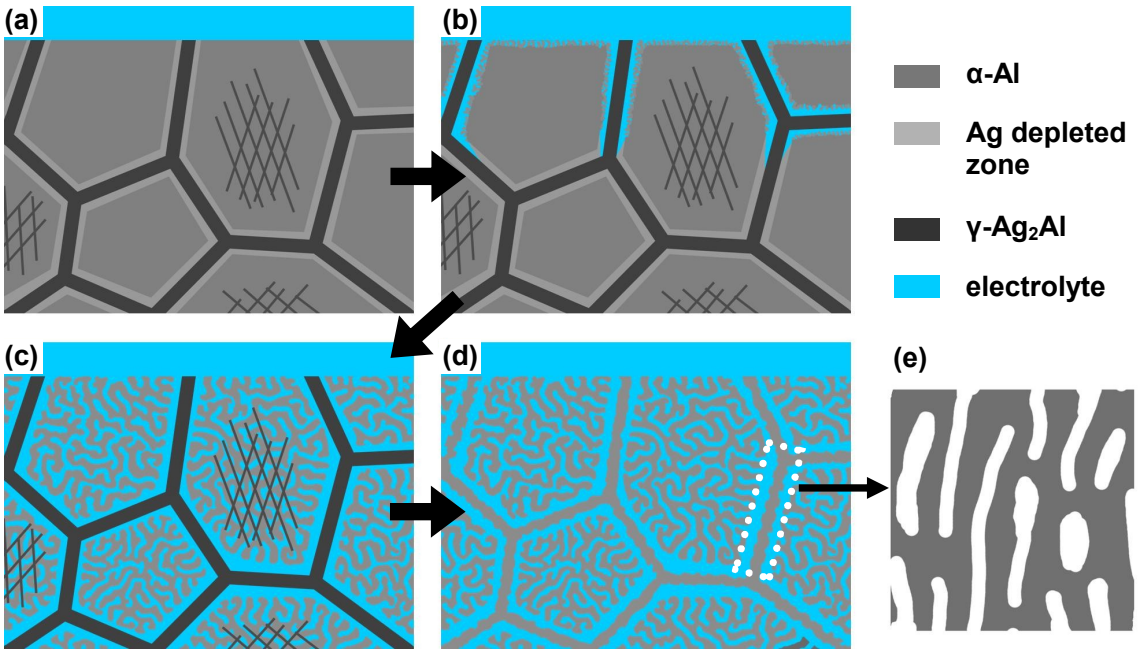

Figure 2.19 Schematic diagram of Al dissolution and Ag nanoporous structure formation sequence of the bi-phase Al-Ag alloy during the dealloying: **(a)** initial state, **(b)** intergranular corrosion and Ag cluster formation at the precursor/electrolyte interface, **(c)** formation of the 3-dimensional Ag nanoporous structure form α-Al, **(d)** formation of the Ag pored-wall structure from γ-Ag_2Al and **(e)** plane figure of the pored-wall structure (*dotted area* in *d*).

the Ag nanoporous structure, as shown in Fig. 2.19(c), and then the residual γ-Ag_2Al was dealloyed, as shown in Fig. 2.19(d). The reason of the formation of pored wall structure from γ-Ag_2Al was mentioned above. Zhang and Zhang [37] concluded that the diffusion distance of NM elements during the whole dealloying reaction was not sufficient to migrate across the channel. For this reason, the initial grain/boundary precipitates structure was kept in the shape, as shown in Fig. 2.19.

2.6 Conclusion

The Ag nanoporous sheet was fabricated using dealloying method from the Al-Ag precursor alloy. The dealloying behavior of Al-20at% Ag ribbon under free corrosion condition with 2 M HCl has been investigated. The fabricated Al-Ag ribbon using melt-spinning was consisted of α-Al (main matrix) and γ-Ag_2Al (grain boundary precipitate and Widmanstätten structure). A considerable amount of γ-Ag_2Al was suppressed by the rapid solidification, 5.6% of γ-Ag_2Al was precipitated. In the early stage of dealloying, the preferential attack on the Ag depleted zone caused the formation of deep channel at the grain boundary . The dealloying rate of α-Al was faster than it of γ-Ag_2Al, so α-Al was preferentially formed Ag nanoporous structure. The Ag nanoporous structure with the size scale of 113 ± 22 nm was obtained through the free corrosion dealloying in HCl for 720 min.

References

[1] A.J. McAlister, “The Ag-Al (silver-aluminum) system”, *Bull. Alloy Phase Diagr.*, **8** (1987) 526 –533.

[2] R.P. Elliott, F.A. Shunk, “The Ag-Au (silver-gold) system”, *Bull. Alloy Phase Diagr.*, **1** (1980) 45–47.

[3] T. Song, Y. Gao, Z. Zhang, Q. Zhai, “Dealloying behavior of rapidly solidified Al–Ag alloys to prepare nanoporous Ag in inorganic and organic acidic media”, *CrystEngComm*, **13** (2011) 7058–7067.

[4] H. Qiu, Z. Zhang, X. Huang, Y. Qu, “Dealloying Ag-Al alloy to prepare nanoporous silver as a substrate for surface-enhanced Raman scattering: Effects of structural evolution and surface modification”, *ChemPhysChem*, **12** (2011) 2118–2123.

[5] T. Song, Y. Gao, Z. Zhang, Q. Zhai, “Influence of magnetic field on dealloying of Al-25Ag alloy and formation of nanoporous Ag”, *CrystEngComm*, **14** (2012) 3694–3701.

[6] E. Detsi, Z. Vuković, S. Punzhin, P.M. Bronsveld, P.R. Onck, J.T.M. De Hosson, "Fine-tuning the feature size of nanoporous silver", *CrystEngComm*, **14** (2012) 5402–5406.

[7] I. Yamauchi, T. Kajiwara, T. Mase, M. Saraoka, "Formation of highly saturated Al-Ag precursor by rapid solidification for skeletal silver synthesis", *J. Alloy. Compd.*, **336** (2002) 206 –212.

[8] C. Xu, Y. Li, F. Tian, Y. Ding, "Dealloying to nanoporous silver and its implementation as a template material for construction of nanotubular mesoporous bimetallic nanostructures", *ChemPhysChem*, **11** (2010) 3320–3328.

[9] C.R. Hubbard, E.H. Evans, D.K. Smith, "The reference intensity ratio, I/I_c, for computer simulated powder patterns", *J. Appl. Crystallogr.*, **9** (1976) 169–174.

[10] C.J. Byrne, A.M. Kueck, S.P. Baker, P.H. Steen, "In situ manipulation of cooling rates during planar-flow melt spinning processing", *Mater. Sci. Eng. A*, **459** (2007) 172–181.

[11] E.M. Ahmed, E.S. Gouda, "Microstructure and physical properties of melt spun Al-17 wt% Ni-10 wt% Cu alloy", *Eur. Phys. J. Appl. Phys.*, **50** (2010) 21301.

[12] R.J.D. Tilley, *Crystal and crystal structures*, John Wiley & Sons, Chichester, 2006.

[13] D. Brandon, W.D. Kaplan, *Microstructural characterization of materials*, 2nd edition, John Wiley & Sons, Chichester, 2008.

[14] B.D. Cullity, *Elements of X-ray diffraction*, Addison-Wesley, Massachusetts, 1956.

[15] D.A. Porter, K.E. Easterling, *Phase transformations in metals and alloys*, 2nd edition, Nelson Thornes, Cheltenham, 1992.

[16] C. Laird, H. Aaronson, "The growth of γ plates in an Al-15% Ag alloy", *Acta Metall.*, **17** (1969) 505–519.

[17] M. Matula, L. Hyspecka, M. Svoboda, V. Vodarek, C. Dagbert, J. Galland, Z. Stonawska, L. Tuma, "Intergranular corrosion of AISI 316L steel", *Mater. Charact.*, **46** (2001) 203–210.

[18] K. Moore, W. Johnson, J. Howe, H. Aaronson, "On the interaction between Ag-depleted zones surrounding plates and spinodal decomposition in an Al-22 at% Ag alloy", *Acta Mater.*, **50** (2002) 943–956.

[19] K.T. Moore, J.M. Howe, "Characterization of γ plate-shaped precipitates in an Al-42 at% Ag alloy - Growth kinetics, solute field, composition and modeling", *Acta Mater.*, **48** (2000) 4083–4098.

[20] K. Inoke, K. Kaneko, M. Weyland, P.A. Midgley, K. Higashida, Z. Horita, "Severe local strain and the plastic deformation of Guinier-Preston zones in the Al-Ag system revealed by three-dimensional electron tomography", *Acta Mater.*, **54** (2006) 2957–2963.

[21] R. Jin, Y. Cao, C.A. Mirkin, K.L. Kelly, G.C. Schatz, J.G. Zheng, "Photoinduced conversion of silver nanospheres to nanoprisms", *Science*, **294** (2001) 1901–1903.

[22] V. Germain, J. Li, D. Ingert, Z.L. Wang, M.P. Pileni, "Stacking faults in formation of silver nanodisks", *J. Phys. Chem. B*, **107** (2003) 8717–8720.

[23] L. Lu, A. Kobayashi, Y. Kikkawa, K. Tawa, Y. Ozaki, "Oriented attachment-based assembly of dendritic silver nanostructures at room temperature", *J. Phys. Chem. B*, **110** (2006) 23234–23241.

[24] W. Liu, S. Zhang, N. Li, J. Zheng, S. An, G. Li, "Influence of dealloying solution on the microstructure of monolithic nanoporous copper through chemical dealloying of Al 30 at.% Cu alloy", *Int. J. Electrochem. Sci.*, **7** (2012) 7993–8006.

[25] D.B. Williams, C.B. Carter, *Transmission electron microscopy: A textbook for materials science*, 2nd edition, Springer, New York, 2009.

[26] J. Erlebacher, "An atomistic description of dealloying: Porosity evolution, their critical potential, and rate-limiting behavior", *J. Electrochem. Soc.*, **151** (2004) C614–C626.

[27] E. Detsi, E. De Jong, A. Zinchenko, Z. Vuković, I. Vuković, S. Punzhin, K. Loos, G. Ten Brinke, H.A. De Raedt, P.R. Onck, J.T.M. De Hosson, "On the specific surface area of nanoporous materials", *Acta Mater.*, **59** (2011) 7488–7497.

[28] X. Wang, Z. Qi, C. Zhao, W. Wang, Z. Zhang, "Influence of alloy composition and dealloying solution on the formation and microstructure of monolithic nanoporous silver through chemical dealloying of Al-Ag alloys", *J. Phys. Chem. C*, **113** (2009) 13139–13150.

[29] G. Andreasen, M. Nazzarro, J. Ramirez, R.C. Salvarezza, A.J. Arvia, "Kinetics of particle coarsening at gold electrode/electrolyte solution interfaces followed by in situ scanning tunneling microscopy", *J. Electrochem. Soc.*, **143** (1996) 466.

[30] J. Erlebacher, M.J. Aziz, A. Karma, N. Dimitrov, K. Sieradzki, "Evolution of nanoporosity in dealloying", *Nature*, **410** (2001) 450–453.

[31] J.M. Dona, J. González-Velasco, "Mechanism of surface diffusion of gold adatoms in contact with an electrolytic solution", *J. Phys. Chem.*, **97** (1993) 4714–4719.

[32] C. Alonso, R.C. Salvarezza, J.M. Vara, A.J. Arvia, L. Vazquez, A. Bartolome, A.M. Baro, "The evaluation of surface diffusion coefficients of gold and platinum atoms at electrochemical interfaces from combined STM-SEM imaging and electrochemical techniques", *J. Electrochem. Soc.*, **137** (1990) 2161–2166.

[33] M.P. García, M.M. Gómez, R.C. Salvarezza, A.J. Arvia, "Effect of the solution composition and the applied potential on the kinetics of roughness relaxation at gold electrodes in slightly acid electrolytes", *J. Electroanal. Chem.*, **347** (1993) 237–246.

[34] L.H. Qian, M.W. Chen, "Ultrafine nanoporous gold by low-temperature dealloying and kinetics of nanopore formation", *Appl. Phys. Lett.*, **91** (2007) 083105.

[35] W.R. Tyson, W.A. Miller, "Surface free energies of solid metals: Estimation from liquid surface tension measurements", *Surf. Sci.*, **62** (1977) 267–476.

[36] N. Hirai, H. Tanaka, S. Hara, "Enhanced diffusion of surface atoms at metal/electrolyte interface under potential control", *Appl. Surf. Sci.*, **130-131** (1998) 506–511.

[37] Q. Zhang, Z. Zhang, "On the electrochemical dealloying of Al-based alloys in a NaCl aqueous solution", *Phys. Chem. Chem. Phys.*, 12 (2010) 1453–1472.

Chapter 3

Solid-state thermo-compression bonding using Ag nanoporous sheet

3.1 Introduction

In the fabrication of the requisite nanoparticle paste, various organic substances including solvents, capping molecules, and binder have been adopted to adjust the final properties of the paste [1], as mentioned in *Chapter 1*. After the joining process, any residual organic material or coffee-ring effect can induce unexpectedly large voids or gaps in the joint area [2,3]. It also showed that the problems of void formation and hindrance of sintering caused by the evaporation of solvent and residual surfactant of nanoparticle [4–6]. To address these problems, this chapter focuses instead on the nanoporous metals [7], and proposes that solid-state nanoporous bonding (NPB) can be achieved using a Ag nanoporous sheet without the need for any solvent, organic substance or flux.

In this study, the Ag nanoporous sheet fabricated by dealloying method from the Al-Ag precursor alloy was applied as a bonding material for the die attach. The microstructure and shear strength of the resulting joint were characterized. The effect of bonding temperature on joint strength, formation of sintered Ag layer and fracture behavior of Ag NPB process with an electroless Ni/ immersion Au (ENIG) surface finished Cu disk in air condition was evaluated. Owing to clearly assess the changes of shear strength results and fracture behavior of Ag NPB joint with various bonding temperatures, Ag NPB process in N_2 was also conducted for the comparison.

3.2 Experimental

3.2.1 Preparation of Ag nanoporous sheet

The Ag nanoporous sheet (thickness = 90-100 um, ligament size = 110 nm) was fabricated by dealloying a melt-spun Al-Ag precursor alloy in a 2 M HCl solution for 3 h at 75 °C. The appearances of Al-Ag precursor and dealloyed Ag nanoporous sheet and microstructure of Ag nanoporous sheet are shown in Fig. 3.1(a,b). The phase change from the α-Al(Ag) and γ-Ag_2Al of the Al-Ag precursor to a single Ag phase of Ag nanoporous sheet as a result of dealloying could be confirmed in Fig. 3.1(c). As shown in Fig. 3.2, an electron probe micro-analyzer (EPMA) mapping results of Ag nanoporous sheet dealloyed at 25 °C for 12 h exhibited residual Al signal, namely the dealloying of Al was not insufficient. The residual Al was significantly reduced in case of the Ag nanoporous sheet dealloyed at 75 °C for 3 h. Afterwards, Ag nanoporous sheet for bonding material (in *Chapter 3-5*) was prepared using dealloying at 75 °C for 3 h.

3.2.2 Ag nanoporous bonding process

The ENIG finished Cu disk as a test specimen, as shown in Fig. 3.3(a), was used to evaluate to strength of NPB joint. The thickness of Ni(P) and Au were about 2 μm and 80 nm, respectively. A cross-section of ENIG finish was observed using owing to confirm initial quality of ENIG surface finish with a scanning electron microscope (SEM, SU-70, Hitachi) and a transmission electron microscope (TEM, JEM-2100F, JEOL) before the bonding process. The TEM sample preparation of ENIG finish was prepared by the *in-situ* lift-out method using a focused ion beam (FIB, JIB-4500, JEOL). Prior to FIB milling, thin Au-Pd (approximately 50 nm) and C (approximately 2 μm) were deposited on surface of ENIG for the preservation from the damage of very thin Au layer by a Ga ion beam. As shown in Fig. 3.3(b-d), uniform ENIG layer was formed without any defect. The ENIG finished Cu disk was immersed in acetone and then degreased using an ultrasonic cleaner for 5 min, in order to remove any surface contamination. From a selected area electron diffraction (SAED) pattern, Ni(P) plating layer showed an amorphous structure, as shown in Fig. 3.3(d). The Ag nanoporous sheet was then applied to the surface of the test specimen. The ENIG finished Cu disks were bonded using a thermo-compression bonding system in both air and N_2 atmosphere for the comparison. An applied pressure of 20 MPa was used, and the bonding temperatures varied from 200 °C to 400 °C. The temperature profile of the bonding process is shown in Fig. 3.4.

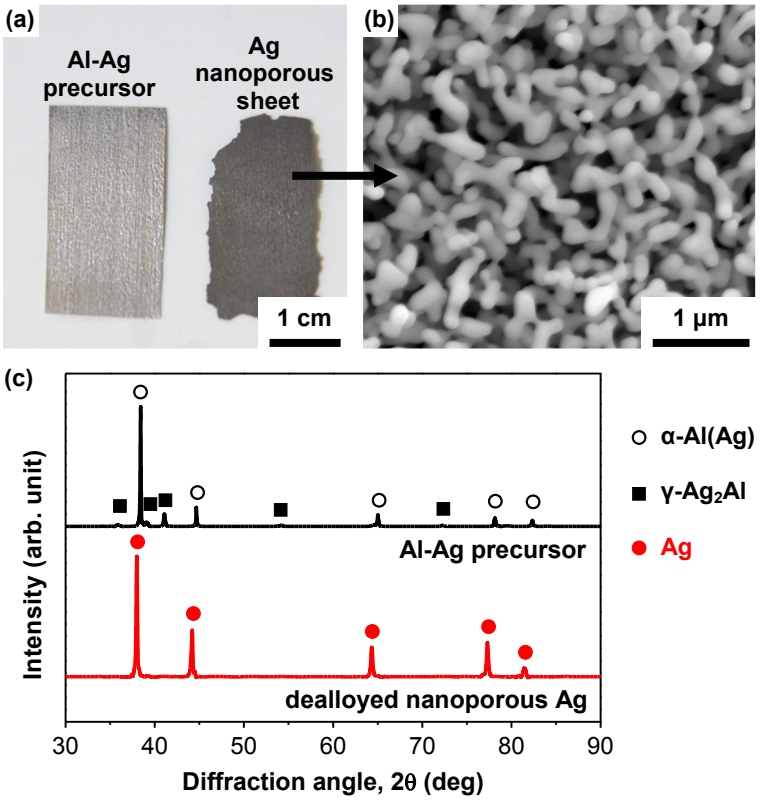

Figure 3.1 **(a)** Optical image of melt-spun Al-Ag precursor and dealloyed Ag nanoporous sheet, **(b)** scanning electron microscopy (SEM) secondary electron (SE) image of Ag nanoporous structure, and **(c)** phase constitution of Al-Ag precursor and the dealloyed nanoporous Ag.

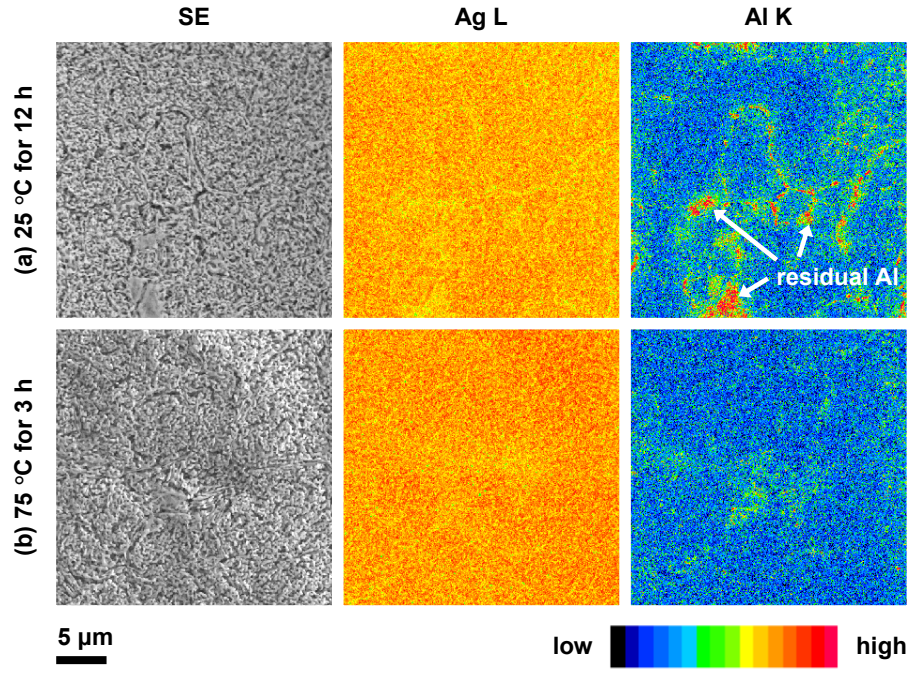

Figure 3.2 SEM SE images and X-ray mapping results of Ag L and Al K on the dealloyed Ag nanoporous sheet **(a)** at 25 °C for 12 h and **(b)** at 75 °C for 3 h.

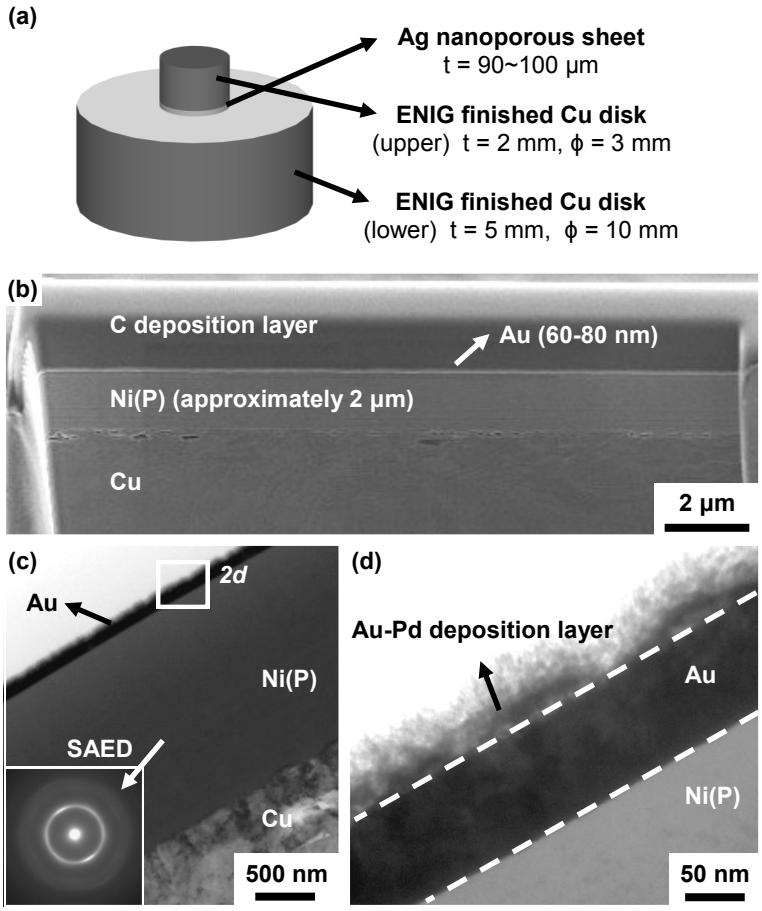

Figure 3.3 **(a)** Schematic diagram of the electroless Ni/immersion Au (ENIG) finished Cu disk, **(b)** SEM SE image of focused ion beam (FIB) milled cross-section of ENIG finished Cu, and **(c, d)** transmission electron microscopy (TEM) bright field (BF) images of ENIG surface finish. *Inset selected area electron diffraction (SAED) pattern* in *(c)* indicates that Ni(P) layer is an amorphous structure.

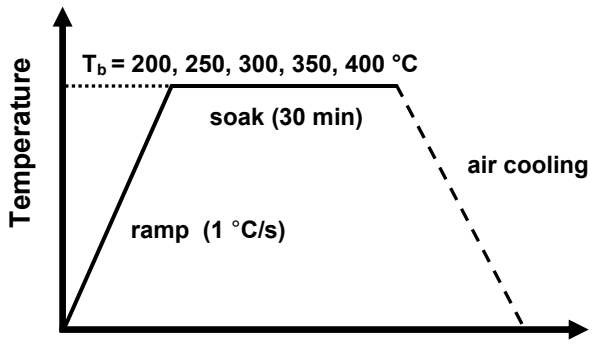

Figure 3.4 A temperature profile of Ag nanoporous bonding process.

3.2.3 Characterization methods

The maximum fracture load of the NPB joint was measured using shear tester (STR-1000, Rhesca) with a shear rate of 1 mm/min and a shear height from the surface of 0.2 mm, where we obtained an average value of the shear strength of five samples. The cross-sections and fracture morphologies of the NPB joints were observed with SEM using an acceleration voltage of 5 kV. The interfacial reaction between Ag and ENIG was investigated using energy-dispersive X-ray spectroscopy (EDS, JED-2200, JEOL) on the scanning TEM (STEM) mode with the probe size of incident beam of 1 nm. Cross-sectional samples were polished using an Ar ion beam with a cross-section polisher (CP, SM-09010, JEOL) using an acceleration voltage of 5 kV, in order to prevent any distortion of microstructure of NPB joints or any particle embedding which can be arisen by the general methods for the metallurgical sample preparation [8]. The distribution of each element on the fracture surface was measured with an electron probe micro-analyzer (EPMA, JXA-8530F, JEOL) using an acceleration voltage of 15 kV, in order to perform image analysis of the fracture mode. The thickness and porosity of the porous layer and area fraction of fracture mode of Ag NPB joint were evaluated using a commercial image analysis program, Image-Pro Plus (Media Cybernetics).

The chemical states of the elements at the fracture surface were examined using X-ray photoelectron spectroscopy (XPS, AXIS-165x, Kratos) with monochromatic Al Kα radiation. The scan range of the survey spectra was 0 - 1000 eV and the scanning step of the binding energy (BE) was 0.1 eV. High-resolution spectra of the Ni $2p_{3/2}$ core-level (the range of BE = 851 - 859 eV), the O 1s core-level (the range of BE = 527 - 535 eV), the Ag $3d_{5/2}$ core-level (the range of BE = 365 - 371 eV) and the Au $4f_{7/2}$ core-level (the range of BE = 81 - 87 eV) were obtained with the scan step of 0.05 eV. The data acquisition and the XPS peak analysis were conducted using the Kratos Vision program. The subtraction of background from the core-level XPS spectra of the selected elements was performed using the Shirley algorithm [9], and the peak fitting was conducted using the Gaussian distribution function.

3.3 Joint formation of Ag nanoporous bonding

3.3.1 Microstructural characteristic of Ag layer

Fig. 3.5 shows cross-sectional SEM and TEM images of the NPB joint created. These images reveal that the Ag layer has a dense/porous sandwich structure, wherein the dense layer provides

interfacial bonding between Ag layer and ENIG, and the porous layer can play role in relaxing stress due to it having a lower elastic modulus than the bulk metal [10,11]. The origin of this unique structure lies in the partial deformation of the Ag nanoporous sheet by compression, as shown in Fig. 3.6. Near the surface area, initial Ag nanoporous structure was collapsed and contacted each other. Consequently, this direct contact of collapsed Ag can lead to densification of collapsed nanoporous structure during joining process, as shown in Fig. 3.6(b). On the other hand, the internal region of the Ag nanoporous structure was not fully deformed; as a result, the densification of internal area was insufficient. The formation of porous Ag layer resulted from the partial densification and thermal coarsening [12] of porous structure by surface diffusion in order to reduce the surface area of the

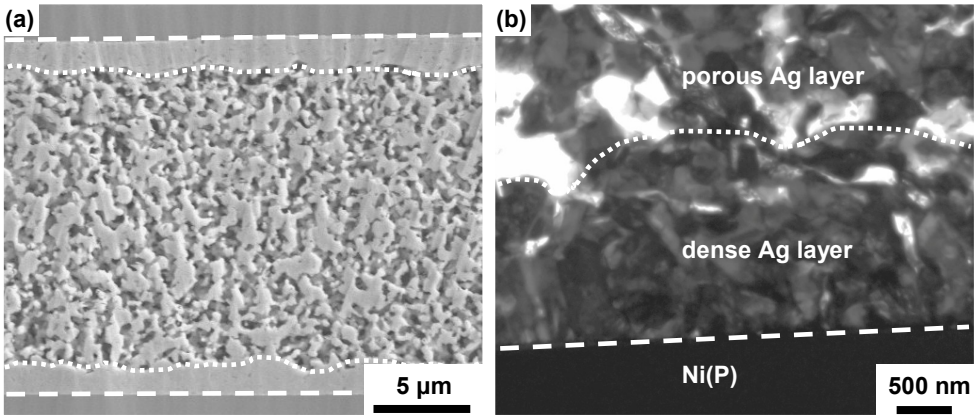

Figure 3.5 **(a)** SEM back-scattered electron (BSE) image, and **(b)** TEM BF image of nanoporous bonding joint bonded at 300 °C on air. The *dotted line* and *broken line* indicate the borderline of porous Ag layer/ dense Ag layer and the interface of Ag/ENIG.

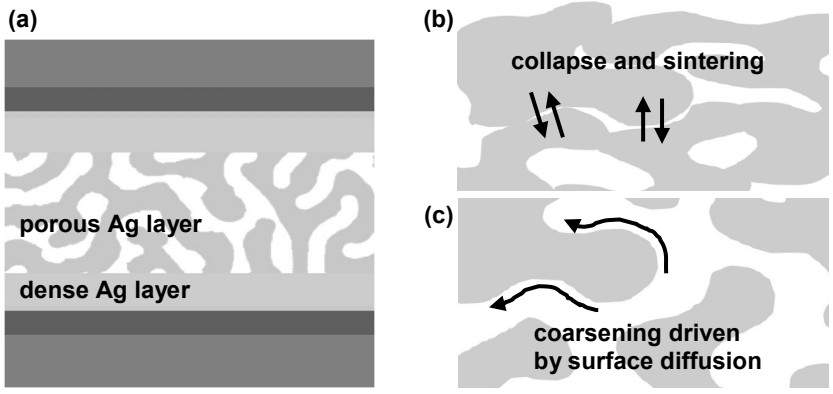

Figure 3.6 Schematic diagrams of **(a)** the dense Ag/porous Ag sandwich structure by thermo-compression, and formation mechanisms of **(b)** the dense Ag layer and **(c)** the porous Ag layer.

nanoporous structure (Fig. 3.6(c)). After the joining process, the dense Ag layer exhibits a sub-micron grain structure and good contact with the ENIG surface. Furthermore, no voids or gaps are evident at the interface, which would otherwise have an adverse effect on the reliability of the joint.

3.3.2 Interfacial reaction between Ag nanoporous sheet and ENIG substrate finish

Fig. 3.7 shows STEM bright field (BF) image of the interface between Ag/ENIG of Ag nanoporous bonding joint which is bonded at 300 °C in air. The interfacial reaction between Ag and ENIG was investigated using energy-dispersive X-ray spectroscopy (EDS) on STEM mode. From the EDS analysis along the dotted line shown, it is confirmed that Au was diffused into the Ag to a length of about 160 nm. Diffusion length of Au into Ag layer during bonding process can be estimated using measured Au diffusivity (D_{Au} = 1.1 × 10^{-18} m^2/s) into Ag at 300 °C, reported by Parknejad et al [13]. They measured D_{Au} into Ag layer through the EDS result of Au at the interface during thermal storage of Ag nanoparticle sintered joint with Au coated substrate at 300 °C. The diffusion length of Au can be

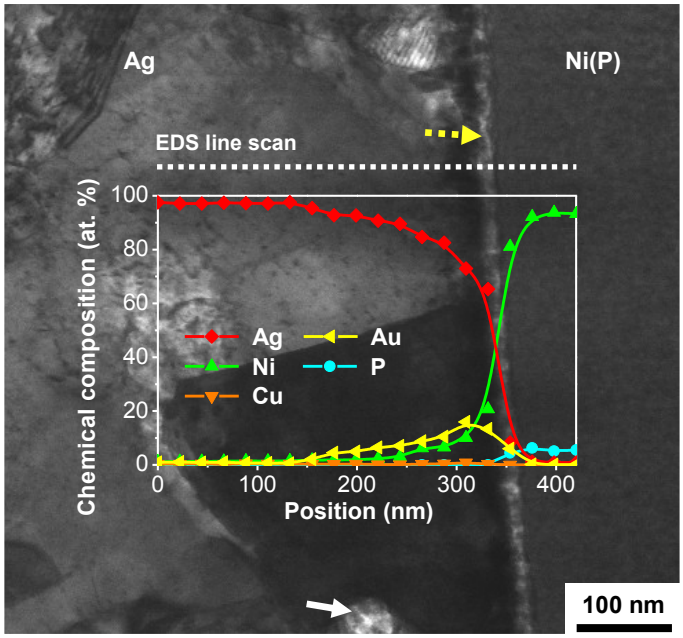

Figure 3.7 Scanning TEM (STEM) BF image and energy dispersive X-ray spectroscopy (EDS) line analysis of interface between Ag and ENIG layers of nanoporous bonding joint. The *inset graph* shows the atomic concentrations of Ag, Au, Ni, P, and Cu which is measured along the *white dotted line*. Nano-sized voids (about 5-10 nm) along the interface between Au and Ni(P) are indicated by a *yellow dotted arrow*, while *white arrows* indicate a void (about 20-50 nm) in the dense Ag layer.

calculated using following equation 3.1,

$$x = \sqrt{2Dt} \quad \cdots\cdots (3.1)$$

where, x is the diffusion length of Au into Ag layer, D_{Au} is the diffusivity of Au and t is the heating time. The estimated diffusion length of Au was approximately 89 nm. Thus, the diffusion length of Au into Ag layer from the EDS result, as shown in Fig. 3.7, seems reasonable value.

Conversely, however, the diffusion of Ag and Au into the Ni layer is not significant. In general, the flux of atoms in substitutional diffusion governed by the vacancy mechanism is influenced by the energy barrier of atom migration in the crystalline lattice, otherwise known as the activation energy of migration. Furthermore, the activation energy of substitutional diffusion involves the possibility of vacancy being and lattice distortion energy at the saddle point.

The equilibrium concentration of vacancies, C_v, can be determined by following equation 3.12 [14],

$$C_v = \frac{N_v}{N + N_v} = \exp(-E_f / k_B T) \quad \cdots\cdots (3.2)$$

where N_v is the number of vacancy, N is the number of atom, E_f is the formation energy of the vacancy, and k_B is the Boltzmann constant. The calculated formation energies of vacancy of Au, Ag, Cu and Ni through the *ab initio* calculation using local density approximation based on density function theory were used [15], where E_f of Au, Ag, Cu and Ni are 0.62, 1.03, 1.29 and 1.66 eV, respectively. The evaluated C_v of Au, Ag, Cu and Ni as a function of the absolute temperature are shown in Fig. 3.8. At 300 °C, the resulting estimate of C_v for Au is two orders of magnitude higher than that of Ag, and eight orders of magnitude higher than that of Ni. Given that, Ag, Au and Ni share the same crystal structure (face centered cubic), the energy necessary for lattice distortion by atomic migration is proportional to the atomic radius (metallic radius) of each element ($r_{met,Ag}$ = 144 pm, $r_{met,Au}$ = 144 pm and $r_{met,Ni}$ = 125 pm) [16]. Thus, the lattice distortion in the case of Ag or Au migration into vacancy sites in the Ni matrix is higher than the inverse case. It can therefore be concluded that the migration of Ag and Au atoms into Ni matrix unlikely to occur to significant extent over a short process time. This is supported by the reference data for the activation energy of tracer diffusion [17].

Meanwhile, the microstructure of matrix also plays an important role which is related with

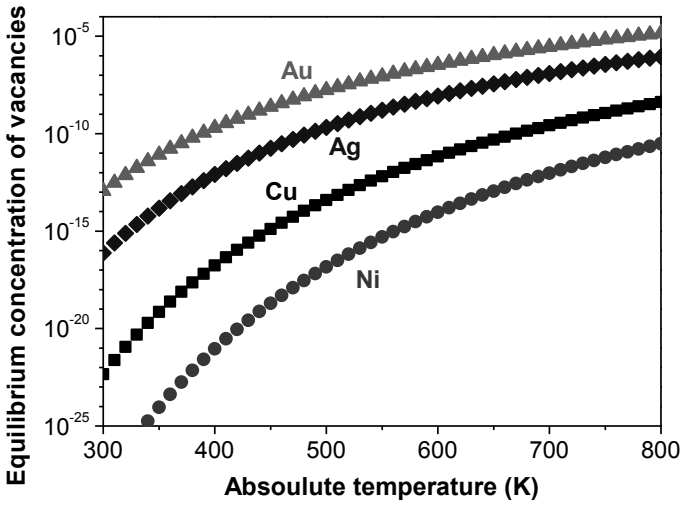

Figure 3.8 Estimated equilibrium concentration of vacancies of Au, Ag, Cu and Ni as a function of absolute temperature (300-800 K).

the high diffusivity paths, such as grain boundaries and microstructural defects [18]. It is difficult that atoms diffuse into the amorphous matrix, compared with the case of diffusion into the crystalline matrix, due to the absence of grain boundaries or dislocation [19,20]. The dense Ag layer shows sub-micron crystalline structure, so there are many high diffusivity paths which can lead to fast diffusion of Au and Ni into Ag layer. The electroless Ni(P) deposits, however, generally show amorphous or nanocrystalline structure according to P contents [21,22] and have been generally used as Cu diffusion barriers in the Sn-based solder joint to retard the growth of intermetallic compounds [23,24]. In the same manner, it seems that the Ni(P) layer acts as a diffusion barrier of Ag and Au.

After the joining process, nano-sized voids were detected within the dense Ag layer and at the interface between Au and Ni(P), as shown in Fig. 3.6. The former one is generally occurred in the sintering process [2,25]. About the latter one, some reports about the void formation at the Ni(P) metallization of solder joint have been reported. Two possible mechanisms for this void formation have been suggested previously: Kirkendall effect [26], and volume shrinkage as a result of formation of Ni_3P from amorphous Ni(P) and Ni-Sn-P contained intermetallic compounds [22,27]. Since no second phases were evident in Ag-Au (solid solution over the whole composition range), Ag-Ni (immiscible) and Au-Ni (spinodal decomposition) systems, volume shrinkage due to interfacial reaction seems improbable in NPB. However, the diffusion of Ni into the Ag region was significantly than the reverse scenario (diffusion of Ag into the Ni(P) region) after joining process, and so, it seems

likely that the Kirkendall effect is the cause of the nano-sized voids at the Ag/ENIG interface. Nevertheless, these voids have no significant effect on the joint strength in this study.

As shown in Fig. 3.9, the high resolution lattice image of the Ag/Au bonding interface, and corresponding fast Fourier transform (FFT) patterns of Ag side and Au side partially exhibited crystallographic orientation relationships, $(111)_{Ag}//(111)_{Au}$. In case of Ag nanoparticle sintering with Au substrate, the mechanism of interfacial bonding between nanoparticle and substrate is the rotation of nanoparticle or partial melting and subsequent rearrangement of lattice along the same crystal orientation with substrate [28]. In case of Ag nanoporous bonding, however, the collapsed nanoporous

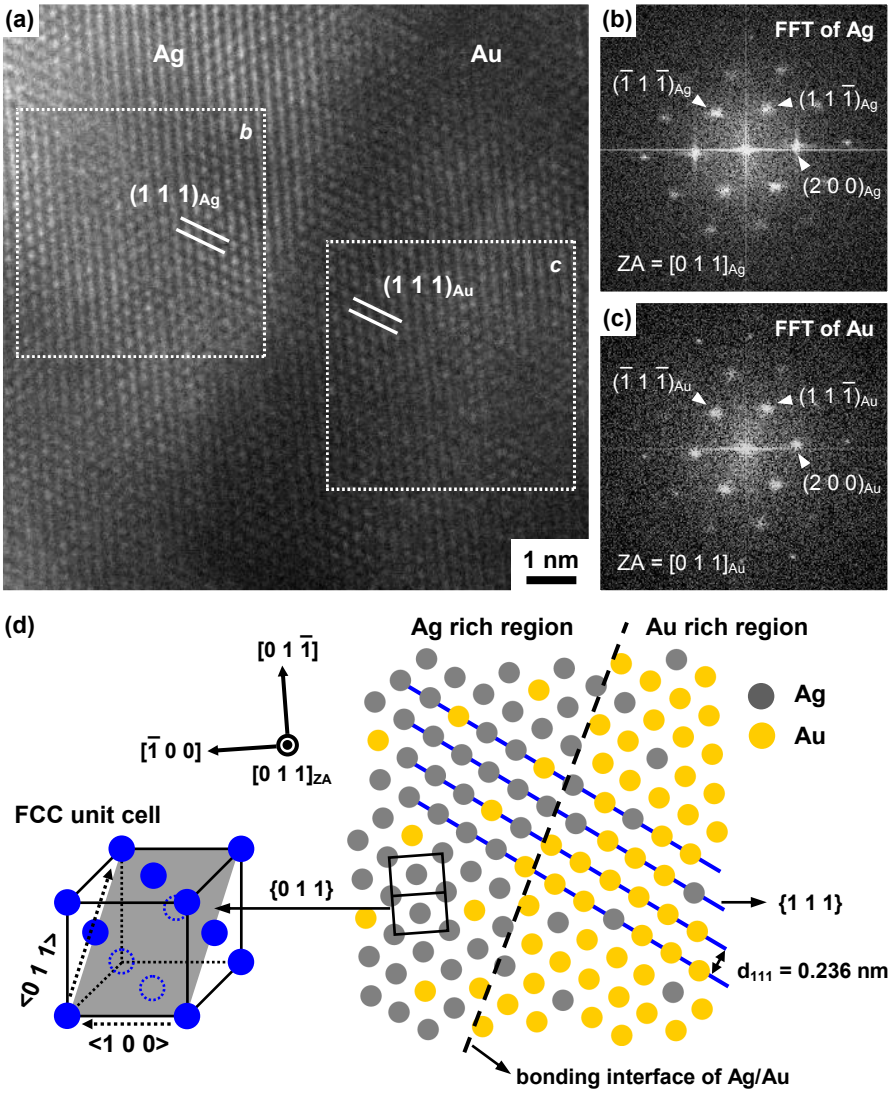

Figure 3.9 **(a)** High resolution TEM (HRTEM) image of Ag/Au interface, and fast Fourier transform (FFT) patterns of *dotted region* in (*a*) of **(b)** Ag and **(c)** Au, and **(d)** schematic diagram of atomic arrangement at the Ag/Au interface.

structure cannot seemed to rotate or rearrangement because of the large size of collapsed nanoporous structures compared with nanoparticle. Thus, a sintering reaction will be occurred at the Ag/Au interface with random distribution of misorientation angle between Ag nanoporous and Au surface finish at the initial bonding stage. At the partial interface, the epitaxial bonding interface between Ag and Au also can be observed, as shown in Fig. 3.9, because of same crystal structure and lattice parameter of Au and Ag. And then the reducing of high-angle boundary and coarsening of grain structure will be occurred in order to reduce the energy of grain boundaries. Further crystallographic investigation, for example electron backscattered diffraction technique, on the formation of the interface of Ag nanoporous and Au surface finish will be necessary.

3.4 Effect of bonding temperature on shear strength and microstructure Ag nanoporous bonding joint

3.4.1 Shear strength of Ag nanoporous bonding joint

The shear strengths of the NPB joints bonded using the various bonding temperatures and environments are given in Fig. 3.10. The values for the NPB shear strength were approximately 14.4 MPa (in air) and 16.2 MPa (in N_2) at 200 °C, and gradually increased with increasing bonding temperature up to a value of 27.0 MPa (in N_2) at 400 °C. The NPB joints exhibited strengths of more

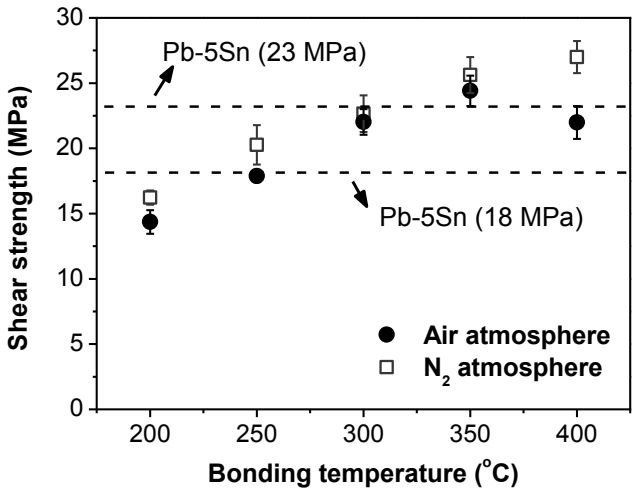

Figure 3.10 Shear strength of Ag nanoporous bonding joint at the various bonding temperature and atmosphere. The dashed lines indicate the shear strength of Pb-5Sn die attach evaluated according to the Japanese Industrial Standards (JIS Z 3198-5) from the literatures [28,29] for the comparison.

than 20 MPa at bonding temperatures above 300 °C, which are values similar to those of the shear strength of conventional Pb-5Sn die attach joints [29,30]. Although the strengths of the joint bonded in N_2 environment were slightly higher than those of the joints bonded in air, the effect of bonding environment (air or N_2) on the joint strength was insignificant, except in case of NPB joint bonded at 400 °C. This similar joint strength, irrespective of bonding environments, seems to come from the air-stable characteristics of Ag (the joining material) and Au (surface finish of the substrate).

Generally, there are two main reasons for degradation of the bonding interface or insufficient densification caused by the environmental conditions employed in the sintering process. When adopting easily oxidizable metals in air condition, such as Cu nanoparticles [31,32] or a Cu substrate [33], the effect of environment on the joint strength becomes very significant. This is because the formation of Cu oxide layers at the interface or around the nanoparticles can hinder metallic interconnection in air. A weak interface is formed due to the oxidation of Cu, resulting in a decrease in the shear strength of joint. The other main reason for the degradation of an interface is the different decomposition behavior of the surfactants generally used to ensure the stable dispersion of nanoparticles in the solvent at the different atmosphere [34]. So the sintering behaviors have been affected by the atmosphere due to the different aspect of decomposition of the surfactant of nanoparticle with the different atmosphere in spite of novel metallic nanoparticle. It is also known that the presence of residual surfactant hinder the densification of nanoparticles.

3.4.2 Microstructural characteristics of the Ag nanoporous bonding joint

The microstructures of the Ag nanoporous bonding joint area at various bonding temperatures in air are shown in Fig. 3.11. The Ag nanoporous bonding layers exhibit a dense and porous sandwich structure for all bonding temperatures, where the Ag nanoporous structures had partially collapsed, formed contacts with each other due to compression stress near the surface, and then densified. It appears that these dense and porous layers were formed through mechanisms of densification and thermal coarsening that occurred during the bonding process, as mentioned in *Section 3.3.1*. As shown in Fig. 3.12(a), the thickness of the total Ag layer and the porous Ag layer decreased from approximately 29 μm to 15 μm and from approximately 28 μm to 12 μm, respectively, with increasing bonding temperature. Besides, the thickness of the dense silver increased from 0.5 μm to 3 μm with increasing bonding temperature. The dense Ag layer may provide a reliable interface between the substrate and the bonding layer. In terms of the role of porous layer, these layers generally

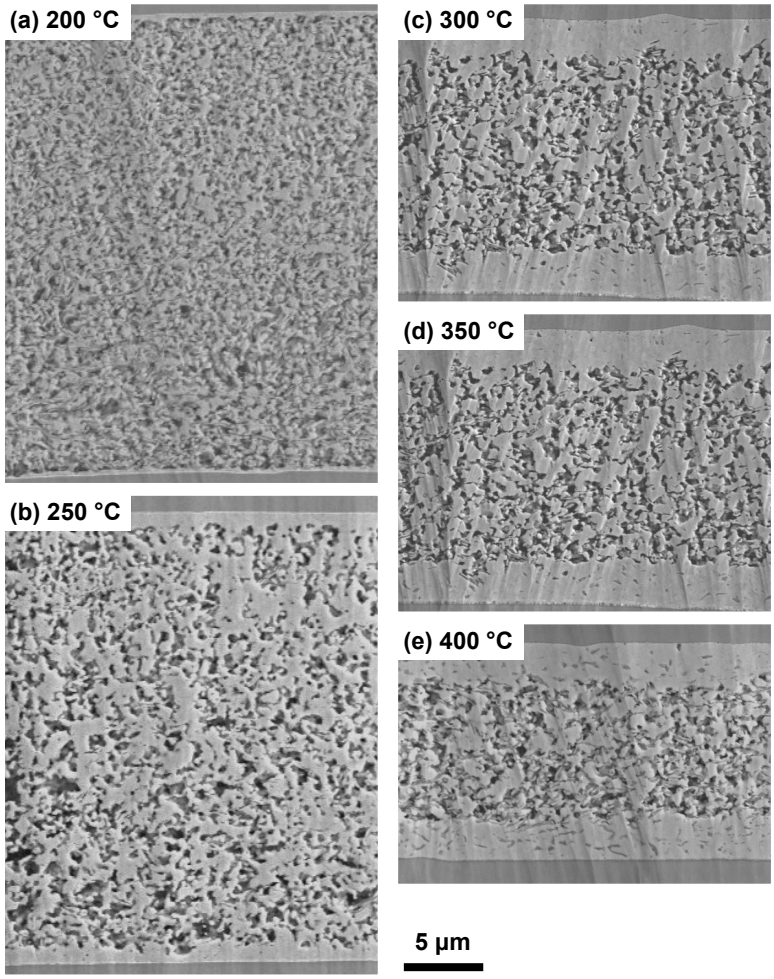

Figure 3.11 Cross-sectional SEM BSE images of nanoporous bonding joints with the various bonding temperature of **(a)** 200 °C, **(b)** 250 °C, **(c)** 300 °C, **(d)** 350 °C and **(e)** 400 °C on air.

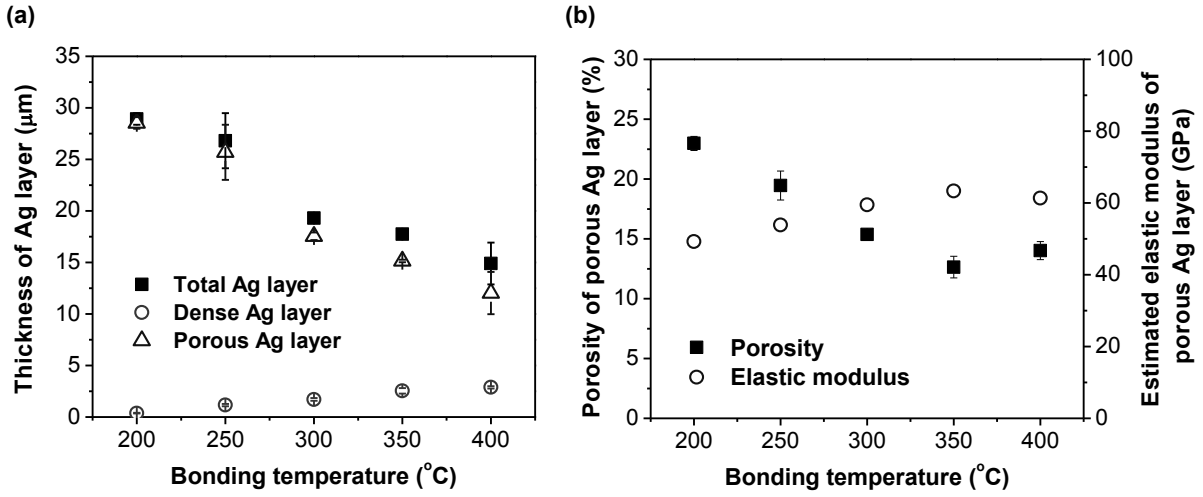

Figure 3.12 **(a)** The variation of thickness of total, dense and porous Ag layers and **(b)** the measured porosity and estimated elastic modulus of porous Ag layer with the bonding temperature.

show low elastic modulus, as shown in Fig. 3.12(b) which can be estimated from the equation 3.3, that is the relationship between elastic modulus and relative density of nanoporous materials [35],

$$\frac{E_p}{E_b} = C\left(\frac{\rho_p}{\rho_b}\right)^m \quad \cdots\cdots (3.3)$$

where, E_p and E_b are the elastic modulus of porous and bulk materials, ρ_p and ρ_b are the relative density of porous and bulk materials, C is a constant of order 1 and m is a constant (2 for perfect porous foam). The porosity of Ag porous layer was calculated from the area ratio of pores in cross-sectional SEM image of Ag NPB joint. The ratio of relative density of porous Ag layer and bulk Ag, ρ_p/ρ_b, was used as a reciprocal value of porosity of Ag porous layer.

The role of the Ag porous layer the with a low elastic modulus can be found Bai's finite-element analysis [36], where a sintered Ag layer with a low elastic modulus was found to reduce stress generation, when compared to an Au-Sn solder using. The mismatch in the coefficients of thermal expansion between a chip and a bonding material or a substrate is the main reason for interconnection failure by cyclic deformation under the thermal cycling condition.

The microstructure of the porous Ag layer became increasingly coarse and dense with increasing bonding temperature, as shown in Fig. 3.11 and Fig. 3.12, due to the proportional dependency of the diffusivity of Ag with respect to temperature. The metallic porous structure generally became coarser with increasing annealing temperature, as reported in the literature [12,37]. A denser and coarser Ag layer with increasing bonding temperature appeared to lead to an increasing joint strength of NPB.

3.5 Effects of bonding temperature and atmosphere on the fracture mode

3.5.1 Image analysis of fracture mode

Fig. 3.13 shows the schematic diagrams of the main fracture modes and their representative features of fracture surface in case of Ag NPB with ENIG finished Cu substrate. There are three main fracture modes which are Ag layer fracture (Fig. 3.13(b)), interfacial fracture (Fig. 3.13(c)) and Au delamination (Fig. 3.13(d)). The surface of Ag layer fracture exhibits elongated feature of Ag porous structure, i.e. a ductile fracture, as shown in Fig. 3.13(b). The Ag side in the interfacial fracture region exhibits collapsed and densified Ag structure, as shown in Fig. 3.13(c). The Ni(P) side of Au

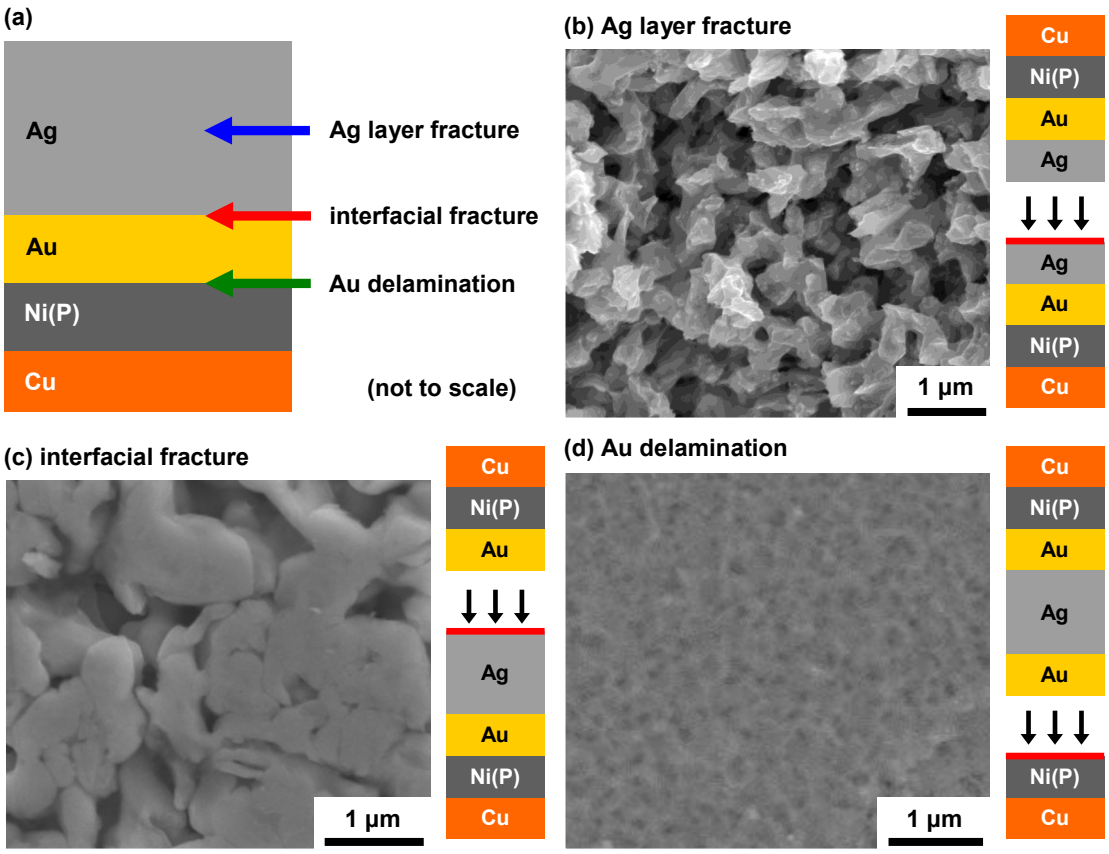

Figure 3.13 **(a)** Schematic diagram of main fracture mode including Ag layer fracture (cohesive fracture in Ag layer), interface fracture (fracture at Ag/Au interface) and Au delamination (fracture at Au/Ni interface), and SEM images of fracture morphology of **(b)** Ag layer fracture, **(c)** interfacial fracture and **(d)** Au delamination. *Inset diagrams* in *(b-d)* indicate aspect of fracture and *red lines* indicate SEM observed surface.

delamination region exhibits brittle fracture morphology, as shown in Fig. 3.12(d).

Fig. 3.14 and 3.15 show representative EPMA mapping results on the fracture surface of NPB joints with the bonding temperature of 200, 300 and 400 °C and the atmosphere of air and N_2. The variation of fracture mode affected by bonding temperature and atmosphere can be clearly identified using X-ray mapping for the fracture surface. The high Ag and Ni signal region indicate Ag layer fracture and Au delamination, respectively, while the signals of Au and Ni are detected together at the interfacial fractured region due to thin thickness of immersion Au layer under 100 nm (a generation depth of characteristics X-ray = about 1-2 μm). There are no significant differences of aspect of fracture occurrence between air and N_2 atmosphere with the bonding temperature of 200 and 300 °C. These results indicate that the effect of atmosphere on the sintering reaction of collapsed Ag

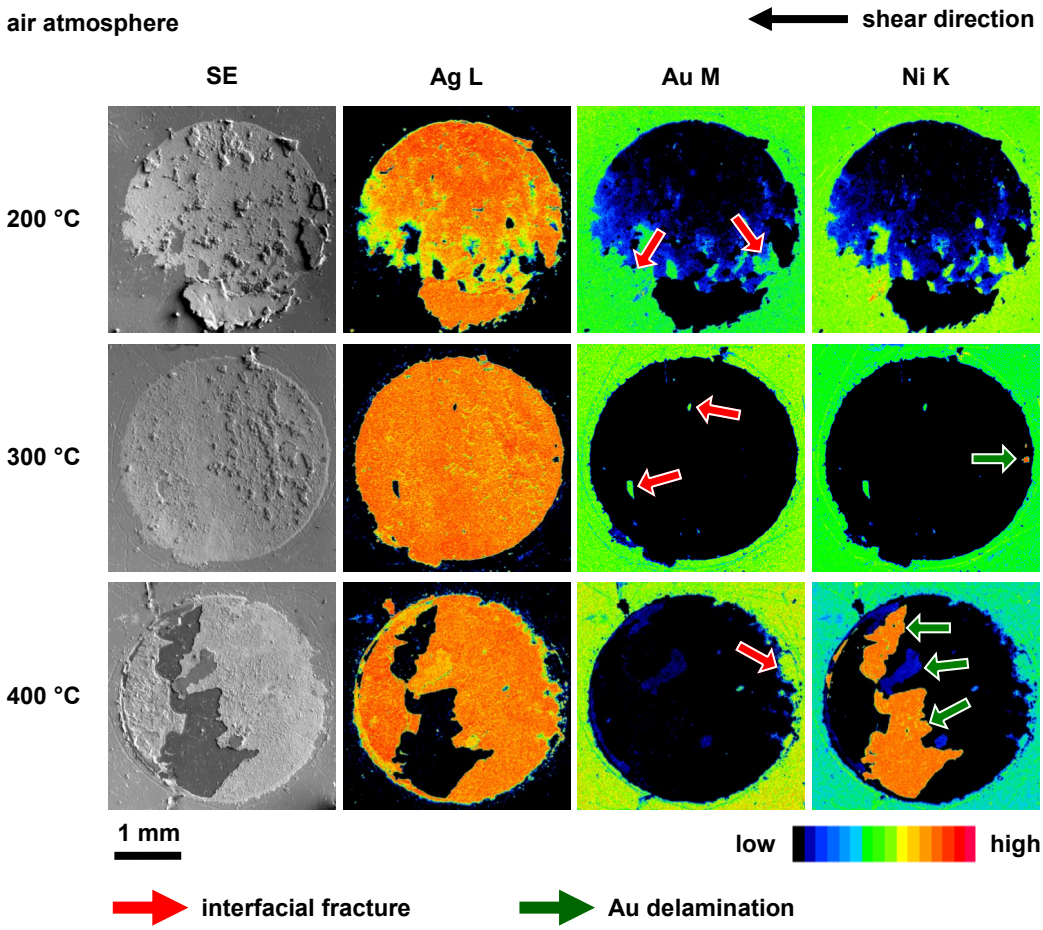

Figure 3.14 SEM SE images and results of X-ray elements mapping (Ag, Au and Ni) of fracture surfaces which are bonded at the 200, 300 and 400 °C on air. High level of Ag region indicates fracture within Ag layer. The *red* and *green arrows* indicate interface fracture and Au delamination, respectively.

nanoporous structure and the interfacial reaction between Ag and Au layers are not significant. In case of bonding temperature of 400 °C, they show great difference between air and N_2 atmosphere. The fraction of Au delamination was significantly increased in air condition, whereas it is rarely observed in N_2 atmosphere.

Fig. 3.16 shows the image analysis results on the area fraction of fracture mode of the joint after the shear test with the various bonding temperature and atmosphere. The area fractions of interfacial fracture of NPB bonded at 200 °C in the air and N_2 atmosphere were 18.8% and 12.4%, respectively, and they gradually decreased with the increase of bonding temperature.

The interfacial fracture seems to weak inter-atomic connection between Ag and Au. Namely, the sintering reaction between Ag nanoporous structure and Au surface was insufficient at 200 °C.

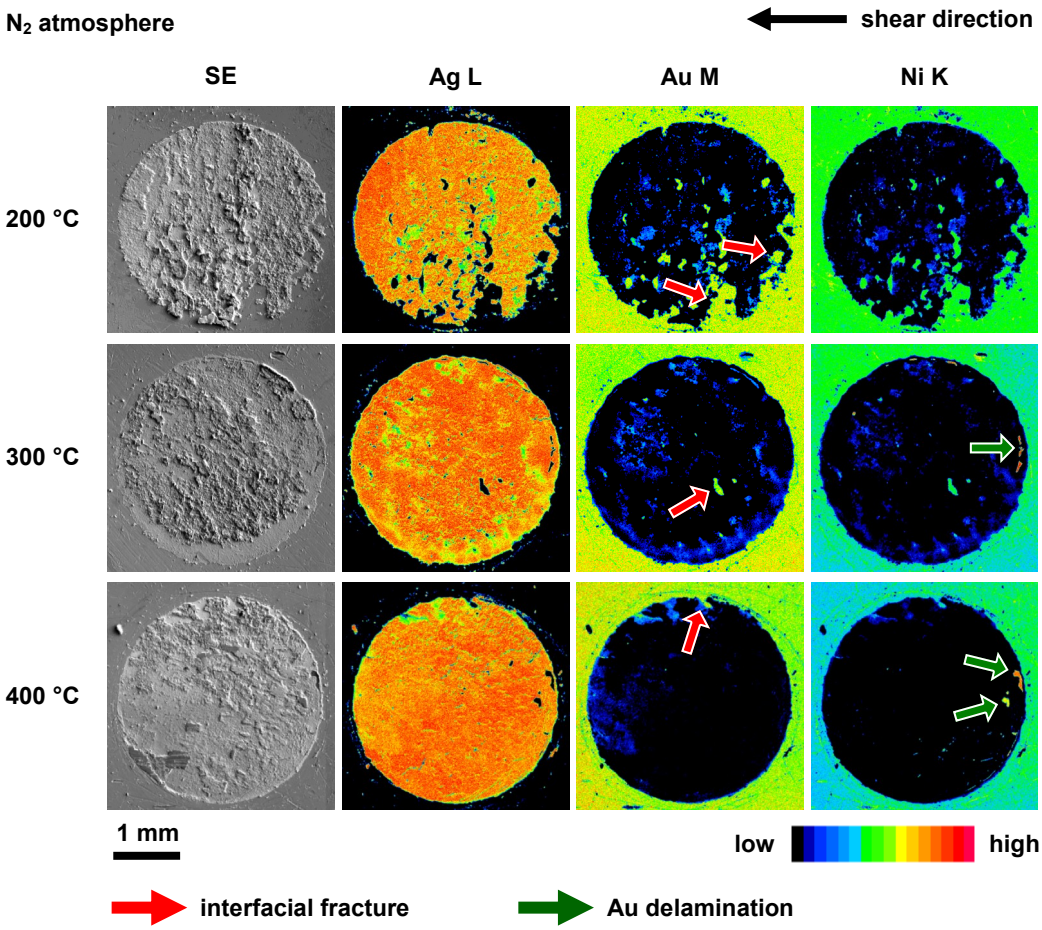

Figure 3.15 SEM SE images and results of X-ray elements mapping (Ag, Au and Ni) of fracture surfaces which are bonded at the 200, 300 and 400 °C in N_2 atmosphere. High level of Ag region indicates fracture within Ag layer. The *red* and *green arrows* indicate interfacial fracture and Au delamination, respectively.

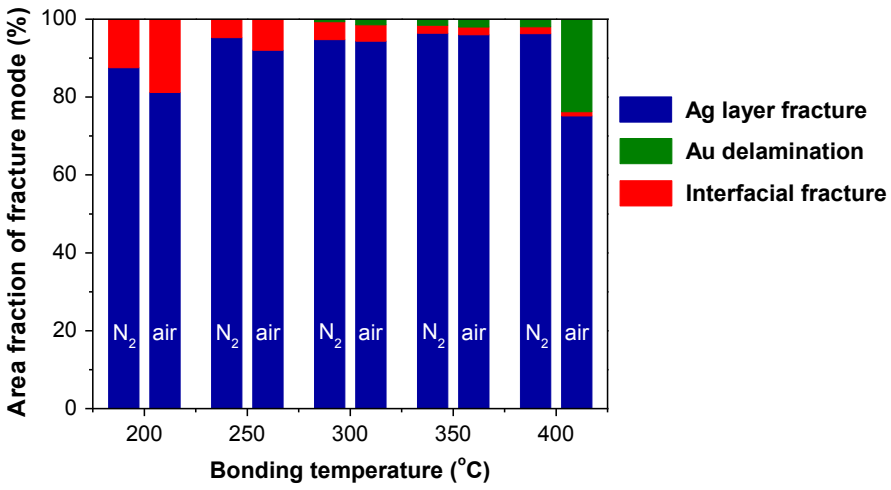

Figure 3.16 Area fraction of Ag layer fracture, interfacial fracture and Au delamination with various bonding conditions.

Besides, the Au delamination was occurred from the bonding temperature of 300 °C, and fraction of it was significantly increased at the bonding temperature of 400 °C in air. Generally, the cause of Au delamination of ENIG finish in solder and wire bonding joint is known as a black pad defect formed during ENIG plating process [38,39]. Zeng et al. [38] argued that spikes that existed in cross-section of ENIG finish are clear evidence of the black pad defect. These spikes act as crack initiation sites and can lead to Au delamination [39]. As shown in Fig. 3.3(b-d), however, there was no evidence of the black pad defect in ENIG finish used in this time, and it seems reasonable that the cause of Au delamination comes from bonding process rather than the black pad defect. The degradation mechanism of NPB joint bonded at 400 °C in air will be mentioned afterwards. We can infer that the fracture mode can directly affect bonding strength of NPB joint. We can infer that the fracture mode can directly affect bonding strength of NPB joint.

3.5.2 Fracture morphology of Ag fractured region

SEM images of the fracture surface of Ag fractured regions with various bonding temperature in air are shown in Fig. 3.17. The fracture of NPB mainly occurred at the Ag layer, with an area fracture of over 75 % for all bonding conditions, and the fracture morphology of the Ag layer affected the shear strength of NPB. The traces of plastic deformation in the Ag layer caused by shear stress became evident with increasing bonding temperature. Although the low magnification SEM images of the fracture surface appear to show a brittle fracture, as shown in Fig. 3.14 and 3.15, the elongated feature and local necking of the Ag porous structure can be observed in the high magnification image, as shown in Fig. 3.18. The microstructural ductile fracture of the nanoporous structure has previously been reported [37,40].

3.5.3 Ni oxidation of Au delamination region

The EPMA mapping results of Ni and O of NPB joint which are bonded at 400 °C on air and in N_2 atmosphere are shown in Fig. 3.19. The high O signal was detected in the Au delamination region in the case of bonding in air. In the case of the joint bonded in N_2, a very small amount of Au delamination was observed and the O signal was also barely detected. From the EPMA results and the image analysis of the fracture modes, we can conclude that Ni oxidation is the main cause of Au delamination in the case of bonding temperature of 400 °C in air.

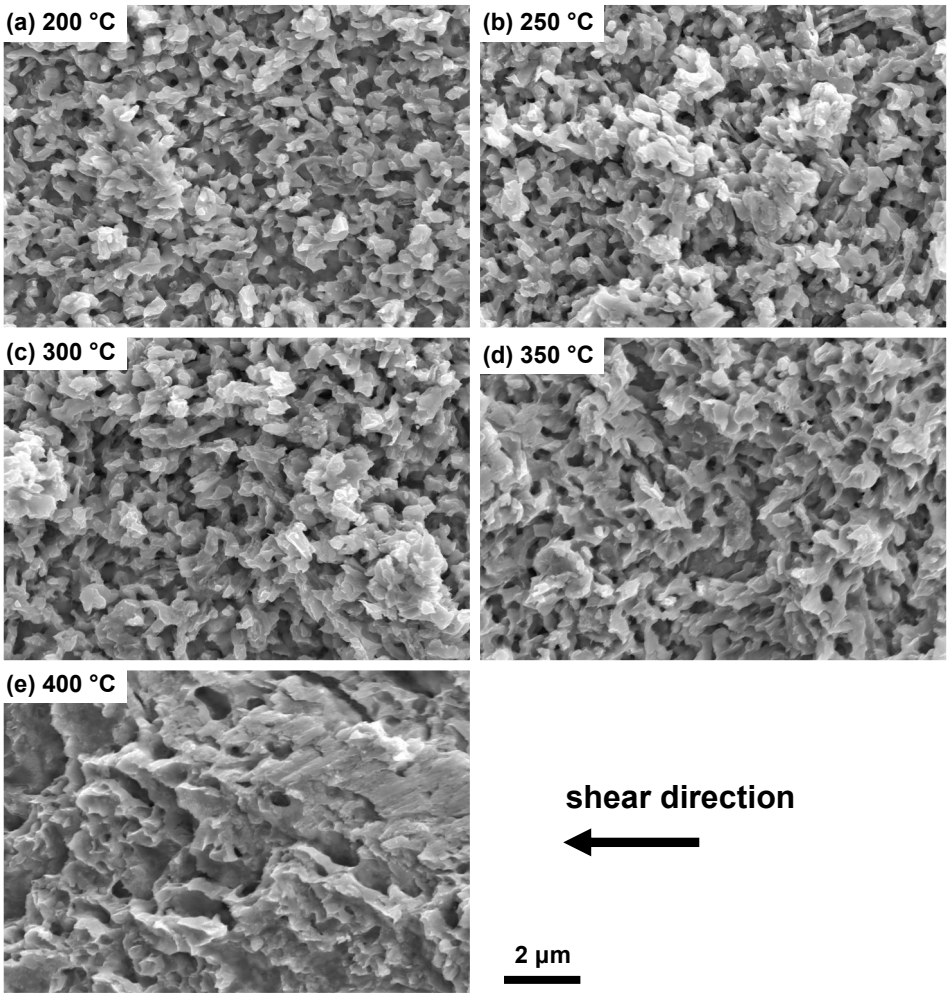

Figure 3.17 SEM SE images of fracture morphology of Ag layer fractured region with the bonding temperature of **(a)** 200 °C, **(b)** 250 °C, **(c)** 300 °C, **(d)** 350 °C and **(e)** 400 °C on air.

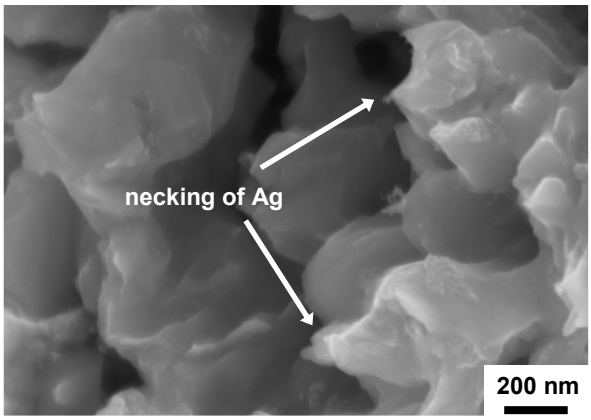

Figure 3.18 Magnified SEM SE image of fracture morphology of Ag layer fractured region with the bonding temperature of 300 °C on air.

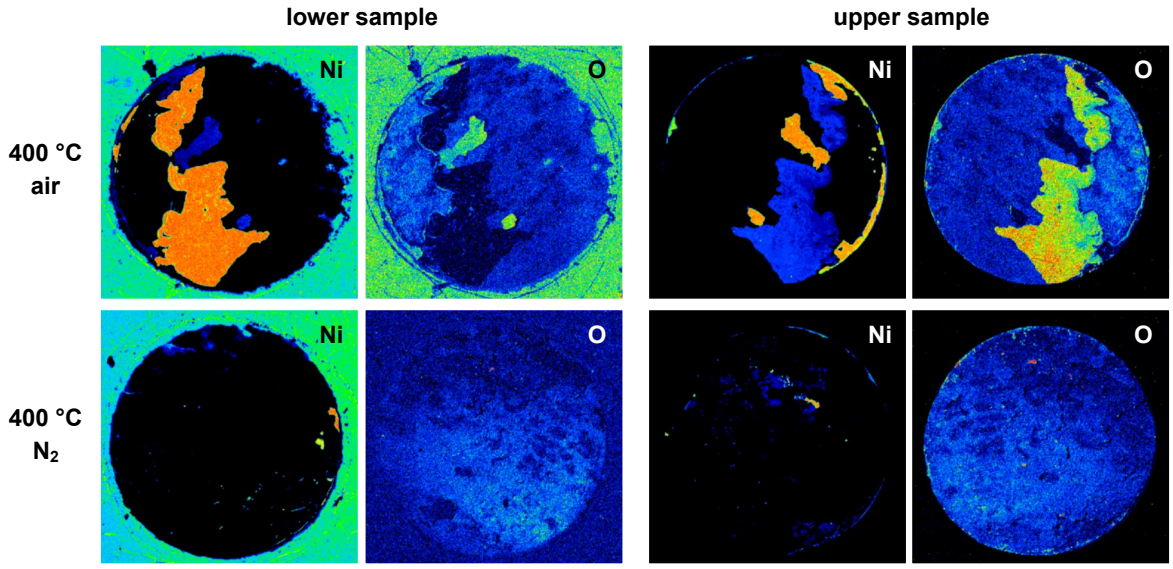

Figure 3.19 X-ray elements mapping of Ni and O of fracture surface of lower and upper sample which are bonded at 400 °C on air and in N_2 atmosphere.

The XPS spectra of the fracture surface of the NPB joint which is the same fractured sample that was bonded at 400 °C in air (upper side sample in Fig. 3.19) are shown in Fig. 3.20. XPS is a powerful technique for the analysis of the chemical states of target elements, with a surface sampling depth of a few nanometers. As shown in Fig. 3.20(a), all of the interest (Ag, Au, Ni, P and O) were detected due to the large scanning area of the X-ray irradiation, of approximately 1 mm^2. The peak values of adventitious C 1s (BE = 248.8 eV) and Au $4f_{7/2}$ (BE = 83.8 eV) were utilized for energy-scale calibration for peak identification. There are three distinct peaks in the Ni $2p_{3/2}$ spectrum in Fig. 3.20(b), including metallic Ni (852.7 eV), NiO (853.7 eV) and Ni_2O_3 (855.6 eV), and four peaks in the O 1s spectrum in Fig. 3.20(c), including two Ni oxides, O existing in the defective sites (like vacancies or grain boundaries), and O-containing adsorbates, in good agreement with the literatures [41–44]. While the spectrum of Ni $2p_{3/2}$ on the fracture surface in Fig. 3.20(b) shows distinct evidence of Ni oxidation, the Ag $3d_{5/2}$ in Fig. 3.20(d) and Au $4f_{7/2}$ in Fig. 3.20(e) spectra show only their single metallic peaks (Ag_{met} = 368.1 eV, Au_{met} = 83.8 eV) [45,46]. There are not any peak shift related with the oxidized Ag compounds (AgO = 367.3 eV, Ag_2O = 367.7 eV) in the Ag $3d_{5/2}$ spectrum [46].

We can inter from the XPS spectra that the O detected in the Au delamination region exists in the form of two Ni oxides, as shown in Fig. 3.20(c), in agreement with the EPMA mapping results in Fig. 3.19. The oxidation of Ni caused Au delamination, and this region exhibited brittle fracture

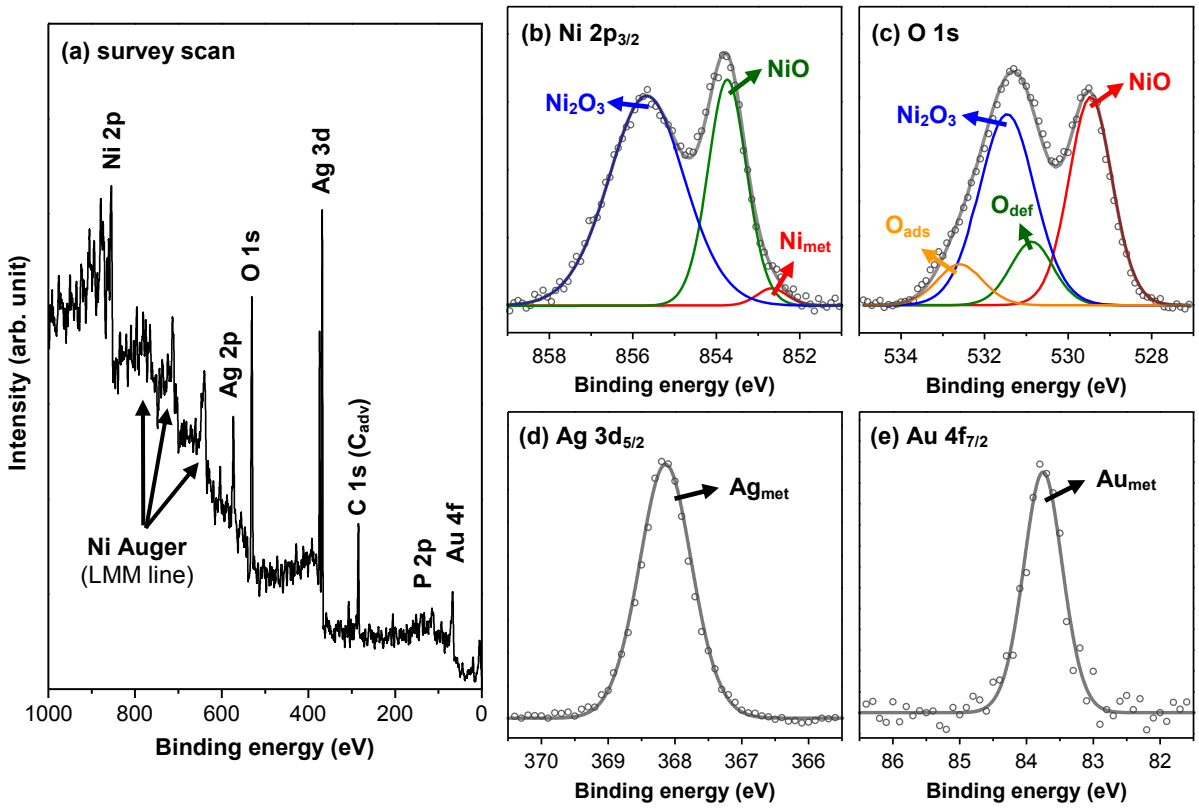

Figure 3.20 **(a)** X-ray photoelectron spectroscopy (XPS) survey spectrum and the core-level spectra of **(b)** Ni $2p_{3/2}$, **(c)** O 1s, **(d)** Ag $3d_{5/2}$ and **(e)** Au $4f_{7/2}$ of fractured surface which is bonded at 400 °C in air. The deconvolution of multi peak core-level spectra (Ni $2p_{3/2}$ and O 1s) were indicated *colored thin lines*. The *dotted data* and *black thick lines* indicate raw data and fitting result of XPS spectra, respectively. The abbreviations of *C adv*, *met*, *O ads*, and *O def* indicate adventitious carbon, metallic, oxygen-containing adsorbates and oxygen existing at defective site, respectively.

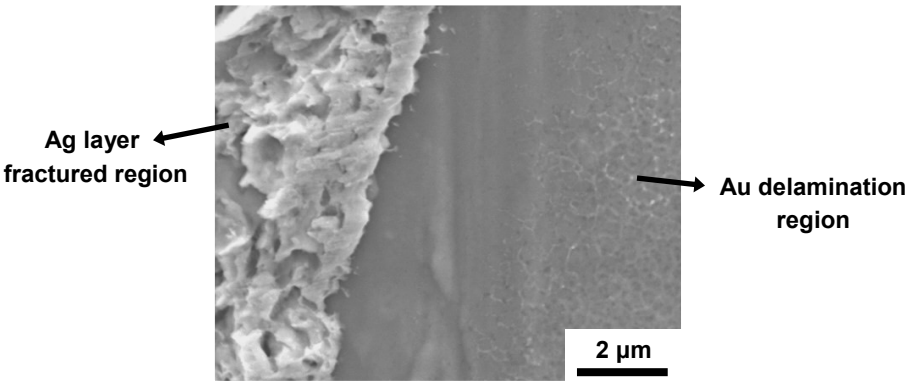

Figure 3.21 SEM SE image of fracture morphology of Au delamination region of bonded at 400 °C on air, where the ductile fracture of Ag layer fractured region and brittle fracture of Au delamination region can be confirmed.

compared to the ductile fracture of the Ag layer fractured region, as shown in Fig. 3.21. These results imply that Ni oxidation at the interface of Au and Ni caused by the infiltration of O through the Au layer is the main reason for degradation of the shear strength of NPB joint bonded at 400 °C in air.

3.6 Conclusion

In this chapter, the joint strength and fracture behavior of the nanoporous bonding (NPB) using an Ag nanoporous sheet are investigated. The effect of the bonding temperature can be distinguished through the comparative study of fracture behavior of the NPB joint at different bonding environments (air and N_2). The joint strength exhibited by NPB was approximately 14.4 - 27.0 MPa, under various bonding conditions. The joint strength of the NPB joint increased with increasing of bonding temperature, and the effect of bonding environmental was insignificant up to bonding temperature of 350 °C. A thicker and dense Ag layer plays the role of forming a sound interface at increased bonding temperature. The porous Ag was gradually coarsened by the high diffusivity of silver at the higher bonding temperature. In case of the 400 °C/air condition, the NPB joint strength was lower than the joint bonded in N_2 environment at same temperature by Ni oxidation. Consequently, it is possible that sound Ag NPB joint can be achieved with the bonding temperature range for NPB in air condition is from 250 °C to 350 °C with ENIG finished substrate. In this bonding temperature range, the results of shear strength NPB joint show similar joint strength with that of conventional Pb-5Sn solder alloy. The insufficient sintering reaction in the Au/Ag interface at a bonding temperature of 200 °C or Ni oxidation in the Au/Ni interface at a bonding temperature of 400 °C in air can lead to degrade joint strength of NPB.

References

[1] K.S. Siow, “Mechanical properties of nano-silver joints as die attach materials”, *J. Alloy. Compd.*, **514** (2012) 6–19.

[2] H. Yu, L. Li, Y. Zhang, “Silver nanoparticle-based thermal interface materials with ultra-low thermal resistance for power electronics applications”, *Scr. Mater.*, **66** (2012) 931–934.

[3] J. Yan, G. Zou, A. Wu, J. Ren, A. Hu, Y.N. Zhou, “Improvement of bondability by depressing the inhomogeneous distribution of nanoparticles in a sintering bonding process with silver nanoparticles”, *J. Electron. Mater.*, **41** (2012) 1924–1930.

[4] D. Kim, S. Jeong, J. Moon, "Synthesis of silver nanoparticles using the polyol process and the influence of precursor injection", *Nanotechnology*, **17** (2006) 4019–4024.

[5] Y. Jianfeng, Z. Guisheng, H. Anming, Y.N. Zhou, "Preparation of PVP coated Cu NPs and the application for low-temperature bonding", *J. Mater. Chem.*, **21** (2011) 15981–15986.

[6] L. Chen, Z. Li, C. Xiao, Z. Wang, W. Han, "Size-controlled synthesis of highly dispersed silver particles", *J. Mater. Sci. Mater. Electron.*, **24** (2013) 1469–1474.

[7] J. Erlebacher, M.J. Aziz, A. Karma, N. Dimitrov, K. Sieradzki, "Evolution of nanoporosity in dealloying", *Nature*, **410** (2001) 450–453.

[8] N. Erdman, R. Campbell, S. Asahina, "Precise SEM cross section polishing via argon beam milling", *Micros. Today*, **14** (2006) 22–25.

[9] D.A. Shirley, "High-resolution X-ray photoemission spectrum of the valence bands of gold", *Phys. Rev. B*, **5** (1972) 4709–4714.

[10] H. Oppermann, L. Dietrich, "Nanoporous gold bumps for low temperature bonding", *Microelectron. Reliab.*, **52** (2012) 356–360.

[11] J. Banhart, "Manufacture, characterisation and application of cellular metals and metal foams", *Prog. Mater. Sci.*, **46** (2001) 559–632.

[12] M. Hakamada, M. Mabuchi, "Thermal coarsening of nanoporous gold: Melting or recrystallization", *J. Mater. Res.*, **24** (2009) 301–304.

[13] S.A. Paknejad, G. Dumas, G. West, G. Lewis, S.H. Mannan, Microstructure evolution during 300 °C storage of sintered Ag nanoparticles on Ag and Au substrates, *J. Alloy. Compd.*, **617** (2014) 994–1001.

[14] K.A. Jackson, *Kinetic processes: Crystal growth, diffusion, and phase transformations in materials*, 2nd edition, Wiley-VCH, Weinheim, 2010.

[15] R. Nazarov, T. Hickel, J. Neugebauer, "Vacancy formation energies in fcc metals: Influence of exchange-correlation functionals and correction schemes", *Phys. Rev. B*, **85** (2012) 144118.

[16] W. Martienssen, H. Warlimont, *Springer handbook of condensed matter and materials data*, Springer, Berlin, 2005.

[17] E.A. Brandes, *Smithells metals reference book*, 6th edition, Butterworths, Cornwall, 1983.

[18] H. Mehrer, *Diffusion in solids: Fundamentals, methods, materials, diffusion-controlled processes*, Springer-Verlag, Berlin, 2007.

[19] R.W. Cahn, "Atomic transport in amorphous alloys: An introduction", *J. Vac. Sci. Technol. A*, **4** (1986) 3071–3077.

[20] A.E. Kaloyeros, E. Eisenbraun, "Ultrathin diffusion barriers/liners for gigascale copper metallization", *Annu. Rev. Mater. Sci.*, **30** (2000) 363–385.

[21] K.-H. Hur, J.-H. Jeong, D.N. Lee, "Microstructures and crystallization of electroless Ni-P deposits", *J. Mater. Sci.*, **25** (1990) 2573–2584.

[22] J.W. Jang, P.G. Kim, K.N. Tu, D.R. Frear, P. Thompson, "Solder reaction-assisted crystallization of electroless Ni–P under bump metallization in low cost flip chip technology", *J. Appl. Phys.*, **85** (1999) 8456.

[23] J.W. Choi, G.H. Hwang, W.K. Han, S.G. Kang, "Phase transformation of Ni–B, Ni–P diffusion barrier deposited electrolessly on Cu interconnect", *Appl. Surf. Sci.*, **253** (2006) 2171–2178.

[24] A. Kumar, M. He, Z. Chen, "Barrier properties of thin Au/Ni–P under bump metallization for Sn–3.5Ag solder", *Surf. Coat. Technol.*, **198** (2005) 283–286.

[25] S. Sakamoto, T. Sugahara, K. Suganuma, "Microstructural stability of Ag sinter joining in thermal cycling", *J. Mater. Sci. Mater. Electron.*, **24** (2013) 1332–1340.

[26] H.-B. Kang, J.-H. Bae, J.-W. Yoon, S.-B. Jung, J. Park, C.-W. Yang, "Characterization of ternary Ni_2SnP layer in Sn–3.5Ag–0.7Cu/electroless Ni(P) solder joint", *Scr. Mater.*, **63** (2010) 1108–1111.

[27] C.K. Chung, Y.J. Chen, W.M. Chen, C.R. Kao, "Origin and evolution of voids in electroless Ni during soldering reaction", *Acta Mater.*, **60** (2012) 4586–4593.

[28] Y. Akada, H. Tatsumi, T. Yamaguchi, A. Hirose, T. Morita, E. Ide, "Interfacial bonding mechanism using silver metallo-organic nanoparticles to bulk metals and observation of sintering behavior", *Mater. Trans.*, **49** (2008) 1537–1545.

[29] E. Ide, A. Hirose, K.F. Kobayashi, "Influence of bonding condition on bonding process using Ag metallo-organic nanoparticles for high temperature lead-free packaging", *Mater. Trans.*, **47** (2006) 211–217.

[30] Y. Shi, W. Fang, Z. Xia, Y. Lei, F. Guo, X. Li, "Investigation of rare earth-doped BiAg high-temperature solders", *J. Mater. Sci. Mater. Electron.*, **21** (2010) 875–881.

[31] T. Yamakawa, T. Takemoto, M. Shimoda, H. Nishikawa, K. Shiokawa, N. Terada, "Influence of joining conditions on bonding strength of joints: Efficacy of low-temperature bonding using Cu nanoparticle paste", *J. Electron. Mater.*, **42** (2013) 1260–1267.

[32] H. Nishikawa, T. Hirano, T. Takemoto, N. Terada, "Effects of joining conditions on joint strength of Cu/Cu joint using Cu nanoparticle paste", *Open Surf. Sci. J.*, **3** (2010) 60–64.

[33] H. Ogura, M. Maruyama, R. Matsubayashi, T. Ogawa, S. Nakamura, T. Komatsu, H. Nagasawa, A. Ichimura, S. Isoda, "Carboxylate-passivated silver nanoparticles and their application to sintered interconnection: A replacement for high temperature lead-rich solders", *J. Electron. Mater.*, **39** (2010) 1233–1240.

[34] M.J. Coutts, M.B. Cortie, M.J. Ford, A.M. McDonagh, "Rapid and controllable sintering of gold nanoparticle inks at room temperature using a chemical agent", *J. Phys. Chem. C*, **113** (2009) 1325–1328.

[35] J.L. Plawsky, J.K. Kim, E.F. Schubert, "Engineered nanoporous and nanostructured films", *Mater. Today*, **12** (2009) 36–45.

[36] J.G. Bai, J.N. Calata, G.-Q. Lu, "Processing and characterization of nanosilver pastes for die-attaching SiC devices", *IEEE Trans. Electron. Packag. Manuf.*, **30** (2007) 241–245.

[37] E. Seker, J.T. Gaskins, H. Bart-Smith, J. Zhu, M.L. Reed, G. Zangari, R. Kelly, M.R. Begley, "The effects of post-fabrication annealing on the mechanical properties of freestanding nanoporous gold structures", *Acta Mater.*, **55** (2007) 4593–4602.

[38] K. Zeng, R. Stierman, D. Abbott, M. Murtuza, "The root cause of black pad failure of solder joints with electroless nickel/immersion gold plating", *JOM*, **58** (2006) 75–79.

[39] P. Snugovsky, P. Arrowsmith, M. Romansky, "Electroless Ni/immersion Au interconnects: Investigation of black pad in wire bonds and solder joints", *J. Electron. Mater.*, **30** (2001) 1262 –1270.

[40] J. Biener, A.M. Hodge, A.V. Hamza, "Microscopic failure behavior of nanoporous gold", *Appl. Phys. Lett.*, **87** (2005) 121908.

[41] K.S. Kim, N. Winograd, "X-ray photoelectron spectroscopic studies of nickel-oxygen surfaces using oxygen and argon ion-bombardment", *Surf. Sci.*, **43** (1974) 625–643.

[42] B.P. Löchel, H.-H. Strehblow, "Breakdown of passivity of nickel by fluoride II surface analytical studies", *J. Electrochem. Soc.*, **131** (1984) 709–713.

[43] B.P. Payne, M.C. Biesinger, N.S. McIntyre, "The study of polycrystalline nickel metal oxidation by water vapour", *J. Electron Spectrosc. Relat. Phenom.*, **175** (2009) 55–65.

[44] M.C. Biesinger, B.P. Payne, A.P. Grosvenor, L.W.M. Lau, A.R. Gerson, R.S.C. Smart, "Resolving surface chemical states in XPS analysis of first row transition metals, oxides and hydroxides: Cr, Mn, Fe, Co and Ni", *Appl. Surf. Sci.*, **257** (2011) 2717–2730.

[45] N.H. Turner, A.M. Single, "Determination of peak positions and areas from wide-scan XPS spectra", *Surf. Interf. Anal.*, **15** (1990) 215–222.

[46] V.K. Kaushik, "XPS core level spectra and Auger parameters for some silver compounds", *J. Electron Spectrosc. Relat. Phenom.*, **56** (1991) 273–277.

Chapter 4

Microstructure evolution of Ag nanoporous bonding joint during thermal storage

4.1 Introduction

In *Chapter 3*, Ag nanoporous bonding is successfully achieved by thermo-compression bonding process which exhibits similar bonding strength with conventional Pb-5Sn solder die attach at the bonding temperature of 300 °C. In this chapter, thermal stability of Ag nanoporous bonding joint with bare Cu and electroless Ni/immersion Au (ENIG) finished Cu substrates during thermal storage test at 250 °C was investigated. An objective of thermal storage test in microelectronics lies on the investigation of thermally activated degradation of joint related with various phenomena, including the oxidation, the diffusion-induced void formation, and the formation of intermetallic compounds [1–5]. Specifically, the fracture behavior of Ag NPB joint and the microstructural change induced by interdiffusion and oxidation during thermal storage test were examined in order to reveal the relationship between the microstructural characteristics at the bonding interface and joint strength of Ag NPB joint. A comparative study on the effect of substrates, including bare Cu and ENIG finished Cu, was also conducted.

4.2 Experimental

4.2.1 Preparation of Ag nanoporous sheet

The Ag nanoporous sheet (thickness = 90-100 um, ligament size = 110 nm) was fabricated by dealloying a melt-spun Al-Ag precursor alloy in a 2 M hydrochloric acid solution for 3 h at 75 °C. Detailed information on the fabrication of Ag nanoporous sheet and characteristics of Ag nanoporous structure can be found in *Section 3.2.1*.

4.2.2 Ag nanoporous bonding process and thermal storage test

An oxygen-free bare Cu substrate and the ENIG finished Cu substrate were used as test specimen. Disk type sample configuration and microstructure of ENIG finish have been given in Fig. 3.2. Before the bonding process, bare Cu disk was polished using abrasive papers with grit number of 400, 1200 and 2000 and diamond paste with particle size of 9, 3 and 1 μm in order to remove Cu native oxide, and then degreased using an ultrasonic cleaner dipping in acetone. ENIG finished Cu disk was degreased in acetone in order to remove surface contamination. The Ag nanoporous sheet was then applied to the surface of the test specimen. The Ag NPB process was conducted using a thermo-compression bonding system under N_2 atmosphere. An applied pressure of 20 MPa was used, and the bonding temperature was 300 °C. The temperature profile of the bonding process has been given in Fig. 3.3.

Thermal storage test of Ag NPB joint was conducted at 250 °C in the convection oven for the storage time up to 1000 h under air atmosphere. It is performed according to the Joint Electron Device Engineering Council (JEDEC) standard for the high temperature storage life (JESD22-A103D), test condition E (storage temperature condition of +250 °C) [6].

4.2.3 Characterization methods

Die shear strength of Ag NPB joint was measured using die shear tester (STR-1000, Rhesca) with a shear rate of 1 mm/min and a shear height of 0.2 mm at room temperature. Elements distribution on the fracture surface was measured using an electron probe micro-analyzer (EPMA, JXA-8530F, JEOL) with an acceleration voltage of 15 kV. Fracture morphology of Ag NPB joint after thermal storage test was observed using a scanning electron microscope (SEM, SU-70, Hitachi) with an acceleration voltage of 10 kV, and a focused ion beam (FIB, JIB-4500, JEOL) with an acceleration

voltage of 30 kV. Microstructure and chemical distribution of the interface of Ag/Cu and Ag/ENIG after thermal storage test were investigated using a transmission electron microscope (TEM, JEM-2100F, JEOL) with an acceleration voltage of 200 kV. The TEM sample preparation of ENIG finish was prepared by the *in-situ* lift-out method using the FIB. Elements distribution at the interface was measured using an energy dispersive X-ray spectroscopy (EDS, JED-2200, JEOL) detector on the scanning TEM (STEM) mode with a beam probe size of 1 nm. A high resolution TEM (HRTEM) observation on the interfaces of Ag/Cu and Ag/ENIG was conducted. TEM image acquisition and image transform of HRTEM image, including fast Fourier transform (FFT) and inverse fast Fourier transform (IFFT), were performed using DigitalMicrograph (Gatan). The phase identification for the diffraction patterns of metals and compounds was performed on the basis of the International Centre for Diffraction Data (ICDD) powder diffraction files (PDF) crystallographic data.

4.3 Metallic bonding at the Ag NPB with bare Cu and ENIG finished Cu substrates

4.3.1 Lattice structure at the Ag/Cu interface

Fig. 4.1 shows microstructure and lattice fringes of Ag and Cu at the Ag/Cu interface of Ag NPB joint with bare Cu disk. A lattice image of Ag/Cu interface in Fig. 4.1(b) indicates that Ag and Cu crystal lattices exhibit no coherent interface due to large misfit of lattice parameters between Ag (PDF no.: 01-071-4613; cubic symmetry; space group: Fm-3m; a=4.0880 Å) and Cu (PDF no.: 01-071 -4610; cubic symmetry; space group: Fm-3m; a=3.6170 Å). In order to form strain-free coherent interphase interface between two different phases, two phases should show almost same lattice parameters, or an interplanar angle, θ, of two phases should shows certain value [7]. In case of Ag and Cu should be satisfied follow relationship (equation 4.1).

$$\theta = \cos^{-1}\left[\frac{d_{hkl,Cu}}{d_{hkl,Ag}}\right] \quad \cdots\cdots (4.1)$$

The calculated interplanar angles for strain-free coherent interphase interface between $(111)_{Ag}$ and $(200)_{Cu}$ and between $(200)_{Ag}$ and $(200)_{Cu}$ are 39.96° and 27.74° from the reference data, respectively. These values show slightly different with measured interplanar angle from fast Fourier transform (FFT) patterns in Fig. 4.1(c). A reciprocal space image calculated by FFT from the HRTEM image of Ag/Cu interface exhibits two different diffraction patterns of Ag and Cu.

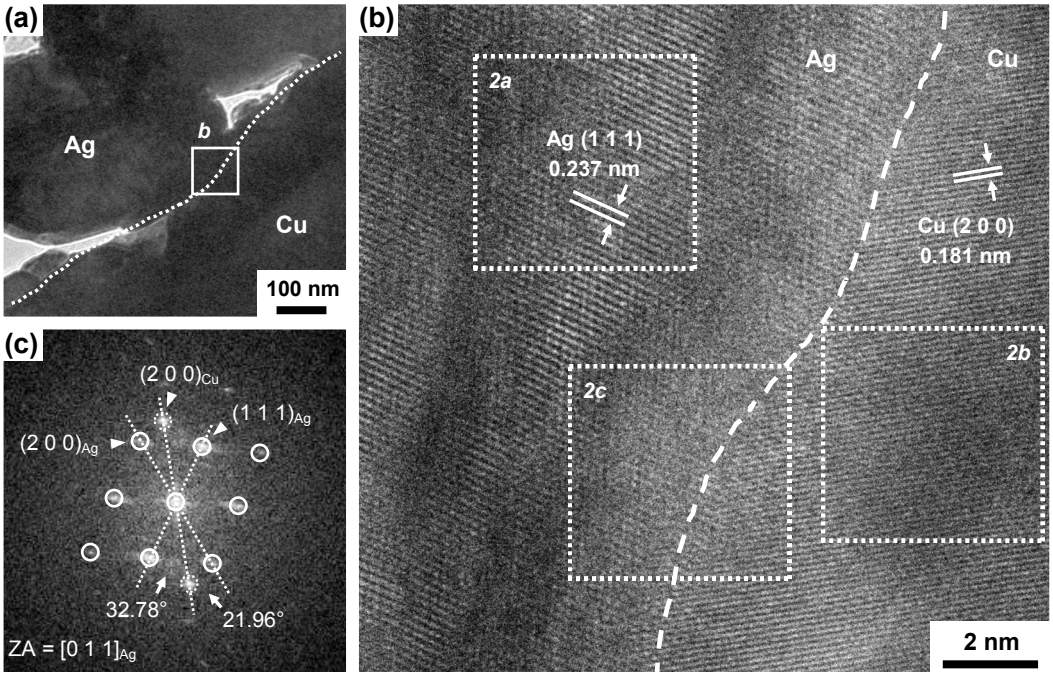

Figure 4.1 **(a)** Transmission electron microscopy (TEM) bright field (BF) image on the Ag/Cu interface of as-bonded Ag nanoporous bonding joint with bare Cu substrate, **(b)** high resolution (HR) TEM image of lattice fringe of Ag/Cu interface magnified in the box in *(a)*, and **(c)** the corresponding fast Fourier transform (FFT) pattern on the *(b)*, where lined circles indicate the patterns of Ag lattice and dotted circles indicate the patterns of Cu lattice.

Fig 4.2 shows regional FFT patterns of Ag side, Cu side and Ag/Cu interface which are denoted in Fig. 4.1 shows clear diffraction pattern of Ag with along the $[011]_{Ag}$ direction, as shown in Fig. 4.2(a), strong pattern of $\{200\}_{Cu}$, as shown in Fig. 4.2(b) and mixed patterns of Ag and Cu, as shown in Fig. 4.2(c). It is possible to obtain distinct images of lattice fringe through the Fourier mask filtering of particular patterns with the spot masks and subsequent inverse FFT calculation as shown in Fig. 4.2. Detailed information on the Fourier mask filtering on the HRTEM image can be found in *Appendix 2*.

There is an interference of $(111)_{Ag}$ and $(200)_{Cu}$ lattices which is called a mixed moiré fringe, as shown in Fig. 4.2(c). This can be foamed through the interfering two sets of lattice plane with the different direction and interplanar distance. The moiré fringe is evidence of overlap of different two crystal lattices. The general expression on the spacing of the moiré fringe (d_m) can be given by following equation 4.2 [8],

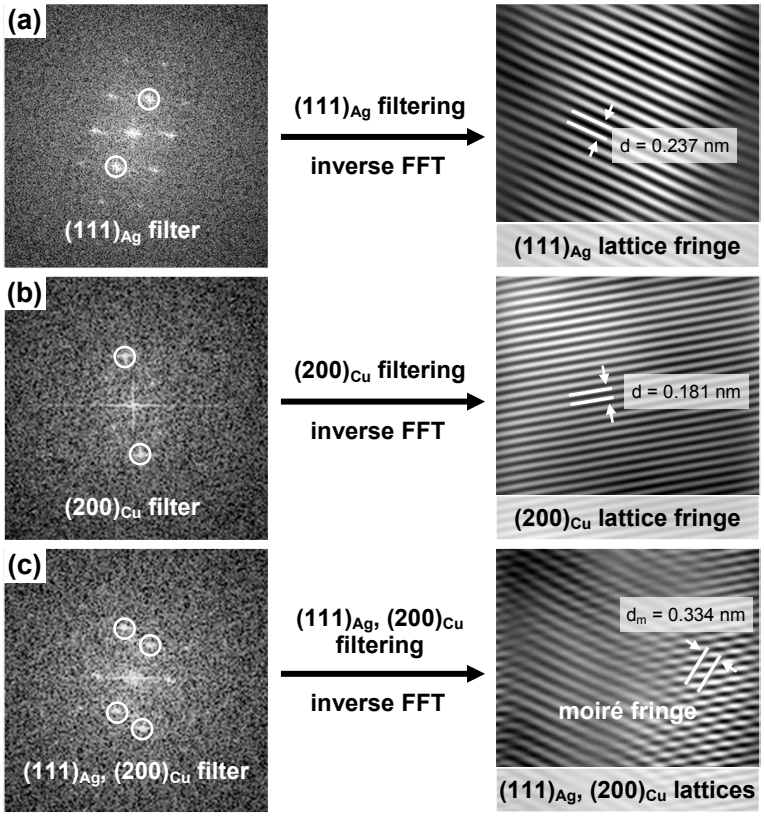

Figure 4.2 The FFT patterns and corresponding Fourier mask filtered inverse FFT (IFFT) images on the **(a)** Ag side, **(b)** Cu side and **(c)** Ag/Cu interface, which are denoted as *2a, 2b* and *2c* in *Fig. 4.1*, respectively.

$$d_m = \frac{d_{111,Ag} d_{200,Cu}}{\sqrt{d_{111,Ag} d_{200,Cu} \theta^2 + \left(d_{111,Ag} - d_{200,Cu}\right)^2}} \quad \cdots\cdots (4.2)$$

where $d_{111,Ag}$ and $d_{200,Cu}$ are interplanar spacings of $(111)_{Ag}$ and $(200)_{Cu}$ lattices, and θ is misorientation angle in radian between $(111)_{Ag}$ and $(200)_{Cu}$ lattices. The measured interplanar spacings of $(111)_{Ag}$ and $(200)_{Cu}$, and misorientation angle between $(111)_{Ag}$ and $(200)_{Cu}$, and moiré fringe spacing from Fig. 4.1 and Fig. 4.2 are 0.237 nm, 0.181 nm, 32.78°, 0.334 nm, respectively. An estimated d_m (0.327 nm) using equation 5.2 exhibits similar value with the measured d_m from filtered IFFT image of $(111)_{Ag}$ and $(200)_{Cu}$ in Fig. 4.2(c). Li et al. [9] also shows mixed moiré fringe between $(200)_{Ag}$ and $(200)_{Cu}$, using HRTEM in Ag nanoparticle sintered joint with Cu substrate, where they suggested some intermediate layer formation by overlapping of Cu and Ag lattices.

4.3.2 Epitaxial interface between Ag and Au

Fig. 4.3 shows microstructure and lattice fringes of Ag and Au at the Ag/Au interface of Ag NPB joint with ENIG finished Cu disk. A lattice image shows epitaxial interface between $(111)_{Ag}$ and $(111)_{Au}$ due to the same crystal structure and almost similar lattice parameters of Ag (a=4.0880 Å) and Au (PDF no.: 01-071-4073; cubic symmetry; space group: Fm-3m; a=4.0789 Å). The corresponding FFT pattern, as shown in Fig. 4.3(c) also exhibits only one pattern of Ag//Au along the $[011]_{Ag//Au}$ direction. The partial FFT pattern of Ag side, Au side and Ag/Au interface also exhibit same crystallographic orientation, as shown in Fig. 4.4. This relationship between Ag and Au lattices can be found elsewhere [10]. Ogura et al. [11] explained that this epitaxial relationship between Ag and Au comes from the reorientation of Ag atoms at the surface of Au in order to reduce surface energy using molecular dynamic simulation.

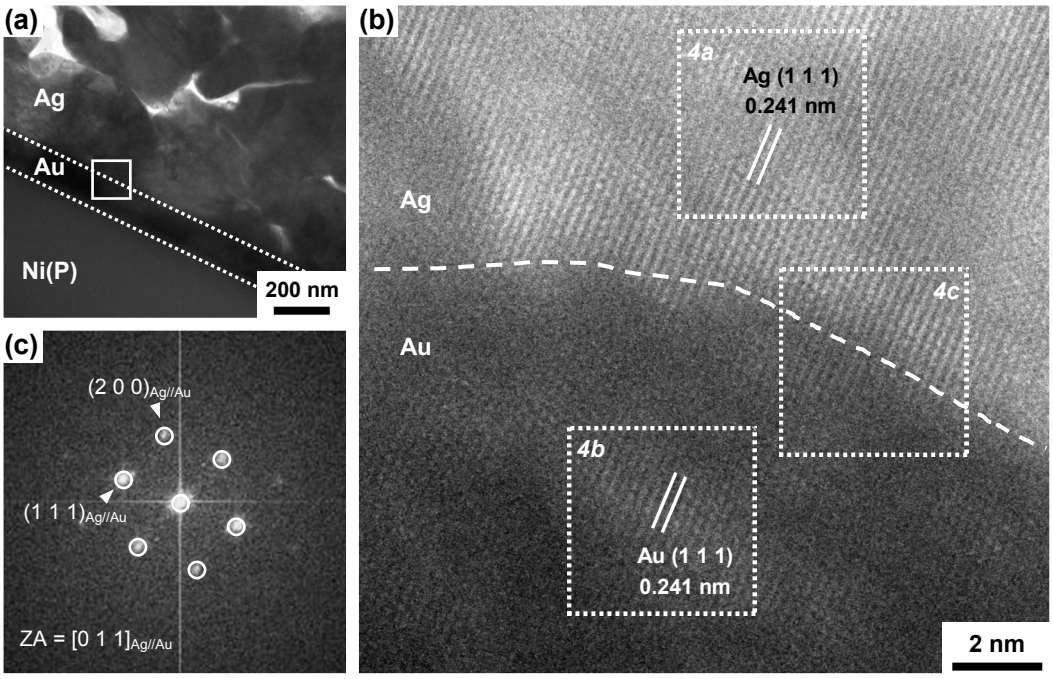

Figure 4.3 **(a)** TEM BF image on the Ag/ENIG interface of as-bonded Ag nanoporous bonding joint with ENIG finished Cu substrate, **(b)** high resolution (HR) TEM image of lattice fringe of Ag/Au interface magnified in the box in *(a)*, and **(c)** the corresponding fast Fourier transform (FFT) pattern on the *(b)*.

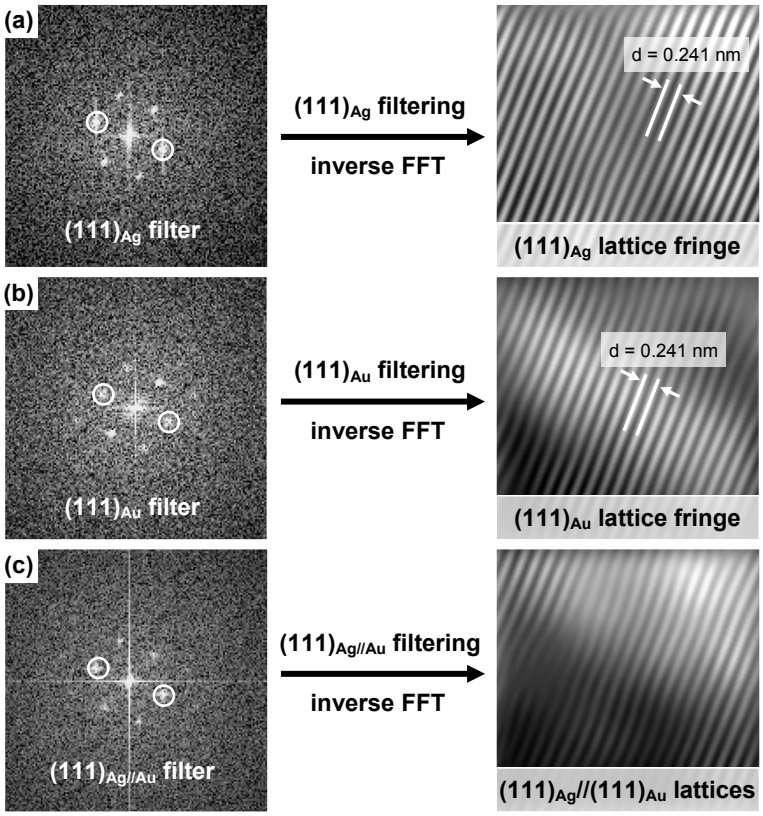

Figure 4.4 The FFT patterns and corresponding Fourier mask filtered IFFT images on the **(a)** Ag side, **(b)** Au side and **(c)** Ag/Ag interface, which are denoted as *4a, 4b* and *4c* in *Fig. 4.3*, respectively.

4.4 Thermal degradation of Ag NPB joint

4.4.1 Change of Ag NPB joint strength during thermal storage

Shear test results of Ag NPB joint with ENIG finished Cu and bare Cu disk during thermal storage test are shown in Fig. 4.5. The results of shear test of as-bonded Ag NPB joint with ENIG finished Cu and bare Cu substrates show 25.7 and 26.6 MPa. Similar shear strength results of as-bonded Ag NPB joint, irrespective of substrates (ENIG finished Cu and bare Cu) indicate that Ag NPB formed good metallic bonding with Cu and Au surface. These values exhibit higher than it of Pb-5Sn die attach reported in the literatures [12,13] and die strength requirement for electronics defined in MIL-STD 883G [14].

The effect of substrate on the shear strength became significant with increasing of thermal storage time. In case of bare Cu substrate, the shear strength gradually decreased with increasing of thermal storage time, and it showed 11.4 MPa with the thermal storage time of 1000 h. Contrariwise,

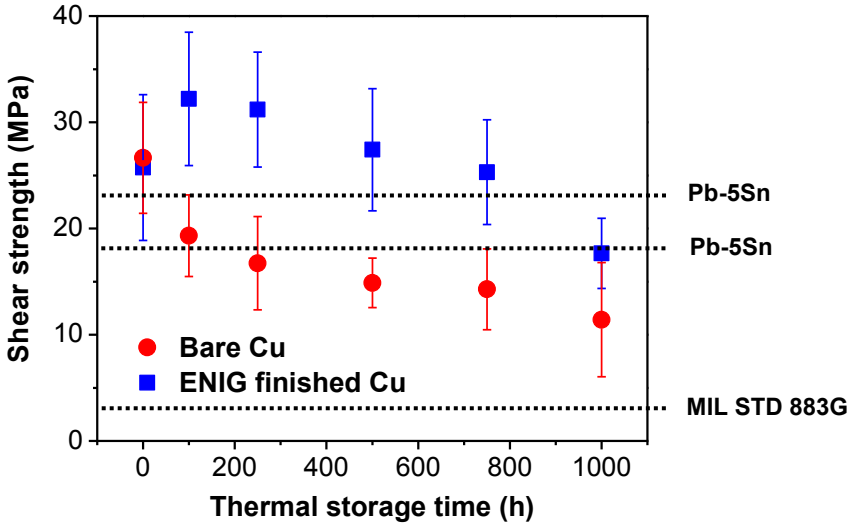

Figure 4.5 Changes of shear strength of Ag nanoporous bonding joint with bare Cu and ENIG finished Cu substrates as a function of thermal storage time at 250 °C. Inset dotted lines indicate shear strength of Pb-5Sn die attach [12,13] and requirement of minimum shear strength for die attach defined in US military standard (MIL- STD-883G) [14].

the shear strength of NPB with the ENIG finished substrate increased to 32.2 MPa for 100 h, and then gradually decreased. After 750 h, the shear strength showed 25.3 MPa, which is similar value with the initial shear strength of NPB. These results may arise from the different oxidation behavior of bare Cu and ENIG finished substrates.

4.4.2 Macroscopic element distribution in the fracture surface

EPMA mapping on the fracture surface was investigated in order to reveal reason of joint degradation during thermal storage test. Through the examination of both of upper and lower fracture surfaces, it is possible to confirm where the fracture is occurred at the joint. As mentioned in *Chapter 3*, the variation of fracture mode is closely related with shear strength of Ag NPB joint.

Fig. 4.6 and Fig. 4.7 show changes of element mapping results on the Ag NPB joint with Cu and ENIG finished Cu after the thermal storage test. The shear direction and cross-circled mark for sample position are indicated based on the lower samples. The fracture of as-bonded samples of Ag/Cu and Ag/ENIG was occurred mainly Ag layer, regardless of substrate. This result supports the shear test results, as shown in Fig. 4.5 that the as-bonded Ag NPB joints with bare Cu and ENIG finished show almost same values. Furthermore, it can be concluded that this Ag NPB process is suitable not

on the ENIG finished substrate but also the bare Cu substrate. Only small portion of interfacial fracture (Ag/Cu interface of bare Cu substrate and Ag/Au interface of ENIG finished Cu substrate) was observed, as indicated with green arrow in Fig. 4.6a and Fig. 4.7a. There are no Ag signals; and high intensity of Cu and Au in both of Cu and ENIG finished Cu substrate at the interfacial fracture region.

In case of Ag NPB with bare Cu substrate, as shown in Fig. 4.6, O signal significantly increased in the same position with Cu after thermal storage test. This indicates that Cu surface is oxidized after thermal storage. The area fraction of fracture at the Cu oxide gradually increased with increasing thermal storage time up to 250 h. After 500 h, the main fracture location of joint is transferred to Cu oxide layer. The Cu oxide layer fractured area displays a tendency to low O level at the fracture surface next to Cu side, which is indicated by *orange arrow* in Fig. 4.6, and high O level at the fracture surface next to Ag side, which is indicated by *blue arrow* in Fig. 4.6.

In case of Ag NPB with ENIG finished Cu substrate, as shown in Fig. 4.7, an aspect of changes of the fracture surface after thermal storage test is more complicated compared with bare Cu substrate. After thermal storage time of 100 h, a fracture occurrence at the interface of Au/Ni appeared. As mentioned in *Chapter 3*, Ni oxidation can lead to a brittle fracture at the Au/Ni interface. The portion of fracture at the Au/Ni interface gradually increased with increasing thermal storage time. Unlike the bare Cu substrate, ENIG finished Cu substrate exhibits mixed fracture mode of Ag layer fracture and Au/Ni interfacial fracture even up to thermal storage time 1000 h, as shown in Fig. 4.7(e). The Au/Ni interfacial fractured area next to Ni(P) side, which is indicated by *blue arrow* in Fig. 4.7, presents Ag, Au, high O and very low Ni signals. On the contrary to this, it next to Ag side, which is indicated by *orange arrow* in Fig. 4.7, presents high Ni and high P signals. This means that the Au/ Ni interfacial fracture is occurred at the interface of Ni(P)/Ni oxide.

Fig. 4.8 shows the variation on area fractions of each fracture modes of Ag NPB joint with Cu and ENIG finished Cu substrate with thermal storage time. The fracture location of Ag NPB joint after thermal storage test can be divided in three types from the fractography; Ag layer, Ag/Cu interface and Cu oxide layer fracture in case of bare Cu, as shown in Fig. 4.8(a), and Ag layer, Ag/Au interface and Au/Ni interface in case of ENIG finished Cu, as shown in Fig. 4.8(b). The variations of fracture mode significantly are different with substrate after thermal storage test. The area fraction of Cu oxide layer exhibits over 60% up to 250 h. After 500 h, it sharply drastically increased that exhibits over 95%. Besides, the Au/Ni interfacial fracture gradually increased with increasing thermal storage

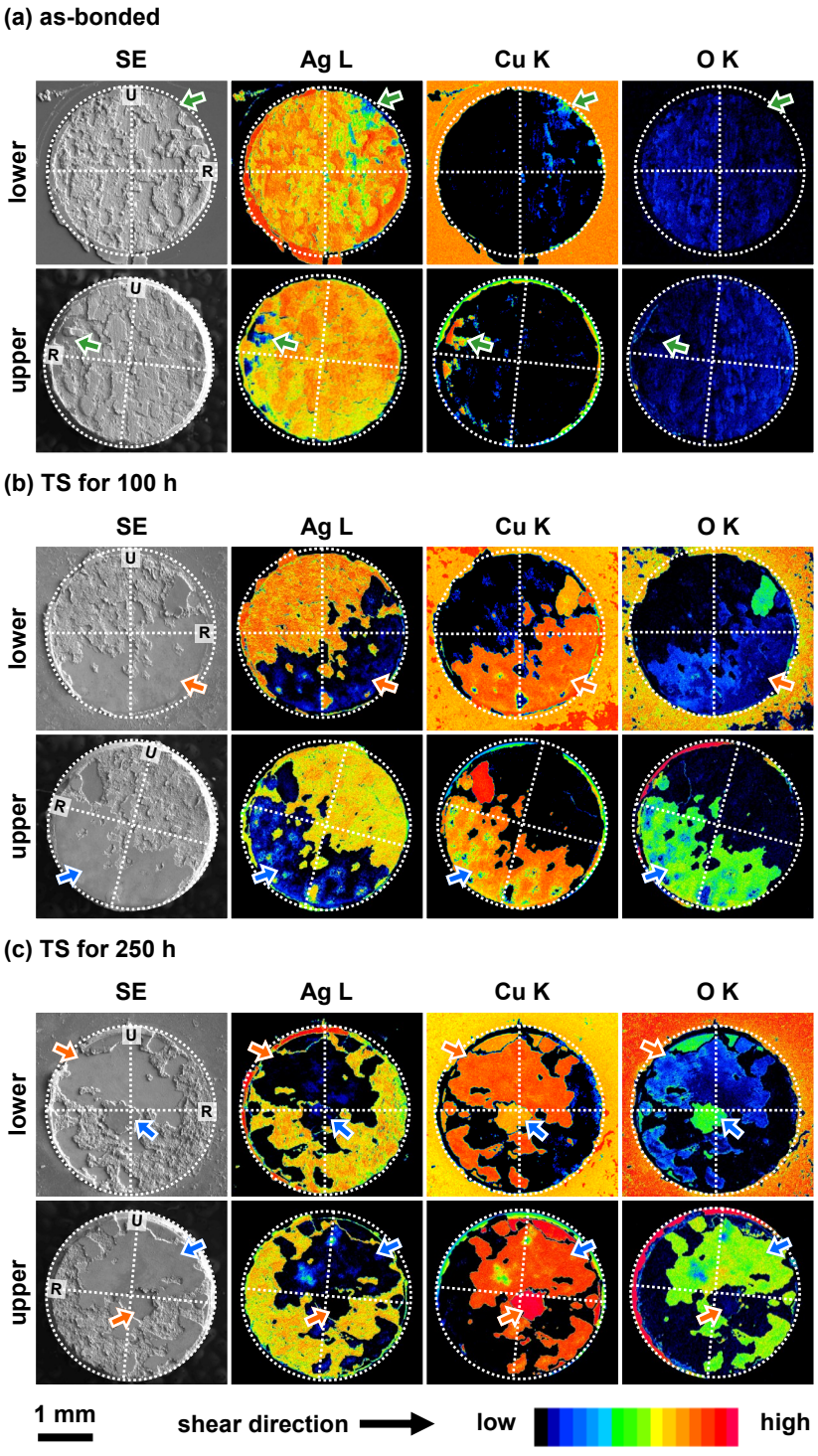

Figure 4.6 Electron probe micro-analyzer (EPMA) element mapping results (Ag, Cu and O) on upper and lower surface of fractured sample of Ag nanoporous bonding joint with bare Cu substrate after thermal storage test at 250 °C: **(a)** as-bonded, **(b)** 100 h, **(c)** 250 h, **(d)** 500 h, **(e)** 750 h and **(f)** 1000 h, and **(g)** fracture positions of Ag layer fracture, Ag/Cu interfacial fracture and Cu oxide fracture. Inset *cross-circles* indicate sample direction, where *U* and *R* indicate upper and right based on the lower sample, respectively. Upper and lower sample surfaces exhibit mirror plane relationship.

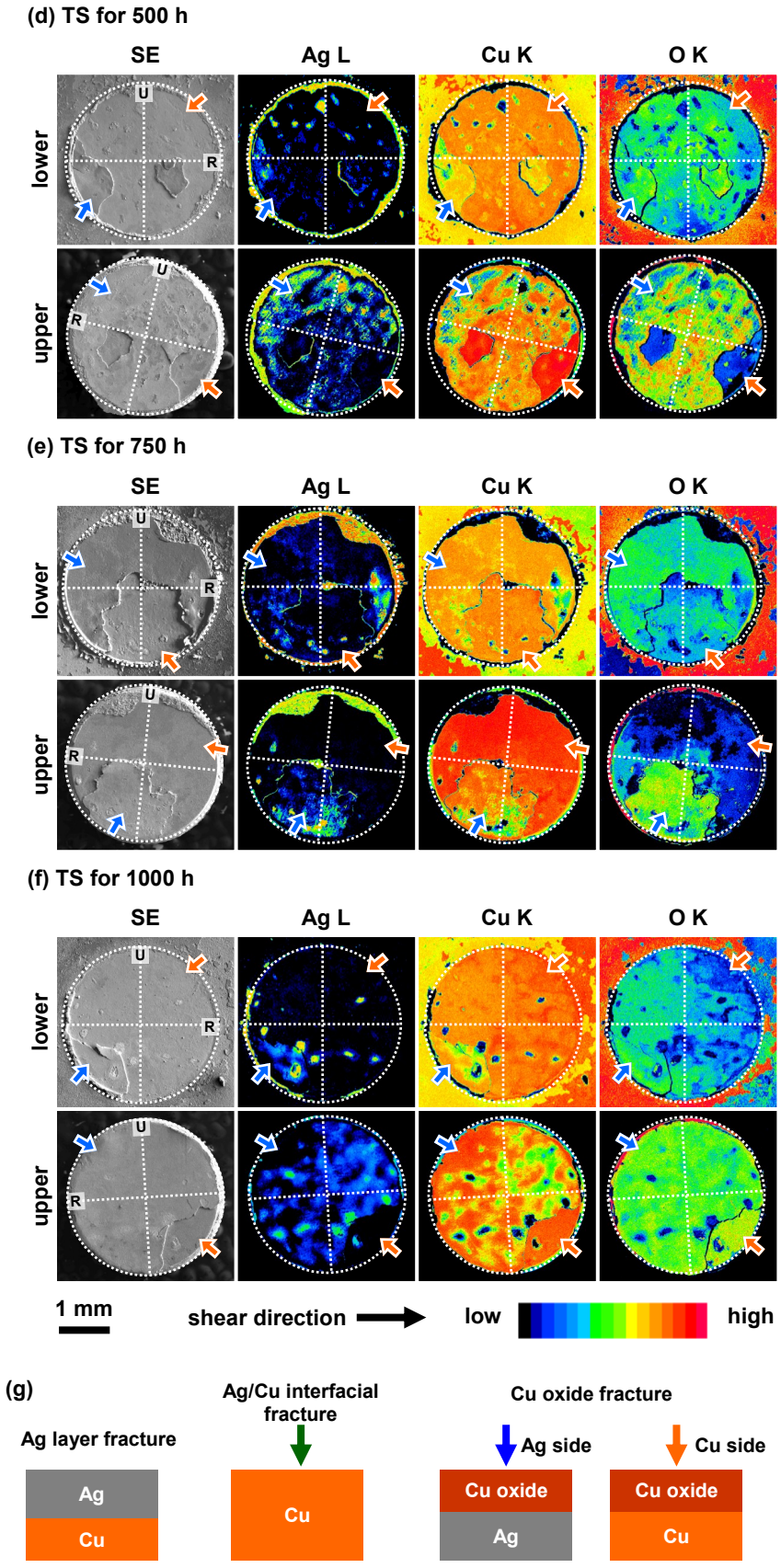

Figure 4.6 (continued)

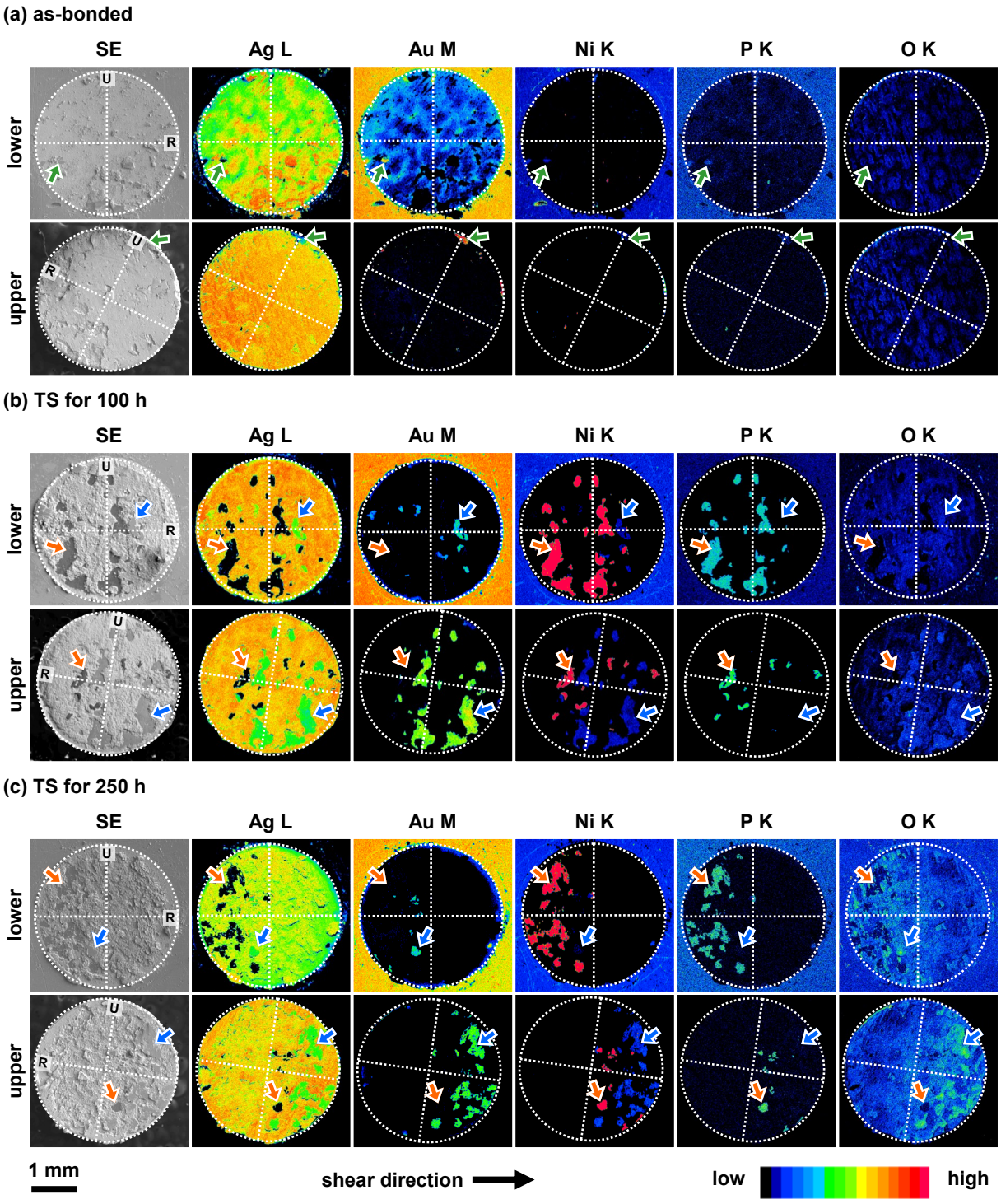

Figure 4.7 EPMA element mapping results (Ag, Au, Ni, P and O) on upper and lower surface of fractured sample of Ag nanoporous bonding joint with ENIG finished Cu substrate after thermal storage test at 250 °C: **(a)** as-bonded, **(b)** 100 h, **(c)** 250 h, **(d)** 500 h, **(e)** 750 h and **(f)** 1000 h, and **(g)** fracture positions of Ag layer fracture, Ag/Au interfacial fracture and Au/Ni interfacial fracture. Inset *cross-circles* indicate sample direction, where *U* and *R* indicate upper and right, respectively. Upper and lower sample surfaces exhibit mirror plane relationship.

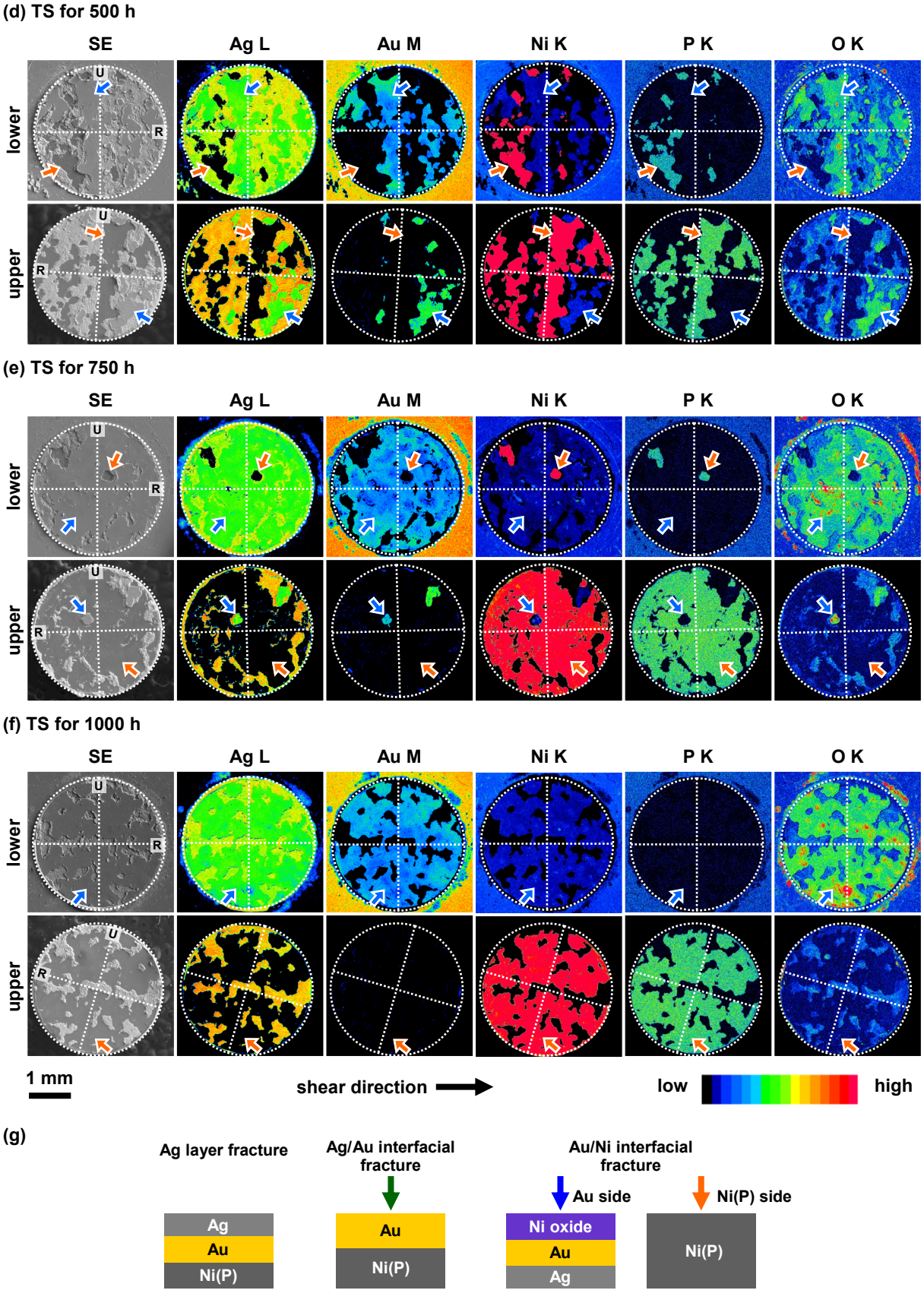

Figure 4.7 (continued)

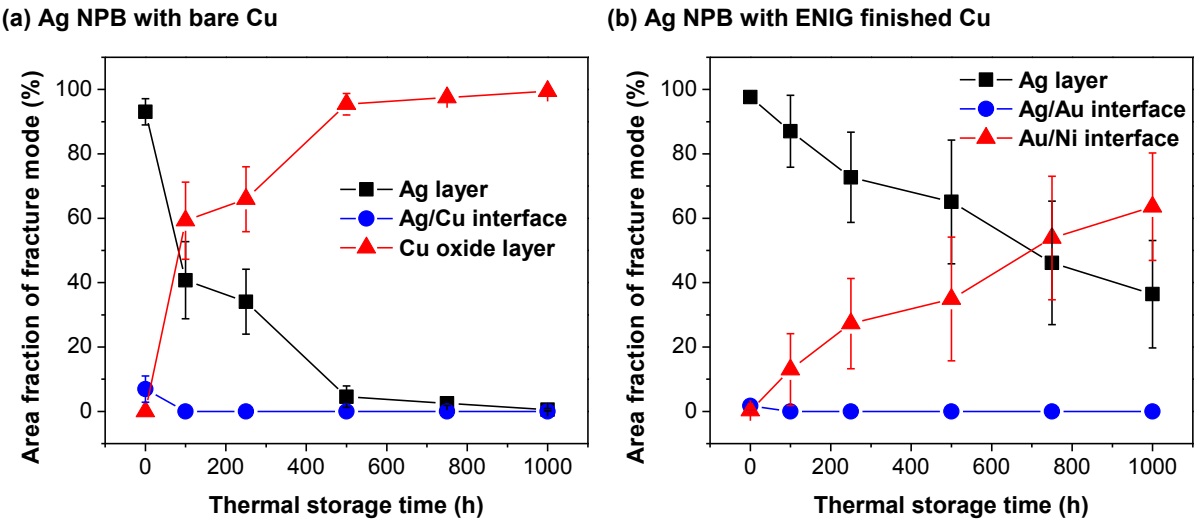

Figure 4.8 The variation on the area fractions of fracture mode of Ag nanoporous bonding joint as a function of thermal storage time with **(a)** bare Cu substrate and **(b)** ENIG finished Cu substrate.

time. The cause of this difference may come from the different oxidation mechanism between bare Cu and ENIG finish. Oxidation behavior of Cu and ENIG finish during thermal storage test will be presented in *Section 4.3.4*.

4.4.3 Morphology of fracture surface

In order to understand an effect of thermal storage on the fracture behavior of Ag NPB with different substrates, the fracture morphology after the shear test were investigated with SEM observation. Low magnification SEM images in Fig. 4.9 and Fig. 4.12 are the same images with SE images in Fig. 4.6 and Fig. 4.7, respectively. The observed positions of high magnification images are denoted using white squares in low magnification images.

Fig. 4.9 exhibits fracture morphology of Ag NPB joint with bare Cu substrate on the as-bonded and after thermal storage for 250 h and 1000 h. The Ag layer fracture region, as shown in Fig. 4.9(b), which is a main fracture portion of as-bonded sample with bare Cu substrate, presents an elongated Ag porous structure. As mentioned in *Chapter 3*, this feature is an evidence of ductile fracture of Ag porous structure. Although the crack is partially propagated along the Ag/Cu interface, as shown in Fig. 4.9(c), the very small portion of this fracture mode is not effective on the shear strength. After 250 h, main fracture mode is transferred from the Ag layer fracture to the Cu oxide layer fracture. The Ag fracture region exhibit slightly coarsened compared with as-bonded joint, as

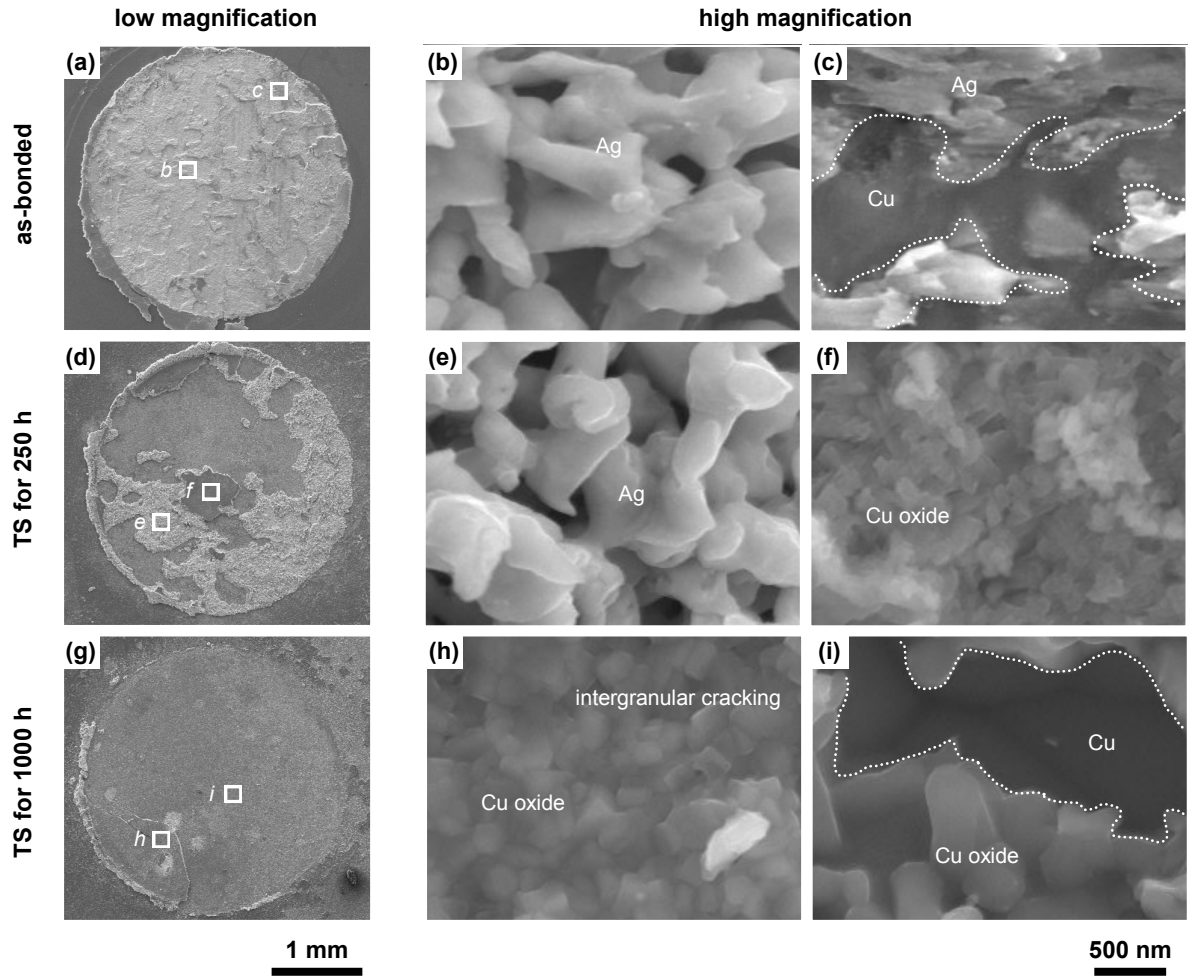

Figure 4.9 Scanning electron microscopy (SEM) secondary electron (SE) images of fracture surface of Ag nanoporous bonding joint with bare Cu substrate after thermal storage test: **(a)** macroscopic feature of fracture at Ag layer dominant, **(b)** elongated Ag porous structure and **(c)** partial Cu/Ag interfacial fracture, of as-bonded Ag NPB joint surface; **(d)** macroscopic feature of mixed fracture modes at Ag layer and Cu oxide, **(e)** elongated Ag porous structure and **(f)** intergranular fracture at Cu oxide, after 250 h; **(g)** macroscopic feature of Cu oxide dominant, **(h)** intergranular fracture at Cu oxide and **(i)** pull out of Cu oxide, after 1000 h.

shown in Fig 4.9(e), due to the coarsening of Ag porous structure during thermal storage [4,5]. The fracture mode in Cu oxide appeared intergranular fracture along the boundaries of Cu oxides, as shown in Fig. 4.9(f). After 100 h, almost of fracture was occurred in the Cu oxide layer, where an intergranular fracture along the Cu oxide grain in Fig. 4.9(h) and a void in Fig. 4.9(i) can be observed. The oxidation of Cu surface could induce the brittle fracture of Ag NPB with bare Cu substrate; as a result, it became a cause of joint strength degradation after thermal storage test.

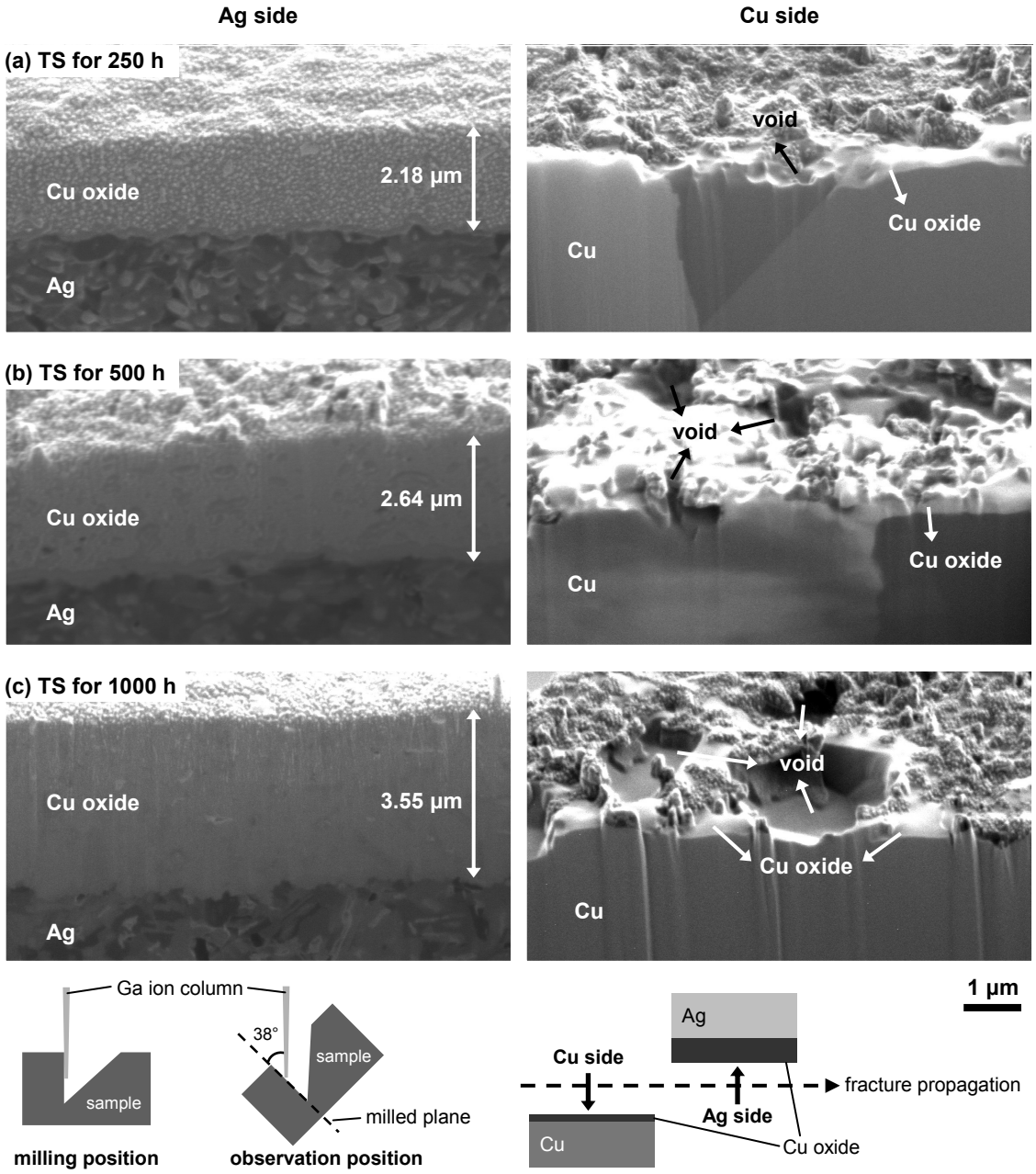

Figure 4.10 Tilted focused ion beam (FIB) SE images on the Cu oxide layer fractured regions (both of Ag side and Cu side) after thermal storage test for **(a)** 250 h, **(b)** 500 h and **(c)** 1000 h.

Fig. 4.10 exhibits FIB milled cross-sectional images underneath fracture surfaces along the Cu oxide layer, where the included angle between the observation plane and the Ga ion beam column was 38°. Accordingly, the length scales along the horizontal and vertical direction are slightly different. The actual length along the horizontal direction is same with inset scale bar, while the actual length along the vertical direction is 1.27 times longer than inset scale bar. The images of Cu side and

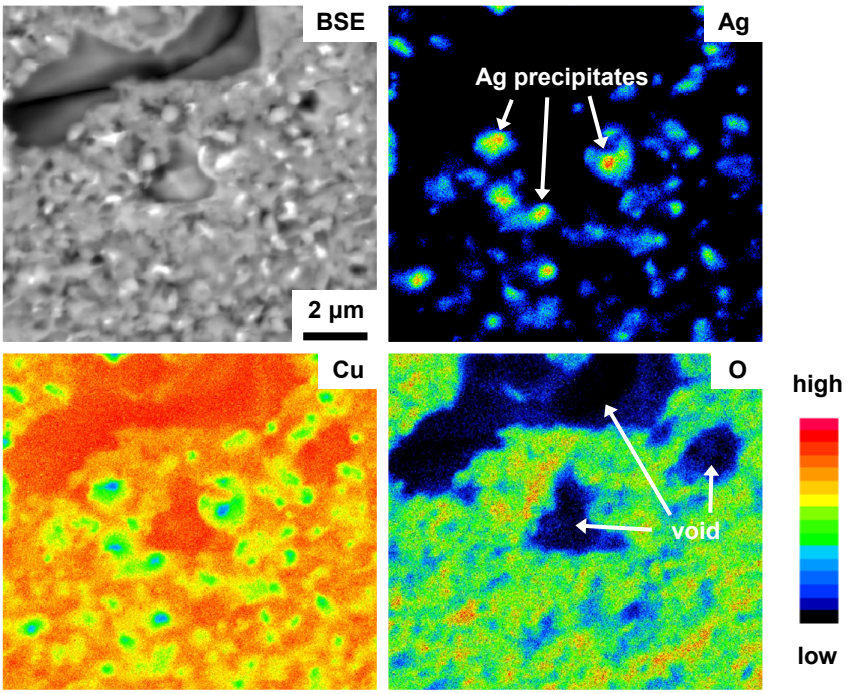

Figure 4.11 EPMA elemental mapping results on the Cu oxide layer fractured region after thermal storage for 1000 h.

Ag side are represented the fracture surface of Cu oxide in the vicinity of Cu substrate and Ag bonding layer, respectively. Cu oxide layer of Ag side were thicker than that of Cu side, regardless of thermal storage time. The thickness of Cu oxide of Ag side gradually increased with thermal storage time. Besides, the Cu oxide of Cu side was very thin compared with that of Ag side. The fracture surface morphologies of Ag side and Cu side also exhibited considerable difference. The fracture surface of Ag side was shown relatively flat morphology, while, it of Cu side was shown rugged morphology. This rugged morphology was seemed to come from the presence of voids in the vicinity of bare Cu substrate. The size of voids gradually increased with increasing of thermal storage time.

Fig. 4.11 shows EPMA mapping results on the fracture surface (Cu side) of Cu oxide layer fractured region after thermal storage test for 1000 h. The non-oxidized Cu underneath of Cu oxide at the void position can be confirmed. The Ag precipitate in Cu oxide layer was also detected, which will be mentioned in *Section 4.3.4*.

Fig. 4.12 exhibits fracture morphology of Ag NPB joint with ENIG finished Cu substrate on the as-bonded and after thermal storage for 500 h and 1000 h. The feature of Ag layer fractured surface of as-bonded Ag NPB with ENIG finished Cu substrate in Fig. 4.12(a) and elongated Ag

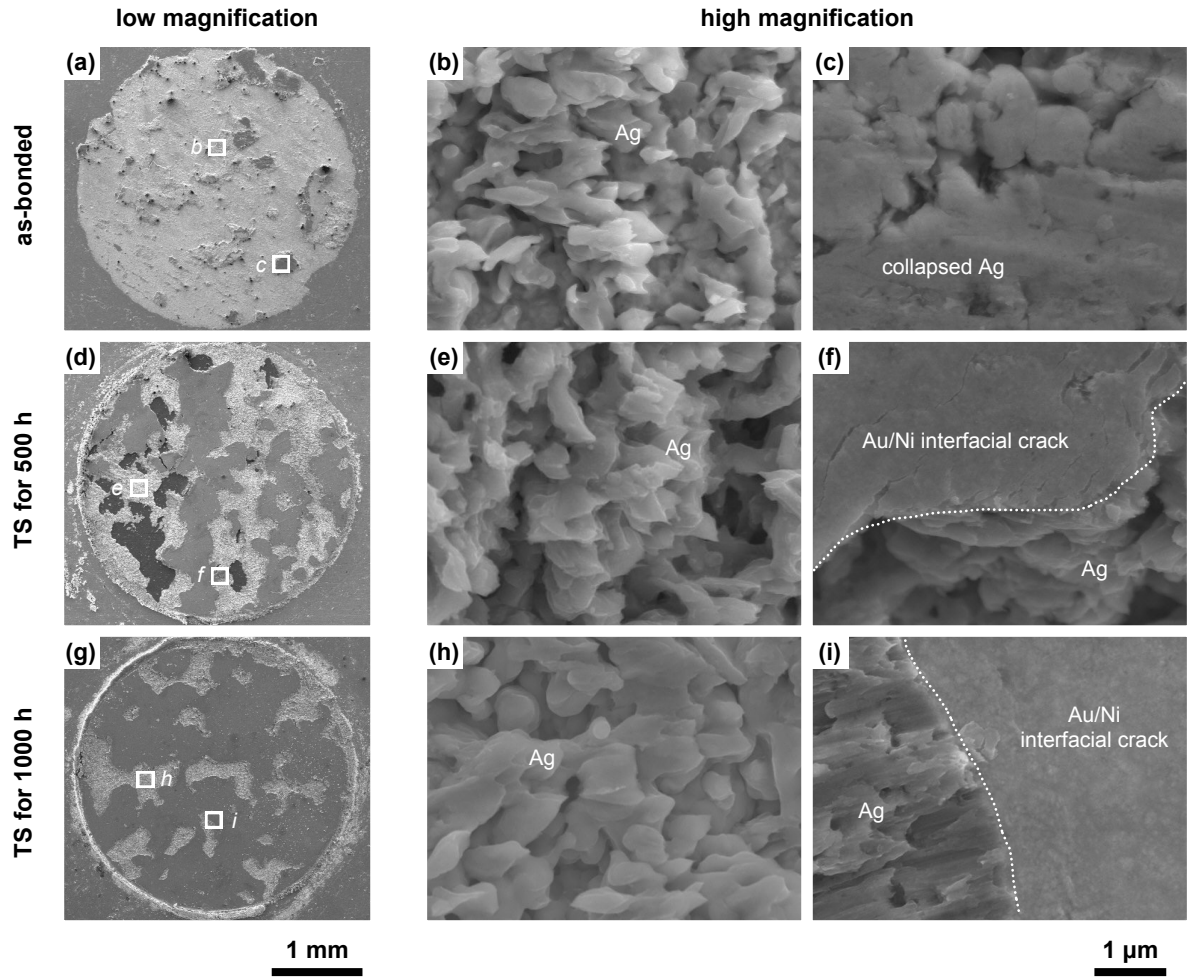

Figure 4.12 SEM SE images of fracture surface of Ag nanoporous bonding joint with ENIG finished Cu substrate after thermal storage test: **(a)** macroscopic feature of fracture at Ag layer dominant, **(b)** elongated Ag porous structure and **(c)** Ag side at the Ag/Au interfacial fractured region, of as-bonded Ag NPB joint surface; **(d)** macroscopic feature of mixed fracture modes at Ag layer and Au/Ni interface, **(e)** elongated Ag porous structure and **(f)** Au/Ni interfacial fracture, after 500 h; **(g)** macroscopic feature of mixed fracture modes at Ag layer and Au/Ni interface, **(h)** elongated Ag porous structure and **(i)** Au/Ni interfacial fracture, after 1000 h.

porous structure in Fig. 4.12(b) exhibit similar results with the fracture surface of bare Cu substrate, as shown in Fig. 4.10(a,b). The collapsed Ag was partially observed, because of the insufficient interfacial reaction between Ag and ENIG surface, as mentioned in *Chapter 3*. The elongated Ag porous structure by shear strength was gradually coarsened with increasing of thermal storage time, as shown in Fig. 4.12(b,e,h). The Au/Ni interfacial fractured region exhibited plane, as shown in Fig. 4.12(f,i).

4.5 Interfacial reaction and microstructure evolution at the interface

4.5.1 Interfacial reaction at the Ag/Cu interface

Fig. 4.13 shows STEM/EDS mapping and line analysis results at the Ag/Cu interface of as-bonded Ag NPB with bare Cu substrate. The Ag/Cu interface exhibits a distinct interphase interface. A small amount of Cu (approximately 5 at.%) was detected in Ag matrix, besides, Ag was rarely detected in Cu matrix, as shown in the composition profile in Fig. 4.13(c). This feature at the interface is a typical composition profile of diffusion couple of eutectic system below the eutectic temperature [15]. Ag-Cu binary system is an eutectic system (eutectic temperature = 779.1 °C) with limited mutual solubility [16]. The thermodynamic calculation method will be necessary in order to estimate the accurate mutual solubility of Ag-Cu diffusion couple at 250 °C.

Fig. 4.14 and 4.15 show EDS mapping and line analysis results at the Ag/Cu interface of Ag NPB with bare Cu substrate after thermal storage for 500 h and 1000 h, respectively. The Cu near the bonding interface was fully oxidized; and Cu oxide phase exhibited nano-crystalline through the oxidation induced recrystallization [17]. A demarcation of Ag phase and Cu oxide phase maintained obviously even after temperature storage from the EDS line analysis results, because of non-mixed phase between Ag-Cu binary system. Interestingly, an isolated Ag phase in Cu oxide matrix was observed. The Ag diffusion along the grain boundary of Cu matrix has been reported [18]. It seemed that this Ag precipitate in Cu oxide matrix was formed by the formation of nano-crystalline Cu oxide and subsequent grain boundary migration of Ag along the Cu oxide matrix.

4.5.2 Oxidation of Cu surface

Fig. 4.16 shows low magnification STEM/EDS mapping of Cu/Ag interface after thermal storage for 1000 h. Table 4.1 shows the EDS point analysis where marked in Fig. 4.16. Cu oxide layer contains two oxides, including thick Cu_2O with thickness of approximately 3.56 μm (spectrum number 4 in Table 4.1) and thin CuO with the thickness of approximately 0.16 μm (spectrum number 2 in Table 4.2).

Generally, there are two stable oxides, Cu_2O and CuO, in Cu-O system [19]. Cu oxidation behaviors of thin film, porous structure and nanoparticle with various annealing temperatures have been extensively studied using X-ray diffraction (XRD), where Cu_2O is a dominant oxide foam at low temperature (below 300 °C) and CuO appeared at elevated temperature (above 300 °C) [20–22]. These

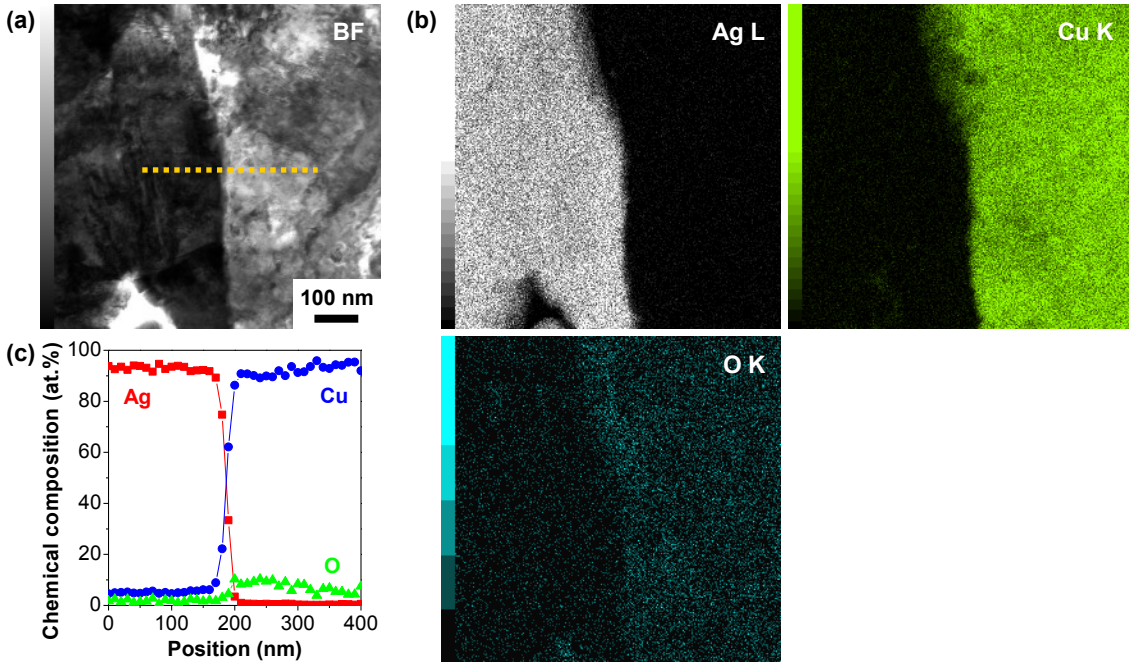

Figure 4.13 **(a)** Scanning TEM (STEM) BF image and **(b)** corresponding elemental mapping results of Ag L, Cu K and O K on the Ag/Cu interface for as-bonded Ag NPB sample with bare Cu substrate, and **(c)** energy dispersive X-ray spectroscopy (EDS) line analysis along the *dotted line* in BF image.

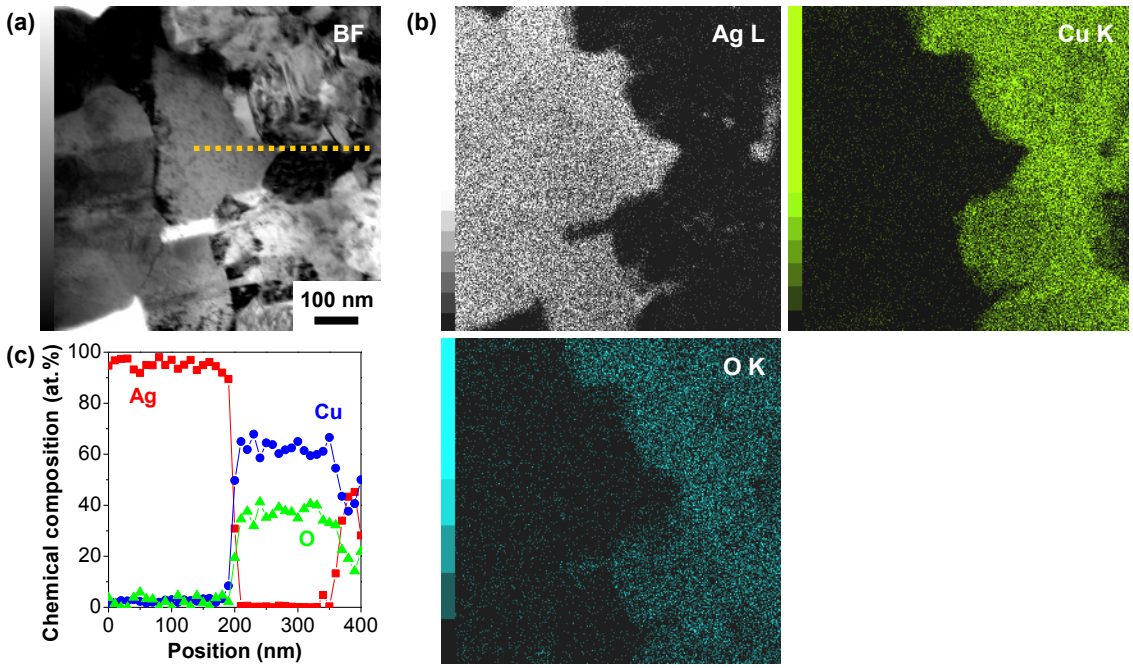

Figure 4.14 **(a)** STEM BF image and **(b)** corresponding elemental mapping results of Ag L, Cu K and O K on the Ag/Cu interface of Ag NPB sample with bare Cu substrate after thermal storage at 250 °C for 500 h, and **(c)** EDS line analysis along the *dotted line* in BF image.

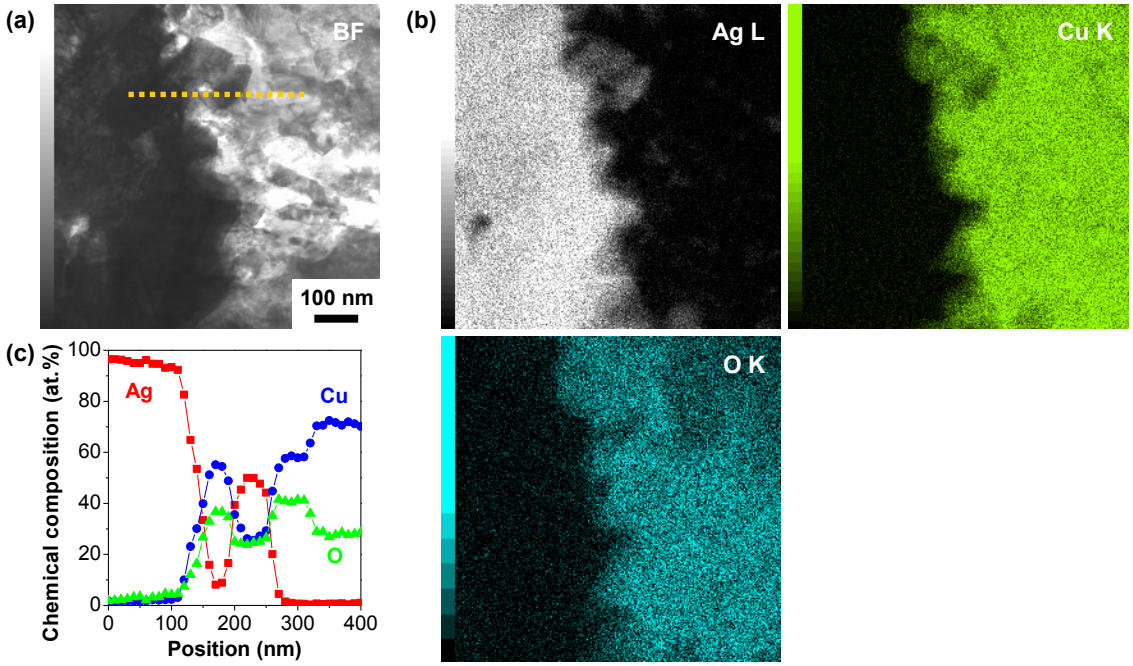

Figure 4.15 **(a)** STEM BF image and **(b)** corresponding elemental mapping results of Ag L, Cu K and O K on the Ag/Cu interface of Ag NPB sample with bare Cu substrate after thermal storage at 250 °C for 1000 h, and **(c)** EDS line analysis along the *dotted line* in BF image.

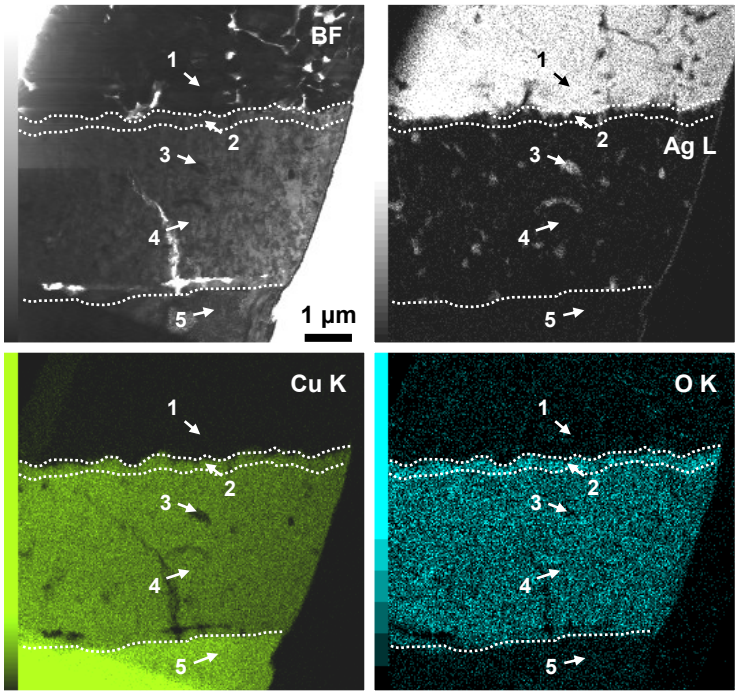

Figure 4.16 Low magnification STEM BF image and corresponding elemental mapping results of Ag L, Cu K and O K on the Ag/Cu interface of Ag NPB sample with bare Cu substrate after thermal storage at 250 °C for 1000 h. The EDS point analysis is performed on the *marked points*.

Table 4.1 EDS point analysis results on the *marked points* in *Fig. 4.16*.

Spectrum number	Chemical composition (at.%)		
	Ag	**Cu**	**O**
1	97.15	1.62	1.23
2	4.53	53.95	41.52
3	83.47	11.13	5.40
4	0.12	69.73	30.15
5	0.09	99.44	0.47

results come from that Cu_2O is more thermodynamically stable than CuO at low temperature [20]. As shown in Fig. 4.16 and Table 4.1, Cu oxidation layer exhibits the dual layer of Cu_2O and CuO, through the two sequential oxidation reactions as following [23]:

$$4Cu + O_2 \rightarrow 2Cu_2O$$

$$2Cu_2O + O_2 \rightarrow 4CuO$$

Fig 4.17 shows TEM BF images on the Ag/Cu interface after thermal storage time for 1000 h. The observation positions for the magnified images of Fig. 4.17(b-d) and for the HRTEM images of Fig. 4.17(e,f) were indicated in Fig. 4.14(a). The borderline of CuO and Cu_2O was inevident, as shown in Fig. 4.17(b). The formation mechanism of voids in the vicinity of Cu (Fig. 4.17d) is seemed Kirkendall void. As mentioned in *Section 4.5.1*, small amount of Cu can migrate into Ag matrix, besides the Ag was can rarely migrate into Cu matrix, because of difference of mutual solubility between Ag and Cu at 250 °C. As a result, the concentration of vacancies will gradually increases in Cu side, and then the accumulation of vacancies leads to formation of Kirkendall voids in Cu side. The two oxides, CuO (PDF no.: 01-076-7800; monoclinic symmetry; space group: C2/c; a=4.7940 Å, b=3.3620 Å, c=5.2280 Å and β=99.790°) and Cu_2O (PDF no.: 01-078-2076; cubic symmetry; space group: Pn-3m; a=4.2670 Å), can confirm by HRTEM images and corresponding FFT patterns, as shown in Fig. 4.17(e,f).

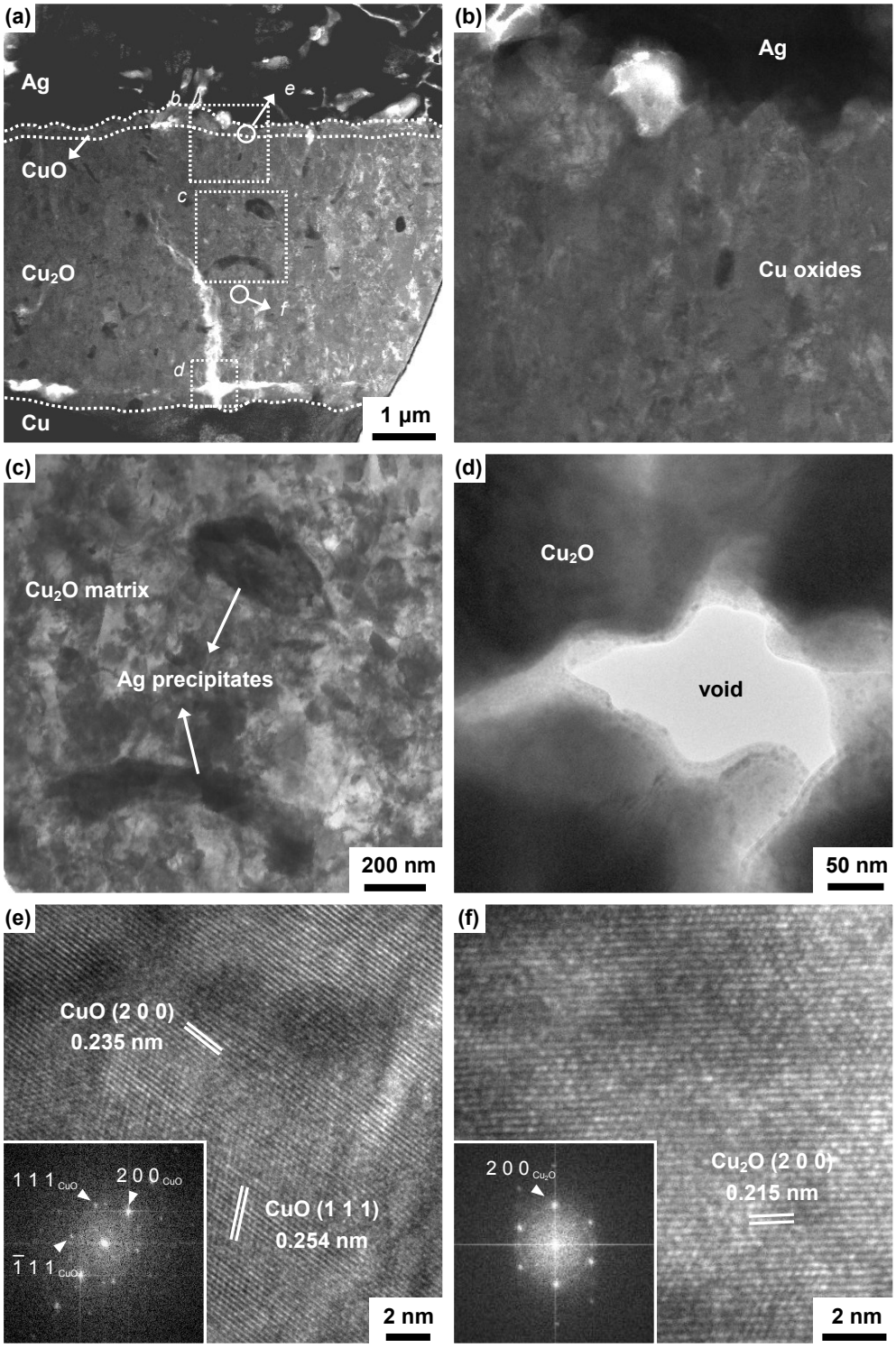

Figure 4.17 TEM BF images of **(a)** Ag/Cu interface after thermal storage for 1000 h, **(b)** interface of Ag/Cu oxides, **(c)** Ag precipitates in Cu_2O layer, **(d)** void formation near the interface of Cu_2O/Cu, and HRTEM images and corresponding FFT patterns of **(e)** CuO and **(f)** Cu_2O.

4.5.3 Interfacial reaction at the Ag/ENIG interface

Fig. 4.18 shows STEM/EDS mapping and line analysis results at the Ag/ENIG interface of as-bonded Ag NPB with ENIG substrate. Unlike the distinct interphase interface between Ag and Cu in case of bare Cu substrate, as shown in Fig. 4.13, the interphase interface between Ag and Au was ambiguous. It came from the interdiffusion of Ag and Au due to the mutual solubility in whole composition range of Ag-Au binary system [24].

Fig. 4.19 and 4.20 show EDS mapping and line analysis results at the Ag/ENIG interface of Ag NPB with ENIG finished Cu substrate after thermal storage for 500 h and 1000 h, respectively. From the EDS line analysis in Fig. 4.18-20, it can be confirmed that the Ag and Au layer was gradually mixed with increasing of thermal storage time. After thermal storage, the oxygen signal was detected at the underneath of Au layer, and it was seemed to form Ni oxide between Au and Ni(P) layer. The diffusion of Ag and Au into Ni(P) layer were not occurred even after thermal storage time for 1000 h, from the EDS line analysis in Fig. 4.18-20.

4.5.4 Formation of NiO and Ni_3P at the Au/Ni interface

Magnified STEM/EDS results shows Ni oxide layer and P-rich layer at the Au/Ni interface after thermal storage for 1000 h. P K signal is also detected in the Au region, as shown in Fig. 4.21; however, it is due to peak overlap of P K line and Au M line, as shown in Fig. 4.22. The energies of characteristic X-ray of O, P, Ni, Cu, Ag and Au are shown in Table 5.3 [25]. The energy differences between P K_α/K_β line and Au M line are 0.109 keV and 0.016 keV, respectively, which are smaller value than the energy resolution of EDS analysis. A typical energy resolution of Si(Li) detector for X-ray spectrometer is approximately 0.15 keV [8]. Further analysis with the high energy resolution will be necessary to resolve Au and P peak, for example, wavelength dispersive X-ray spectroscopy (WDS) or electron energy loss spectroscopy (EELS).

As shown in Fig. 4.23, the HRTEM image shows two phases, including NiO (PDF no.: 01-078-0423; cubic symmetry; space group Fm-3m; a=4.1790 Å) and Ni_3P (PDF no.: 01-074-1384; tetragonal symmetry; space group: I-4; a=8.9540 Å, c=4.3860 Å), were formed at the Au/Ni interface. A spotty FFT pattern of NiO, as shown in Fig. 4.23(b), indicates that NiO is nanocrystalline. The corresponding FFT pattern on the P-rich layer in Fig. 4.23(c), including a diffraction pattern of Ni_3P and a ring pattern of Ni, indicates that this layer consists of the mixture of Ni_3P and amorphous Ni.

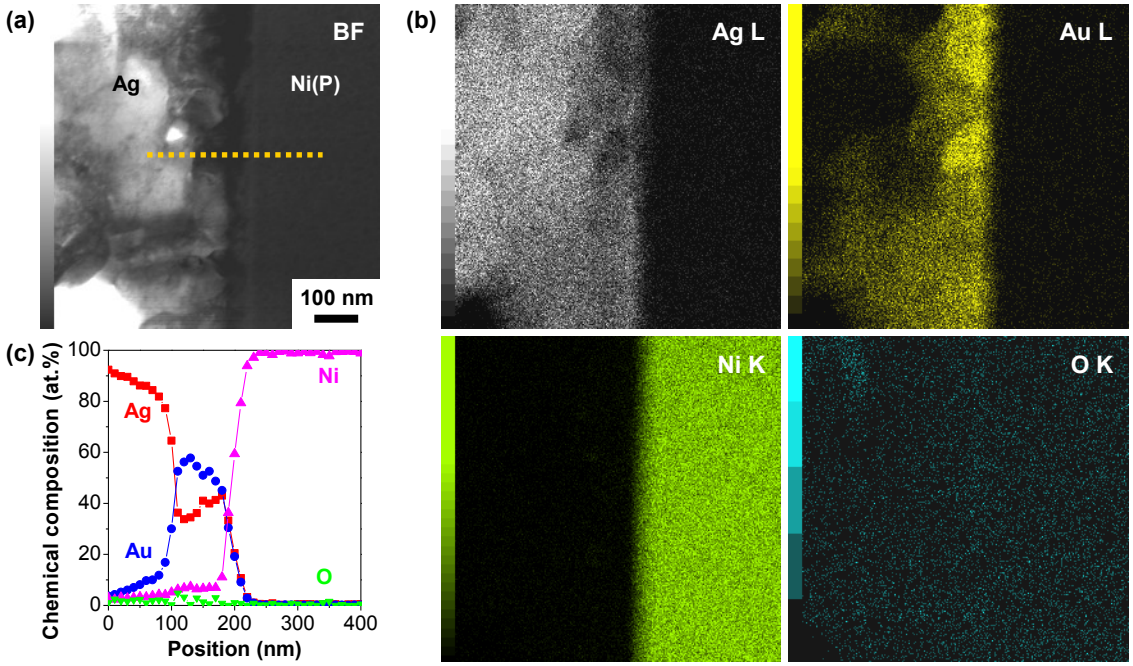

Figure 4.18 **(a)** STEM BF image and **(b)** corresponding elemental mapping results of Ag L, Au L, Ni K and O K on the Ag/ENIG interface for as-bonded Ag NPB sample with ENIG finished Cu substrate, and **(c)** EDS line analysis along the *dotted line* in BF image.

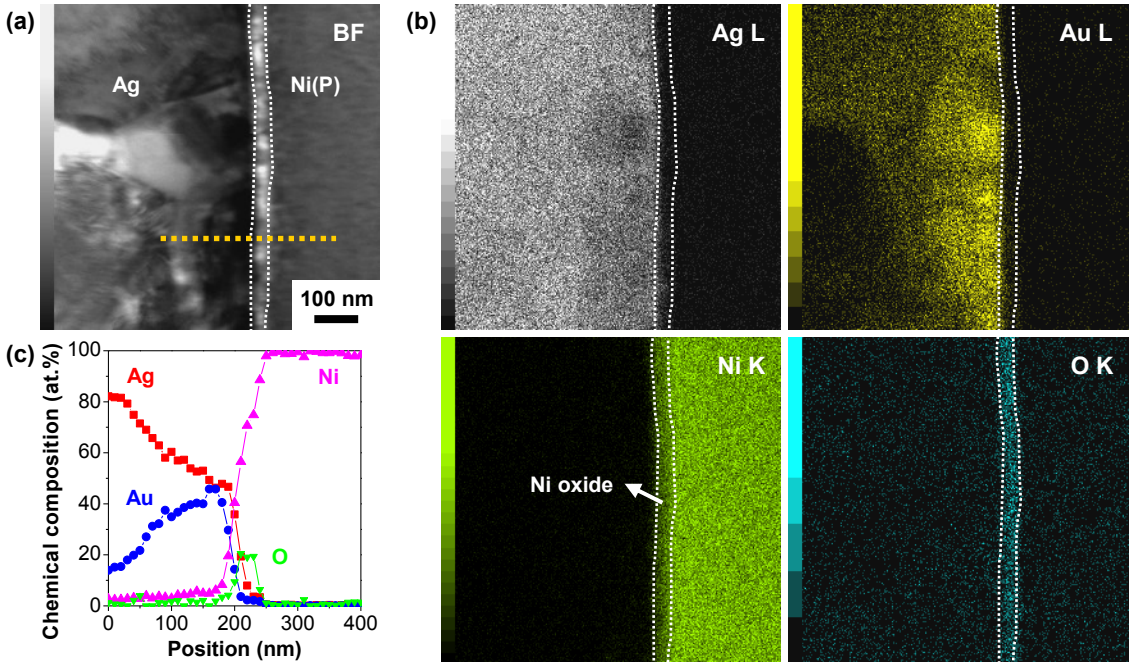

Figure 4.19 **(a)** STEM BF image and **(b)** correspond elemental mapping results of Ag L, Au L, Ni K and O K on the Ag/ENIG interface of Ag NPB sample with ENIG finished Cu substrate after thermal storage at 250 °C for 500 h, and **(c)** EDS line analysis along the *dotted line* in BF image.

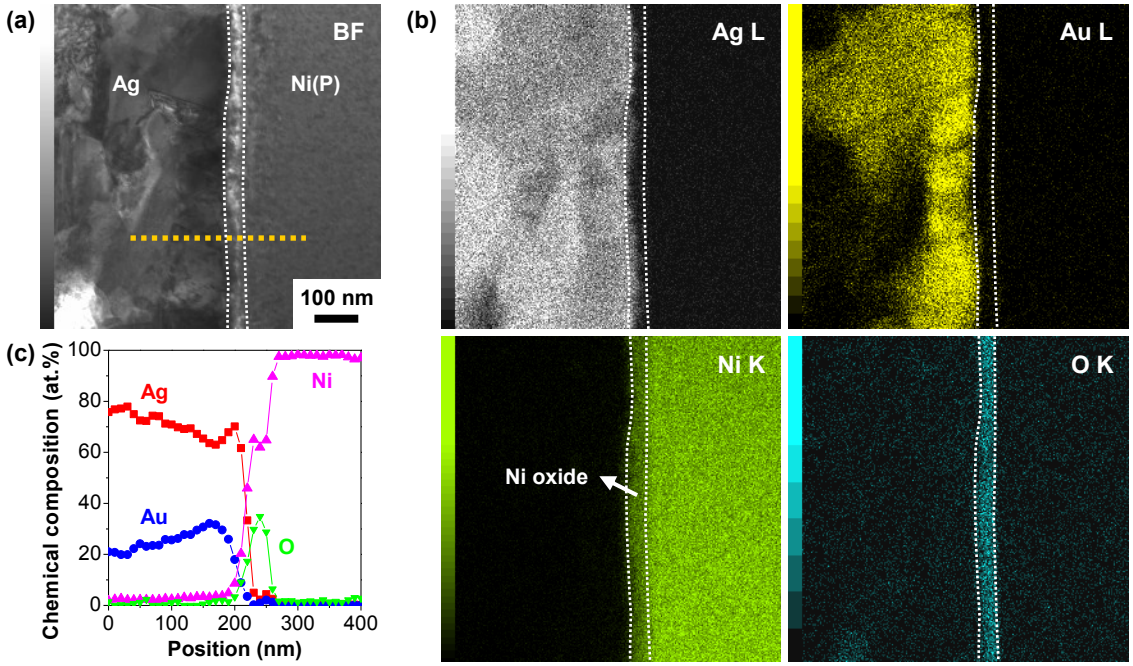

Figure 4.20 **(a)** STEM BF image and **(b)** corresponding elemental mapping results of Ag L, Au L, Ni K and O K on the Ag/ENIG interface of Ag NPB sample with ENIG finished Cu substrate after thermal storage at 250 °C for 1000 h, and **(c)** EDS line analysis along the *dotted line* in BF image

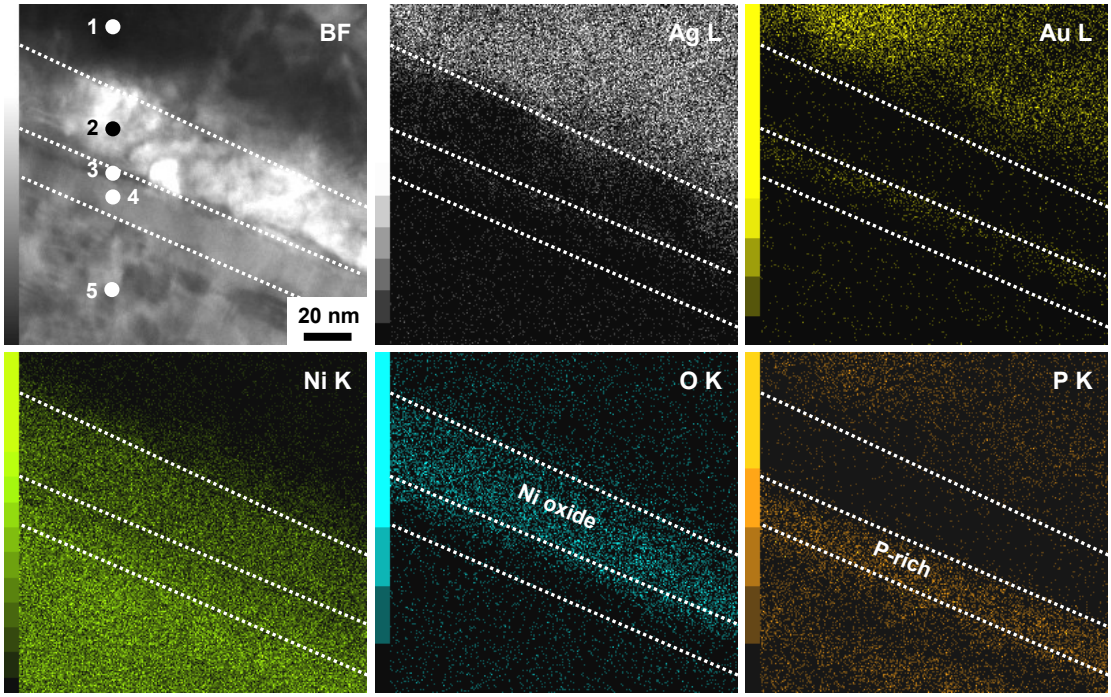

Figure 4.21 High magnification STEM BF image and corresponding elemental mapping results of Ag L, Au L, Ni K and O K on the Ag/ENIG interface of Ag NPB sample with ENIG finished Cu substrate after thermal storage at 250 °C for 1000 h. The EDS point analysis is performed on the *marked points*.

Table 4.2 EDS point analysis results on the *marked points* in *Fig. 4.21*.

Spectrum number	Chemical composition (at.%)				
	Ag	**Au**	**Ni**	**O**	**P**
1	60.01	32.02	3.00	4.97	-
2	3.00	0.01	56.12	40.88	-
3	6.72	4.92	52.62	31.63	4.11
4	1.00	0.17	80.31	1.89	16.63
5	0.71	0.04	90.11	-	9.14

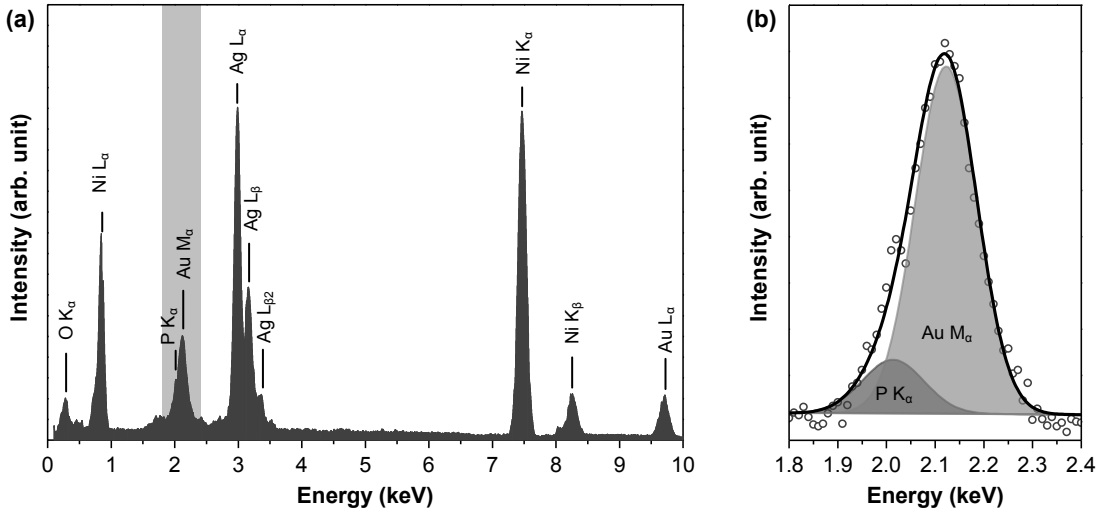

Figure 4.22 **(a)** X-ray energy spectrum for the EDS mapping of *Fig. 4.19* and **(b)** deconvolution of P K_α and Au M_α peaks on the energy level of 1.8 - 2.4 keV, denoted range as *grey box* in *(a)*.

Table 4.3 Energies of characteristic X-ray (K, L and M lines) of O, P, Ni. Cu, Ag and Au [27].

Element	Atomic number	Energies of characteristic X-ray (in keV)						
		K_α	K_β	L_α	$L_{\beta1}$	$L_{\beta2}$	L_γ	M
O	**8**	0.5429						
P	**15**	2.0137	2.1390					
Ni	**28**	7.4782	8.2647	0.8515	0.8688			
Cu	**29**	8.0478	8.9053	0.9297	0.9498			
Ag	**47**	22.1629	24.9424	2.9843	3.1509	3.3478	3.5196	0.5680
Au	**79**			9.7133	11.4423	11.5847	13.3817	2.1229

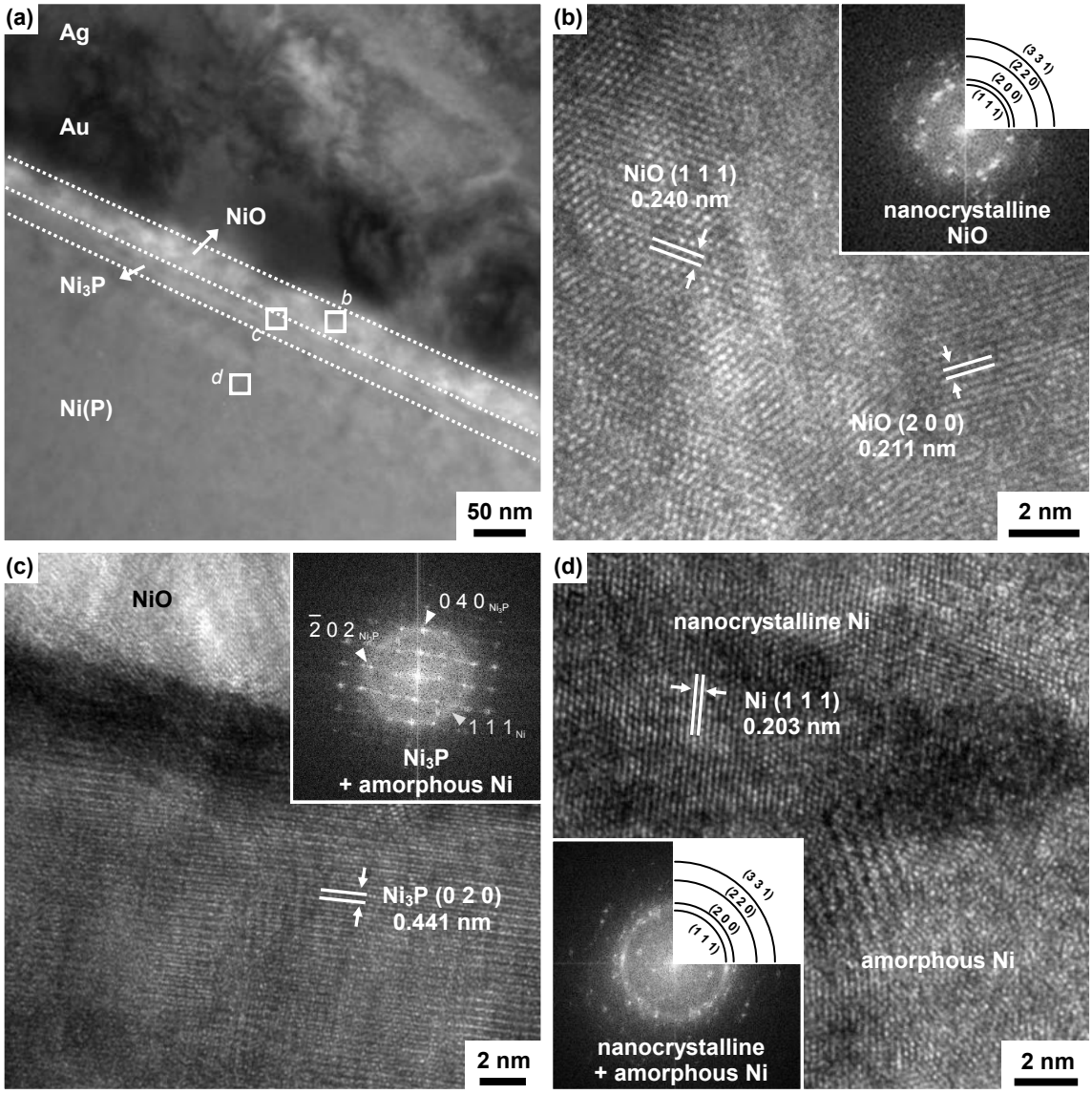

Figure 4.23 **(a)** TEM BF image of Ag/ENIG interface after thermal storage for 1000 h, and HRTEM images and corresponding FFT patterns of **(b)** NiO, **(c)** Ni_3P and **(d)** Ni(P) layer.

The Ni(P) layer shows mixture of nanocrystalline and amorphous Ni, as shown in Fig. 4.23(d). Measured values on the interplanar spacing of NiO in Fig. 4.23(b), Ni_3P in Fig. 4.23(c) and crystalline Ni in Fig. 4.23(d) from the HRTEM lattice images show good agreement with the reference data (ICDD PDF) on them.

4.5.5. Comparison of oxidation behavior between Cu and ENIG finish

The thicknesses of NiO layers formed at the Au/Ni after thermal storage for 500 h and 1000

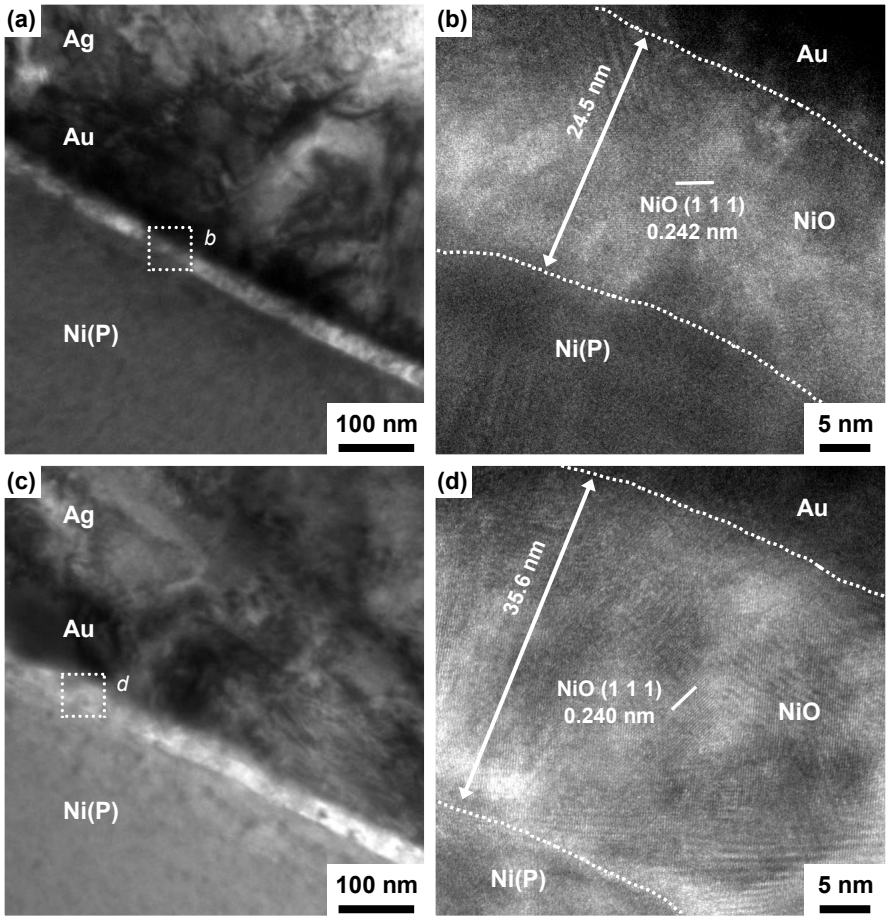

Figure 4.24 **(a)** TEM BF image of Ag/ENIG interface and **(b)** HRTEM image of NiO layer after thermal storage for 500 h. **(c)** TEM BF image of Ag/ENIG interface and **(b)** HRTEM image of NiO layer after thermal storage for 1000 h.

h exhibit approximately 24.5 nm and 35.6 nm, respectively, as shown in Fig. 4.24. The growth rate of NiO was four orders of magnitude slower than it of Cu oxides (approximately 3.65 μm after 1000 h, as shown in Fig. 4.17). Zhao et al. argued that the oxygen can permeate through porous Ag layer at relative high temperature. Their result indicated that there was no oxidation of Cu substrate at 150 °C up to 960 h, while Cu substrate was oxidized at 250 °C for 72 h [5]. Cu surface can be directly exposed to the air (permeated oxygen through Ag porous layer) during thermal storage test at 250 °C; besides Ni surface (covered with thin Au layer) is not exposed to the air directly. As a result, the growth rate of NiO is dependent on the oxygen permeability through Au layer, which is called as internal oxidation. The oxygen permeability in bulk Au (approximately 1.47×10^{-33} m^2/s at 250 °C), according to the temperature dependence of oxygen permeability reported by Kawamura et al. [26],

can be negligible. It can be infer that oxygen diffusion in Au lattice is frozen at 250 °C; and can be classified type C kinetic regime according to Harrison's classification for diffusion kinetics in polycrystalline materials [27]. In this regime, oxygen can migrate only along the grain boundary of Au layer. The immersion Au layer exhibits columnar grain structure with grain size of tens of nanometer scale [28], which can act as a diffusion path of oxygen and Ni through Au layer. Unfortunately, there is no report on the kinetics of internal oxidation through the grain boundary of Au layer at low temperature.

From the results of this study, ENIG surface finish can impede the degradation by oxidation at the interface compared with bare Cu substrate; however cannot completely prevent the oxidation. For the better stability of Ag NPB joint at high temperature, an electroless nickel/electroless palladium/immersion gold (ENEPIG) is seemed to be possible solution to prevention of oxidation due to the presence of amorphous Pd interlayer. The amorphous Pd interlayer successfully act as a diffusion barrier of Ni or O at 150 °C for 200 h, because of the lack of grain boundaries [28].

4.6 Microstructure evolution at the Ag/Cu and Ag/ENIG interfaces

As shown in Fig. 4.25, it is possible to describe comprehensively on the microstructure evolution at the interface of Ag NPB joint after thermal storage test, from the change of microstructure and elements distribution at the interface of Ag/Cu and Ag/ENIG (Fig. 4.13-4.24). After thermal storage test, the interface of Ag and Cu are distinct due to limited mutual solubility between Cu and Ag. The CuO and Cu_2O were formed at the surface of Cu substrate. Kirkendall voids in the vicinity of Cu was heavily formed. The brittle Cu oxide and Kirkendall voids act as a weak point to propagate the crack easily. Meanwhile, Ag and Au in case of Ag with ENIG finished Cu substrate, Au was disolved into Ag layer by thermal storage test. The diffusion of Ag and Au into Ni(P) layer was limited due to the limited solubility of Ag and Au in Ni(P). The NiO and Ni_3P were formed between Au and Ni(P) layer. Small amount of voids, which is seemed Kirkendall voids, were also formed at the interface of NiO and Ni_3P. The interface of NiO and Ni_3P act a weak point. Consequentially, the oxidation of substrates (Cu; and Ni in ENIG finish) and the formation of Kirkendall voids are seemed the cause for the degradation of Ag NPB joint.

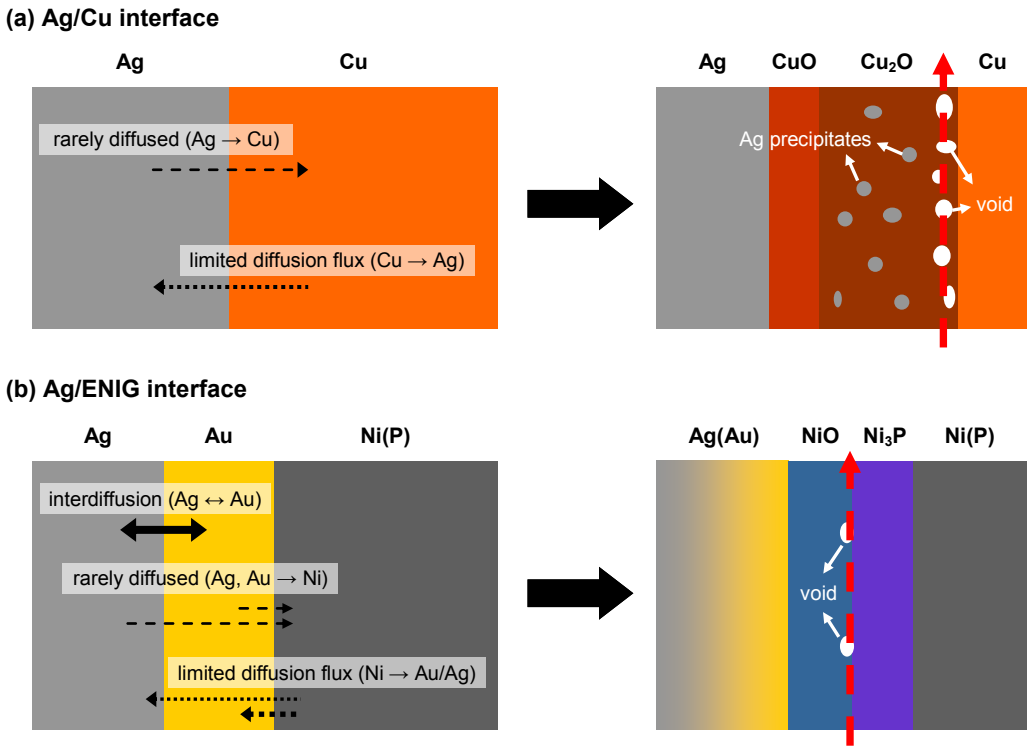

Figure 4.25 Schematic diagram of microstructure evolution at the interface of Ag nanoporous bonding joint after thermal storage: **(a)** Ag/Cu interface and **(b)** Ag/ENIG interface. The thicknesses of each layers are not to scale. There are three types of diffusion flux of each elements which are indicated as *line arrows* (mutual diffusion flux), *dotted arrows* (limited diffusion flux due to limited solubility in the matrix) and *broken arrows* (rare diffusion), where the thickness of each arrows is proportional to amount of diffusion flux.

4.7 Conclusion

The change of shear strength, fracture morphology and microstructure evolution of Ag nanoporous bonding joint with bare Cu and ENIG finished Cu during thermal storage test at 250 °C were investigated. The aspect of fracture varied with increasing thermal storage time, where the area of Au layer delamination in case of ENIG and interfacial failure in case of bare Cu increased. The results of shear test of as-bonded Ag NPB joints with ENIG finished Cu and bare Cu substrates show 25.7 and 26.6 MPa. The effect of surface finish became significant with increasing of aging time. In case of bare Cu substrate, the shear strength gradually decreased with increasing of thermal storage time, and it showed 11.4 MPa with the aging time of 1000 h. Contrariwise, the shear strength of NPB

with the ENIG finished substrate increased to 32.2 MPa for 100 h, and then gradually decreased. After 750 h, the shear strength showed 25.3 MPa, which is similar value with the initial shear strength of NPB. The effects of substrate on the degradation rate of Ag NPB joint were slightly different. These results arise from the different oxidation behavior of bare Cu and ENIG finished substrates. The oxidation of Ni and Cu seem to lead the Au delamination of ENIG finished Cu joint and interfacial fracture of bare Cu joint.

References

[1] H. Xu, C. Liu, V.V. Silberschmidt, S.S. Pramana, T.J. White, Z. Chen, V.L. Acoff, "Behavior of aluminum oxide, intermetallics and voids in Cu–Al wire bonds", *Acta Mater.*, **59** (2011) 5661–5673.

[2] S.W. Park, S. Nagao, T. Sugahara, K.S. Kim, K. Suganuma, "Retarding intermetallic compounds growth of Zn high-temperature solder and Cu substrate by trace element addition", *J. Mater. Sci. Mater. Electron.*, **24** (2013) 4704–4712.

[3] Y. Yang, J.N. Balaraju, Y. Huang, H. Liu, Z. Chen, "Interface reaction between an electroless Ni–Co–P metallization and Sn–3.5Ag lead-free solder with improved joint reliability", *Acta Mater.*, **71** (2014) 69–79.

[4] S.A. Paknejad, G. Dumas, G. West, G. Lewis, S.H. Mannan, "Microstructure evolution during 300°C storage of sintered Ag nanoparticles on Ag and Au substrates", *J. Alloy. Compd.*, **617** (2014) 994–1001.

[5] S.-Y. Zhao, X. Li, Y.-H. Mei, G.-Q. Lu, "Study on high temperature bonding reliability of sintered nano-silver joint on bare copper plate", *Microelectron. Reliab.*, **55** (2015) 2524–2531.

[6] JEDEC standard, *JESD22-A103D: High temperature storage life*, 2010.

[7] D.A. Porter, K.E. Easterling, *Phase transformations in metals and alloys*, 2nd edition, Nelson Thornes, Cheltenham, 1992.

[8] D.B. Williams, C.B. Carter, *Transmission electron microscopy: A textbook for materials science*, 2nd edition, Springer, New York, 2009.

[9] W.-H. Li, P.-S. Lin, C.-N. Chen, T.-Y. Dong, C.-H. Tsai, W.-T. Kung, J.-M. Song, Y.-T. Chiu, P.-F. Yang, "Low-temperature Cu-to-Cu bonding using silver nanoparticles stabilised by saturated dodecanoic acid", *Mater. Sci. Eng. A*, **613** (2014) 372–378.

[10] Y. Akada, H. Tatsumi, T. Yamaguchi, A. Hirose, T. Morita, E. Ide, "Interfacial bonding mechanism using silver metallo-organic nanoparticles to bulk metals and observation of sintering behavior, *Mater. Trans.*, **49** (2008) 1537–1545.

[11] T. Ogura, M. Nishimura, H. Tatsumi, W. Takahara, A. Hirose, "Interfacial bonding behavior between silver nanoparticles and gold substrate using molecular dynamics simulation", *Mater. Trans.*, **53** (2012) 2085–2090.

[12] E. Ide, A. Hirose, K.F. Kobayashi, "Influence of bonding condition on bonding process using Ag metallo-organic nanoparticles for high temperature lead-free packaging", *Mater. Trans.*, **47** (2006) 211–217.

[13] Y. Shi, W. Fang, Z. Xia, Y. Lei, F. Guo, X. Li, "Investigation of rare earth-doped BiAg high-temperature solders", *J. Mater. Sci. Mater. Electron.*, **21** (2010) 875–881.

[14] US Military Standard, *MIL-STD-883G, Method 2019.7: Die shear strength*, 2003.

[15] K.A. Jackson, *Kinetic processes: Crystal growth, diffusion, and phase transitions in materials*, 2nd edition, Wiley-VCH, Weinheim, 2010.

[16] P.R. Subramanian, J.H. Perepezko, "The Ag-Cu (silver-copper) system", *J. Phase Equilibria*, **14** (1993) 62–75.

[17] D. Liu, W.A. Miller, K.T. Aust, "Diffusion induced grain boundary migration and recrystallization during oxidation of a Ni-48.5 pct Cu alloy", *Metall. Trans. A*, **19** (1988) 1667–1675.

[18] M. Zhu, Z.F. Wu, M.Q. Zeng, L.Z. Ouyang, Y. Gao, "Bimodal growth of the nanophases in the dual-phase composites produced by mechanical alloying in immiscible Cu–Ag system", *J. Mater. Sci.*, **43** (2008) 3259–3266.

[19] L. Schramm, G. Behr, W. Löser, K. Wetzig, "Thermodynamic Reassessment of the Cu-O Phase Diagram", *J. Phase Equilibria Diffus.*, **26** (2005) 605–612.

[20] W. Gao, H. Gong, J. He, A. Thomas, L. Chan, S. Li, "Oxidation behaviour of Cu thin films on Si wafer at 175 – 400 °C", *Mater. Lett.*, **51** (2001) 78–84.

[21] N.A.M. Shanid, M.A. Khadar, "Evolution of nanostructure, phase transition and band gap tailoring in oxidized Cu thin films", *Thin Solid Films*, **516** (2008) 6245–6252.

[22] I.C. Cheng, A.M. Hodge, "Morphology, oxidation, and mechanical behavior of nanoporous Cu foams", *Adv. Eng. Mater.*, **14** (2012) 219–226.

[23] X. Jiang, T. Herricks, Y. Xia, "CuO nanowires can be synthesized by heating copper substrates in air", *Nano Lett.*, **2** (2002) 1333–1338.

[24] R.P. Elliott, F.A. Shunk, “The Ag-Au (silver-gold) system”, *Bull. Alloy Phase Diagr.*, **1** (1980) 45–47.

[25] J.A. Bearden, “X-ray wavelengths”, *Rev. Mod. Phys.*, **39** (1967) 78–124.

[26] K. Kawamura, T. Kajino, M. Nanko, T. Maruyama, “Oxygen permeability in gold by internal oxidation of gold alloy”, in: E. Opila, P. Hou, T. Maruyama, B. Pieraggi, D. Shifler, E. Wuchina (Eds.), *High temperature corrosion and materials chemistry IV*, The Electrochemical Society, Pennington, pp. 107–116, 2003.

[27] L.G. Harrison, “Influence of dislocations on diffusion kinetics in solids with particular reference to the alkali halides”, *Trans. Faraday Soc.*, **57** (1961) 1191–1199.

[28] C.C. Li, W.L. Shih, C.K. Chung, C.R. Kao, “Amorphous Pd layer as a highly effective oxidation barrier for surface finish of electronic terminals”, *Corros. Sci.*, **83** (2014) 419–422.

Chapter 5

Reliability of Ag nanoporous die attach under temperature cycling

5.1 Introduction

Automotive electronics are exposed to various detrimental environments, such as extreme temperature fluctuation, corrosive atmosphere and vibration. Reliability of electronics is generally defined as the life-time while maintaining its functions during usage under these environments. A temperature cycling test has been generally performed in order to examine the durability of die attach for high temperature electronics on the thermal stress induced by coefficient of thermal expansion (CTE) mismatch between the dissimilar materials under temperature fluctuation. So, it is necessary to investigate on the long-term reliability of Ag NPB joint under temperature cycling for the replacement of high temperature Pb-5Sn solder.

The temperature cycling tests on the Sn-based solder joint have been extensively carried out under various temperature swing conditions, where dealt with from the determination of life time of solder joint to failure mechanism [1,2]. The failure criterion of solder joint for the electrical interconnection has been established in industrial standards. Specifically, the “failure” is defined the first event of exceeding electrical resistance over 1000 Ω in IPC-9701 standard [3]. Meanwhile the failure criterion of die attach is not established clearly. A principal function of die attach is a mechanical bonding between semiconductor and substrate, as mentioned in *Section 1.2.2*. It also can

be act as a thermal pass for the dissipation of heat generation from the Si/SiC power semiconductors in order to reduce the junction temperature. Thus, the joint strength and thermal conductivity of joint can be the evaluation factors for the assessment of die attach reliability [4].

In this chapter, the reliability test of Ag NPB joint with bare Si chip on an active metal brazed (AMB) Cu Si_3N_4 substrate under temperature cycling from -55 °C to 150 °C up to 1500 cycles was performed. The long-term reliability of Ag NPB joint was estimated in terms of shear strength change after temperature cycling. The comparative consideration on the variation of shear strength after temperature cycling test from the literatures on the high temperature solders and Ag nanoparticles sintered joint was also presented.

5.2 Experimental

5.2.1 Ag nanoporous bonding process

Ag nanoporous sheet was fabricated by dealloying method in 2M hydrochloric acid solution from Al-20at.%Ag precursor. The dealloying treatment was conducted for 3 h for 75 °C. The detailed information on the microstructure, phase constitution of Al-Ag precursor and dealloyed Ag nanoporous sheet has been given in the *Chapter 2* and *Chapter 3*.

The schematic diagram of Ag NPB process with Si chip and AMB Cu Si_3N_4 substrate is shown in Fig. 5.1. The bare Si chip (3 mm × 3 mm × 0.4 mm) with the backside metallization of Ti/Ni (P)/Au, and Si_3N_4 substrate (10 mm × 10 mm × 0.635 mm) with the double-side AMB Cu electrodes (8 mm × 8 mm × 0.3 mm) with electroless Ni/immersion Au (ENIG) finish purchased from Denka were used for the examination of temperature cycling test, as shown in Fig. 5.1(a). The thickness of Ti, Ni(P) and Au in the backside metallization of Si chip were 100 nm, 2 μm and 50 nm, respectively, and the thickness of Au and Ni(P) in the surface finish of AMB Cu Si_3N_4 substrate were 50 nm and 2 μm, respectively, as shown in Fig. 5.1(b). Ti, Ni(P) and Au were adopted as an adhesion layer, a diffusion barrier and an oxidation prevention layer, respectively.

Before the bonding process, Si chip and Si_3N_4 substrate were rinsed with acetone for 5 min in order to eliminate surface contaminations. The Ag nanoporous sheet was inserted between Si chip and AMB Si_3N_4 substrate. A graphite rubber sheet was placed on the top of joint to avoid the damage to Si chip resulting from the applied pressure during bonding process. The Ag NPB process was performed by a thermo-compression bonding system with double-side graphite heating plates at 300

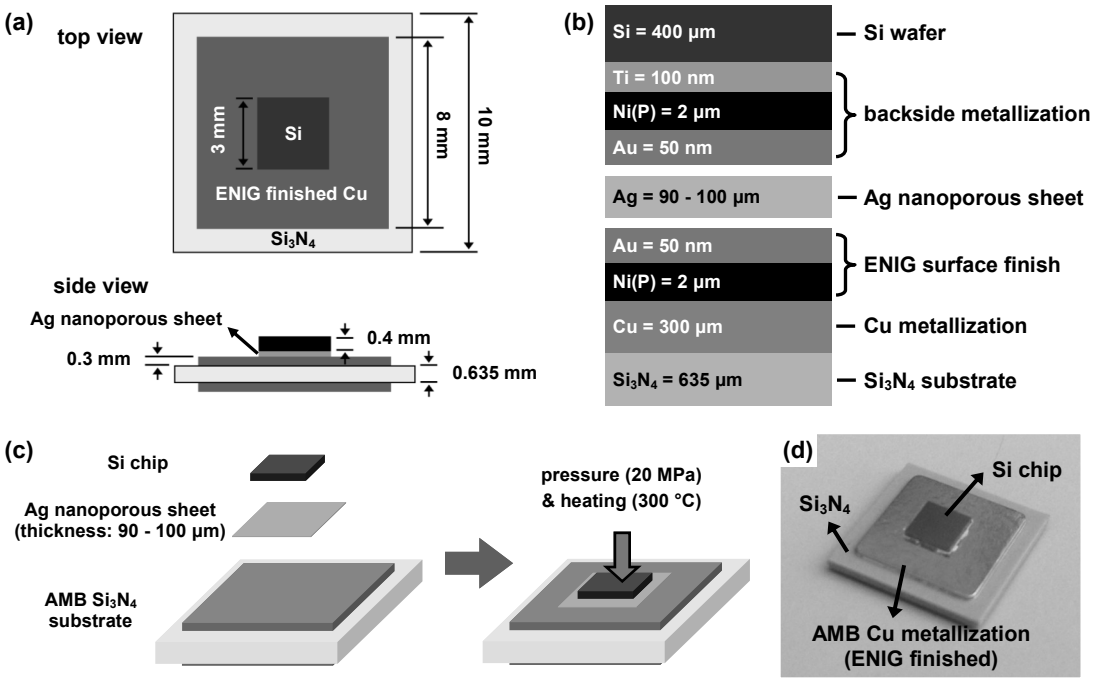

Figure 5.1 Schematic diagrams of **(a)** sample configuration of Ag nanoporous bonding joint with Si chip and active metal brazed (AMB) Cu silicon nitride (Si_3N_4) substrate, **(b)** structures of Si chip with Ti/Ni(P)/Au backside metallization and electroless Ni/immersion Au (ENIG) finished AMB Cu Si_3N_4 substrate, **(c)** thermo-compression Ag nanoporous bonding process, and **(d)** appearance of Si attached on the AMB Cu Si_3N_4 substrate.

°C for 30 min, as shown in Fig. 5.1(c). The applied pressure was 20 MPa, which was controlled using an air compressor. The final appearance of Ag NPB die attach with the Si and the AMB Si_3N_4 substrate was shown in Fig. 5.1(d).

5.2.2 Temperature cycling test

Temperature cycle test was carried out in the temperature test chamber (VCS 7027-15, Vötsch) up to 1500 cycles in accordance with the joint electron device engineering council (JEDEC) standard for temperature cycling (JESD22-A104E), test condition H (temperature cycle from –55 °C to 150 °C) [5]. The nominal minimum soaking temperature (T_{min}) and maximum soaking temperature (T_{max}) were -55 °C and 150 °C (temperature variation, ΔT = 205 °C). The nominal soaking time at T_{max} and T_{min} was 10 min and; the heating and cooling rate was 15 °C/min. The temperature profile on the nominal and the measured temperatures during temperature cycling is shown in Fig. 5.2. The nominal and measured temperature cycling conditions are given in Table. 5.1. The measured

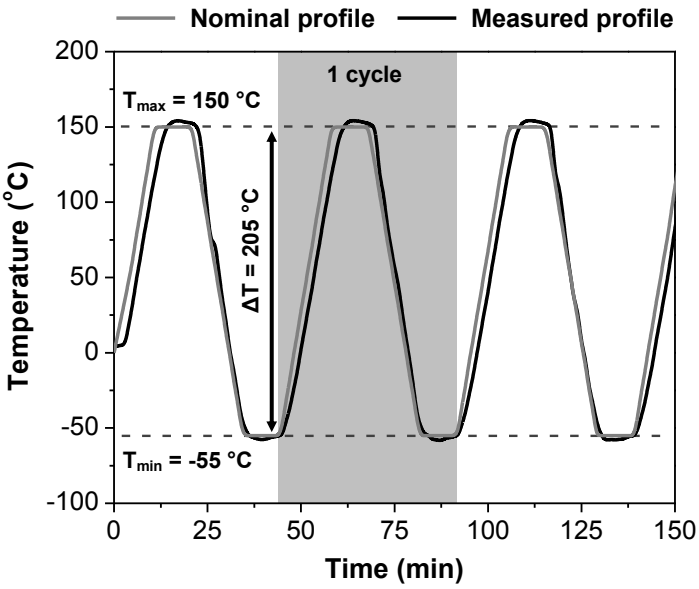

Figure 5.2 A temperature profile of temperature cycling test (temperature swing range from –55 °C to 150 °C, ΔT = 205 °C) according to JEDEC standard (JESD22-A104E). *Grey* and *black lines* in the graph indicate the nominal and the measured temperature inside of the cycling chamber, respectively.

Table 5.1 Nominal and measured temperature cycling conditions.

Parameters	Nominal values	Measured values
T_{max}	150 °C	154.2 °C
T_{min}	- 55 °C	- 57.5 °C
Heating rate	15 °C/min	14.28 ± 0.11 °C/min
Cooling rate	-15 °C/min	-15.63 ± 0.19 °C/min
Soak time at T_{max}	10 min	8 min 2 s ± 10 s
Soak time at T_{min}	10 min	8 min 26 s ± 14 s

temperature variation well meets the tolerance temperatures (+10 °C for T_{max} and -10 °C for T_{min}).

5.2.3 Characterization methods

In order to examine an occurrence of some defects, such as voids or cracks, at the Ag NPB joint by thermal stress, a nondestructive inspection of die attach was carried out using scanning acoustic tomograph (SAT, FS300III, Hitachi) with a high frequency transducer (frequency: 200 MHz,

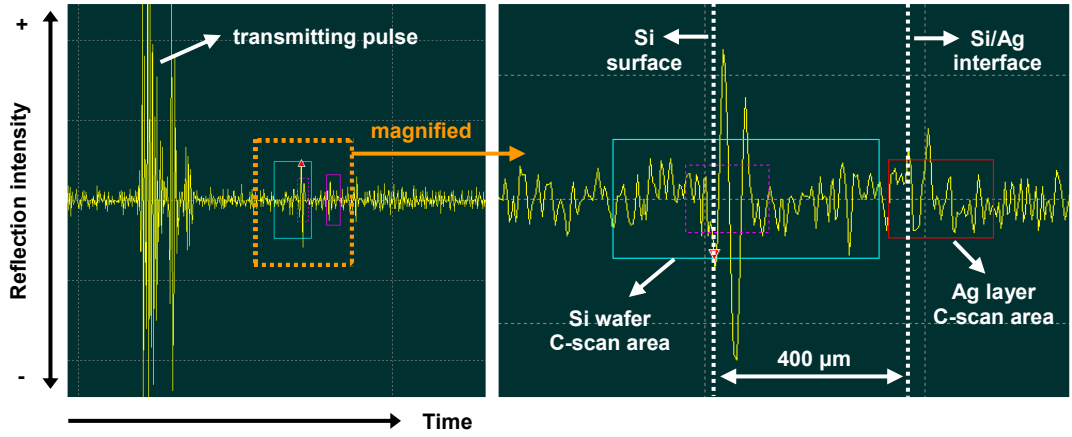

Figure 5.3 Scanning acoustic tomography (SAT) ultrasonic reflection signal (A-scan) for Si die attach using Ag nanoporous sheet and magnified signal for the designating detecting depth for 2-dimensional plane image (C-scan).

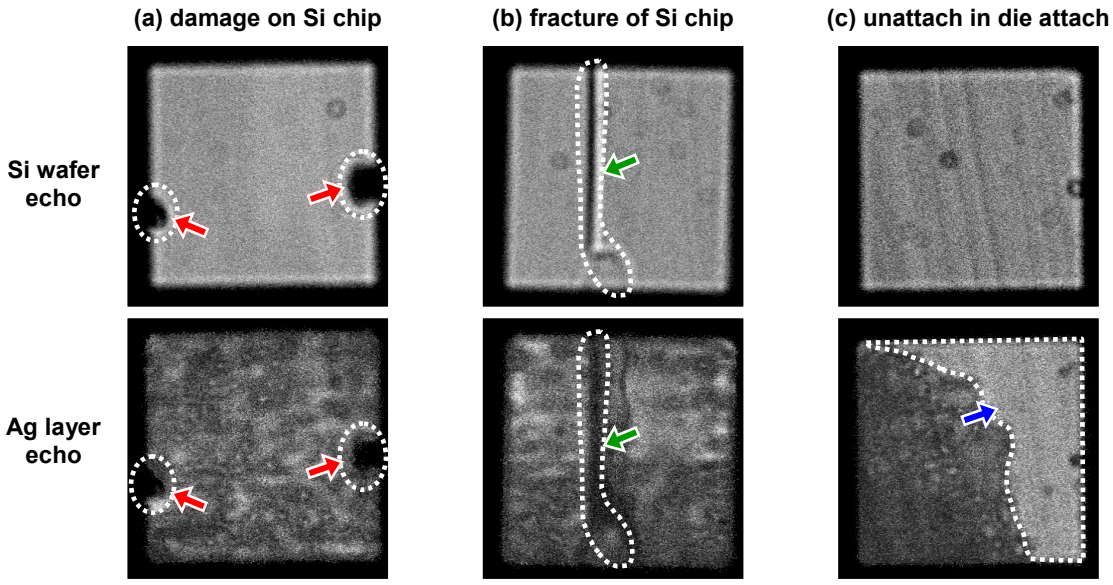

Figure 5.4 Typical illustrations on the detectable defects using SAT: **(a)** damage on Si chip indicated with *red arrows*, **(b)** fracture of Si chip indicated with *green arrows* and **(c)** unattach or delamination between Si and die attach indicated *blue arrow*.

focal distance: 6.9 mm) before and after temperature cycling test. The position of the interface between two dissimilar materials with different or air gap can be detected through the ultrasonic reflection intensity (acoustic impedance) as a function of time, called as A-scan mode, as shown in Fig. 5.3. The first reflection signals on the Si wafer denoted as a *green colored box* and Ag layer denoted as a *red colored box* in Fig. 5.3 were selected for the 2-dimensional plane scanning images,

called as C-scan mode. The typical Si wafer reflection images by SAT inspection, as shown in Fig. 5.4, can provide information on the damage of Si wafer (Fig. 5.4(a)) or the fracture of Si wafer (Fig. 5.4(b)) and tiny surface contaminations on the Si surface. The Ag layer reflection images were affected by these defects of Si wafer as shown in Fig. 5.4(a,b). The unattach or delamination at the interface also can be confirmed, as shown in Fig. 5.4(c).

Shear strength of Ag NPB joint was measured using die shear tester (STR-1000, Rhesca) with a shear rate of 1 mm/min and a shear height of 80 μm from the surface. The fracture surfaces of Ag NPB after temperature cycling test was examined using an electron probe microanalyzer (EPMA, JXA-8530F, JEOL) with an acceleration voltage of 15 kV, a scanning electron microscope (SEM, SU-70, Hitachi) with an acceleration voltage of 10 kV and focused ion beam (FIB, JIB-4500, JEOL) with an acceleration voltage of 30 kV.

5.3 Stability of Ag nanoporous bonding layer after temperature cycling

5.3.1 Non-destructive inspection on the Si wafer and Ag layer

There are two possible causes of crack propagation in the Si chip. One is the excessive pressure during the bonding process. The non-uniform or excessive compression stress can cause the crack of Si due to the fragile nature of Si wafer. Another one is crack propagation in the Si chip induced by thermal stress during temperature cycling test [6]. During the temperature swing, a large stress is generated at the joint, resulting from the CTE mismatch between the Si wafer and the bonding material/substrate. There was no evidence of crack occurred in the Si chip, despite after temperature cycling up to 1500 cycles.

Meanwhile, the bonding layer reflection image using SAT inspection can provide information on the void or crack propagation after temperature cycling, as shown in Fig. 5.5. In this time, the bonding layer reflections exhibit partially different contrast, regardless of number of temperature cycle. In the case of as-bonded condition, the white area was seemed to be observed due to the porous part of Ag layer, as mentioned in *Chapter 3*. Before 1000 cycles, as shown in Fig. 5.5(a-d), there was no clear evidence of Ag layer delamination before 100 cycles. After 1000 and 1500 cycles, as shown in Fig. 5.5(e,f), the delamination of bonding layer was partially observed at the corner of bonding layer. Mei et al. [7] have been reported that the maximum thermal stress of Ag sintered joint induced by temperature cycling is mainly generated at the corner of joint using finite

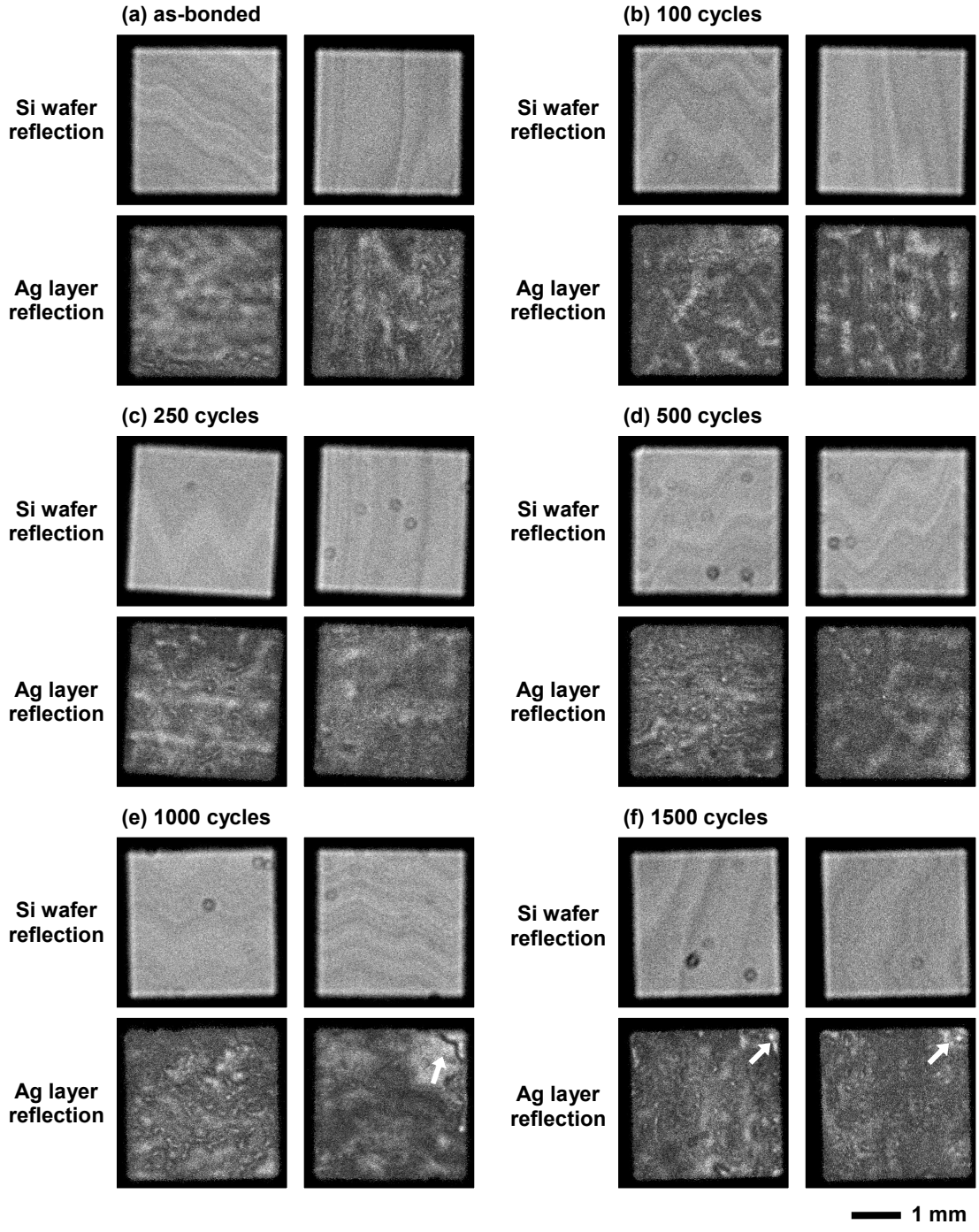

Figure 5.5 SAT 2-dimensional plane scanning (C-scan) images on the Si wafer and Ag layer reflections of the Ag nanoporous bonding joint of **(a)** as-bonded; and after temperature cycling test for **(b)** 100 cycles, **(c)** 250 cycles, **(d)** 500 cycles, **(e)** 1000 cycles and **(f)** 1500 cycles. *Inset white arrows* indicate the delamination at the Ag bonding layer.

element method. Navarro et al. [6] have also been showed that the maximum normal stress is generated at the corner of bonding interface; and it sharply decreased to get closer to the center of joint at 275 °C. It seems reasonable that the fracture at the Ag porous bonding layer initiates at the corner of joint. Nevertheless, the delamination of Ag layer was not significant up to 1500 cycles.

5.3.2 Shear strength of Ag NPB and fracture mode after temperature cycling

Fig. 5.6 shows the change of shear strength of Ag NPB joint after temperature cycling test. The shear strength of as-bonded Ag NPB joint exhibits approximately 22 MPa. It is almost same value with the shear strength of Ag NPB with ENIG finished Cu disk, as shown in *Section 3.4.1*, and it of Pb -5Sn die attach [8]. They show no significant change on the average value of shear test results up to 1500 cycles compared with it of as-bonded Ag NPB joint. Furthermore, there is no serious crack propagation in the Ag layer. It can be judged that the Ag NPB joint can withstand under temperature cycle from -55 °C to 150 °C up to 1500 cycles, from the SAT inspection (Fig. 5.5) and shear test results (Fig. 5.6). The individual shear test results are also presented as a dot and classified according to fracture mode of each samples. The crack was mainly propagated along the Si, metallization of Si and Ag layer, as shown in Fig. 5.7.

The typical fracture surface images on the substrate side of Ag NPB joint after temperature cycling are shown in Fig. 5.8, where the samples in the upper row numbering by odd number exhibited higher shear strength and the samples in bottom row numbering by the even number exhibited lower shear strength for each number of cycles. The fracture mode was determined by the area fraction of each fracture location. The criterion of area fraction for classification was 5%. For example, the area fractions Ag layer fracture, Si fracture and metallization fracture of *sample 1* exhibit 5.71%, 21.02% and 73.27%, respectively, as shown in Fig. 5.8(a). So, it can be classified in Ag/Si/metallization mixed fracture. In case of *sample 2*, the area fractions of Si fracture and metallization fracture exhibit 2.85% and 97.15%, respectively, as shown in Fig. 5.8(a). So, it can be classified in metallization dominant fracture.

The fracture mode could be classified into 5 types, including Ag layer dominant (indicated as black squares), metallization dominant (red circles), Ag/Si mixed (blue triangles), Si/metallization mixed (green diamonds), Ag/Si/metallization mixed (pink stars), as shown in Fig. 5.6 and Fig. 5.8. The fracture modes of as-bonded Ag NPB joint exhibit almost Ag layer dominant fracture. The samples which demonstrate Ag layer fracture, Ag/Si mixed fracture or Ag/Si/metallization mixed

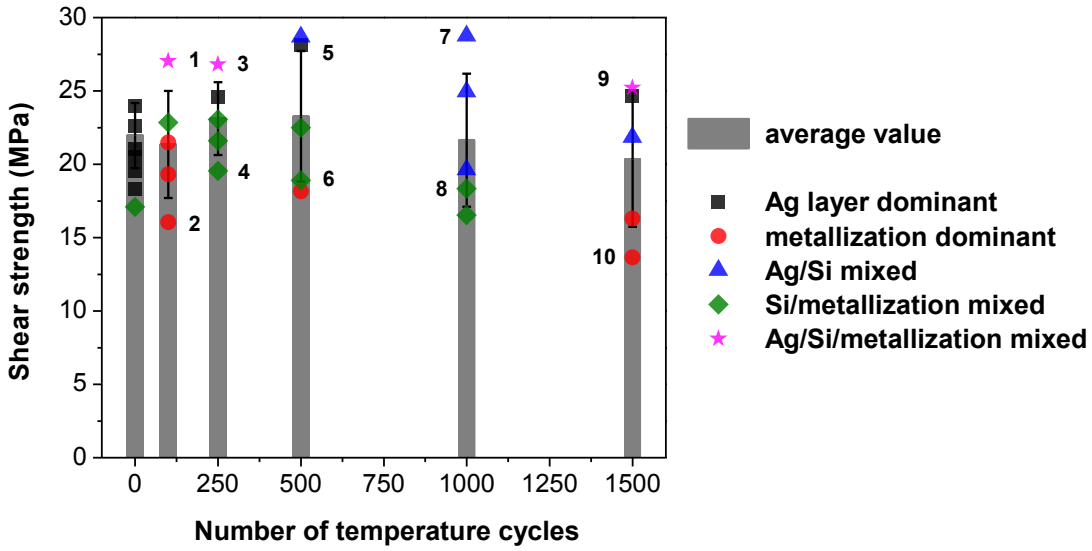

Figure 5.6 The variation of shear strength of Si die attach on the AMB Cu Si_3N_4 substrate after temperature cycling test. *Inset number marks (1-10)* are corresponding with fracture surface images in *Fig. 5.7*. The odd and even numbered sample exhibit higher and lower shear strength for each temperature cycling, respectively.

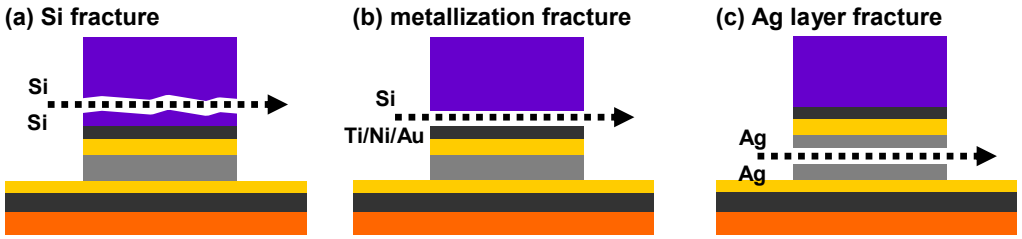

Figure 5.7 Schematic diagram of fracture modes of Ag nanoporous bonding joint after temperature cycling test: **(a)** Si fracture, **(b)** metallization fracture and **(c)** Ag layer fracture.

fracture, tend to show higher shear strength compared with the average value. Besides, the samples which demonstrate metallization layer delamination or Si/metallization mixed fracture, tend to show lower shear strength compared with the average value.

5.4 Fracture behavior of Ag NPB after temperature cycling test

5.4.1 Macroscopic element distribution in the fracture surface

Fig. 5.8 and 5.9 show typical EPMA elemental distribution (Ag, Ag, Ni, Ti, Si and O) at the fracture surface of substrate sides and Si sides after temperature cycling test. The high Ni and Ti

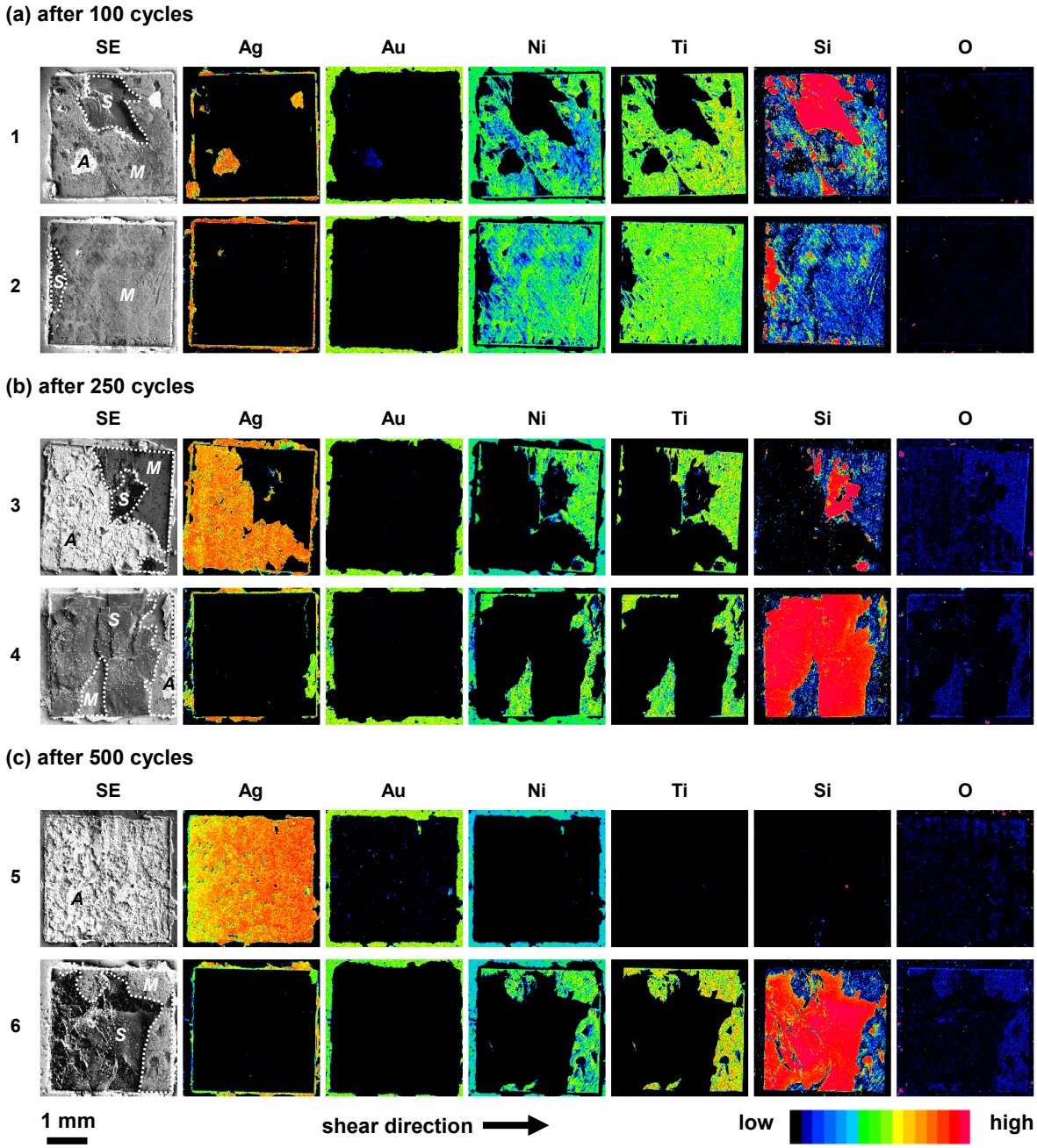

Figure 5.8 Electron probe micro-analyzer (EPMA) element mapping results (Ag, Au, Ni, Ti, Si and O) on the fracture surface (substrate side) of Ag nanoporous bonding joint after temperature cycling for **(a)** 100 cycles, **(b)** 250 cycles, **(c)** 500 cycles, **(d)** 1000 cycles and **(e)** 1500 cycles. The sample numberings are correspond with marked in *Fig. 5.6*. The marked regions on the SE images with *A*, *S* and *M* indicate Ag layer fracture, Si fracture and metallization delamination, respectively.

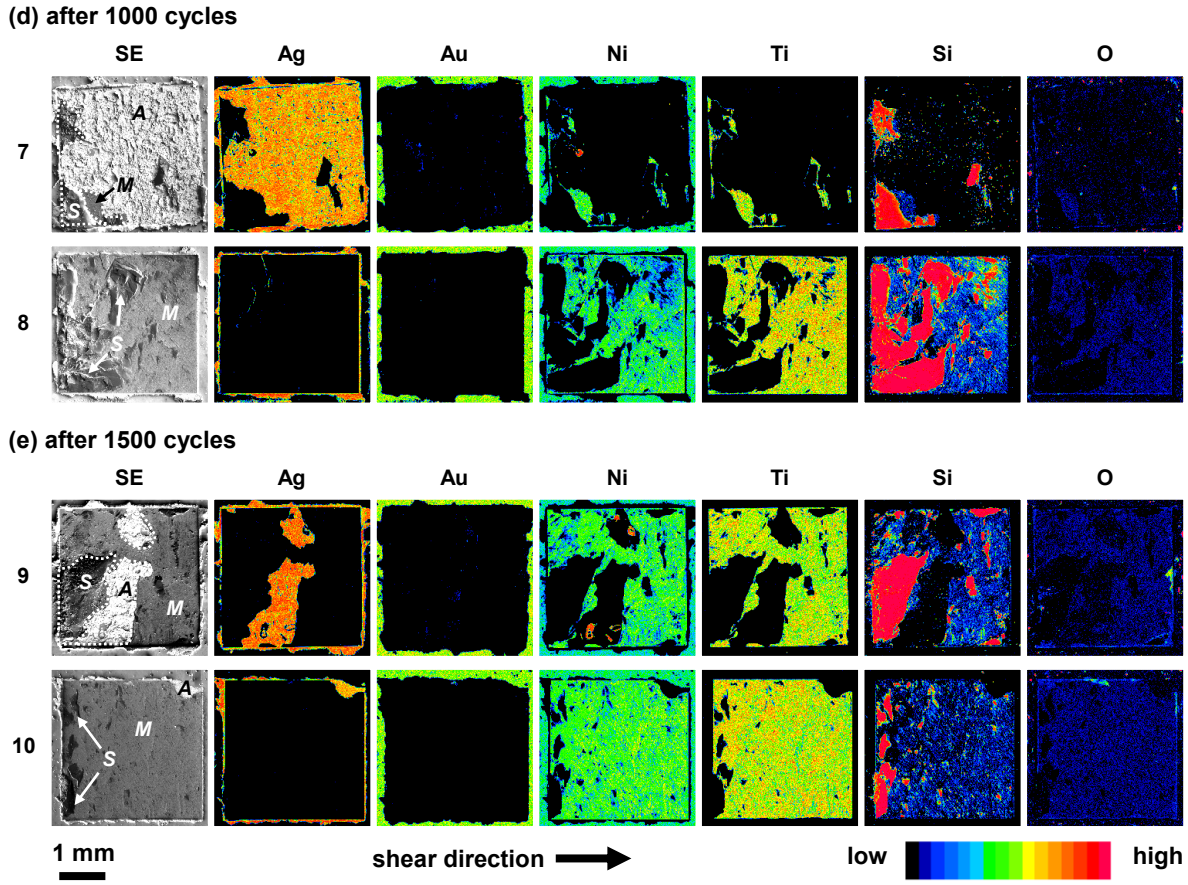

Figure 5.8 (continued)

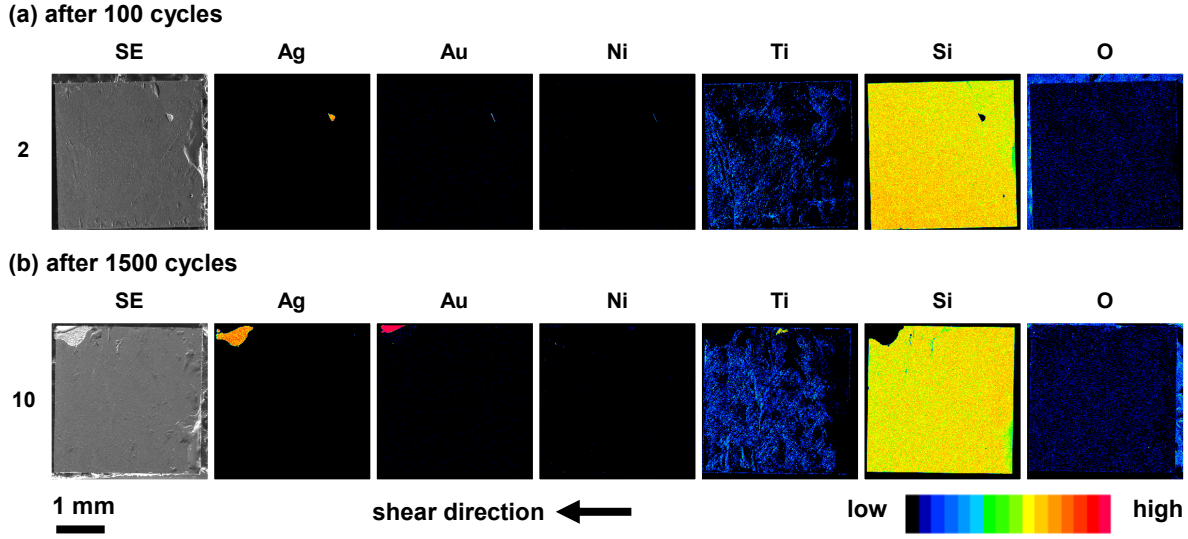

Figure 5.9 EPMA elemental mapping results (Ag, Au, Ni, Ti. Si and O) on the fracture surface (Si side) of Ag nanoporous bonding joint after temperature cycling for **(a)** 1000 cycles (sample 2) and **(b)** 1500 cycles (sample 10).

signals and very weak Si and O signals are detected in metallization fractured region on substrate side from the EPMA results on the *sample 3*, *4*, *6*, *8*, *9* and *10*, as shown in Fig. 5.8. Besides, high Si signal and very weak Ti signal were detected on metallization fractured region Si side as shown in Fig. 5.9. From the EPMA results on the both fracture surfaces of substrate side and Si side, it was confirmed that the metallization fracture was occurred along the Si/Ti interface. Unfortunately, it was unclear whether the Si backside metallization was degraded or not during temperature cycling. Further study on the interfacial reaction between Si chip and backside metallization after temperature cycling will be needed, in order to reveal a cause of metallization fracture and its effect on the shear strength of Ag NPB joint.

5.4.2 Stability of Ag layer after temperature cycling

Fig 5.10 exhibits the cross-sectional FIB images underneath fracture surface after temperature cycling for 1000 cycles (Fig. 5.10(a), same with *sample 8* in Fig. 5.8(d)) and 1500 cycles (Fig. 5.10(b), same with *sample 10* in Fig. 5.8(e)). The stability of Ag layer after temperature cycling could be confirmed from the cross-sectional images of the edge part of Ag NPB joint. The Ag layer exhibits porous structure, as reported in *Chapter 3*. There was no crack propagation in Ag layer after 1500 cycles. It seems that Ag NPB layer shows good stability under temperature cycling, because of the ductile property of Ag and the low elastic modulus due to porous structure.

5.4.3 Fracture morphology of Ag layer and metallization fractured regions

The features of fractured Ag porous layers by shear test and by temperature cycling after 1500 cycles were drastically different, as shown in Fig. 5.11. These fracture morphologies were observed near the corner of Ag NPB joint (substrate side). The fractured Ag layer by shear test, namely no crack propagation during temperature cycling, exhibited clear ductile deformation (necking) along the shear direction, as shown in Fig. 5.11(a). Besides, the fractured Ag layer during temperature cycling exhibits no evidence of necking, as shown in Fig. 5.11(b).

Meanwhile, the metallization fractured region after temperature cycling test for 1500 cycles exhibits cleavage fracture, which was a typical feature of brittle fracture, as shown in Fig. 5.12. It seems that brittle fracture of metallization layer leads to lower joint strength of Ag NPB compared with Ag layer dominant fractured cases.

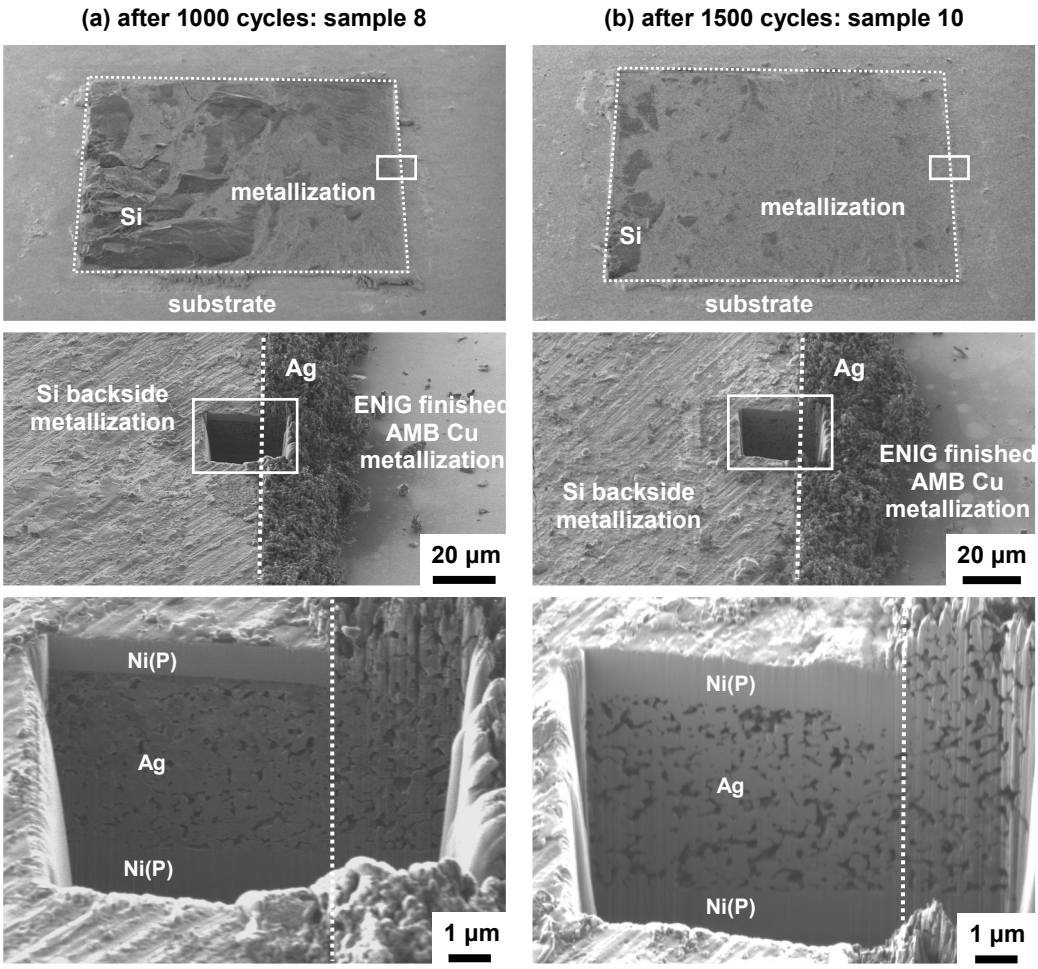

Figure 5.10 Focused ion beam (FIB) secondary electron (SE) images of tilted view of fracture surface (substrate side) and FIB-milled cross-sectional view on the edge parts of Ag nanoporous bonding layer under the fracture surface after temperature cycling for **(a)** 1000 cycles (*sample 8*) and **(b)** 1500 cycles (*sample 10*).

5.5 Comparison of shear strength variation after temperature cycling

5.5.1 Comparison with high temperature solder joint

Fig. 5.13 exhibits a comparison of shear strength change after temperature cycling test between Ag NPB joint, which was conducted in this study, and high temperature solder joints from their reports [9,10]. Kim et al. [9] and Suganuma et al. [10] have been reported on the change of shear strength of high temperature solder joints, including Pb-5Sn, Au-20Sn and Zn-30Sn, with the Si chip and AlN DBC substrate after temperature cycling from -40 °C to 125 °C (ΔT = 165 °C) up to 2000

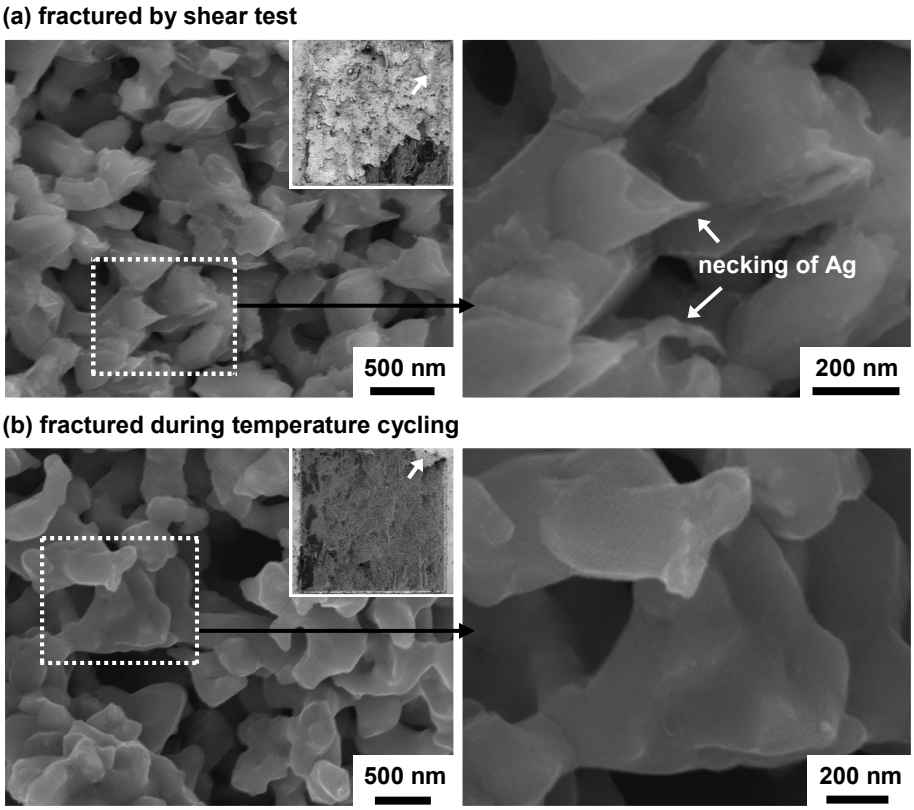

Figure 5.11 Scanning electron microscope (SEM) SE image of fracture morphology on the Ag layer fractured region after temperature cycling for 1500 cycles: (a) fractured by shear test and (b) fractured during temperature cycling. The observation positions are indicated with the *white arrows* in inset low magnification image.

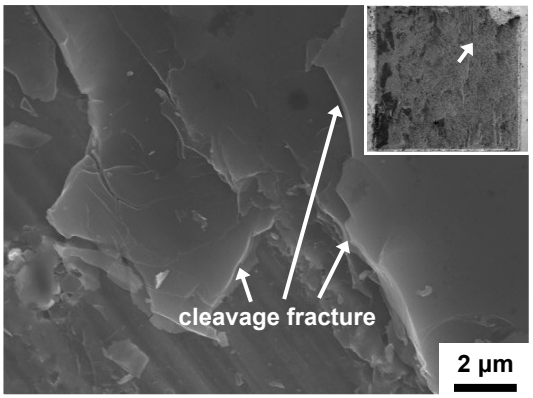

Figure 5.12 SEM SE image of fracture morphology on the metallization fractured region after temperature cycling for 1500 cycles. The observation position is indicated with the *white arrow* in inset low magnification image.

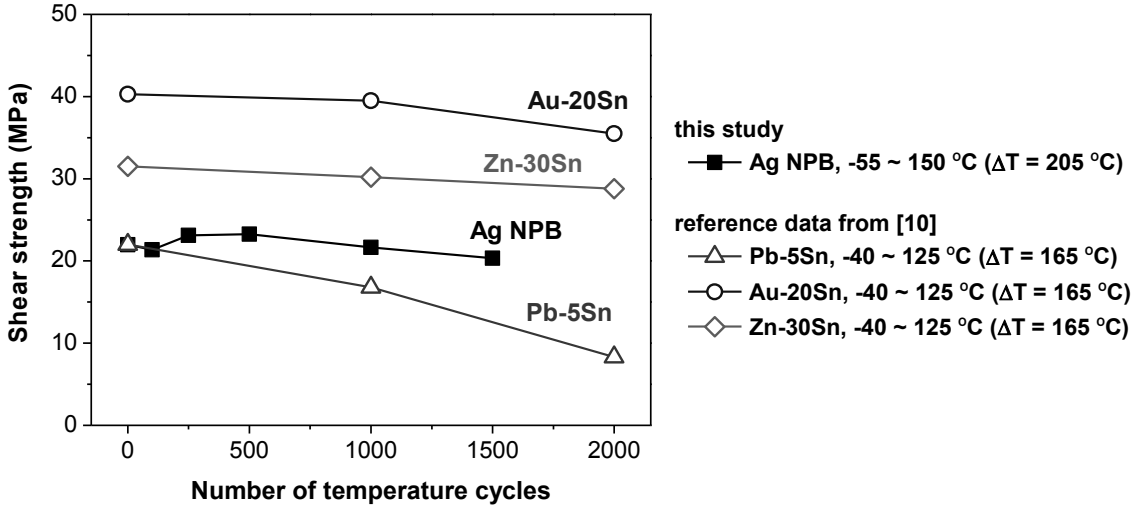

Figure 5.13 Variation of shear strength after temperature cycling for Ag nanoporous bonding joint, marked with *black solid square*, and high temperature solders joints, marked with *color open symbols*. The ranges of temperature cycling test are written in the *legend*. The comparative data for the high temperature solders are reprinted with permission from [10]. Copyright 2009, Springer.

cycles. They have adopted the diffusion barrier of TiN on the substrate finish in order to improve durability of Zn-30Sn and Au-20Sn solder joint under temperature cycling.

The shear strength of Au-20Sn and Zn-30Sn solder joints were relatively stable after 2000 cycles and exhibited higher values than it of Ag NPB. Kim et al. [9] argued that TiN is effective surface finish for the Zn-30Sn solder joint for the improvement of temperature cycle stability by means of retardation of the intermetallic compound (IMC) growth at the bonding interface and prevention of crack propagation between solder and IMC layer. Meanwhile, the shear strength of Pb-5Sn solder gradually degraded as increasing of the number of cycles despite the lower temperature variation (ΔT = 165 °C) compared with this study (ΔT = 205 °C). The Pb-5Sn solder joint exhibited sever cracking in the solder layer after temperature cycling test, and it became the cause of degradation of shear strength. For the comparison of Pb-5Sn joint, it can be concluded that the Ag NPB joint is stable under temperature cycling enough to substitute for Pb-5Sn solder.

5.5.2 Comparison with Ag nanoparticle sintered joint

Fig. 5.14 exhibits a comparison of shear strength change after temperature cycling test between Ag NPB joint and Ag nanoparticle sintered joint from the literatures [11,12]. The detailed

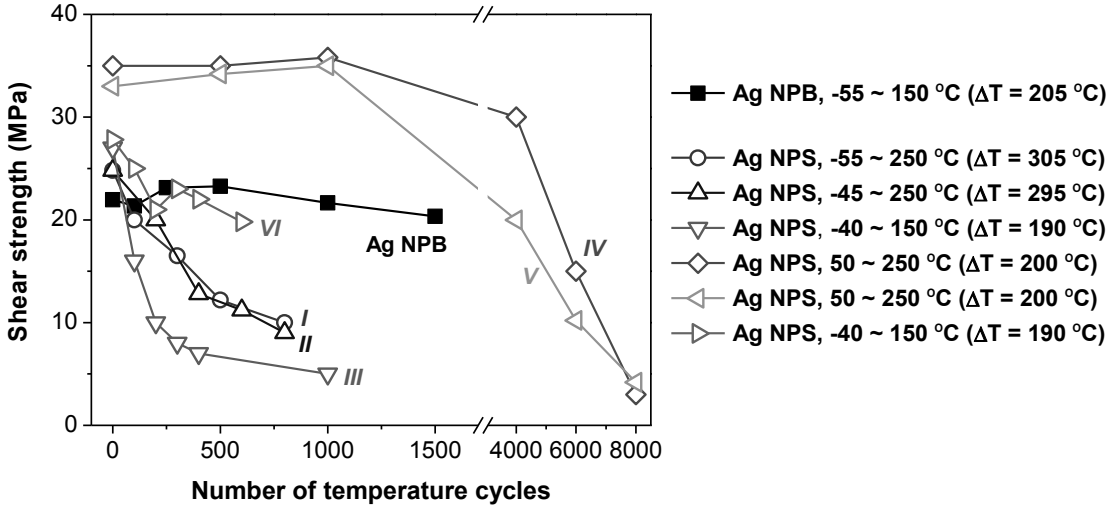

Figure 5.14 Variation of shear strength after temperature cycling for Ag nanoporous bonding (Ag NPB, marked with *black solid square*) and Ag nanoparticle sintering (Ag NPS, marked with *color open symbols*) joints. The ranges of temperature cycling test are written in the *legend*. The comparative data for the Ag NPS are reprinted with permission from [11]. Copyright 2014, Springer

Table 5.2 Chip and substrate materials and conditions of temperature cycling test in the literature [11].

Case	Chip / backside metallization	Substrate / surface finish	Temperature swing condition	Temperature range (ΔT)
I	Si / Ag	AlN DBA / Ni	-55 ~ 250 °C	305 °C
II	SiC / Ag	Al_3O_4 DBC	-45 ~ 250 °C	295 °C
III	Si / Ag	Cu / Ag	-40 ~ 150 °C	190 °C
IV	SiC / Ag	AlN DBC / Au	50 ~ 250 °C	200 °C
V	SiC / Ag	Al_3O_4 DBC / Au	50 ~ 250 °C	200 °C
VI	Si / Ag	Al_3O_4 DBC / Ag	-40 ~ 150 °C	190 °C

component of Ag sintered joint and temperature cycling conditions of each cases are given in Table 5.2. For the case of I, II, III and IV, the shear strength of Ag nanoparticle sintered joint were gradually degraded with increasing of number of cycles.

For the case of IV and V, Bai et al. [12] have been reported on the reliability of Ag sintered joint with SiC on the two direct bond copper (DBC) Al_2O_3 and AlN substrates under temperature

cycling from 50 °C to 250 °C (ΔT = 200 °C). They also performed the comparative study on the effect of surface finish (Ag and Au) together. This report presented that the DBC AlN shows good thermal stability compared with DBC Al_2O_3, since AlN exhibits lower CTE than it of Al_2O_3. In detail, shear strength of them maintained up to 2000 cycles and gradually decreased with increasing of number of cycles. They concluded that Ag sintered die attach with Ag- and Au-coated DBC substrate can withstand up to 4000 cycle and 6000 cycles, respectively, with an assumption that failure criterion is 50 % drop of the shear strength.

5.6 Conclusion

In this chapter, the long-term reliability of Ag NPB joint with the Si chip and AMB Cu Si_3N_4 substrate under temperature cycling from -55 °C to 150 °C was investigated. The shear strength of as-bonded Ag NPB exhibited 22 MPa, and the change of joint strength of Ag NPB after temperature cycling was not significant in average values. The Ag NPB layer also showed good stability with the limited crack propagation along the Ag layer up to 1500 cycles. The fracture occurrence at the Si backside metallization, especially Si/Ti interface, was shown tendency to decrease shear strength; however, it is uncertain whether the degradation of Si/Ti interface resulting from the temperature cycling is occurred.

References

[1] J. Hokka, T.T. Mattila, H. Xu, M. Paulasto-Kröckel, “Thermal cycling reliability of Sn-Ag-Cu solder interconnections—part 1: Effects of test parameters”, *J. Electron. Mater.*, **42** (2013) 1171 –1183.

[2] J. Hokka, T.T. Mattila, H. Xu, M. Paulasto-Kröckel, “Thermal cycling reliability of Sn-Ag-Cu solder interconnections—part 2: Failure mechanisms”, *J. Electron. Mater.*, **42** (2013) 963–972.

[3] IPC standard, *IPC-9701: Performance test methods and qualification requirements for surface mount solder attachments*, 2002.

[4] W. Sabbah, S. Azzopardi, C. Buttay, R. Meuret, E. Woirgard, “Study of die attach technologies for high temperature power electronics: Silver sintering and gold-germanium alloy”, *Microelectron. Reliab.*, **53** (2013) 1617–1621.

[5] JEDEC standard, *JESD22-A104E: Temperature cycling*, 2014.

[6] L.A. Navarro, X. Perpiñà, M. Vellvehi, V. Banu, X. Jordà, "Thermal cycling analysis of high temperature die-attach materials", *Microelectron. Reliab.*, **52** (2012) 2314–2320.

[7] Y.-H. Mei, J.-Y. Lian, X. Chen, G. Chen, X. Li, G.-Q. Lu, "Thermo-mechanical reliability of double-sided IGBT assembly bonded by sintered nanosilver", *IEEE Trans. Device Mater. Reliab.*, **14** (2014) 194–202.

[8] Y. Shi, W. Fang, Z. Xia, Y. Lei, F. Guo, X. Li, "Investigation of rare earth-doped BiAg high-temperature solders", *J. Mater. Sci. Mater. Electron.*, **21** (2010) 875–881.

[9] S. Kim, K.-S. Kim, S.-S. Kim, K. Suganuma, G. Izuta, "Improving the reliability of Si die attachment with Zn-Sn-based high-temperature Pb-free solder using a TiN diffusion barrier", *J. Electron. Mater.*, **38** (2009) 2668–2675.

[10] K. Suganuma, S.-J. Kim, K.-S. Kim, "High-temperature lead-free solders: Properties and possibilities", *JOM*, **61** (2009) 64–71.

[11] R. Khazaka, L. Mendizabal, D. Henry, "Review on joint shear strength of nano-silver paste and its long-term high temperature reliability", *J. Electron. Mater.*, **43** (2014) 2459–2466.

[12] J. Bai, G.-Q. Lu, "Thermomechanical reliability of low-temperature sintered silver die attached SiC power device assembly", *IEEE Trans. Device Mater. Reliab*., **6** (2006) 436–441.

Chapter 6
Summary

6.1 Summary

In this dissertation, solid-state bonding method using Ag nanoporous sheet for high temperature die attach as substitution of Pb-5Sn solder was presented. Objective of this research was the development of Ag nanoporous bonding for high temperature die attach without any organic substances for bonding process as a substitution for high Pb-containing solder. The fabrication of Ag nanoporous sheet, and Ag nanoporous bonding method and its reliability assessment were presented.

In Chapter 1, the immersing issues on the increase of demand for electric-powered vehicle and consequent power electronic devices were summarized. The recent research trends on the power electronics packaging materials which can endure for a long time at severe service conditions and research objective of this research were also presented.

In Chapter 2, the fabrication of Ag nanoporous structure from the Al-Ag precursor alloy using dealloying method was conducted. The microstructural characteristics and its related dealloying behavior in hydrochloric acid of Al-Ag precursor were presented. The fabricated Al-Ag precursor using melt-spinning was consisted of α-Al (main matrix) and γ-Ag_2Al (grain boundary precipitate and Widmanstätten structure). A considerable amount of γ-Ag_2Al was suppressed by the rapid

solidification, 5.6% of γ-Ag_2Al was precipitated. In the early stage of dealloying, the preferential attack on the Ag depleted zone at the grain boundary caused the formation of deep channel. The dealloying rate of α-Al was faster than it of γ-Ag_2Al, so α-Al was preferentially formed Ag nanoporous structure. The Ag nanoporous structure with the size scale of 113 ± 22 nm was obtained through the free corrosion dealloying in HCl for 720 min.

In Chapter 3, the thermo-compression bonding using Ag nanoporous sheet with electroless Ni/immersion Au (ENIG) finished substrate was conducted. The effect of bonding temperature on the microstructure, shear strength and fracture behavior of Ag nanoporous bonding joint were presented The bonding process was conducted under air and N_2 conditions for the comparison. The microstructure of resulting joint exhibited a dense/porous layered sandwich structure, which originated from the simultaneous partial deformation and densification of the nanoporous structure and thermal coarsening. Over the entire interfacial area, there were no large voids or gaps observed. The shear strength of Ag nanoporous bonding joint shows about 15-28 MPa with various joining conditions which was similar value with that of conventional Pb-5Sn solder alloy. The shear strength of Ag nanoporous bonding joint increased with the increase of bonding temperature and the effect of atmosphere was not significant. The atmosphere effect was remarkable only in case of joining temperature of 400 °C.

In Chapter 4, the microstructural evolution and its influence on the shear strength of Ag nanoporous bonding joint with bare Cu and ENIG finished Cu substrate during thermal storage at 250 °C in air condition up to 1000 h were investigated. The results of shear test of Ag nanoporous bonding joint with ENIG finished Cu and bare Cu substrates show 25.7 and 26.6 MPa. The effect of surface finish became significant with increasing of aging time. In case of bare Cu substrate, the shear strength gradually decreased with increasing of thermal storage time, and it showed 11.4 MPa with the aging time of 1000 h. Contrariwise, the shear strength of Ag nanoporous bonding joints with the ENIG finished substrate increased to 32.2 MPa for 100 h, and then gradually decreased. After 750 h, the shear strength showed 25.3 MPa, which is similar value with the initial shear strength of NPB. The formation of two Cu oxides and Kirkendall void at the Cu/Ag interface in case of bare Cu substrate, and formation of brittle NiO and Ni_3P at the interface of Au/Ni in case of ENIG finished Cu substrate were the causes of degradation of Ag nanoporous bonding joint under thermal storage test.

In Chapter 5, the reliability assessment on the Ag nanoporous bonding joint with Si chip and active metal brazed Cu metalized Si_3N_4 substrate under temperature cycling from -55 °C to 150 °C up to 1500 cycles were investigated. The change of joint strength of Ag nanoporous bonding joint after temperature cycling was not significant in average values. The Ag NPB layer also showed good stability with the limited crack propagation along the Ag layer up to 1500 cycles. The fracture occurrence at the Si backside metallization, especially Si/Ti interface, was shown tendency to decrease shear strength.

Consequently, the solid-state thermo-compression bonding method using Ag nanoporous sheet was successfully demonstrated in this research. Initial shear strength of Ag nanoporous bonding joint which was bonded at 300 °C for 30 min with applied pressure of 20 MPa exhibited similar shear strength with it of Pb-5Sn solder joint. Moreover, the long-term reliability of Ag nanoporous bonding joint was superior to Pb-5Sn solder joint. From these results, it can be concluded that Ag nanoporous bonding method strong candidate for the substitution of Pb-5Sn solder for high temperature die attach.

6.2 Environmental assessment on Ag nanoporous bonding

As mentioned above, Ag nanoporous bonding method can be Pb-free die attach method for high temperature electronics with similar bonding strength and superior reliability under temperature cycling compared with Pb-5Sn solder die attach. Besides, other factors should be considered for the practical use, for example environmental aspect and cost . In this section, fabrication process of bonding materials, including Pb-5Sn solder paste, Ag nanoparticle paste and Ag nanoporous sheet were summarized. And qualitative evaluation on the environmental assessment of the bonding process was also performed

6.2.1 Fabrication process of bonding materials

Typical fabrication process of Pb-5Sn solder paste, Ag nanoparticle paste and Ag nanoporous sheet are shown in Fig. 6.1. Pb-5Sn solder is generally applied as a paste which is a mixture of Pb-5Sn solder powder and additives, as shown in Fig. 6.1(a). The micro-sized Pb-5Sn solder powder is fabricated by gas-atomization from the molten solder from 350 – 500 °C. And then, some additives, such as a flux for enhancing wettability of solder and a diluent for controlling the viscosity of paste, are

added [1]. Ag nanoparticle was fabricated by reducing silver nitrate ($AgNO_3$) with sodium citrate dihydrate ($Na_3C_3H_5O_7{\cdot}2H_2O$). $AgNO_3$ and sodium citrate dihydrate was used as a raw material and reducing agent. The reducing process was conducted at 90 °C. Detailed information on the fabrication of Ag nanoparticle paste using reduction of $AgNO_3$ can be found in the literature [2]. Ag nanoporous sheet was fabricated by dealloying method from the Al-Ag melt-spun precursor alloy. Detailed information on the fabrication of Ag nanoporous sheet was given in *Chapter 2* and *Chapter 3*.

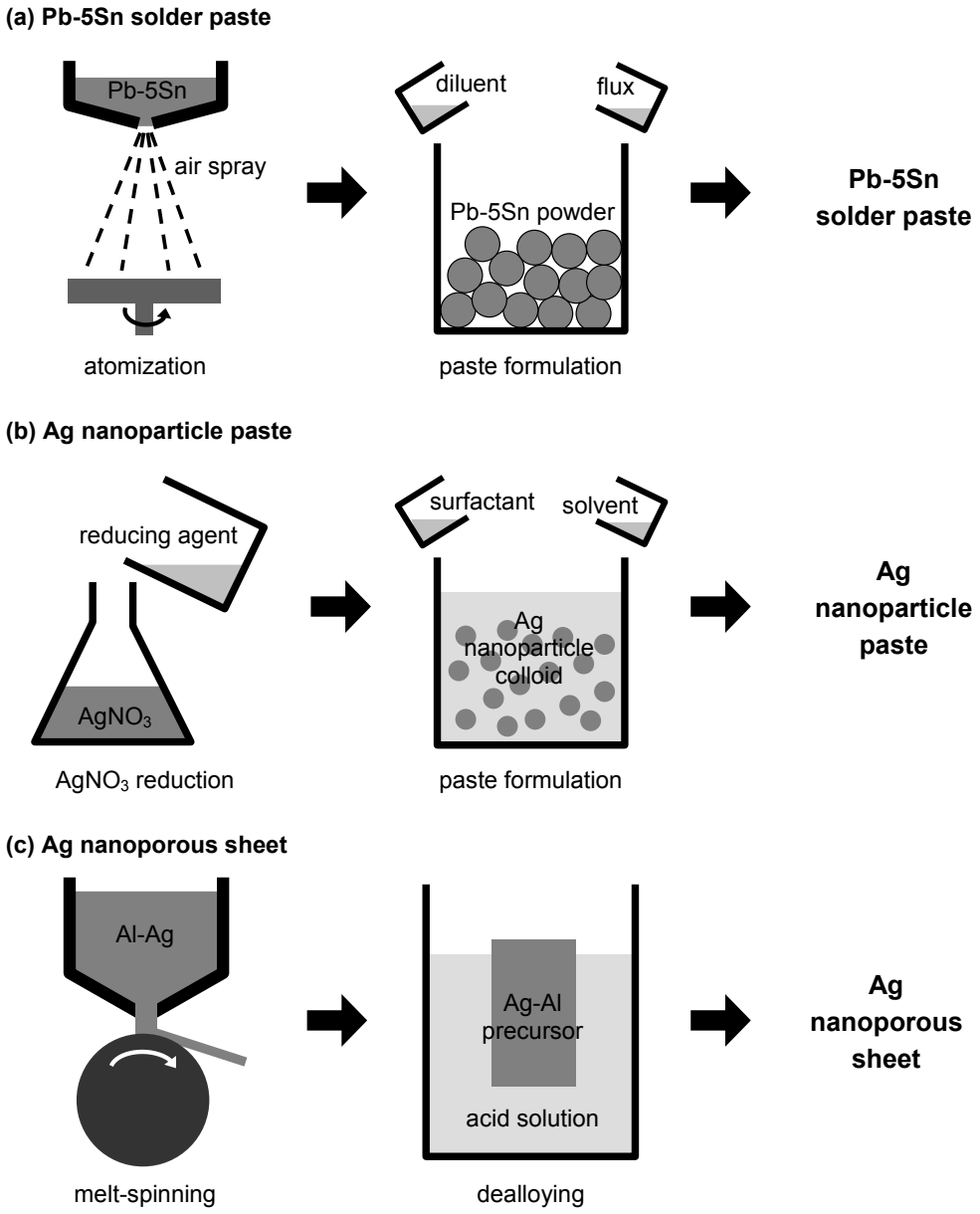

Figure 6.1 Schematic diagrams on the fabrication process of bonding materials, including Pb-5Sn solder paste [1], Ag nanoparticle paste [2] and Ag nanoporous sheet.

6.2.2 Comparative consideration on environmental assessment of bonding materials

The qualitative environmental assessment on the fabrication process of bonding materials, including Pb-5Sn solder, Ag nanoparticle paste and Ag nanoporous sheet, in terms of energy consumption, waste fluid, toxicity of bonding materials, additional materials for bonding process and cost are summarized in Table 6.1. Fabrication of Pb-5Sn solder paste shows good in terms of environmental and economical perspective. As mentioned in *Chapter 1*, however, usage of Pb should be eliminated in order to response environmental regulation. Ag nanoporous sheet have an advantage for bonding material by the elimination of usage of any organic substances. Energy consumption for the fabrication process of Al-Ag melt-spun precursor and waste fluid after dealloying process, however, still remain problems should be solved for the practical use. The quantitative evaluation on the energy consumption, waste fluid and cost of fabrication process of bonding materials also should be necessary.

6.3 Future work

6.3.1 Improvement of bonding process for practical use

In this dissertation, the applied pressure of 20 MPa for Ag nanoporous bonding method was adopted. This value is high for the Si/SiC die attach. An excessive pressure can lead to fracture and damage of Si/SiC chip and electric circuit on the surface of chip. The applied pressure of Ag nanoporous

Table 6.1 Environmental assessment on the fabrication of bonding materials, Pb-5Sn solder paste, Ag nanoparticle paste and Ag nanoporous sheet.

Assessment items	Pb-5Sn solder paste		Ag nanoparticle paste		Ag nanoporous sheet	
Energy consumption (process temperature)	○	350 - 500 °C for melting	◎	80 °C for reduction	△	750 °C for melt-spinning
Waste fluid	◎	-	○	$NaNO_3$	✖	chloride solution
Toxicity of bonding materials	✖	toxic ban from RoHS	○	concern on toxicity of nano material	◎	-
Additional material for bonding process	△	flux	△	solvent vehicle	◎	-
Cost	◎	cheap	△	expensive	△	expensive

◎ excellent ○ good △ need to modification ✖ bad

bonding method should be lowered as low as possible.

It is seemed that the lowering of applied pressure can be achieved by fine tuning of Ag nanoporous structure. It can be achieved by two different ways, including suppression of γ-Ag_2Al in Al -Ag precursor [3] and change of precursor alloy composition [4]. Detsi et al. reported that the fine tuning of Ag nanoporous structure with the ligament size of approximately 30 nm can be achieved by the suppression of γ-Ag_2Al [3]. They prepared Al-Ag precursor alloy with the single phase of α-Al through the heat treatment at 546 °C and subsequent quenching to 3 °C of cold-rolled Al-Ag sheet. Meanwhile, Wang et al. reported that the ligament size of Ag nanoporous structure from Al-Ag precursor alloy gradually decreased with decreasing concentration of Ag in Al-Ag precursor [4]. These are effective methods on the fine tuning of Ag nanoporous structure. And it can be possible to lower the applied pressure of Ag nanoporous bonding process by means of fine tuning of Ag nanoporous sheet.

6.3.2 Large-area bonding

One of the expected advantage of Ag nanoporous bonding technique is same bonding quality at the same bonding condition regardless of bonding area, because it is not necessary to remove any organic substances during the bonding process. In this dissertation, small-area substrates and chip were applied for the solid-state Ag nanoporous bonding. In detail, ENIG finished Cu disk with a radius of 3 mm was used for solid-state bonding in Chapter 3 and thermal storage test in Chapter 4; and Si chip with 3 mm × 3 mm was used for temperature cycle test in Chapter 5. As a next-step, the large-area die attach above 10 mm × 10 mm by Ag nanoporous bonding technique will be necessary for the practical use.

6.3.3 Surface finish selection for high reliability

As presented in Chapter 4, ENIG surface finish of Cu disk can impede the thermal degradation by oxidation at the bonding interface compared with bare Cu substrate; however cannot completely prevent oxidation under thermal storage in air. The oxygen was permeated through Au layer, and then reacted with Ni. This Ni oxidation can lead to degrade the shear strength of Ag nanoporous bonding joint. Thus, another surface finish will be considered for the complete oxidation prevention for higher reliable joint. Li et al. showed the electroless Ni/electroless Pd/immersion Au (ENEPIG) can prevent the Ni migration to surface and the oxygen permeation due to no diffusion path of amorphous Pd layer [5]. ENEPIG can be accepted as a potential candidate of surface finish for high temperature electronics.

6.3.4 Reliability assessment under temperature cycling and power cycling

In Chapter 5, the reliability of Ag nanoporous bonding joint under temperature cycling from –55 °C to 150 °C test was conducted. The Ag bonding layer showed good stability without any significant crack propagation during temperature cycling. The junction temperature of power device gradually increases from the advance in the integration and high performance of power semiconductor, thus, extreme temperature swing with higher maximum temperature (over 200 °C) compared with temperature swing condition in Chapter 5 will be necessary.

Meanwhile, power cycling is a comprehensive reliability test generally adopted for the life-time assessment of power device. A failure of power device during power cycle test can be judged as a voltage increase by 5% or 20% resulting from the wire bond lift-off or a thermal impedance increase by 20% resulting from the thermal fatigue of die attach. Difference between temperature cycling and power cycling is a method. Temperature is varied by temperature controlled chamber during temperature cycling, namely external heating and cooling. In contrast, the power device is heated by the power loss of power semiconductor and is cooled using heat sink during power cycling, namely internal heating and external cooling [6]. The power cycling can offer the similar temperature swing with the practical application. Thus, the additional reliability assessment on the Ag nanoporous bonding joint under power cycle condition will be necessary.

References

[1] J.S. Hwang, “Solder technologies for electronic packaging and assembly”, in: C.A. Harper (Ed.), *Electronic materials and processes handbook*, 3rd edition, McGraw-Hill, New York, 2004.

[2] H. Alarifi, A. Hu, M. Yavuz, Y.N. Zhou, “Silver nanoparticle paste for low-temperature bonding of copper”, *J. Electron. Mater.*, **40** (2011) 1394–1402.

[3] E. Detsi, Z. Vuković, S. Punzhin, P.M. Bronsveld, P.R. Onck, J.T.M. De Hosson, “Fine-tuning the feature size of nanoporous silver”, *CrystEngComm*, **14** (2012) 5402–5406.

[4] X. Wang, Z. Qi, C. Zhao, W. Wang, Z. Zhang, “Influence of alloy composition and dealloying solution on the formation and microstructure of monolithic nanoporous silver through chemical dealloying of Al-Ag alloys”, *J. Phys. Chem. C*, **113** (2009) 13139–13150.

[5] C.C. Li, W.L. Shih, C.K. Chung, C.R. Kao, “Amorphous Pd layer as a highly effective oxidation barrier for surface finish of electronic terminals”, *Corros. Sci.*, **83** (2014) 419–422.

[6] J. Lutz, H. Schlangenotto, U. Scheuermann, R. De Doncker, *Semiconductor power devices: Physics, characteristics, reliability*, Springer, Heidelberg, 2011.

Appendix 1

In-situ lift-out method for TEM sample preparation using FIB/SEM

A1.1 TEM analysis and sample preparation

A transmission electron microscopy (TEM) is a powerful analysis technique for the characterization of materials, and is becoming much more important with the growth of nanomaterials [1]. It can offer meaningful information on the microstructure of materials at high resolution as well as a chemical composition using an energy dispersive X-ray spectroscopy (EDS) and an analysis on the crystal structure using a selected area electron diffraction (SAED) or high resolution lattice image [2–5]. The major advantage of the TEM based X-ray spectroscopy is a great improvement of spatial resolution compared with the scanning electron microscopy (SEM) based X-ray spectroscopy, because of a very fine probe of electron beam (around 0.5-2 nm in STEM mode) and a narrow electron trajectory due to the thin sample. A typical spatial resolution of EDS analysis on TEM with a field emission gun (FEG) can be achieved is approximately under 10 nm [1]. Moreover, the crystallographic information via diffraction related analysis techniques, such as a selected area electron diffraction or an atomic resolution image, can be obtained at the coincident position with EDS analysis [3,5,6]. In this dissertation, the TEM technique has been also widely employed in order to acquire more detailed information on the various phenomena occurred at the nanoscale.

There are several sample preparation techniques for the TEM observation, such as, replica, ion

milling, electro-polishing, ultramicrotomy, tripod polishing and focused ion beam (FIB) methods. Detailed information on the TEM sample preparation methods using FIB can be found elsewhere [7,8]. A proper preparation method should be selected to the materials or objective of analysis. Among these, the FIB technique has been widely employed in the microelectronics field, due to its possibility of site-specific TEM sample preparation [3,5,9]. The maskless milling and deposition in the interesting area can be achieved in FIB. However, there are still some problems of FIB method, for example a surface amorphizing by ion beam induced damage and Ga contamination [7,9,10]. Some researchers has adopted additional surface cleaning method, such as Ar ion beam milling [5] or plasma cleaning [11], in order to avoid this problems.

A1.2 Procedures of *in-situ* lift-out method

The TEM sample was prepared using a multi-beam FIB/SEM system (JIB-4500, JEOL) equipped with two beam columns (electron beam and Ga ion beam) for the milling and observation, two gas injection nozzles (tungsten and carbon) for the deposition and one micro-manipulator (AutoProbe 300, Onmiprobe) for the *in-situ* lift-out, as shown in Fig. A1.1. The procedures of *in-situ* lift-out method can divide three steps: **(1)** preparation of wedge-shaped sample, **(2)** lift-out and mounting to TEM grid, and **(3)** thinning to the final thickness.

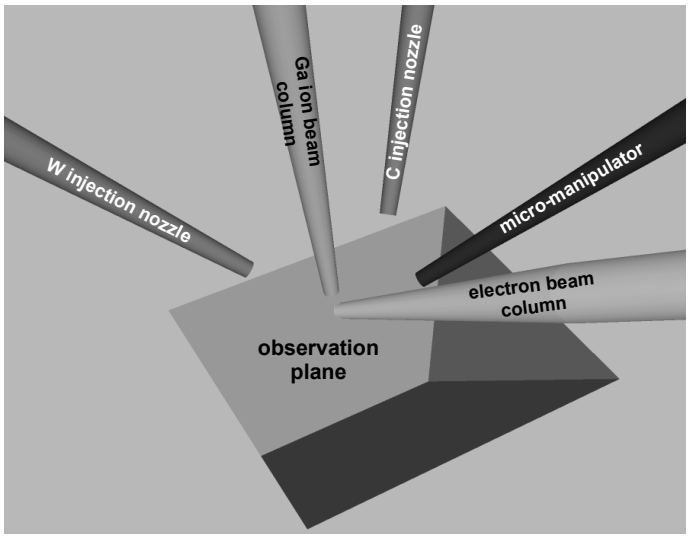

Figure A1.1 Schematic diagram of arrangement of Ga ion beam and electron beam columns of multi-beam FIB/SEM system. The angle between Ga ion beam column and electron beam column is 52°. Two gas injection nozzles (tungsten and carbon) and a micro-manipulator are also installed.

The required thickness of TEM sample was varied with the analysis method and acceleration voltage of electron gun. For the general observation or EDS analysis with 200 kV TEM, the required thickness is approximately 100 nm. For the high resolution TEM observation or electron energy loss spectroscopy (EELS), the required thickness should be under 50 nm. Meanwhile, thick sample with micro scale thickness can be observed using a high voltage TEM (the acceleration voltage over 1 MV) [12]. The minimum thickness which can be achieved using FIB milling is approximately 100 nm, which is suitable for the general TEM observation. The additional milling process, such as a precision ion polishing system (PIPS) [5], in order to obtain more thinner sample for HRTEM or EELS.

(1) Step 1: Preparation of wedge-shaped sample by rough-milling (Fig. A1.2)

Before the loading the sample into the FIB chamber, the surface of bulk or cross-sectioned sample was coated with carbon or palladium-gold by sputtering for the protection layer. As a first step, the carbon layer was deposited with the thickness of 1.5 - 2 μm in the interesting area (height = 5-7 μm, width = 15 - 25 μm), as shown in Fig. A1.2a. Next, the periphery of the target area was milled using the rough Ga ion beam (an acceleration voltage of 30 kV and a current of 1000 pA), except for the bridge

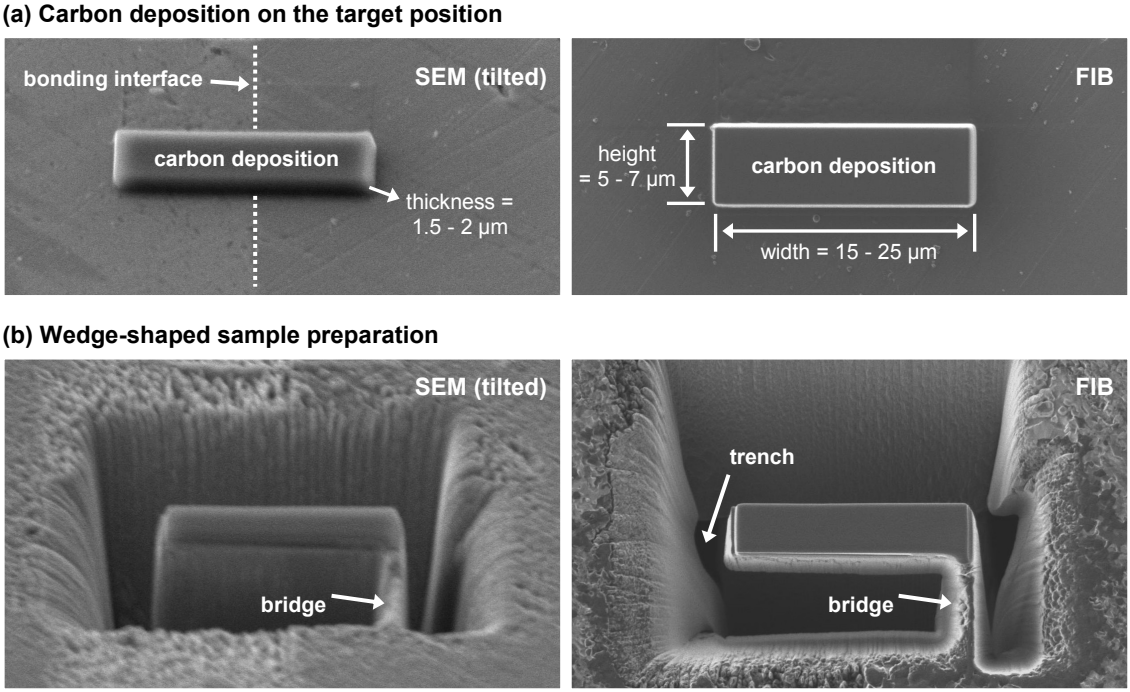

Figure A1.2 Preparation of wedge-shaped sample by rough-milling: **(a)** carbon deposition on the target position and **(b)** wedge-shaped sample preparation by rough-milling.

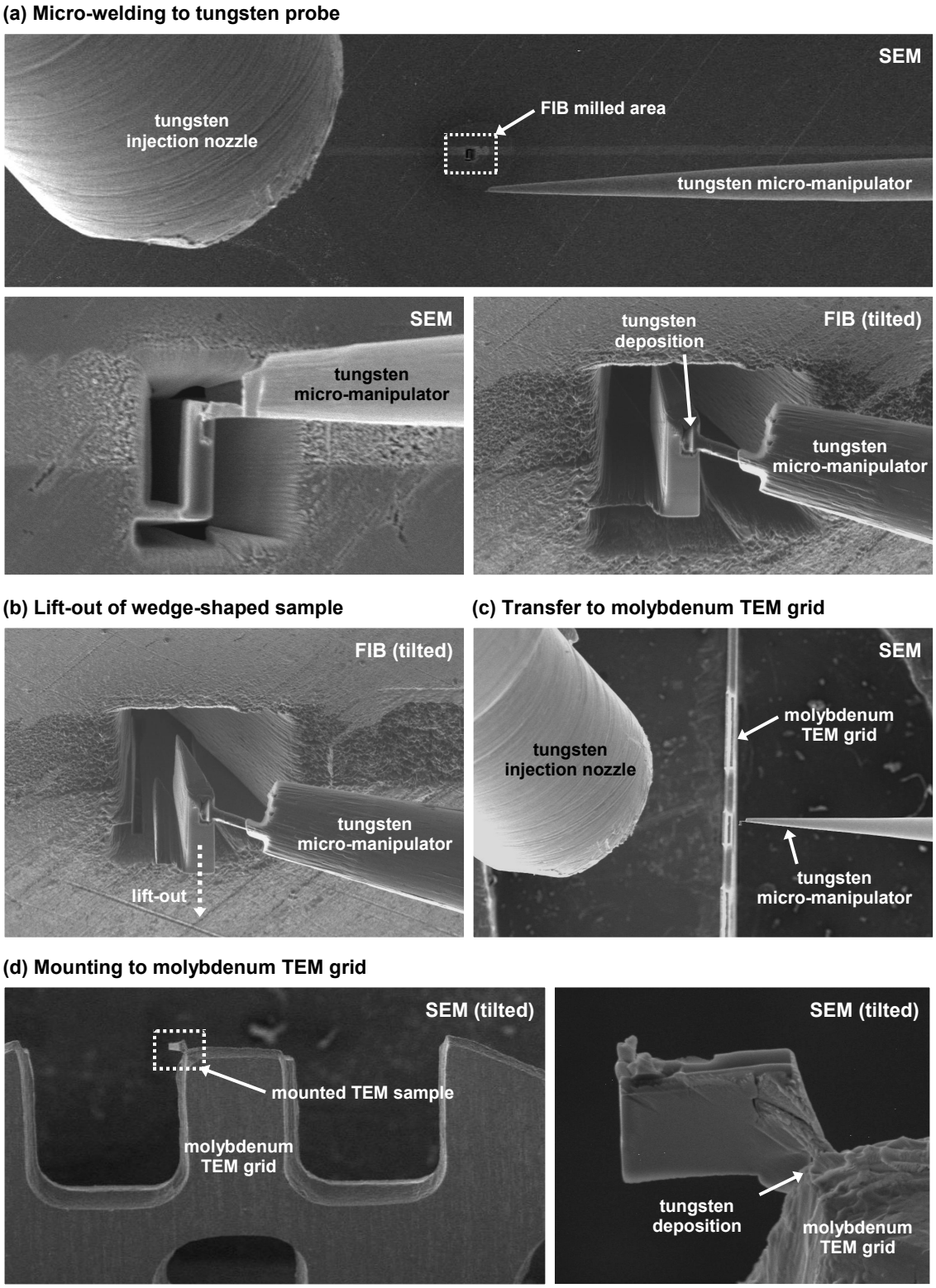

Figure A1.3 Procedures of *in-situ* lift-out: **(a)** micro-welding on the tungsten probe of micro-manipulator via tungsten deposition and in-situ lift-out, **(b)** lift-out from the bulk specimen, and **(c)** transferring and **(d)** mounting of wedge-shaped sample to molybdenum TEM grid.

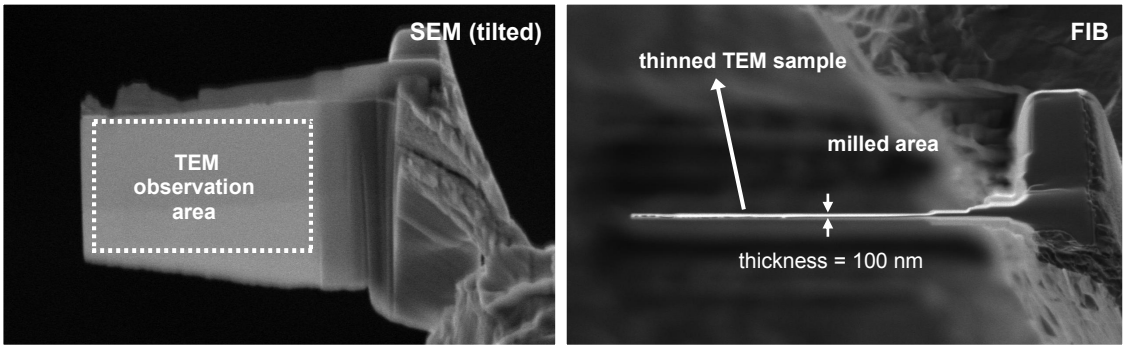

Figure A1.4 Fine-milled sample for TEM observation.

part connected to the bulk sample, As shown in Fig. A1.2b. The trench parts should be sufficiently deep and wide to lift-out except the bridge part.

(2) Step 2: Lift-out of wedge-shaped sample and mounting to TEM grid (Fig. A1.3)

Next step is lift-out of wedge-shaped sample frrom the bulk specimen using micro-manipulator. The micro-manipulator can precisely move in three-dimensional direction (X, Y, and Z axis). The wedge-shaped sample was attached to tungsten micro-manipulator by means of tungsten deposition (Fig. A1.3a). And then, the bridge part was cut in order to separate wedge-shaped sample from the bulk specimen (Fig. A1.3b). The sample stage was changed to molybdenum TEM grid mounted holder (Fig. A1.3(c)). The wedge-shaped sample was mounted on the tip of molybdenum TEM grid by means of tungsten deposition. Finally, the connection between wedge-shaped sample and micro -manipulator was cut using FIB milling (Fig. A1.3(d)).

(3) Step 3: Thinning to the final thickness by fine-milling (Fig. A1.4)

The final step is thinning to the final thickess for the fabrication of electron-transparent sample. In order to minimize the surface damage induced by ion beam, a fine Ga ion beam with the current of 10 pA was adopted for final thinning.

References

[1] D.B. Williams, C.B. Carter, *Transmission electron microscopy: A textbook for materials science*, 2nd edition, Springer, New York, 2009.

[2] P.J. Shang, Z.Q. Liu, X.Y. Pang, D.X. Li, J.K. Shang, "Growth mechanisms of Cu_3Sn on polycrystalline and single crystalline Cu substrates", *Acta Mater*., **57** (2009) 4697–4706.

[3] H. Xu, C. Liu, V.V. Silberschmidt, S.S. Pramana, T.J. White, Z. Chen, V.L. Acoff, "Behavior of aluminum oxide, intermetallics and voids in Cu–Al wire bonds", *Acta Mater*., **59** (2011) 5661–5673.

[4] N. Lu, D. Yang, L. Li, "Interfacial reaction between Sn–Ag–Cu solder and Co–P films with various microstructures", *Acta Mater*., **61** (2013) 4581–4590.

[5] H.G. Kim, S.M. Kim, J.Y. Lee, M.R. Choi, S.H. Choe, K.H. Kim, J.S. Ryu, S. Kim, S.Z. Han, W.Y. Kim, S.H. Lim, "Microstructural evaluation of interfacial intermetallic compounds in Cu wire bonding with Al and Au pads", *Acta Mater*., **64** (2014) 356–366.

[6] R.R. Juluri, A. Rath, A. Ghosh, A. Bhukta, R. Sathyavathi, D.N. Rao, K. Müller, M. Schowalter, K. Frank, T. Grieb, F. Krause, A. Rosenauer, P.V. Satyam, "Coherently embedded Ag nanostructures in Si: 3D imaging and their application to SERS", *Sci. Rep.*, **4** (2014) 4633.

[7] T. Kamino, T. Yaguchi, T. Hashimoto, T. Ohnishi, K. Umemura, "A FIB micro-sampling technique and a site specific TEM specimen preparation method", in L.A. Giannuzzi, F.A. Stevie (eds.), *Introduction to focused ion beams: Instrumentation, theory, techniques and practice*, Springer, New York, pp. 229–246, 2005.

[8] J. Mayer, L.A. Giannuzzi, T. Kamino, J. Michael, "TEM sample preparation and FIB-induced damage", *MRS Bull*., **32** (2007) 400–407.

[9] C.K. Chung, Y.J. Chen, W.M. Chen, C.R. Kao, "Origin and evolution of voids in electroless Ni during soldering reaction", *Acta Mater*., **60** (2012) 4586–4593.

[10] S. Kuwano, T. Fujita, D. Pan, K. Wang, M. Chen, "TEM sample preparation for microcompressed nanocrystalline Ni", *Mater. Trans*., **49** (2008) 2091–2095.

[11] Y. Huh, K. Hong, K. Shin, "Amorphization induced by focused ion beam milling in metallic and electronic materials", *Microsc. Microanal*., **19** (2013) 33–37.

[12] D.-S. Ko, Y.M. Park, S.-D. Kim, Y.-W. Kim, "Effective removal of Ga residue from focused ion beam using a plasma cleaner", *Ultramicroscopy*, **107** (2007) 368–373.

[13] K. Nogita, X.Q. Tran, T. Yamamoto, E. Tanaka, S.D. McDonald, C.M. Gourlay, K. Yasuda, S. Matsumura, "Evidence of the hydrogen release mechanism in bulk MgH_2", *Sci. Rep*., **5** (2015) 8450.

Appendix 2
Fourier mask filtering of HRTEM image

A2.1 Relationship between HRTEM image and corresponding FFT pattern

Fig. A2.1 shows a mathematical relationship between the HRTEM lattice image and the fast Fourier transform (FFT) pattern, where the HRTEM image and the FFT pattern are correspond with real space and reciprocal space, respectively [1]. FFT patterns generally exhibit same results with a selected area diffraction (SAED) pattern. The real space (HRTEM image) can be converted to reciprocal space image (diffraction pattern) using the FFT, and reverse conversion can be achieved by using inverse FFT (IFFT). It is possible to identify crystal structure from the HRTEM image using this FFT calculation [2].

A2.2 Fourier mask filtering and its practical use

Detailed information on the Fourier mask filtering technique has been reported by Kim et al [1]. The designated periodical signal (lattice plane of crystalline material in this case) in HRTEM image only remained through the Fourier mask fintering and subsequent IFFT calculation. As a result it is possible to reduce the noise and to remove particular signal from the HRTEM image on the specific area. This technique has been widely utilized to reveal the dislocation [3] and to reduce the noise of HRTEM image [4,5].

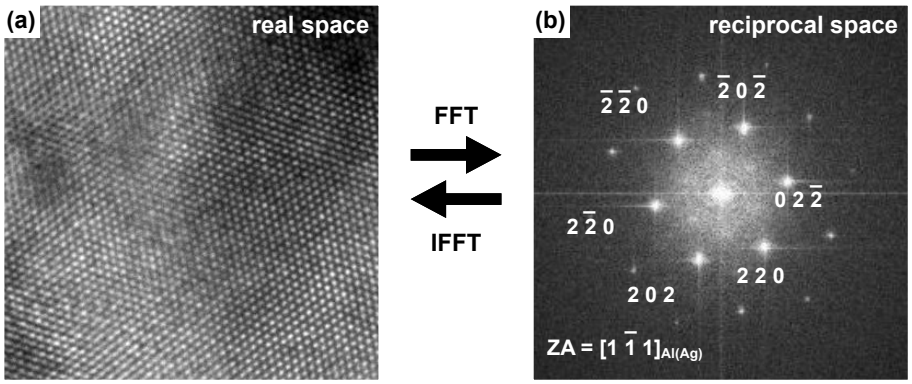

Figure A2.1 Mathematical relationship between **(a)** HRTEM image (real space) and **(b)** corresponding FFT pattern (reciprocal space).

Fig. A2.2 and A2.3 exhibit examples on the utilization of two Fourier mask filtering methods using array mask and spot mask on the HRTEM images. Image processing of HRTEM images was performed using DigitalMicrograph (Gatan), in this dissertation. The noise reduction of HRTEM images can be obtained using an array mask filter on the diffraction patterns and subsequent IFFT calculation, as shown in Fig. A2.2(a) and A2.3(a). Meanwhile, the lattice fringes on the particular plane can be obtained using the spot mask filtering on the particular pair of diffraction patterns on subsequent IFFT

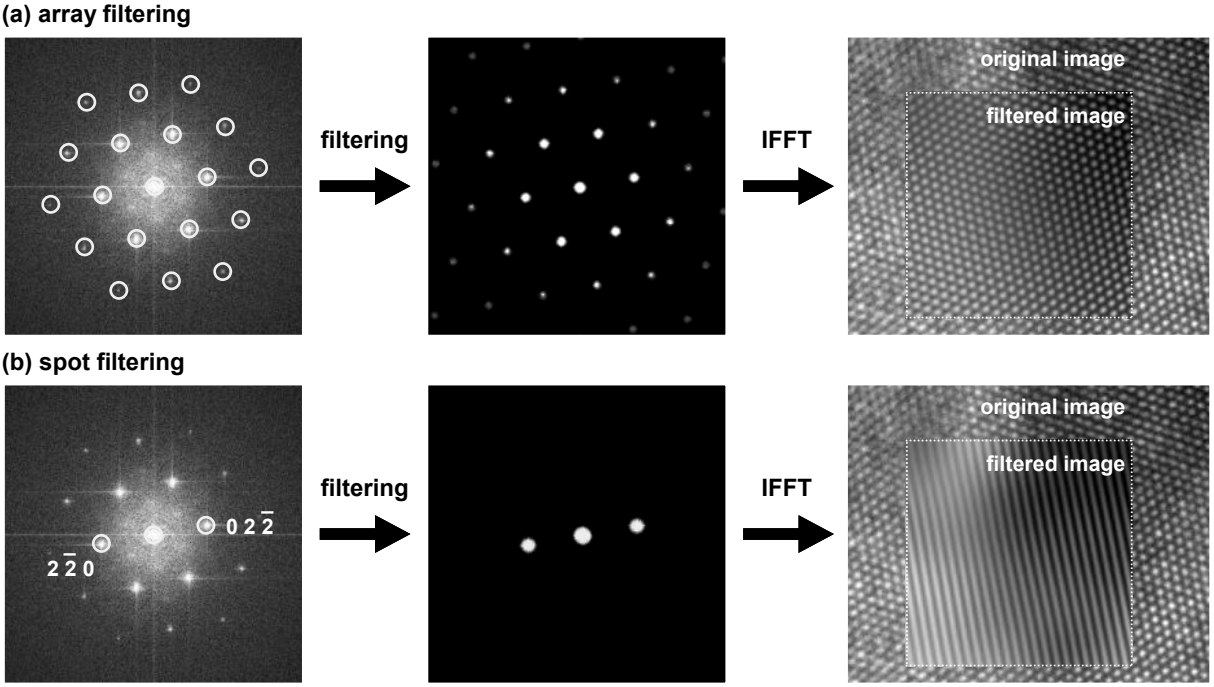

Figure A2.2 The mask filtered FFT pattern and corresponding IFFT image on the HRTEM image of α-Al (Ag) precursor using **(a)** array filter and **(b)** spot filter.

calculation, as shown in Fig. A2.2(b) and A2.3(b). The more accurate measurement of interplanar distance of particular planes also can be achieved using the Fourier mask filtered lattice fringe image, as shown in Fig. A2.4. From the filtered image (Fig. A2.4(a)), the intensity of brightness along the designated line (Fig. A2.4(b)) can be obtained. This technique can reduce the measurement error on the determination of interplanar distance compared with the direct measurement from the raw HRTEM data.

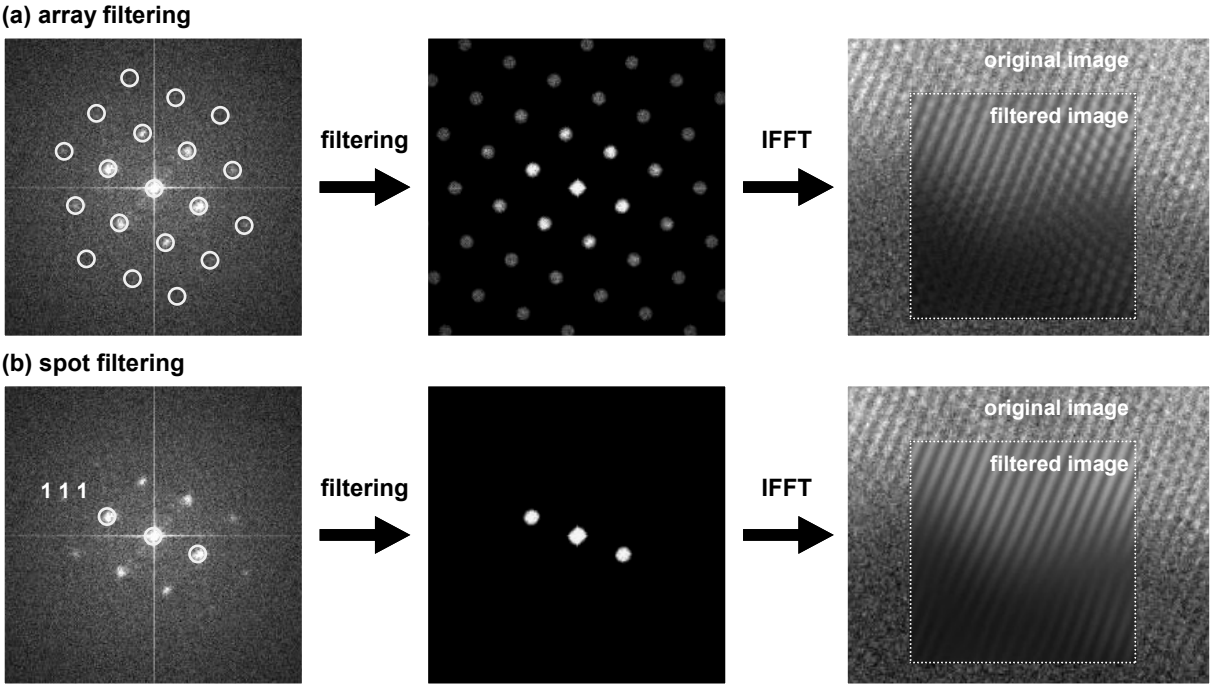

Figure A2.3 The mask filtered FFT pattern and corresponding IFFT image on the HRTEM image of Ag/ Au bonding interface using **(a)** array filter and **(b)** spot filter.

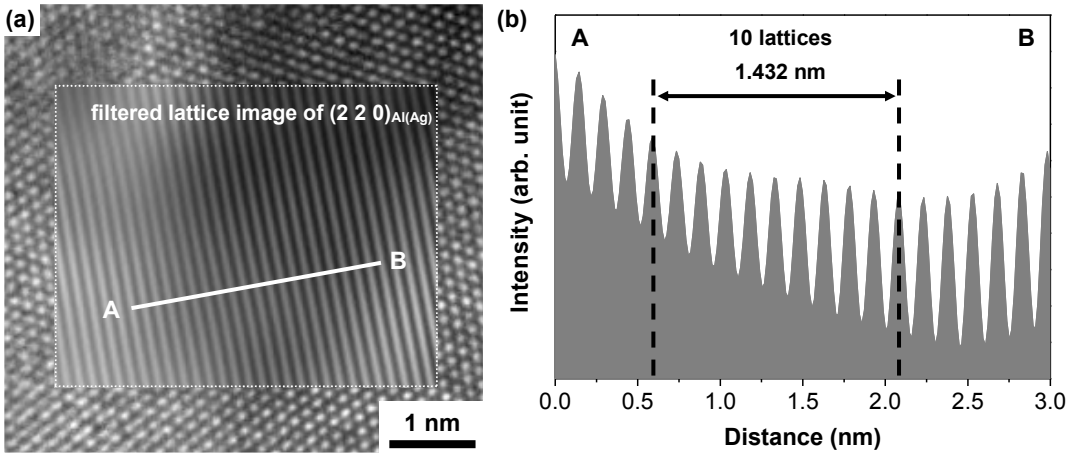

Figure A2.4 **(a)** The spot mask filtered (220) plane image of α-Al(Ag) precursor and **(b)** the intensity profile on the brightness along the designated line in *a*.

References

[1] Y.-M. Kim, J.-M. Jeong, J.-G. Kim, Y.-J. Kim, Y.S. Lim, "Image processing of atomic resolution transmission electron microscope images", *J. Kor. Phys. Soc*., **48** (2006) 250–255.

[2] H.G. Kim, S.M. Kim, J.Y. Lee, M.R. Choi, S.H. Choe, K.H. Kim, J.S. Ryu, S. Kim, S.Z. Han, W.Y. Kim, S.H. Lim, "Microstructural evaluation of interfacial intermetallic compounds in Cu wire bonding with Al and Au pads", *Acta Mater*., **64** (2014) 356–366.

[2] S. Han, L. Zhao, Q. Jiang, J. Lian, "Deformation-induced localized solid-state amorphization in nanocrystalline nickel", *Sci. Rep*., **2** (2012) 493.

[3] S. Godefroo, M. Hayne, M. Jivanescu, A. Stesmans, M. Zacharias, O.I. Lebedev, G. Van Tendeloo, V.V. Moshchalkov, "Classification and control of the origin of photoluminescence from Si nanocrystals", *Nat. Nanotechnol*., **3** (2008) 174–178.

[4] D. Yang, Z. Zheng, Y. Yuan, H. Liu, E.R. Waclawik, X. Ke, M. Xie, H. Zhu, "Sorption induced structural deformation of sodium hexa-titanate nanofibers and their ability to selectively trap radioactive Ra(II) ions from water", *Phys. Chem. Chem. Phys*., **12** (2010) 1271–7.

Research achievements

I List of publications

Peer-reviewed journal articles

1. **Min-Su Kim**, Hiroshi Nishikawa, “Fabrication of nanoporous silver and microstructural change during dealloying of melt-spun Al-20 at.% Ag in hydrochloric acid”, *Journal of Materials Science*, **48** (2013) 5645–5652.
2. **Min-Su Kim**, Hiroshi Nishikawa, “Silver nanoporous sheet for solid-state die attach in power device packaging”, *Scripta Materialia*, **92** (2014) 43–46.
3. Omid Mokhtari, **Min-Su Kim**, Hiroshi Nishikawa, Fumiyoshi Kawashiro, Satoshi Itoh, Takehiko Maeda, Tetsuya Hirose, Takaki Eto, “Investigation of formation and growth behavior of Cu/Al intermetallic compounds during isothermal aging”, *Transactions of the Japan Institute of Electronics Packaging*, **7** (2014) 1–7.
4. **Min-Su Kim**, Hiroshi Nishikawa, “Effects of bonding temperature on microstructure, fracture behavior and joint strength of Ag nanoporous bonding for high temperature die attach”, *Materials Science and Engineering A*, **645** (2015) 264–272.
5. **Min-Su Kim**, Kaori Matsunaga, Yong-Ho Ko, Chang-Woo Lee, Hiroshi Nishikawa, “Reliability of Ag nanoporous bonding joint for high temperature die attach under temperature cycling”, *Materials Transactions*, accepted for publication.
6. **Min-Su Kim**, Hiroshi Nishikawa, “Microstructure evolution and fracture behavior of Ag nanoporous bonding joint with bare Cu and ENIG finished Cu substrate during thermal storage”, in preparation.
7. **Min-Su Kim**, Hiroshi Nishikawa, “Intergranular corrosion of bi-phase Al-Ag precursor for preparation of nanoporous Ag”, in preparation.

Conference proceedings

1. **Min-Su Kim**, Hiroshi Nishikawa, “Effect of joining conditions on the joint strength of Ag nanoporous bonding”, *Proceedings of International Conference on Electronic Packaging (ICEP 2014)*, pp. 521–525, 2014.
2. Omid Mokhtari, **Min-Su Kim**, Hiroshi Nishikawa, Fumiyoshi Kawashiro, Satoshi Itou, Takehiko Maeda, Tetsuya Hirose, Takaki Eto, “Effect of isothermal aging on the growth behavior of Cu/Al intermetallic compounds”, *Proceedings of International Conference on Electronic Packaging (ICEP 2014)*, pp. 144–147, 2014.
3. **Min-Su Kim**, Hiroshi Nishikawa, “Changes of microstructural and interfacial characteristics of Ag nanoporous bonding joint during thermal aging“, *Proceedings of 2014 4th IEEE International Workshop on Low Temperature Bonding for 3D Integration (LTB-3D 2014)*, pp. 151–152, 2014.
4. **Min-Su Kim**, Hiroshi Nishikawa, “Thermal stability of electroless nickel/immersion gold surface finish for direct bond copper”, *Proceedings of 4th Electronics System-Integration Technology Conference (ESTC 2014)*, pp. S94P3/1–4.
5. Kaori Matsunaga, **Min-Su Kim**, Hiroshi Nishikawa, Mikiko Saito, Jun Mizuno, “Relationship between bonding conditions and shear strength of joints using Au nanoporous sheet”, *Proceedings of 4th Electronics System-Integration Technology Conference (ESTC 2014)*, pp. S95P5/1–5, 2014.
6. **Min-Su Kim**, Hiroshi Nishikawa, “Interfacial reaction of Ag nanoporous bonding on electroless nickel/immersion gold substrate“, *Proceedings of International Symposium on Visualization in Joining & Welding Science through Advanced Measurements and Simulation (Visual-JW 2014)*, pp. 193–194, 2014.
7. Kaori Matsunaga, **Min-Su Kim**, Hiroshi Nishikawa, Mikiko Saito, Jun Mizuno, “Effect of Au nanoporous structure on bonding strength”, *Proceedings of International Conference on Electronic Packaging (ICEP 2015)*, pp. 830–833, 2015.
8. **Min-Su Kim**, Hiroshi Nishikawa, “Interfacial reaction and fracture behavior of Ag nanoporous bonding joint during thermal storage at 250 °C”, *Proceedings of International Microsystems, Packaging, Assembly and Circuits Technology Conference (IMPACT 2015)*, pp. 237–239, 2015.
9. Hiroshi Nishikawa, Kaori Matsunaga, **Min-Su Kim**, Mikiko Saito, Jun Minuno, “Effect of isothermal aging at 250 ℃ on shear strength of joints using Au nanoporous bonding for die attach”, *Proceedings of International Conference on High Temperature Electronics (HiTEC 2016)*, pp. 143–147, 2016.

II List of presentations

International conferences

1. **Min-Su Kim**, Hiroshi Nishikawa, "Silver nanoporous structure evolution and microstructural change during dealloying of Al-Ag precursor alloy", *The 15th International Conference on Electronic Materials and Packaging (EMAP 2013)*, Seoul/Ilsan, Korea, October 6–9, 2013.
2. **Min-Su Kim**, Hiroshi Nishikawa, "Microstructure and mechanical behavior of Ag nano-porous bonding layer of Cu/Cu joint", *The 8th International Conference on Processing and Manufacturing of Advanced Materials (THERMEC 2013)*, Las Vegas, USA, December 2–6, 2013.
3. **Min-Su Kim**, Hiroshi Nishikawa, "Effect of joining conditions on the joint strength of Ag nanoporous bonding", *The 14th International Conference on Electronic Packaging (ICEP 2014)*, Toyama, Japan, April 20–22, 2014.
4. Omid Mokhtari, **Min-Su Kim**, Hiroshi Nishikawa, Fumiyoshi Kawashiro, Satoshi Itou, Takehiko Maeda, Tetsuya Hirose, Takaki Eto, "Effect of isothermal aging on the growth behavior of Cu/Al intermetallic compounds", *The 14th International Conference on Electronic Packaging (ICEP 2014)*, Toyama, Japan, April 20–22, 2014.
5. **Min-Su Kim**, Hiroshi Nishikawa, "Changes of microstructural and interfacial characteristics of Ag nanoporous bonding joint during thermal aging", *The 4th IEEE International Workshop on Low Temperature Bonding for 3D Integration (LTB-3D 2014)*, Tokyo, Japan, July 15–16, 2014.
6. **Min-Su Kim**, Hiroshi Nishikawa, "Effect of dealloying time on the ligament size and microstructure of Ag nanoporous structure", *The 15th IUMRS - International Conference in Asia (IUMRS-ICA 2014)*, Fukuoka, Japan, August 24–30, 2014.
7. **Min-Su Kim**, Hiroshi Nishikawa, "Thermal stability of electroless nickel/immersion gold surface finish for direct bond copper", *The 4th Electronics System-Integration Technology Conference (ESTC 2014)*, Helsinki, Finland, September 16–18, 2014.
8. Kaori Matsunaga, **Min-Su Kim**, Hiroshi Nishikawa, Mikiko Saito, Jun Mizuno, "Relationship between bonding conditions and shear strength of joints using Au nanoporous sheet", *The 4th Electronics System-Integration Technology Conference (ESTC 2014)*, Helsinki, Finland, September 16–18, 2014.
9. Kaori Matsunaga, **Min-Su Kim**, Hiroshi Nishikawa, Mikiko Saito, Jun Mizuno, "Shear strength of Cu/Cu joints using Au nanoporous sheet for high-temperature application", *The 5th International Symposium on Advanced Materials Development and Integration of Novel Structured Metallic and Inorganic Materials (AMDI-5)*, Tokyo, Japan, November 19, 2014.

10. Hiroshi Nishikawa, Kaori Matsunaga, **Min-Su Kim**, Mikiko Saito, Jun Mizuno, "Pressure-assisted bonding process using nanomaterials for electronic packaging", *The 5th International Symposium on Advanced Materials Development and Integration of Novel Structured Metallic and Inorganic Materials (AMDI-5)*, Tokyo, Japan, November 19, 2014.
11. **Min-Su Kim**, Hiroshi Nishikawa, "Interfacial reaction and joint strength of Ag nanoporous bonding on electroless nickel/immersion gold substrate", *The 3rd International Symposium on Visualization in Joining & Welding Science through Advanced Measurements and Simulation (Visual-JW 2014)*, Osaka, Japan, November 26–28, 2014.
12. Kaori Matsunaga, **Min-Su Kim**, Hiroshi Nishikawa, Mikiko Saito, Jun Mizuno, "Effect of Au nanoporous structure on bonding strength", *The 15th International Conference on Electronic Packaging (ICEP 2015)*, Kyoto, Japan, April 20–22, 2015.
13. Kaori Matsunaga, **Min-Su Kim**, Hiroshi Nishikawa, Mikiko Saito, Jun Mizuno, "Microstructure of Cu-to-Cu joint using nanoporous bonding", *The 6th International Symposium on Advanced Materials Development and Integration of Novel Structured Metallic and Inorganic Materials (AMDI-6)*, Tokyo, Japan, June 9, 2015.
14. **Min-Su Kim**, Hiroshi Nishikawa, "Effect of isothermal aging on microstructure and joint strength of Ag nanoporous bonding for high temperature die attach", *The 10th International Microsystems, Packaging, Assembly and Circuits Technology Conference (IMPACT 2015)*, Taipei, Taiwan, October 21–23, 2015.
15. **Min-Su Kim**, Hiroshi Nishikawa, "Reliability of die attach using Ag nanoporous sheet for high temperature electronics", *TMS 145th Annual Meeting and Exhibition (TMS 2016)*, Nashville, USA, February 14–18, 2016.
16. Hiroshi Nishikawa, Kaori Matsunaga, **Min-Su Kim**, Mikiko Saito, Jun Minuno, "Effect of isothermal aging at 250 ℃ on shear strength of joints using Au nanoporous bonding for die attach", *International Conference on High Temperature Electronics (HiTEC 2016)*, Albuquerque, USA, May 10–12, 2016.
17. **Min-Su Kim**, Hiroshi Nishikawa, "High temperature die attach without organic materials using Ag nanoporous material", *International High-Technology Environment, Safety and Health Conference 2016 (IHTESH 2016)*, Kobe, Japan, May 31–June 2, 2016.

Domestic conferences

1. 松永　香織, **Min-Su Kim**, 西川　宏, 斎藤　美紀子, 水野　潤, "Au ナノポーラスシートを用いた接合部のせん断強度評価", *平成 26 年スマートプロセス学会春季総合学術講演会*, 大阪, 2014 年 5 月.

2. 松永　香織, **Min-Su Kim**, 西川　宏, 斎藤　美紀子, 水野　潤, “Au ナノポーラス接合の接合材表面構造と接合強度の関係”, *第 24 回マイクロエレクトニクスシンポジウム*, 大阪, 2014 年 9 月.
3. 松永　香織, **Min-Su Kim**, 西川 宏, 斎藤 美紀子, 水野　潤, “ダイボンディング用の Au ナノポーラスシートの作製”, *第 21 回「エレクトロニクスにおけるマイクロ溶接・実装技術」シンポシウム*, 横浜, 2015 年 2 月.
4. 松永　香織, **Min-Su Kim**, 西川　宏, 斎藤　美紀子, 水野　潤, “Au ナノポーラスシートを用いた接合体の高温信頼性”, *第 25 回マイクロエレクトニクスシンポジウム*, 大阪, 2015 年 9 月.
5. **Min-Su Kim**, 西川　宏, “銀ナノポーラス材料を用いた接合部の高温放置試験による微細組織変化”, *第 22 回「エレクトロニクスにおけるマイクロ溶接・実装技術」シンポシウム*, 横浜, 2016 年 2 月.
6. 松永　香織, **Min-Su Kim**, 西川　宏, 斎藤　美紀子, 水野　潤, “定電位電解 Au ナノポーラスシートによる Cu/Cu 接合の検討”, *第 22 回「エレクトロニクスにおけるマイクロ溶接・実装技術」シンポシウム*, 横浜, 2016 年 2 月.

Acknowledgment

I would like to express my sincere gratitude to my supervisor, *Assoc. Prof. Hiroshi Nishikawa,* for his support and academic guidance throughout my doctoral course. I would also like to appreciate members of doctoral committee, *Prof. Shinsuke Yamanaka, Prof. Michihiko Ike* and *Prof. Akio Hirose*, for their insightful comments and helpful discussion for this dissertation. I would also appreciate staff of Joining and Welding Research Institute, *Assoc. Prof. Makoto Takahashi, Mr. Kenji Asano, Mr. Makoto Murakami* and *Mr. Takuya Ogura,* for technical supports.

I would like to express the appreciation to members and alumni of Nishikawa Laboratory, *Ms. Kimiko Ikkai, Dr. Myong-Hoon Roh, Dr. Omid Mohktari, Ms. Kaori Matsunaga, Mr. Xiangdong Liu, Mr. Siliang He, Mr. Jun Tajima, Mr. Jun Matsunobu, Dr. Li-Ngee Ho, Mr. Keiichi Niwa, Mr. Kunio Ueda, Mr. Shinya Kubota, Mr. Makoto Ujino* and *Mr. Shinya Ojima*. for their kind support.

I would like to express the appreciation to my colleagues of Osaka University, *Dr. Kwang-Woon Jung, Dr. Su-Jin Lee, Dr. Sun-Woog Kim, Dr. Youngseok Kim, Dr. Se-Min Park, Dr. Jung-Nam Bae, Dr. Eun-Jun Chun* and *Dr. Jong-Uk Park*., for their warm encouragement and invaluable friendship.

I wish to express my thanks to members of Micro-Joining Center of Korea Institute of Industrial Technology, *Dr. Jung-Han Kim, Dr. Jong-Hoon Kim, Dr. Chang-Woo Lee, Dr. Jun-Ki Kim, Dr. Sehoon Yoo, Dr. Jung-Hwan Bang* and *Dr. Yong-Ho Ko,* for their useful advice on my research.

Finally, I would like to express my sincere appreciation and love to my parents and sister, for their careful concern, moral support and dedication.

Min-Su Kim
Division of Sustainable Energy and Environmental Engineering, Graduate School of Engineering
Department of Smart Green Processing, Joining and Welding Research Institute
Osaka University